



**HAL**  
open science

# Manipulation of the nuclear spin states of $^{87}\text{Sr}$ in degenerate $\text{SU}(N)$ -symmetric Fermi gases

Andrea Litvinov

► **To cite this version:**

Andrea Litvinov. Manipulation of the nuclear spin states of  $^{87}\text{Sr}$  in degenerate  $\text{SU}(N)$ -symmetric Fermi gases. Quantum Physics [quant-ph]. Sorbonne Paris Nord, 2023. English. NNT: . tel-04201342

**HAL Id: tel-04201342**

**<https://sorbonne-paris-nord.hal.science/tel-04201342>**

Submitted on 9 Sep 2023

**HAL** is a multi-disciplinary open access archive for the deposit and dissemination of scientific research documents, whether they are published or not. The documents may come from teaching and research institutions in France or abroad, or from public or private research centers.

L'archive ouverte pluridisciplinaire **HAL**, est destinée au dépôt et à la diffusion de documents scientifiques de niveau recherche, publiés ou non, émanant des établissements d'enseignement et de recherche français ou étrangers, des laboratoires publics ou privés.

Public Domain

UNIVERSITE PARIS XIII - SORBONNE PARIS NORD  
Ecole Doctorale Sciences, Technologies, Santé Galilée

---

**Manipulation des états de spin nucléaires du  $^{87}\text{Sr}$   
dans des gaz de Fermi dégénérés en symétrie SU(N)**

**Manipulation of the nuclear spin states of  $^{87}\text{Sr}$   
in degenerate SU(N)-symmetric Fermi gases**

---

THESE DE DOCTORAT  
présentée par

**Andréa LITVINOV**  
Laboratoire de Physique des Lasers

Pour l'obtention du grade de  
DOCTEUR EN PHYSIQUE

Soutenue le 10 Janvier 2023 devant le jury d'examen composé de:

<b>FERLAINO Francesca, IQOQI</b>	<b>Présidente du Jury</b>
<b>BOUCHOULE Isabelle, LCF</b>	<b>Rapporteuse</b>
<b>BEUGNON Jérôme, LKB</b>	<b>Rapporteur</b>
<b>CHEVY Frédéric, ENS</b>	<b>Examineur</b>
<b>DUBESSY Romain, LPL</b>	<b>Examineur</b>
<b>ROBERT-DE-SAINT-VINCENT Martin, LPL</b>	<b>Examineur</b>
<b>LABURTHE-TOLRA Bruno, LPL</b>	<b>Directeur de thèse</b>
<b>GORCEIX Olivier, LPL</b>	<b>Co-directeur de thèse</b>



# Contents

<b>1 Fermi gases of <math>^{87}\text{Sr}</math> in 3D optical lattices - Experimental Setup</b>	<b>13</b>
1.1 Cooling $^{87}\text{Sr}$ to Fermi degeneracy	14
1.1.1 Energy levels	14
1.1.2 Oven - Transverse cooling and Zeeman slower	16
1.1.3 $^1S_0 \leftrightarrow ^1P_1$ broadband MOT - $^3P_2$ shelving	17
1.1.4 Repumping metastable $^3P_2$	18
1.1.5 $^1S_0 \leftrightarrow ^3P_1$ narrow MOT	19
1.1.6 Optical dipole trap loading	22
1.1.7 Forced evaporation	27
1.2 Optical lattices	27
1.2.1 1064 nm 1D lattice	30
1.2.2 532 nm 2D lattice	35
<b>2 Absorption imaging of objects smaller than the resolution limit</b>	<b>37</b>
2.1 Motivations	38
2.1.1 Measuring the interaction energy of an SU(10) degenerate Fermi gas	38
2.1.2 Distorsion of imaged in-situ density	39
2.1.3 Incorrect estimation of the pixelated local density	40
2.2 Non-linear correction on the measurement of the sub-resolved local density	42
2.2.1 Parametrization of the density dependent correction	43
2.2.2 Calibration of the non-linear correction	45
2.3 Experimental demonstration	47

2.3.1	Production of degenerate Fermi gases expanding along one direction only	47
2.3.2	Recovery of the unresolved transverse sizes $\sigma_x$ of elongated gases	47
2.3.3	Recovery of the distorted longitudinal density profiles	52
2.4	Measurement attempt of the mean field interaction energy in a SU(10) degenerate Fermi gas	55
<b>3</b>	<b>Preparation and measurement of the spin populations in a Fermi gas of <math>^{87}\text{Sr}</math></b>	<b>59</b>
3.1	Measurement of the spin populations	60
3.1.1	Experimental procedure	61
3.1.2	Adiabatic following - Dressed-states picture	63
3.1.3	Spin sensitivity	68
3.1.4	Spin dependent momentum transfer in SU(10) manifold	70
3.1.5	Simultaneous measurement of four spin populations	75
3.1.6	Intensity window for improved adiabaticity	77
3.2	Selective preparation of polarized Fermi sea of $^{87}\text{Sr}$	79
3.2.1	Optical pumping	79
3.2.2	Controlling the number of spin components from 1 to 10	88
3.2.3	Spin purification to prepare a polarized Fermi sea	94
3.2.4	Polarized Fermi sea	96
<b>4</b>	<b>Coherent manipulation of the nuclear spin states of <math>^{87}\text{Sr}</math></b>	<b>99</b>
4.1	Degeneracy lift associated with spin dependent light shift	101
4.1.1	Tensor dynamic polarizability	101
4.1.2	Scattering rate	105
4.1.3	Tensor light shift associated with the intercombination line	108
4.2	Engineering the degeneracy lift of $^{87}\text{Sr}$ ground state manifold	112
4.2.1	Experimental design	112
4.2.2	Measurement of the spin dependent light shifts	112
4.2.3	Measurement of the scattering rate	115
4.2.4	Spin depolarization	118

4.3	Selective global manipulation of the spin states	118
4.3.1	Scheme overview	119
4.3.2	Spectrum of the Raman transitions in the $^1S_0$ manifold	119
4.3.3	Engineering selective spin flips	125
4.4	Site selective adiabatic passage to prepare spin textures - Outlook	129
4.4.1	General Idea	129
4.4.2	Geometry of the lattices	130
4.4.3	Site dependent Raman resonances	133
4.4.4	Predicted texture writing	134
<b>5</b>	<b>2D Fermi gases in the lowest band of a low recoil 1D lattice</b>	<b>137</b>
5.1	Limit to the atom number for fermions in the lowest band	139
5.2	Adiabatic loading of the lowest band : collision requirements	140
5.3	Loading experiments and measurement of the band populations with a Boltzmann approximation	141
5.4	Band populations in the semi classical approximation for a 2D gas of Fermions	146
5.4.1	Derivation of the number of atoms in each band	146
5.4.2	Accounting for multiple layers in the lattice	149
5.4.3	Fit function with time of flight imaging	151
5.5	Semi-classical measurement of the bands populations of several independent 2D layers	153
5.5.1	Analysis of a single image	153
5.5.2	Systematic study as a function of the evaporation depth, for SU(3) and SU(10) gases	157
5.5.3	Preparation of degenerate Fermi 2D gases with improved adiabaticity	159
5.6	Conclusion and outlook	161
<b>A</b>	<b>Basic theory for d-dimensional Fermi gases in harmonic traps</b>	<b>167</b>
A.1	Density of states and Fermi energy	167
A.1.1	3D harmonic trap tightly confined along one direction only	168

A.2 Density and chemical potential, exact derivation in the semi-classical regime . . . . .	170
A.3 Thermodynamics and entropy, derivation in the semi-classical regime . . . . .	171
A.4 Thermodynamics, entropy and chemical potential, degenerate approximations . . . . .	174
A.5 Thermodynamics, entropy and chemical potential, classical gas approximations . . . . .	177
<b>B Basic theory for optical lattices</b>	<b>179</b>
B.1 Eigenstates and energy bands . . . . .	179
B.2 Adiabatic lattice loading with fermions . . . . .	182
<b>C Adiabatic passages in <math>\Lambda</math> scheme</b>	<b>185</b>
C.1 Two ground states . . . . .	185
C.2 Three states manifold . . . . .	188
C.3 Experimental optimization of adiabatic passage . . . . .	191
<b>D Guided expansion - parallaxe - anticonfinement</b>	<b>195</b>
D.1 Derivation . . . . .	196
D.1.1 Effective gravity . . . . .	196
D.1.2 Center of mass . . . . .	197
D.1.3 Cloud width . . . . .	198
D.2 Measurements . . . . .	199

# Introduction

Emergent properties arise from collective systems whose whole is not reducible to its individual components [Lew75]. Pioneering discoveries on superconductivity and superfluidity illustrate the complexity of such systems for which experimental research prevailed in the realm of quantum physics. The sudden vanishing resistance of mercury at 4.2 K, first observed by Heike Kamerlingh Onnes in 1911 [DK10], is an outstanding example of collective phenomena as superconductivity was just discovered. Later, the observation of abnormally low viscosity in ultra cold helium 4 [Kap38; AM38] marked the discovery of superfluidity.

*Degenerate quantum gases* have become an ideal platform for the study of collective phenomena. The high degree of control and tunability of lasers and magnetic fields gives the possibility to shape arbitrary potentials [GWO00; BDZ08; LZB19] and to tune inter-atomic interactions [Chi+10; FJL00]. On the one hand, the first realization of a Bose-Einstein condensate [And+95] paved the way for extensive research on superfluids, from the study of the hydrodynamic oscillations in a Bose gas [Sta+98], to the realization of phase coherent arrays of superfluid droplets [Nor+21]. On the other hand, it was also demonstrated that gases of fermions can be cooled to quantum degeneracy [DJ99]. Following the original idea of Feynman [Fey82], proposals have suggested the realization of quantum simulators for the Fermi-Hubbard model [Hof+02]. Repulsive fermions in an optical lattice allow to realize an ideal and tunable version of the Hubbard model [Hub63; Hub64], a paradigm for the multitude of strong correlation problems in condensed matter physics. The experimental trapping of fermions in optical lattices [Köh+05], and later entering into the strongly correlated regime [Sch+08; Jör+08], are the first steps for the study of quantum magnetism with fermions [BDZ08].

*Active research on the Fermi-Hubbard model* led to the realization of numerous quantum simulators [BDZ08; Ess10; GB17]. Typically, two spin states of alkali fermions such as potassium 40 [Che+15; Dre+17], or lithium 6 [Gre+16; Bol+16; Par+16], are trapped in optical lattices in the strongly interacting regime. Most of these experiments are suited to the analogy with spin half solid states physics, in the so-called SU(2) symmetry in the case of spin-independent interaction properties. Spin ordering and antiferromagnetic correlations, emerging from the collective spin system, are probed with single site resolution using most advanced atomic microscopes [Bak+09].

*Beyond spin half physics*, proposals suggested the study of quantum magnetism in enlarged SU(N) symmetry [CHU09; HGR09; Gor+10; CR14], with no solid states analog. Involving an enhanced number of configurations due to the large spin degree of freedom, exotic collective phenomena are expected. For instance, SU(N)-symmetric exchange interaction shall result in frustrated spin ordering [HGR09]. Experimental realizations of the SU(N) Hubbard model yielded the measurements of the antiferromagnetic correlations [Oza+18; Tai+20] with alkaline-earth like ytterbium, and showed the enhanced correlations compared to that ones of SU(2) spin systems. Furthermore, these experiments with SU(N) gases show evidence of enhanced large-spin Pomeranchuk cooling [Tai+12], which is a practical advantage to reach stronger spin-correlations at constant entropy, and to approach singlet states [Rey+07]. Regarding ultra cold quantum gases of alkaline-earth like fermions, SU(N) symmetry arises from the decoupling of the nuclear spin with the electronic degrees of freedom [Gor+10]. Most importantly, this symmetry results in the conservation of the nuclear spin of degree freedom. Moreover, these species have a large nuclear spin, and strontium 87, with largest nuclear spin  $I = 9/2$  in the atomic ground state  $^1S_0$ , is an ideal candidate for the study of magnetism in enlarged SU(N) symmetry.

*Strontium 87* degenerate quantum gases were first realized in 2010 [DeS+10]. The mHz clock transition  $^1S_0 \leftrightarrow ^3P_0$ , associated with weak magnetic sensitivity, raised particular interest for the realization of optical lattice clocks [Boy07; Mic+09; Mic10], and proved high performances with up to  $10^{-18}$  precision [Blo+14]. We are most interested in the 7.4 kHz narrow intercombination line  $^1S_0 \leftrightarrow ^3P_1$ , with associated hyperfine

splitting orders of magnitude larger than the linewidth. This transition offers ideal conditions for the realization of spin orbit coupling schemes [GD10; LJS11] with minimal spontaneous emission [CR14]. For instance, it has been demonstrated that spin components can be separated using conservative spin dependent forces [SGS11]. In lattices, strong artificial magnetic fields can be tailored at the optical wavelength scale with light, realizing spin dependent superlattices [GB17; Sch+20]. Neutral atoms moving in such lattices can acquire a geometric phase [Aid+11], simulating the Aharonov-Bhom effect [AB59].

Our experiment is designed to realize the 2D Fermi-Hubbard model with strontium 87 with enlarged  $SU(N)$  symmetry. It is specifically planned to study the dynamics of spin entanglement. Using a spin dependent optical superlattice [Li+16; Hei+20] associated with the intercombination line, a texture of alternating spins without interactions [Sun+18] can be prepared, realizing a Néel spin order [Née48]. By slowly reducing the depth of the superlattice, spin dynamics are enabled by the time dependent spin orbit coupling. It will be possible to slowly approach the regime where many-body physics are driven by super-exchange interactions, within a spin-independent lattice. The spin system shall, at least locally, adiabatically approach the singlet state [Sun+21]. The (quasi-)long range spin correlations, that can result effectively in squeezing of the alternate magnetization [Com+22], will be detected using the same spin dependent optical superlattice. The goal of my PhD was to set up the tools to carry out this experiment, first focusing on the  $SU(2)$  case, which is the most simple to demonstrate the practicability of the proposed schemes.

## Thesis overview

The first chapter reviews our protocol to prepare degenerate Fermi gas of strontium 87. I show that the loading of our optical dipole trap can be significantly improved by increasing the capture volume. This is realized by superimposing another set of far off detuned laser beams five times larger than the dipole trap used for evaporation. Twice the number of atoms is loaded into the dipole trap, which facilitates the preparation of Fermi seas with higher phase space densities. Typically, we can produce degenerate

Fermi gases at  $T/T_F \simeq 0.2$  with 40 000 atoms and 10 spin components.

These degenerate gases are next loaded in lattices, made of a combination of a 1D lattice with  $2\ \mu\text{m}$  site spacing, with a 2D square lattice with 270 nm site spacing. I applied the quantum magnifier scheme demonstrated in [Ast+21] to spatially separate the different sites of the 1D lattice, and infer the number of atoms in each layer. The obtained spatial resolution is of the order of approximately 220 nm along the lattice eigen axis. Finally, I show that we are able to load the 2D lattice with approximately 95 % strontium 87 atoms into the first Brillouin zone.

In the second chapter, I present our method to measure local densities with absorption imaging of objects smaller than the resolution limit of our imaging setup [Lit+21]. The method is based on the local Beer Lambert absorption law, and it takes into account the effect of fast local variations that are averaged by the detector (inducing strong bias). This method is demonstrated on elongated Fermi gases, from which we infer the unresolved transverse size, as small as one fourth of our imaging resolution limit, and can surpass the diffraction limit, or other limits due to aberrations. Then, I discuss an application of this method to attempt to measure the mean field interaction energy of a SU(10) degenerate Fermi gas of  $^{87}\text{Sr}$ .

The next chapters focus on the implementation of the key protocols that will be used: for the preparation of spin textures from single spin component band insulators, for the adiabatic approach to the singlet state, and for the measurement of the alternate magnetization.

In the third chapter, I first discuss our demonstrated method [Bat+20] to measure the nuclear spin populations with a spin orbit coupling scheme associated with the intercombination line [SGS11]. The robustness of our method is provided by adiabatic following of a quasi-dark state, ensuring minimal spontaneous emission. Using the strong difference of magnetic sensitivity of the coupled states, we selectively transfer, with a resonant passage, well defined momentum recoils to well defined spin states, with a simple retro-reflected laser beam. The overall efficiency is yet 85 %, up to now limited by available light power. I show then that we can selectively prepare a polarized Fermi sea of  $^{87}\text{Sr}$ , without requiring sympathetic cooling by another atomic

species [Tey+10]. A comparison with the preparation of a degenerate ten spins mixture shows that our scheme doesn't affect the phase space density of the evaporated gases. Finally, I estimate that the Fermi sea is polarized with  $90 \pm 10\%$  fidelity accounting for the overall efficiency of our detection scheme.

In the fourth chapter, I demonstrate an adiabatic scheme to selectively and coherently manipulate the nuclear spin states of  $^{87}\text{Sr}$  with light. Taking advantage of the tensor light shift associated with the narrow intercombination line, we lift the degeneracy of the two photon Raman transitions within the  $^1S_0$  ground spin states manifold. The spins are coherently flipped with an adiabatic passage through the resonance of a selected Raman transition. This scheme is demonstrated in bulk gases. I then present expectations for the fidelity of preparation of alternate spin textures, based on the same principle. With a time dependent resolution of the Lindblad equation, I estimate that the spin fidelity of the spin texture writing is  $85\%$  with respect to an alternate spin pattern, in the actual conditions, and should raise to  $97\%$  with ongoing experimental improvements.

In the fifth chapter, I focus on the loading of the lowest band of our 1D lattice with large site spacing  $2\mu\text{m}$ . We are able to prepare several independent 2D Fermi gases with approximately  $99\%$  atoms in the lowest band and strictly positive chemical potential. By comparing two methods, I show that the adiabatic following of the 3D to 2D dimensionality cross over is better ensured by maintaining a sufficient collision rate rather than by reaching very deep evaporation and low temperature prior to the lattice loading. I also developed a thermodynamic model to analyze our time-of-flight imaging in order to provide a proper estimate of the degeneracy parameter in each of the 2D layers. We find an optimal  $\mu/\varepsilon_F \geq 0.4$ , signaling that the 2D gases are strongly degenerate.



# Chapter 1

## Fermi gases of $^{87}\text{Sr}$ in 3D optical lattices - Experimental Setup

Ten years after the first proposal [WE89], it was demonstrated in the late 90's, on ytterbium first [Kuw+99] then on strontium [Kat+99; Muk+03], that it is possible to produce colder and denser atomic clouds with narrow line laser cooling associated with the intercombination line, than with broadband cooling. The Doppler limit is proportionnal to the inverse lifetime of the coupled excited state allowing to reach lower temperatures. The radiation trapping limit [WSW90; SWW91; CCL98] arising from multiple light scattering is lower for the longer lived excited states, allowing to reach higher densities [Ben+17]. While the use of large magnetic traps with alkali atoms was quickly spreading to produce degenerate gases with collision assisted evaporation, closed shell strontium with zero dipole moment in its ground state cannot be loaded in magnetic traps. The high phase space densities reached thanks to narrow line cooling are compatible with the use of far off resonant optical dipole traps [IHK00; GWO00], in that the  $1/e$  size of the magneto-optical trap is on the order of magnitude of the waist of the lasers. Since then, the production of degenerate Fermi gases of  $^{87}\text{Sr}$  [DeS+10; SGS13; SSK14; Ste13] has spread [DeS+10; Tey+10; SGS11; Son+20], but remains difficult with few experiments worldwide.

This chapter presents an overview of our setup and experimental procedures to prepare degenerate Fermi gases of strontium that we trap in 3D optical lattices.

Atoms produced in an oven at  $490^\circ\text{C}$  and Zeeman slowed are captured in a broadband magneto-optical trap (MOT) associated with the 30 MHz wide transition  $^1S_0 \leftrightarrow ^1P_1$  at 461 nm, cooling atoms down to the Doppler limit  $T_D \simeq 1$  mK. The transition is not closed so that atoms are accumulated and magnetically trapped in metastable state  $^3P_2$ . We repump them in the ground state with the 403 nm transition  $^3P_2 \leftrightarrow ^3D_2$ , to begin a second MOT stage. The second MOT is associated with the 7.4 kHz narrow intercombination line  $^1S_0 \leftrightarrow ^3P_1$ . This narrow MOT allows us to cool fermionic strontium down to  $T \simeq 3 \mu\text{K}$ , which is higher than the typical temperature  $T < 1 \mu\text{K}$  reached for bosonic species of strontium [SSK14]. The gas is then loaded in an optical dipole trap to start forced evaporation, which is our last step of phase space compression to reach Fermi degeneracy, down to approximately  $T \simeq 0.15 T_F$  in our experiment. Finally, atoms are adiabatically loaded in 3D optical lattices, made of the combination of a vertical 1D lattice with large site spacing and a square 2D lattice.

I will first present the most relevant energy levels for laser cooling. Then I will focus on the main features of each cooling stage, to ensure a sufficient understanding of the experimental discussions in the next chapters. A complete description of the setup can be found in Pierre Bataille's thesis [Bat22] which reviews all technical specifications.

## 1.1 Cooling $^{87}\text{Sr}$ to Fermi degeneracy

### 1.1.1 Energy levels

Strontium atom is an alkaline-earth species with four naturally stable isotopes. Three of them,  $^{84}\text{Sr}$ ,  $^{86}\text{Sr}$ ,  $^{88}\text{Sr}$  are bosonic isotopes all with  $I=0$  nuclear spin, and the only fermionic isotope with 7% natural abundance  $^{87}\text{Sr}$  has  $I=9/2$  large nuclear spin, which is the largest of stable alkaline-earth species. Our platform makes use of fermionic  $^{87}\text{Sr}$  only, and hence I will focus on this isotope.

The ground state  $^1S_0$  of strontium has closed-shell electronic structure  $[Kr]5s^2$ , and zero electric spin. The transition at 461 nm connects  $^1S_0$  to the singlet state  $^1P_1$  which has a very short life time 5 ns [Wer+92; Yas+06], corresponding to a broad linewidth  $\Gamma/2\pi$  of 30 MHz, as shown on figure 1.1. This broad band transition is used

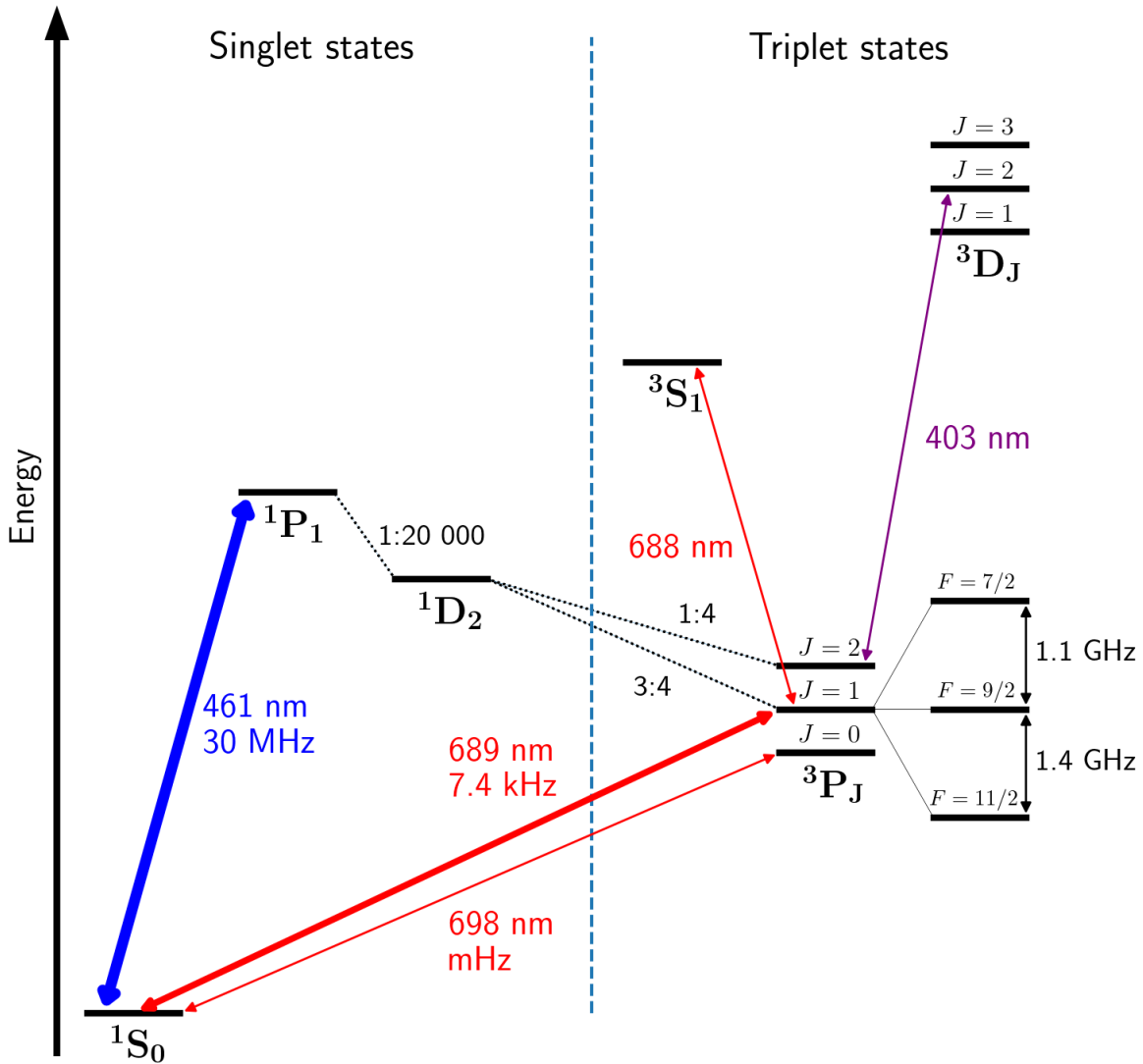


Figure 1.1: Energy levels and optical transitions (solid double arrowed lines) associated with electric dipoles (E1), for fermionic strontium 87. The dotted lines indicate spontaneous decay paths:  $^1P_1$  state has 1:20 000 probability to decay toward  $^1D_2$ , and the latter has 3:4 chance to decay to  $^3P_1$ , and 1:4 chance to decay to metastable  $^3P_2$ . The three energy levels  $F = 7/2, 9/2, 11/2$  are the three hyperfine states of  $^3P_1$ . The energy splitting and optical transitions are not to scale.

for capturing atoms out of our oven and for absorption imaging. From  $^1P_1$ , 1 out of 20

000 atoms can decay to the singlet  $^1D_2$  state, and then atoms have 1:4 probability to decay to  $^3P_2$  or 3:4 probability to decay to  $^3P_1$ .

While  $^3P_1$  triplet state can decay directly to the ground state  $^1S_0$  with electric dipole transition (E1) at rate 7.4 kHz, the  $^3P_2$  triplet state is a long lived metastable state. The decay paths to lower energy states require high order processes such as magnetic quadrupole (M2) transitions, and the associated life time has been measured up to 500 s [YK04]. Hence, on experimental time scale,  $^1S_0 \leftrightarrow ^1P_1$  is an open cycle and with optical excitation at 461 nm, atoms are continuously shelved from the ground state into  $^3P_2$  at rate  $\Gamma_{shelving} \simeq \Gamma_{1P_1}/2 \times 1.25 \cdot 10^{-5}$ .

The total electronic spin is not conserved on singlet-triplet transitions such as the intercombination line  $^1S_0 \leftrightarrow ^3P_1$ , hence a one photon decay path associated with an electron spin flip should be forbidden, and these excited states should be stable. However, higher-order processes reduce the life-time of these excited states and may allow for single photon electric dipole (E1) transitions. For instance,  $^3P_1$  is mixed with broad-band  $^1P_1$  state through spin-orbit interaction (SOC), such that the life-time of  $^3P_1$  is reduced to  $25 \mu\text{s}$ , corresponding to linewidth  $\Gamma/2\pi = 7.4 \text{ kHz}$ . This is much smaller than typical MHz broad transitions resulting in reduced spontaneous emission, but still large compared to clock transitions. This typically means that the intercombination line can be used at advantage both for dissipative processes and for coherent processes with associated reduced spontaneous emission.

### 1.1.2 Oven - Transverse cooling and Zeeman slower

A deposit of pure solid strontium lies inside a stainless steel reservoir. It is heated by radiation with a network of isolated heating resistances. The strontium reservoir is then attached to a nest of microtubes to ensure a velocity selection on the hot atomic vapor, so that fewer atoms with large transverse velocities can leave the oven.

The temperature of the oven is set with continuous voltage control, and it is monitored with one thermocouple probe, at contact with the external surface of the reservoir. In our experiment, we typically set the temperature of the oven at 760 K

with input power 110 W which corresponds to an outgoing collimated flux of atoms  $\dot{N} \simeq 6.10^{12}$  atoms/s, with Boltzman velocity distribution and most probable axial velocity  $v \simeq 500$  m/s. With this operating mode, the estimated lifetime of the oven is nearly 5 years in our experiment. The strontium deposit has been reloaded only once since the experiment launch in 2014.

The hot atomic vapor is optically collimated with 2D optical molasses at the exit of the oven [SVH05]. Two orthogonal laser beams are retroflected along the transverse velocities of the atomic flux. Transverse cooling is ensured with anisotropic beams, the largest dimension being along the atomic flux to ensure maximal interaction time with the atoms, and the frequency of the lasers is set red detuned  $\Delta = -\Gamma/2$  from the  $^1S_0 \leftrightarrow ^1P_1$  transition. This stage ensures an increase of the number of atoms later captured by a factor of 3 in our experiment. The axial flux of atoms is then slowed with a 50 cm long Zeeman slower [PM82], from  $v \simeq 500$  m/s down to the capture velocity  $v_c \simeq 20$  m/s of our broadband MOT.

The frequency of the blue lasers is set from a master laser with extended cavity, whose frequency is locked on a hot atomic flux with modulation transfer spectroscopy [MKC08; Lee+21]. The optical light used for transverse cooling and the zeeman slower are generated by slave laser diodes whose frequency is set and stabilized by injected light from the master laser into the slave diode cavities [Bat22]. The same procedure is done for a slave dedicated to the MOT.

### 1.1.3 $^1S_0 \leftrightarrow ^1P_1$ broadband MOT - $^3P_2$ shelving

The atoms are then captured in a 3D MOT on the broad-band transition at 461 nm, and cooled down to the Doppler limit  $T_D \simeq 1$  mK. The magnetic coils in anti-Helmoltz configuration are supplied by 170 Amper during the MOT stage, producing a magnetic quadrupole with strong field gradient  $\nabla B = 51$  G/cm. The  $^1S_0 \leftrightarrow ^1P_1$  transition is not cyclic, and atoms are continuously shelved at rate  $\Gamma_{shelving} \simeq \Gamma_{^1P_1}/2 \times 1.25 \cdot 10^{-5}$  from the ground state into the state  $^3P_2$ . This metastable state has a large magnetic dipole moment, so that metastable atoms stay trapped in the magnetic quadrupole.

The metastable state has long lifetime 9 min [YK04], but into the magnetic trap it is lowered by the background collisions, down to nearly 10 s. In our experiment, we typically set the time for loading atoms in  $^3P_2$  to 5 s, and it can be tuned from 2 to 10 seconds depending on the best balance between signal to noise ratio and time of sequence for the on-going experiment. After 10 seconds of loading, the populations reach steady state and no more atoms can be accumulated in  $^3P_2$ . After then, the blue MOT is turned off.

### 1.1.4 Repumping metastable $^3P_2$

The temperature of the atoms accumulated in  $^3P_2$  is approximately the Doppler temperature of the broadband MOT, which is too hot to be directly loaded in our optical dipole trap. To pursue optical cooling until the gas is sufficiently cold, we use a second narrow MOT stage, which requires that atoms are in the ground state. Hence, we use the optical transition  $^3P_2 \leftrightarrow 5s6d^3D_2$  at 403 nm [SS14] to repump atoms back in the ground state with a two photon radiative decay through  $^3P_1$ , as sketched in figure 1.1. When shelved in metastable  $^3P_2$ ,  $^{87}\text{Sr}$  atoms are spread in different hyperfine states, and the  $^3P_2 \leftrightarrow ^3D_2$  hyperfine resonances are resolved in the GHz range. Hence, to maximize the efficiency of the repumping, we modulate the frequency of the repumper laser to scan through the three most populated hyperfine resonances, and this is done by modulating the voltage of the piezo-electric crystal of the cavity of the laser. The resulting amplitude of the laser frequency modulation is 3 GHz in our experiment, which allows to repump up to 40 million atoms after loading the metastable during 5 seconds with oven heated at 760 K.

Although repumping through other  $5snd^3D_2$  states can be used, for instance  $n=5$  [Pol+05; SGS13] at 497 nm or  $n=4$  [Mic+09; Aka+21] where the decay paths are favorable to minimize atom loss, we stick to using the 403 nm line for its easier implementation and low cost laser. It is also possible to continuously repump atoms during the broadband MOT stage in order to reach lower temperatures, at the cost of atom loss [SSK14]. Since the number of atoms is critical for our experiment to produce deeply degenerate Fermi gas, we rather repump atoms to the ground state

after turning off the blue MOT. Note that it was recently demonstrated [Aka+21] that it is possible to take advantage of the cyclic transition  $^3P_2 \leftrightarrow 5s4d^3D_3$  at  $3\ \mu\text{m}$  inside the magnetic quadrupole, and produce ultra-cold gas at  $T \simeq 200\ \text{nK}$  with one dimensional polarization gradient cooling.

### 1.1.5 $^1S_0 \leftrightarrow ^3P_1$ narrow MOT

#### The MOT

The second and most critical optical cooling stage in our experiment is associated with the 7.4 kHz intercombination line  $^1S_0 \leftrightarrow ^3P_1$  at 689 nm. While the achievable temperature is limited in a broadband MOT due to high Doppler temperature, and the density is limited due to the effective repulsive force associated with multiple light scattering [WSW90; SWW91; CCL98], MOT associated with the intercombination line allows to produce much colder and denser atomic clouds [Kat+99], since the Doppler temperature is as cold as  $T_D = 177\ \text{nK}$  for strontium, which is very convenient for further loading optical dipole traps.

Within  $^3P_1$ , the hyperfine states are highly resolved with  $\Delta_{HFS}/\Gamma_{^3P_1} > 100\,000$ , and the MOT laser beams are chosen red detuned from the  $^3P_1$ ,  $F = 11/2$  hyperfine state such that  $m_F = \pm 9/2$  spin states can be trapped with  $\sigma_{\pm}$  laser beams. For this transition the Doppler limit is  $T_D = 177\ \text{nK}$  while the associated recoil temperature  $T_R = 462\ \text{nK}$ , defined as  $T_R = \hbar^2 k^2 / 2m$  where  $k = 2\pi/\lambda$ , so that MOT cooling is limited by the recoil energy of one photon and not by the Doppler effect. This allows to directly cool atoms in the  $\mu\text{K}$  range with standard MOT without using sub-Doppler cooling techniques, which is very convenient. However, the capture velocity is limited by the narrow linewidth, such that artificial broadening is needed to capture repumped atoms at 1 mK, either with frequency modulation or with power broadening. Hence, the 689 nm laser light is initially at full power, nearly 12 mW distributed over the 3 MOT axes, and its frequency is triangularly modulated over 4 MHz at rate 20 kHz. Simultaneously, the input current of the MOT coils is lowered to 3.5 Amperes for a weak magnetic field gradient  $\nabla B \simeq 1\ \text{G/cm}$ . At this stage, we capture up to 40 millions atoms at  $T \simeq 25\ \mu\text{K}$ . Then the modulation is reduced in two steps down to zero and

the intensity down to a few  $I_{sat} \simeq 3 \mu\text{W}/\text{cm}^2$ .

For this narrow line cooling, and any optical scheme associated with the intercombination line, high laser stability and finesse are required. Hence, the frequency of our master laser is locked onto an ultra-stable cavity using a Pound-Drever-Hall feedback signal [Dre+83]. The laser spectrum is as narrow as 1 kHz which is sufficient for the targeted 7.4 kHz linewidth. The optical beams used for the narrow MOT come from slave laser diodes, whose frequency is set and stabilized by injecting light from the master laser into the slave diode cavity [Bat+20].

### Stirring laser

The narrow MOT for  $^{87}\text{Sr}$  requires a second laser to prevent strong atom loss [SSK14]. With high nuclear spin  $I = 9/2$  and long lifetime  $\tau \simeq 20 \mu\text{s}$  of the excited state  $^3P_1$ , atoms can remain in excited spin states transparent to light for a sufficiently long duration such that they leave the trap. This is illustrated on figure 1.2, left. If considering a single spin state for simplicity, here  $m_F = 5/2$ , the dissipative force is localised on the left hand side of the zero field position. Actually, this scheme is symmetric in  $m_F$ , accordingly with the Zeeman shift, and considering negative spin states, the dissipative force is localised on the right hand side of the zero field position. Hence, atoms would need to flip from  $m_F$  to  $-m_F$  when crossing the zero field to feel a global restoring force, as shown by the average over all spin states as the blue dashed line on the top figure. While magnetic atoms such as alkalis can flip spin when crossing the trap center and always remain in a stable trap configuration, alkaline earth atoms with zero magnetic moment need light assistance to change spin states.

It was then proposed [Muk+03] to use a second laser beam for the narrow MOT stage to randomize the spin states such that every atom feels a restoring force on average, minimizing the probability of atom loss. This second laser, so called *stirring* laser for the  $^{87}\text{Sr}$  narrow MOT, has its setup in MOT configuration, and is actually superimposed to the MOT laser, and its frequency is set red detuned from the  $^3P_1$ ,  $F = 9/2$  hyperfine state. Figure 1.2, right, shows the spatial dependence of the STIR saturation parameter, here defined as:

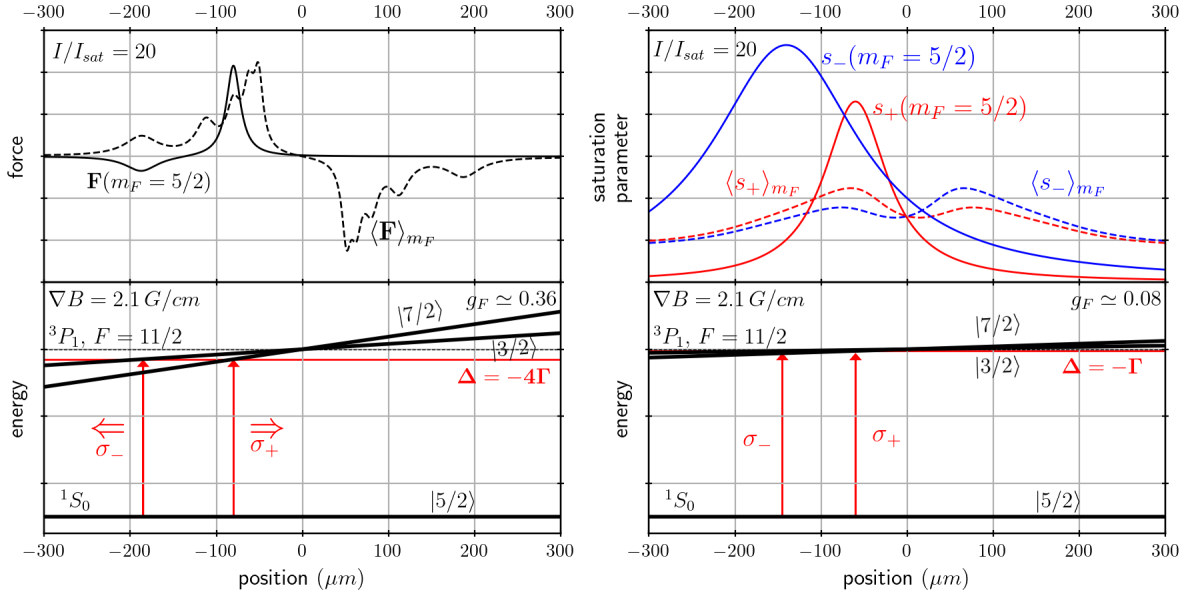


Figure 1.2: Instability of the narrow red MOT for large spin  $^{87}\text{Sr}$  isotope. Left: spatial dependence of the restoring force (a.u.) for the narrow MOT associated with the intercombination line  $|^1S_0\rangle \leftrightarrow |^3P_1, F = 11/2\rangle$ . The ground spin state  $m_F = 5/2$  is coupled to Zeeman shifted excited 3/2 and 7/2 spins of  $F = 11/2$  hyperfine state with Lande factor  $g_F \simeq 0.36$ . For a given detuning (here  $\Delta = -4\Gamma$ ), the corresponding restoring force is plotted on the upper figure as the solid line. The restoring force averaged over all the spin states is plotted as the dashed line. Right: spatial dependence of the saturation parameter (a.u.) associated with  $\sigma_+$  and  $\sigma_-$  excitation on the STIR line  $|^1S_0\rangle \leftrightarrow |^3P_1, F = 9/2\rangle$  with detuning  $\Delta = -\Gamma$ , as solid line for the ground spin 5/2, and dashed line for the average over all ground spin states.

$$s(r) = \frac{\Omega^2}{4\Delta^2 + \Gamma^2} \quad (1.1)$$

where  $\Delta = \delta - m_F g_F \mu_B B$  for atoms at rest, and  $\Omega^2 = (\Gamma^2/2) \times (I/I_{sat})$  for both  $\sigma_+$  and  $\sigma_-$  excitation. Since the  $g_F$  factor is 4.5 smaller than that one of  $^3P_1, F = 11/2$  state, atom-light interaction is much less localized than the MOT line so that atoms are no more transparent to light and hence have the possibility to change spin states. With an efficient randomization of the spin states associated with the STIR line, all atoms feel an averaging restoring force (dashed line, upper left figure [1.2](#)), and remain confined into the MOT. The intensity and frequency of the stirring laser are set with the

same conditions than the MOT laser, starting with a frequency modulation of 6 MHz and strong intensity, and with final single frequency at a few  $I_{sat}$  with no modulation.

In the final narrow MOT stage with field gradient  $\nabla B \simeq 2.5 \text{ G/cm}$  and detuning  $\Delta \simeq \Gamma_{3P_1}$  for both stirring and MOT lasers, the bulk gas of  $^{87}\text{Sr}$  extends over nearly  $600 \mu\text{m}$  with 7 million atoms at  $T \simeq 3 \mu\text{K}$ . The next critical step to reach Fermi degeneracy is to transfer trapped atoms from the narrow MOT to the optical dipole trap to perform forced evaporation.

### 1.1.6 Optical dipole trap loading

The transfer of atoms from the narrow MOT in our optical dipole trap (ODT) [GWO00] is associated with a few critical difficulties. First, there is the strong difference of size of the two traps. With simple geometry considerations, a straight volume mapping of the narrow MOT bulk gas onto the ODT shape would mean that less than 1% of the atoms would be transferred from one trap to the other. To increase the loading efficiency, the MOT is further compressed [IHK00] simultaneously to loading the ODT. However, inside the ODT, the differential light shift associated with the intercombination line has to be managed to prevent strong atom loss. Because the ground state is more red-shifted than the excited state  $^3P_1$ , the  $^1S_0 \leftrightarrow ^3P_1$  transition acquires a blue shift much stronger than  $\Gamma_{3P_1}$ . Moreover, the light shift varies spatially as a function of the intensity profile of the ODT, which is much smaller than the size of the narrow MOT. Hence, if we choose the MOT light to be slightly red detuned at the center of the dipole trap in presence of the light shift, it is blue detuned at the edge of the ODT and atoms are expelled. I will here first introduce the properties of the ODT and the space dependent resonance for the intercombination line, then I will quickly describe our method to circumvent those two major difficulties and maximize the phase space density when loading the ODT.

*Geometry:* our optical dipole trap is made of two crossed far-off red detuned laser beams at 1070 nm. The first beam is nearly horizontal with small tilt  $\simeq 1^\circ$ , and its shape is elliptic with large horizontal waist  $\simeq 150 \mu\text{m}$  and small vertical waist  $\simeq 80 \mu\text{m}$

at the atoms position, for a strong vertical confinement. The second beam is nearly vertical with angle  $\simeq 30^\circ$  with respect to gravity, and its shape is isotropic with waist  $\simeq 80 \mu\text{m}$  at the atoms position, for strong confinement in the horizontal plane. The crossing of the two beams defines a rather spherical volume of radius  $\simeq 80 \mu\text{m}$ , which is nearly 500 times smaller than the size of the  $600 \mu\text{m}$  wide narrow MOT before loading. The depth of initial trap at loading is  $50 \mu\text{K}$  at the crossing, accounting for gravity sag, with power distribution  $P=9.6 \text{ W}$  in the horizontal beam and  $P=4.7 \text{ W}$  in the *vertical* beam.

*Differential light shift:* atoms are transferred from the narrow MOT associated with the  $^1S_0 \leftrightarrow ^3P_1$  transition at  $689 \text{ nm}$ , to the ODT at  $1070 \text{ nm}$ . For far-off detuned atom-light interaction and non-resolved hyperfine structure, the light shift is determined only by the rotationally invariant contribution to the dynamic polarizability and reads as the dipole potential which can be computed from resolution of the optical Bloch equations [CDG98]:

$$U_{dip} = -\frac{\hbar|\Omega|^2}{4\bar{\Delta}} \quad (1.2)$$

Here,  $1/\bar{\Delta} = 1/(\omega_L - \omega_0) - 1/(\omega_L + \omega_0)$ , such that both the resonant and anti-resonant contributions to the atom-light dipole interaction are considered.  $\Omega$  is the Rabi coupling frequency, which is easily computed from the inverse lifetime  $\Gamma$  and light intensity  $I$ :

$$\Omega^2 = \frac{\Gamma^2}{2} \frac{I}{I_{sat}} \quad (1.3)$$

where  $I_{sat}$  is the saturation intensity of the considered optical transition.

Regarding the light shift of  $^1S_0$ , the contribution from  $5snp^1P$  states,  $n < 11$ , accounts for more than 99% according to Thomas-Reiche-Kuhn sum rule of oscillator strengths [Lud08]. The light shift can then be computed from the sum of the relative dipole potentials  $U_{ak} \propto A_{ak}/\bar{\Delta}_{ak}$  where  $A_{ak}$  is the transition probability, according to the known values of the transition probabilities and wavelengths [Wer+92; SN10]. The light shift of triplet state  $5s5p^3P_1$  can be properly defined by considering

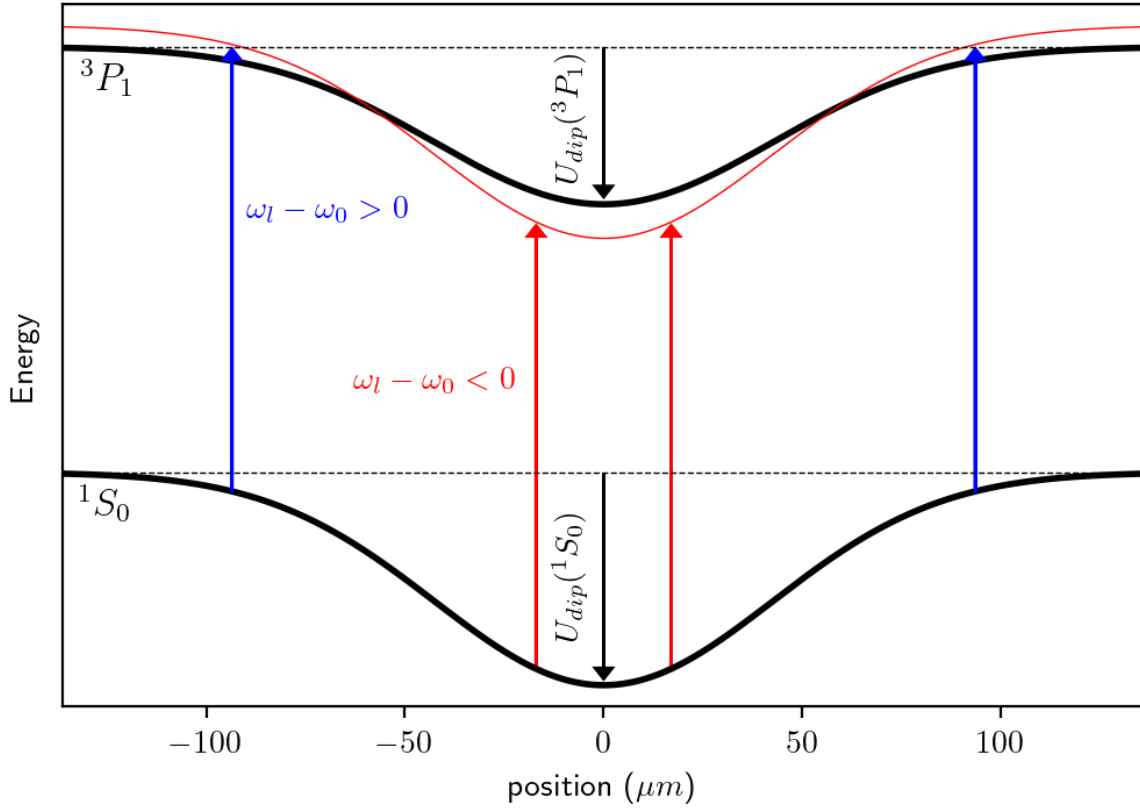


Figure 1.3: Differential light shift of the  $^1S_0 \leftrightarrow ^3P_1$  intercombination line during the loading of the optical dipole trap at 1070 nm. Black solid lines indicate the energy levels light shifted and the red solid line indicates the MOT light frequency with the ground state space dependent offset. For this frequency, the MOT light is red detuned at the bottom of the trap and blue detuned outside.

the triplet-triplet transitions involving excited  $^3S$ ,  $^3P$ , and  $^3D$  states, with according oscillator strengths and line wavelengths [Wer+92; SN10]. The shift  $\delta$  of the transition  $^1S_0 \leftrightarrow ^3P_1$  is then simply the difference between the two introduced light shifts  $\hbar\delta = U_{dip}(^3P_1) - U_{dip}(^1S_0)$ . In our experiment,  $U_{dip}(^1S_0) \simeq -1.5$  MHz for the ground state and  $U_{dip}(^3P_1) \simeq -1.2$  MHz, such that the intercombination line is shifted by nearly 300 kHz to the blue at the bottom of the trap, and is spatially proportional to the intensity shape of the dipole trap laser beams. This is shown on figure 1.3.

*ODT loading:* the 1070 nm laser beams are quickly turned on after the narrow MOT stage, and atoms in continuous motion are attracted by the dipole trap of depth  $50 \mu\text{K}$ . In the bottom of the ODT, the MOT resonance is so much shifted that it can be neglected and atoms simply run their phase space trajectory for conservative dipole interaction with no capture nor compression. Hence, we want to shift the light frequency to the blue to get closer to resonance at the bottom of the trap. This way, atoms are slowed down and captured, and we can obtain further phase space compression with MOT light induced dissipation inside ODT. Note that because of the differential light shift, atoms outside the ODT see blue detuned light. We then slowly ramp the frequency of the MOT light by 170 kHz during 120 ms, further compressing the position selectivity of cooling inside the differential light shift, and increasing phase space density. The intensity of the MOT light is simultaneously and slowly turned down to zero, so that it is as low as possible when getting close to resonance in the high atomic density region at the bottom of the dipole trap. This way, a balance is found between dissipative cooling and heating at the outskirts. With this method, we are able to load up to 1.4 million atoms at  $3.8 \mu\text{K}$  inside the ODT, which corresponds to nearly 25% atoms transferred from the MOT to ODT with depth to temperature ratio  $U/k_B T \simeq 13$ , with density  $n_0 \simeq 1.15 \times 10^{20} \text{atoms.m}^{-3}$ .

*Enhanced capture volume:* with this setup, we are limited by the capture volume of the ODT compared to the volume of the narrow MOT. To increase the number of atoms captured, we take advantage of a later used far-off detuned optical lattice to increase the capture volume of the dipole trap, as shown on figure [1.4](#). We use a 1D optical lattice at 1064nm (introduced in section [1.2.1](#)) with larger vertical waist  $100 \mu\text{m}$  and horizontal waists  $170 \mu\text{m}$ , such that the capture volume is more than 5 times larger. This lattice is one dimensional with vertical eigen axis, defining layers of large  $170 \times 170 \mu\text{m}^2$  dipole traps with approximately 500 kHz depth, spaced by  $2 \mu\text{m}$ .

This 1D lattice is turned on quickly and simultaneously to the ODT. The combination of the ODT and lattice makes a deeper trap reaching almost  $90 \mu\text{K}$ , and we are able to load up to 2.6 million atoms with temperature  $7.2 \mu\text{K}$ , which corresponds to nearly 43% atoms transferred from the MOT to ODT with depth to temperature ratio  $U_{ODT}/k_B T \simeq 12.5$ . This way, twice the number of atoms are loaded,

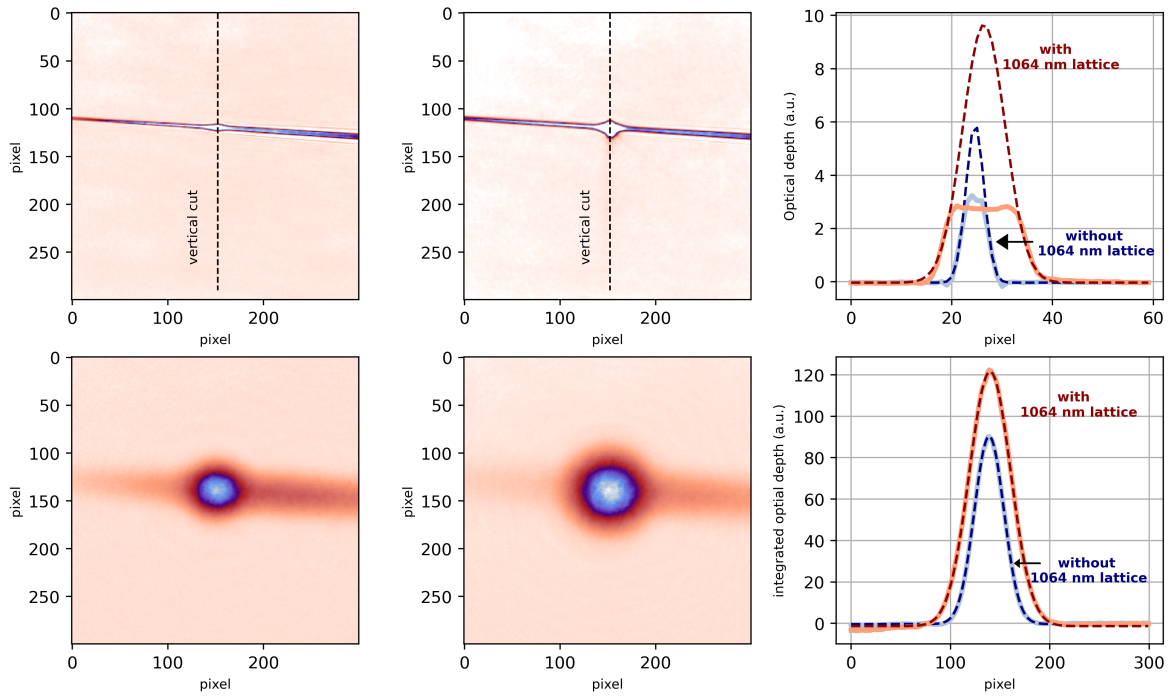


Figure 1.4: Enhanced capture volume of the optical dipole trap. Left: optical dipole trap loading without 1064 nm lattice, in situ (top) and after time of flight (bottom), absorption images. Middle: enhanced loading using the 1064 nm lattice. Top right: vertical cut of the saturated in situ absorption images, the dashed line is the in-situ density on the saturated region inferred from a Boltzmann distribution and the low density wings. Bottom right: integrated optical depth from the time of flight images (bottom) used to measure the number of loaded atoms and temperatures with gaussian fits for Boltzmann gases in harmonic traps.

while the density  $n_0 \simeq 3.3 \times 10^{19}$  is approximately unchanged, accounting for the weak increase of confinement  $\omega'^2 = \omega_{ODT}^2 + \omega_{1064}^2$ , and  $U/k_B T$  1.3 times smaller. At this step, the collision rate is approximate one collision per atom per millisecond.

Note that the efficiency of loading could be further improved with additional lasers. An ODT at magic wavelength 840 nm for the intercombination line [Muk+03] circumvents the differential AC Stark shift and hence allows to have homogeneous MOT cooling inside the dipole trap. Also, it is possible to use a transparency beam [Son+20], detuned by a few GHz from the  $^3P_1 \leftrightarrow ^3S_1$  transition, resulting in a localized light shift

for the intercombination line. Atoms inside the transparency beam are protected from MOT light, and the energy is dissipated through collisions to outside atoms which are continuously optically cooled, allowing to further pass the radiation pressure limit and reach even higher densities and lower temperatures before evaporation.

### 1.1.7 Forced evaporation

The gas is finally cooled down to Fermi degeneracy, see figure [1.5](#), with forced evaporation. The 1D optical lattice used to help loading the optical dipole trap is smoothly turned off during the first 2.5 seconds of evaporation. This way, atoms are transferred from vertically stacked 2D harmonic traps to a three dimensional (3D) harmonic trap, which permits a more efficient evaporation [\[LRW96\]](#) within higher dimensionality. In the meantime, the power of the horizontal ODT beam is lowered from 11.6 W to 2.4 W and from 4.7 W to 2 W for the vertical beam. This corresponds to a reduction of the geometric mean of the trap frequency  $\bar{\omega} = (\omega_x \omega_y \omega_z)^{1/3}$  from 275 Hz to 140 Hz. The powers of the dipole trap laser beams are then reduced much more slowly at the end of the evaporation, the horizontal beam from 2.4 W to 1.2 W and the vertical beam from 2 W to 0.84 W, during 5 seconds. All in all, in our experiment, forced evaporation runs over 8 to 10 seconds, and the gas reaches degenerate regime with 10 Fermi seas at  $T \leq 0.5 T_F$  with approximately 7 500 atoms per spin state, and the phase space density  $\rho \propto N\bar{\omega}^3/T^3$  is increased by three orders of magnitude, with respect to the dipole trap loading, as shown on figure [1.5](#). Note that our evaporation efficiency is limited by the background collisions, with typical time  $\tau \simeq 8$  s which is approximately the duration of evaporation.

## 1.2 Optical lattices

The objective of our experiment is to realize a quantum simulator for the Fermi Hubbard model. In our experiment, this is realized by trapping spinor atoms at the sites of several independent 2D optical lattices which are vertically stacked. The resulting 3D optical lattice is presented in figure [1.6](#). It is made of a vertical 1D lattice at 1064 nm, defining horizontal 2D layers at its maxima, and a 2D lattice at 532 nm shaping 2D square

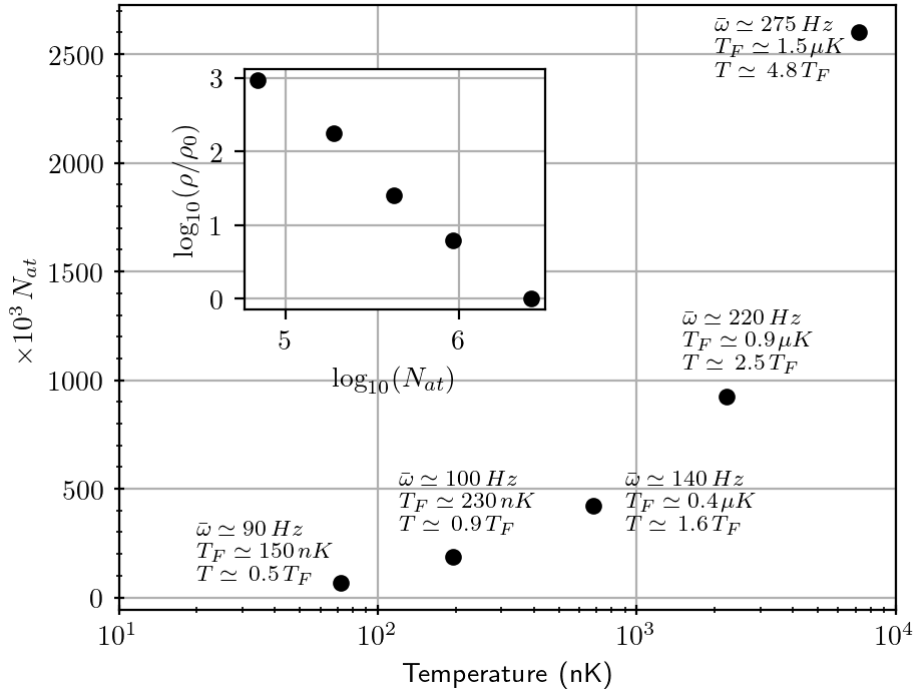


Figure 1.5: Forced evaporation dynamics. The temperatures and number of atoms are measured from time of flight images, and the trapping frequencies of the dipole trap are inferred from an independent calibration of the trap geometry. At each evaporation step, the gas thermalizes during 330 ms before time of flight. In inset, the phase space density  $\rho$  increase with respect to the initial gas  $\rho_0$  at ODT loading, where the phase space density is computed as  $N\bar{\omega}^3/T^3$ .

lattices within each horizontal layer. The combination of the two lattices is a set of horizontal 2D square lattices with sites spacing 256 nm separated by  $\simeq 2 \mu\text{m}$ . The tunneling within the 2D bravais lattices is controlled by the intensity of the 532 nm laser beams, while the tunneling from layer to layer is separately controlled by the depth of the 1064 nm lattice. The tunneling from layer to layer is negligible on the timescale of to the 2D spin dynamics.

In this section, I first introduce the geometry of the vertical 1D lattice at 1064 nm, and our method to measure the depth of the low recoil lattice. Moreover, several sites of the 1D lattice are loaded in our experiment, typically 8 layers, and I discuss our

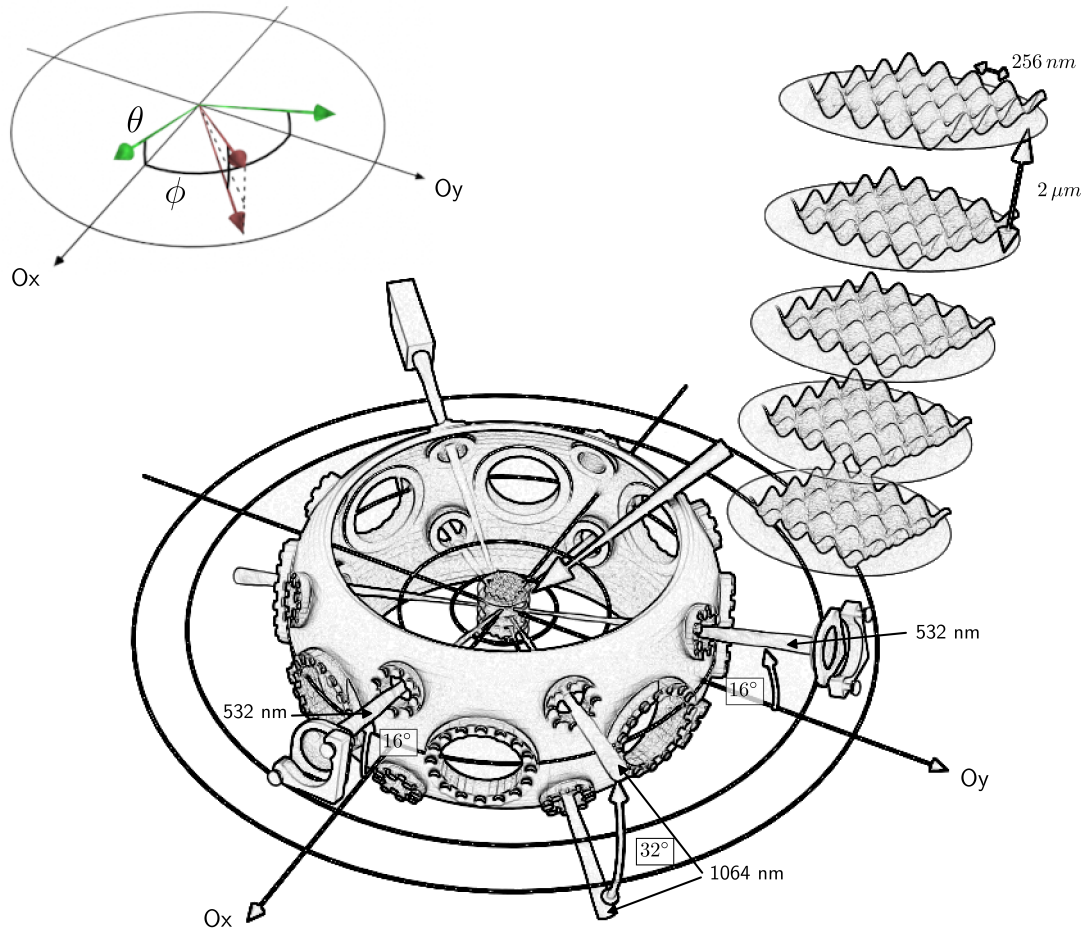


Figure 1.6: Optical lattices setup. Two laser beams at 532 nm with  $\theta = 16^\circ$  elevation are retroreflected to shape a 2D lattice, and the 1D lattice is made of two interfering laser beams at 1064 nm separated by  $\theta = 32^\circ$  elevation. The resulting lattices are layers of 2D lattices separated by  $2 \mu\text{m}$ , with sites spacing of 256 nm.

application of the quantum magnifier scheme [Ast+21] to measure the distribution of atoms in the several layers. Then, I introduce the geometry of the 2D lattice.

### 1.2.1 1064 nm 1D lattice

#### Geometry

The 1D lattice is made from the interference of two laser beams at 1064 nm with wavevectors  $\vec{k}_1, \vec{k}_2$ . In a spherical basis  $(r, \theta, \phi)$ , where elevation angle  $\theta$  and azimuthal angle  $\phi$  are defined on upper left inset of figure [1.6](#), the wavevector  $\vec{k}$  of each laser beam is here defined as:

$$\vec{k} = \frac{2\pi}{\lambda} \begin{pmatrix} \cos\phi \sin\theta \\ \sin\phi \sin\theta \\ \cos\theta \end{pmatrix} \quad (1.4)$$

The two laser beams at 1064 nm have same azimuthal angle  $\phi$  and elevation angle  $\theta = \pm 16^\circ$  so that they are separated by  $\delta\theta = 32^\circ$  elevation and  $\vec{k}_1 \cdot \vec{k}_2 = k_1 k_2 \cos(32^\circ)$ . The stationary wave resulting from the interference of the two laser beams is a vertical 1D lattice with eigen-axis  $\vec{a}$  along  $\vec{k}_1 - \vec{k}_2$ , and the sites spacing is  $a = \lambda/2 \sin(16^\circ) \simeq 2 \mu\text{m}$ . The two beams are controlled by the same AOM and separated right before crossing at the position of the Fermi gas, ensuring that the phase coherence between the interfering beams is maximally maintained.

#### Depth and band gap calibration of low recoil 1D lattice

Lattice depth calibration is usually done with diffraction calibration [\[Den+02\]](#). In the case of low recoil lattices, the diffraction orders cannot be resolved with time of flight imaging since they are separated by only a few nK, 7 nK in the case of  $2 \mu\text{m}$  sites spacing for  $^{87}\text{Sr}$ , which is much lower than the lowest momentum spread that can be reasonably attained for degenerate Fermi gases of strontium, ( $\simeq 20 \text{ nK}$  with approximately 20 000 atoms in our experiment). To circumvent this issue, we rather observe the time evolution of the gas momentum distribution inside the lattice potential [\[Huc+09\]](#) after suddenly switching it on. The low recoil lattice is pulsed on bulk gas, long enough such that the atoms are accelerated into the lattice potential. Atoms initially laying next to the negative interferences of the lattice will acquire maximal acceleration when reaching the bottom of the sites. When the lattice is turned off, with time of flight, then the atoms will expand with the kinetic energy acquired from the

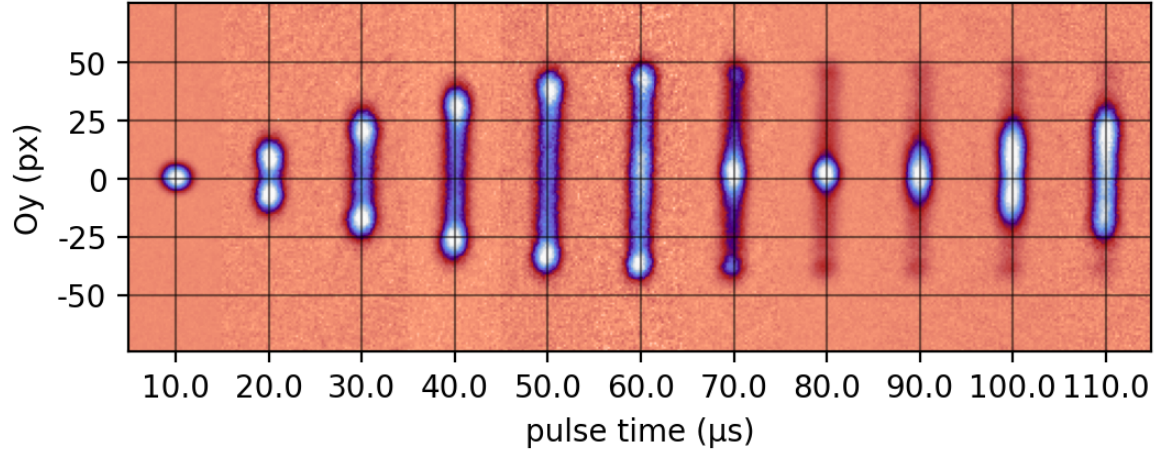


Figure 1.7: Experimental images for the depth calibration of a low recoil 1D lattice. For each duration of the lattice pulse, in bottom axis, a time of flight image is recorded.

lattice depth. If the pulse time is long enough, then atoms must have had enough time to explore the whole depth of the lattice sites, and then the maximal velocity measured in time of flight maps the depth of the lattice.

Figure 1.7 shows experimental images of the scheme for different pulse times. If the pulse time is long enough, then the atoms have explored the whole depth, which happens from  $60 \mu\text{s}$  in this measurement. Figure 1.8 shows a cut of the optical depth from figure 1.7 along the longitudinal axis for each time of flight, from which it is possible to detect the atoms with maximal velocity. At  $60 \mu\text{s}$  of pulse, the maximal separation in the imaged density is nearly  $dx \simeq 100 \text{ px}$ , such that the maximal velocity acquired is  $v_{max} = \frac{dx}{2t_{tof}}$ . This gives the maximum acquired kinetic energy, which gives the measurement of the depth  $V_0$  of the lattice:

$$V_0 = \frac{1}{2}mv_{max}^2 \quad (1.5)$$

From this measurement, the trap depth is  $113 \text{ kHz}$ , which corresponds to  $V_0 = 791 E_R$ . The band gap can then be directly inferred from  $\hbar\omega_{BG} = 2\sqrt{V_0 E_R}$ , which is  $8 \text{ kHz}$  in this case.

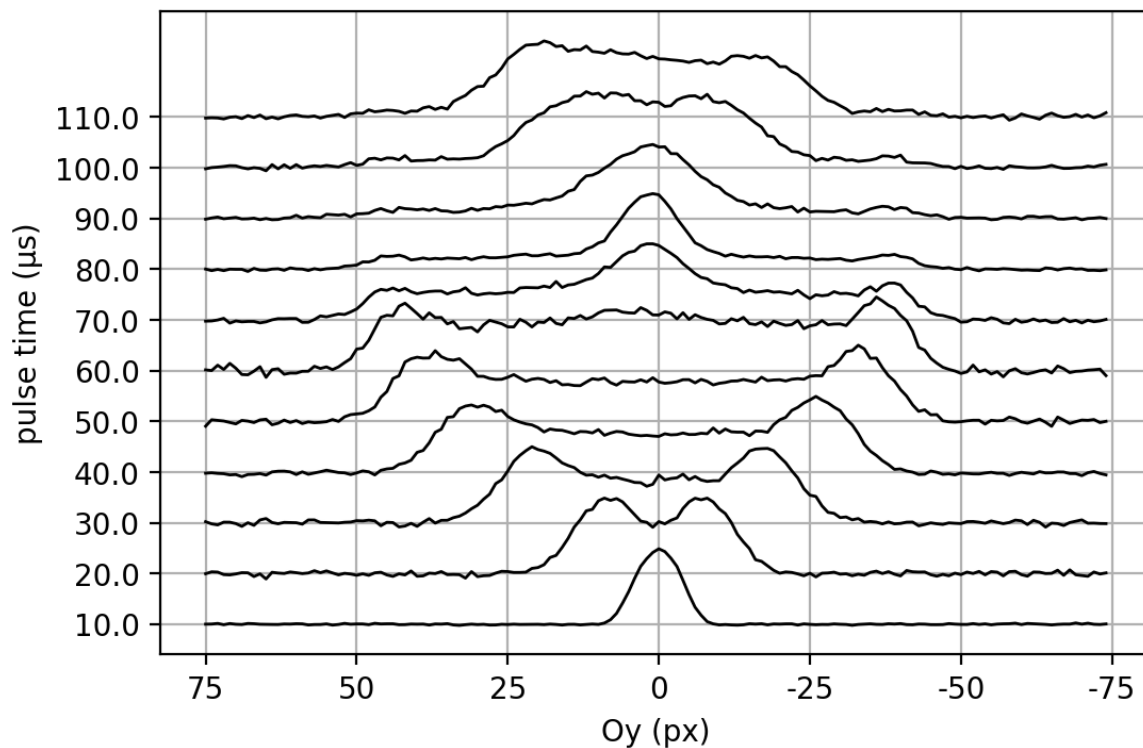


Figure 1.8: Longitudinal cut profile through the experimental images of the depth calibration shown in figure 1.7, for each pulse time, shown in left axis. There no axis showing the density.

### Distribution of atoms in the several layers

To measure the number of atoms in each layer, I applied the quantum magnifier scheme recently demonstrated by [Ast+21]. This scheme relies on exchanging the position and momentum distributions of the atoms with a  $\pi/2$  phase space rotation, and this is realized in a conservative harmonic potential of period  $T$  every  $\delta t = T/4$ . In the experiment, this is done by suddenly turning on and off a harmonic potential during one fourth of the period  $T = 2\pi/\omega$  where  $\omega$  is the trapping frequency along the magnification direction, vertical in this case, and this way, initial positions  $\{x_i\}$  of trapped atoms converted to initial momenta  $\{p_i\}$ . Then, the gas is released for a time of flight measurement. Since the measured positions map the initial momentum distribution, this is actually a measurement of the spatial distribution of the atoms in the lattice

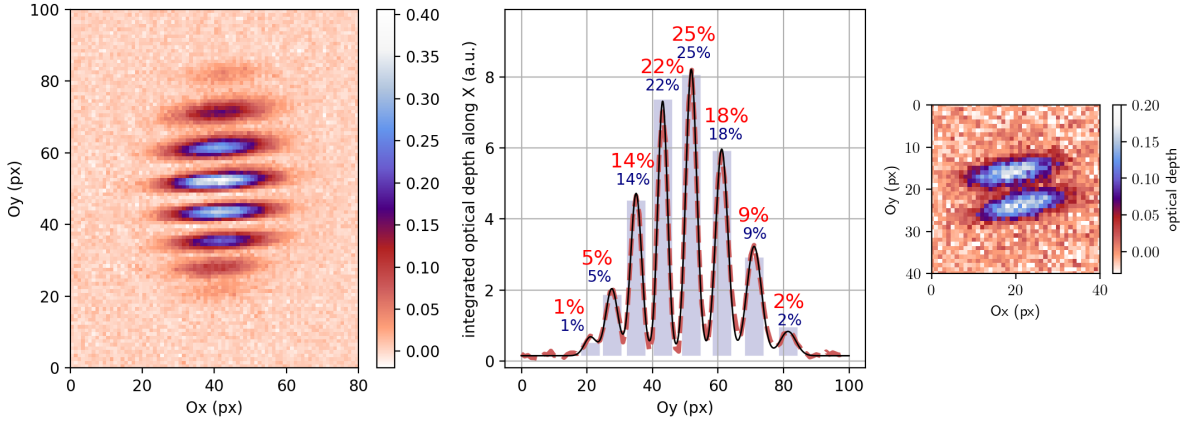


Figure 1.9: Magnification of the sites of the 1D lattice using the quantum magnifier scheme [Ast+21] along the vertical axis. Left: experimental absorption image of the magnification of the sites, with approximately  $85 \times 10^3$  atoms at  $T/T_F \simeq 0.3$  before loading. The color bar represents the optical depth per pixel surface. Center: fit of the integrated optical depth to measure the populations into the different 2D layers. The relative population measured in each layer is noted as a percentage above each peak picturing a layer, in red, big font. The bins represent a guess of the populations with respect to the size  $\sigma$  of the initial gas and the sites spacing  $a$  of the lattice. Here,  $\sigma \simeq 3.1 \mu m$  and  $a \simeq 2 \mu m$ . The relative population guessed in each layer is noted as a percentage above each peak picturing a layer, in dark blue, small font. Right: loading of two layers only.

$\{x_i\}$  thanks to the harmonic pulse. If the eigenaxis of the harmonic pulse is perfectly colinear with the eigenaxis of the bravais lattice, then this measurement results in a magnification  $M = \omega\tau$  of the bravais lattice, where  $\omega$  is the harmonic frequency and  $\tau$  the time of flight.

In our experiment, I used the horizontal laser beam used for the dipole trap with strong trapping frequency essentially along the vertical axis,  $\omega_z \simeq 2\pi \times 450$  Hz, which is parallel to the lattice eigenaxis. With a  $T/4$  pulse and 10 ms of time of flight, the vertical magnification is  $M \simeq 30$  for sites spacing  $a \simeq 2 \mu m$  of the 1D lattice, which corresponds to approximately 9 pixels of size  $6.45 \mu m$  in our camera. The resulting experimental absorption imaging is shown in figure 1.9, left, where we can see that the 2D layers are well resolved. Figure 1.9, center shows the integrated optical depth along

the axis of the layers, such that it is possible to measure the number of atoms in each layer. From this data, I deduce the relative populations in each site, as noted above the integrated density of each layer in red, big font. The measure let us know that approximately 50 % of atoms are into the 2 equally populated middle layers, and about 30 % in the two next equally populated layers. This measure is compared with a guess of the populations, inferred from the size  $\sigma_z = \sqrt{k_B T / m \omega_z^2}$  of the initial Boltzmann gas and the sites spacing  $a$ . This indicates that the atoms barely move while being loaded into the 1D lattice, as a consequence of the long period of the potential that rapidly kills tunneling at bar lattice depth. The initial density is sliced into bins mapped on the lattice sites, as shown on the figure, and then the relative number of atoms are inferred from the binned density. The result, for a gas of initial size  $\sigma_z \simeq 3.1 \mu\text{m}$ , corresponding to an initial 3D trap with frequency  $\omega_z / 2\pi \simeq 130 \text{ Hz}$  at temperature  $T \simeq 65 \text{ nK}$ , is texted above the bins in dark blue, small font. The guess fits very well with an average deviation of less than 1 %. In the guess, the lattice sites are shifted by  $a/5$  to match the asymmetry in the populations of the sites. Finally, we show that the number of loaded layers can be tuned, as it depends on the initial extension of the 3D gas. Hence, adiabatic compression of the gas along the lattice eigen-axis reduces the number of lattice sites that are loaded, and figure [1.9](#), right, shows that we are able to load two layers only, which moreover have approximately the same number of atoms.

### Layers independence

The layer to layer tunneling is suppressed thanks to the very low recoil, *i.e.* very large sites spacing  $a$ , of the lattice. Strontium atoms in the ground state have zero electric dipole moment, and the magnetic dipolar interaction of the nuclei are negligible [\[Gor+10\]](#). The 2D layers defined by the 1D lattice are then completely independent. This is actually a very interesting feature since it allows to simultaneously run independent quantum simulations in each layer, and hence increases the experiment capability to acquire much data and increase the quality of statistical analysis.

## 1.2.2 532 nm 2D lattice

### Geometry

The 2D lattice is made of two retro-reflected laser beams with waists  $150 \mu\text{m}$  at the atoms position and powers  $P_1$  and  $P_2$ . The intensities are controlled with two independent AOMs detuned by 200 MHz to prevent interferences. The azimuthal angle  $\delta\phi$  between the two laser beams is exactly  $90^\circ$  and both have  $\theta = 16^\circ$  elevation. The spherical coordinates of the wavevectors of the two beams can then be written as  $\vec{k}_1 = (k, \theta_1 = +16^\circ, \phi_1 = \phi)$  and  $\vec{k}_2 = (k, \theta_2 = \theta_1, \phi_1 = \phi + 90^\circ)$ , where  $k = 2\pi/\lambda$ ,  $\lambda = 532 \text{ nm}$ . The intensity of resulting stationary wave is

$$I(\vec{r}) = 4P_1 \sin(\vec{k}_1 \cdot \vec{r})^2 + 4P_2 \sin(\vec{k}_2 \cdot \vec{r})^2 \quad (1.6)$$

Within each 2D layer defined by the maxima of the 1D lattice at 1064 nm, the projected 2D bravais lattice can be then written as:

$$\vec{R}_{m,n} = m \frac{\lambda}{2 \cos \theta} \vec{a}_1 + n \frac{\lambda}{2 \cos \theta} \vec{a}_2 \quad (1.7)$$

where  $\theta = 16^\circ$ . Here,  $m$  and  $n$  are the sites indices of the bravais lattice and  $a_1$ ,  $a_2$  the eigen-axis, respective normalized projections of  $k_1$  and  $k_2$  along the  $(Oxy)$  plan defined on figure [1.6](#).

Note that  $k_1$  and  $k_2$  are not orthogonal,  $\vec{k}_1 \cdot \vec{k}_2 \propto \cos(\theta)^2 \neq 0$ , but the projection of the 2D lattice on the horizontal planes defined by the 1D lattice maxima is a proper 2D square lattice. Indeed,  $\vec{a}_1 = (1, \theta = 0, \phi_1 = \phi)$  and  $\vec{a}_2 = (1, \theta_2 = 0, \phi_1 = \phi + 90^\circ)$  so that  $\vec{a}_1 \cdot \vec{a}_2 = 0$ . Moreover, the  $\delta = 200 \text{ MHz}$  detuning between the two lattice arms is negligible with respect to the light frequency  $\nu_l = c/\lambda$ , *i.e.*  $\delta/\nu_l \simeq 3 \cdot 10^{-7}$ , so that the lattice can be considered square, with sites spacing  $a = 276 \text{ nm}$ .

### Ground band population

To measure the number of atoms in the ground band of the 2D lattice, I first identified the first Brillouin zone (FBZ) with a diffraction measurement. The 2D lattice is quickly turned on and off during a few microseconds on the bulk gas, and the diffraction orders

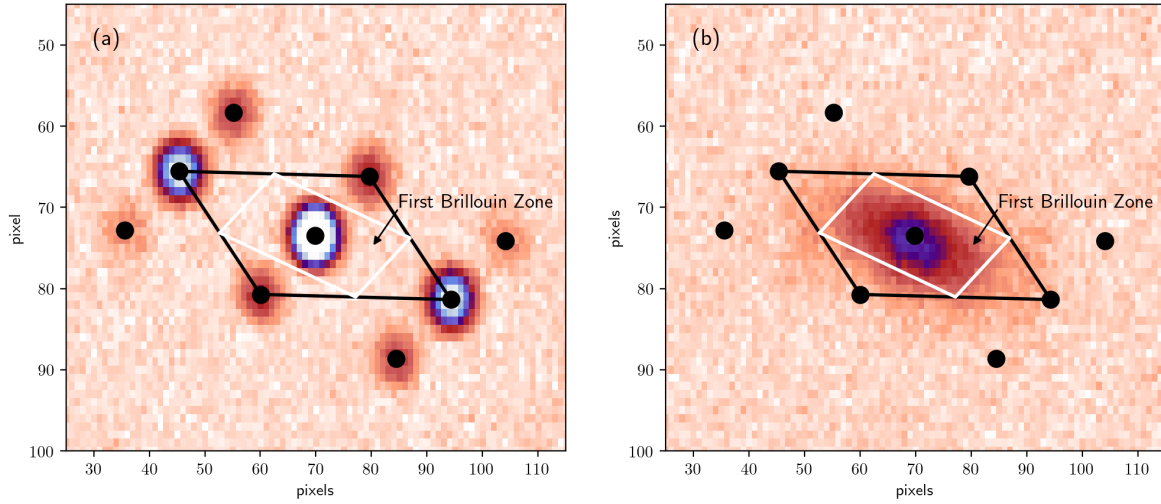


Figure 1.10: Absorption images of atomic clouds after diffraction (a) and band mapping (b) of the 2D lattice at 532 nm. (a) Simultaneous diffraction of the atomic cloud by the two arms of the 2D lattice. The first Brillouin zone (FBZ) at  $\pm 1\hbar\vec{k}_R$  is graphically inferred from the first diffraction orders at  $\pm 2\hbar\vec{k}$  momentum recoils. The non diffracted population is the brightest central cloud. (b) Measurement of the population in the ground of band of the 2D lattice with 2D band mapping after adiabatic loading of the lattice, where the FBZ is mapped from the diffraction measurement.

are identified after a time of flight. The first diffraction orders of each arm of the 2D lattice give a measurement  $\pm 2\hbar\vec{k}_R$ , where  $\vec{k}_R$  is the momentum recoil of each lattices, which further allows to identify the FBZ. This is shown on figure 1.10, (a), where the FBZ is identified as the white rectangle at  $\pm 1\hbar\vec{k}_R$  of each lattice. Then, the number of atoms in the FBZ after adiabatic loading of the 2D lattice can be measured from a band-mapping [Köh+05]. In our experiment, this is done by slowly turning off the 2D lattice within 2 ms before time of flight. By mapping the FBZ identified with lattice diffraction onto the band mapping, it is possible to count the number of atoms loaded in the FBZ. With this measurement, I infer that 91 % to 97 % atoms are loaded in the ground band of the lattice, allowing for  $\pm 1$  pixel uncertainty on the identification of the FBZ.

## Chapter 2

# Absorption imaging of objects smaller than the resolution limit

In our experiment and more generally in the whole community, we study physics in cold and ultra cold gases which are typically tiny objects not much larger than a micrometer. Such objects are sometimes not resolved by standard imaging setups with low numerical aperture, and we typically consider that the data provided by *in-situ* absorption imaging cannot be used in that case. In this chapter, I present our method [Lit+21] to recover the actual size of our *in-situ* object even when this is below our imaging resolution limited by either low numerical aperture, pixelation, or aberrations such as out of focus imaging. It relies on an estimate of the fraction of absorbed photons inferred from two absorption pictures, with and without atoms, which depends non-linearly on the local density of atoms when the optical depth is large enough. By using a convenient ansatz on the density profile, and an independant measurement of the number of atoms, we show that the actual size of the sample can be known. We have tested our method on absorption images of elongated gases, unresolved along the transverse axis only, in which case a straight application of the integrated Beer-lambert law leads to strong distortions of the measured local density, so that even the longitudinal axis, assumed resolved, is distorted. Our results show that we are able to measure *RMS* sizes as small as one fourth of our resolution limit, and we confirm the validity of our method by comparing our measurements to expected sizes from equi-partition of energy. Finally, I will show that this method also permits to recover the density profile along the elongated

axis. We verified this result with a comparison to expected density profiles from both Boltzmann statistics for hot gases and Fermi statistics for degenerate gases.

## 2.1 Motivations

### 2.1.1 Measuring the interaction energy of an $SU(10)$ degenerate Fermi gas

This work was first motivated by an experiment to measure the enhanced mean-field interaction in the weakly interacting regime of a  $SU(10)$  degenerate Fermi gas [Son+20] of fermionic  $^{87}\text{Sr}$ , which has 10 degenerate ground spin states and spin-independent scattering length  $a_S = 97 a_0$ , in Bohr radius units. In a two components Fermi gas with equal populations, the mean-field energy  $E_{int}^{SU(2)}/E_{ho} \simeq k_F a_s/3$  [VS99; MPS02] is small, where  $k_F$  is the Fermi momentum,  $a_s$  the scattering length and  $E_{ho}$  the oscillator energy. However, a Fermi gas with enlarged  $SU(N)$  symmetry [CHU09; Gor+10; Tai+12] has increased interaction energy  $E_{int}^{SU(N)} = (N-1)E_{int}^{SU(2)}$  due to reduced role of the Pauli exclusion principle. When a trapped ultra cold quantum gas is released by switching off the trap, the local density decreases during expansion and hence so does the mean-field energy  $E_{int}$ , which is progressively converted to kinetic energy due to energy conservation. A measurement of the velocity distribution after time of flight provides the release energy  $E_R$  [Bou04], which is the sum of the initial kinetic energy prior to the release  $E_K$ , with the mean-field energy [GPS08]. In a given direction, the release energy is then given by

$$E_{R,tof}^{1D} = \frac{1}{3}E_K + \frac{1}{3}E_{int} \quad (2.1)$$

In our experiment with fermionic  $^{87}\text{Sr}$ , we wanted to further enhance the mean-field signal with a 1D expansion, *i.e.* by allowing the gas to expand along one axis only, so that the full mean-field energy is converted to kinetic energy into this axis only. In this case, the release energy along a given direction is then given by:

$$E_R^{1D} = \frac{1}{3}E_K + E_{int} \quad (2.2)$$

The mean field energy can finally be inferred by comparing these two quantities, *i.e.* the release energy measured from a 1D expansion and measured independently from a time of flight. This method has the advantage that it is twice as sensitive as a single time of flight measurement of the release energy to infer the mean field energy.

### 2.1.2 Distorsion of imaged in-situ density

We first did the measurement of the release energy with a 1D expansion. The gas, initially trapped in a 3D harmonic potential, is suddenly released along one direction only while it remains confined in the two other directions. After expanding along this single direction, we take *in-situ* absorption images of the elongated gas inside the 2D confinement, which is presented in figure 2.1 (a). From this measurement, we identify several problems. First, the imaged gas is confined into the 2D trap, and figure 2.1 (b) shows that the density distribution along the short axis, which is along the 2D confinement, is pixelated as it is spread over a few pixels only, and the negative signals indicate imaging aberrations such as light diffraction on the atomic cloud, and out of focus imaging. Moreover, from the imaged density of atoms  $n(i, j)$ , measured from the standard application of the Beer Lambert law on each pixel (i,j):

$$n(i, j) = -\frac{1}{\sigma_0} \log \frac{I(i, j)}{I_0(i, j)} \quad (2.3)$$

we obtain an integrated density profile along the elongated axis which shows significant deviations from the expected gaussian distributions at temperatures  $T > T_F$  as shown in figure 2.1 (c). Here,  $\sigma_0 = 3\lambda^2/2\pi$  is the resonant atom-light absorption cross-section, and  $I$  ( $I_0$ ) the recorded light intensity with (without) atoms. Finally, the number of measured atoms on the 1D expansion measurement,  $N_{at}^{1D} \simeq 9 \times 10^3$  did not match ones of the time of flight experiments  $N_{at}^{tof} \simeq 14 \times 10^3$ , which are shown on figure 2.1, (d). This is explained because the density profile is not resolved along the short axis, resulting in pixelation, and the local density of atoms cannot be directly inferred from the Beer-Lambert law used for absorption imaging because of its non linearity. Hence, using the Beer-Lambert law induces non-linear error on the estimated local atomic density, which results on a distorted image, and any straight estimate of the release energy is mistaken, even along the *a priori* resolved elongated axis.

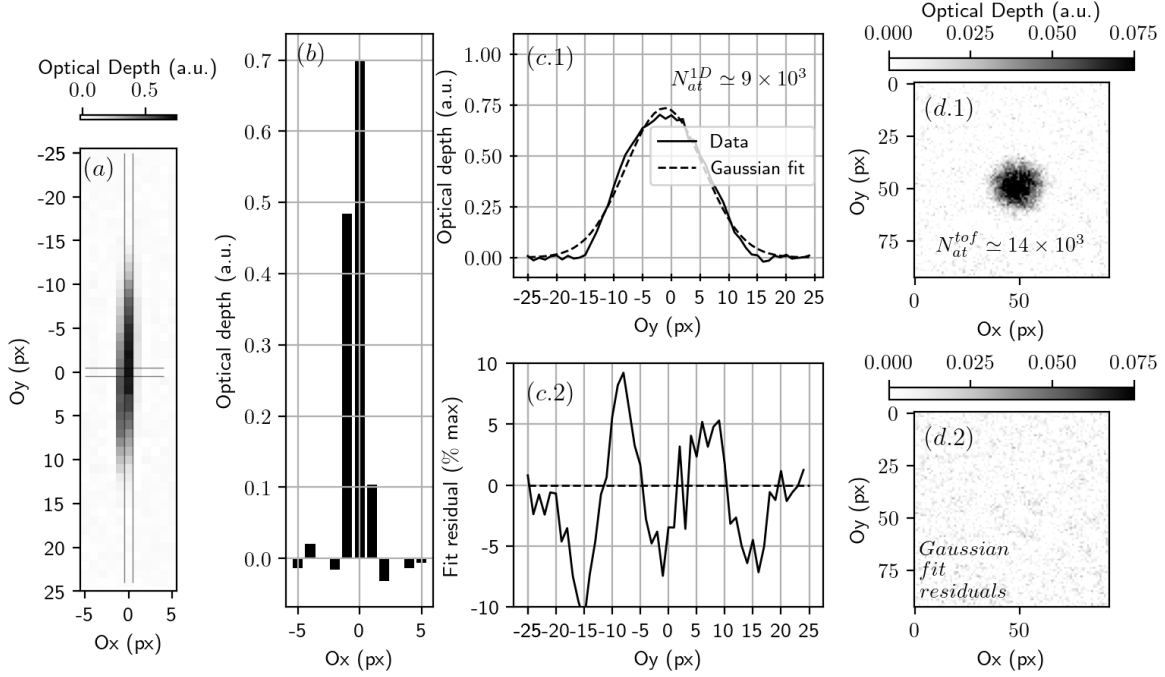


Figure 2.1: Distorsion of optical depth with in-situ absorption imaging of an elongate gas inside a 2D confinement. (a) Optical depth measured with absorption imaging and the Beer Lambert law. The grey solid lines indicate horizontal, and vertical, cuts shown on figures (b), and (c.1), respectively. (b) Each vertical bin corresponds to a single pixel of the horizontal cut. (c.1) Vertical cut of the optical depth in solid black line, and gaussian fit in dashed red line. The residuals of the fit, normalized by the signal maximum amplitude, are shown on figure (c.2). (d.1) Time of flight measurement, and (d.2) residuals of the gaussian fit from which we measure the number of atoms.

### 2.1.3 Incorrect estimation of the pixelated local density

The local intensity loss of a weakly saturating laser beam propagating through an atomic cloud is proportionnal to the atom-light absorption cross section  $\sigma$  and the local density of atoms  $n$ . This is the well known Beer-Lambert law, and for resonant light propagating along  $O_z$ , it is written as:

$$\frac{dI}{I} = -n\sigma_0 dz \quad (2.4)$$

Assuming that the length of the gas along the propagation axis is smaller than the

Rayleigh length of the imaging laser beam, diffraction effects along propagation can be neglected, and the  $x,y,z$  intensity variations are independent. Then, the optical depth  $OD(x, y) = \sigma_0 \int n(x, y, z) dz$  is defined after integration of the Beer-Lambert law along the propagation axis:

$$OD(x, y) = -\log \frac{I(x, y)}{I_0(x, y)} \quad (2.5)$$

where  $I$  is the light intensity after passing through the atomic cloud, and  $I_0$  is the light intensity without gas. The column density  $\tilde{n}(x, y)$  is then directly inferred from

$$\tilde{n}(x, y) = \frac{OD(x, y)}{\sigma_0} \quad (2.6)$$

On experiments, the light intensity is recorded on cameras with pixel size  $a$ . The recorded power  $P(i, j)$  on pixel  $(i, j)$  is then the light intensity integrated over the surface  $a^2$  of a pixel at location  $(i, j)$ :

$$P(i, j) = \iint_{\text{pixel}(i, j)} I(x, y) dx dy \quad (2.7)$$

where  $\text{pixel}(i, j) = [\{ia, (i + 1)a\} \times \{ja, (j + 1)a\}]$  is the domain of integration. If the intensity profiles vary slowly enough over the pixel length  $a$ , *i.e.*  $dI/dx \ll I/a$  and  $dI/dy \ll I/a$ , then the double sum in equation [2.7](#) can be approximated to  $P(i, j) \simeq a^2 I(ai, aj)$ . In this case, the local density of atoms, average over pixel  $(i, j)$ , can be measured with the optical depth that is inferred from the averaged local intensity using equation [2.5](#)

$$\langle \tilde{n} \rangle_{(i, j)} \sigma_0 \equiv \langle OD \rangle_{(i, j)} \simeq -\log \frac{P(i, j)}{P_0(i, j)} \quad (2.8)$$

However, if the gas is too small so that the intensity profile varies quickly with respect to the pixel size, the approximation for the Beer-Lambert in equation [2.8](#) doesn't hold. In this case, the logarithm of the averaged absorbed light is not equal to the averaged optical depth:

$$\log \frac{P(i, j)}{P_0(i, j)} \neq \frac{1}{a^2} \iint_{\text{pixel}(i, j)} \log \frac{I(x, y)}{I_0(x, y)} dx dy \quad (2.9)$$

which is due to the non-linearity of the logarithm. Hence, it is generally not possible to infer the local density of atoms by using the integrated Beer-Lambert law with the recorded light power on each pixel, and this is what we observed on the 1D expansion measurement shown on figure 2.1. It is interesting to note here that even if only one of the two dimensions are not resolved, it is enough to forbid the approximation 2.8 and the data remains in the non valid case similarly to equation 2.9.

This shows that a straight use of the integrated Beer-Lambert law to measure the optical depth is mistaken and leads to distorted density profiles in case of pixelation, but it is also true if the resolution limit, larger than the imaged object, is due to the diffraction limit for instance. This effect is even more significant for large optical depths with quickly varying profiles, but our problem is different from the total absorption regime [Rei+07]; we consider here that there is light collected at every pixel, accordingly to our measurement presented on figure 2.1. In this regime, the error on the measured number of atoms can be compensated for by rescaling the absorption cross section [Est+06], giving a first order correction on the measurement of the local density of atoms. However, here we show that the error on the measurement of the local density of atoms is non linear, so that it is important to consider an effective absorption cross section which depends on the density  $\sigma_0 \rightarrow \tilde{\sigma}(\tilde{n})$ . I will now show how to apply this correction.

## 2.2 Non-linear correction on the measurement of the sub-resolved local density

In this section, I describe how to account for the resolution problem by making use of the fact that when light passes through an atomic cloud, the amount of absorbed photons depends on the density of atoms and the depth of the crossed cloud. The first met atoms absorb some quantity of light, so that the next atoms are in their shadow and hence are not exposed to the same intensity. Hence, for a fixed number of atoms in a given light beam, the total number of absorbed photons depends only on the size of the atomic cloud, since the shadowing effect increases for larger densities. I will now show that relying on this principle, it is possible to dodge the resolution limit and

infer the local density from the number of missing photons, thanks to an independent measurement, *e.g.* the total number of atoms. This way, we infer both the size of the gas along the non resolved axis  $Ox$ , and the longitudinal density profile along the elongated axis  $Oy$ .

### 2.2.1 Parametrization of the density dependent correction

We focus here on elongated gases with a slowly varying longitudinal profile, as shown on figure 2.1, (c.1), and non-resolved density profile along the transverse axis, as shown on figure 2.1, (b), accounting for possible light diffraction on the tightly confined axis and defocusing. Let's first derive an equation for the total number of absorbed photons as a function of the local column density  $\tilde{n}(x, y)$ . From two images of the imaging beam, one with atoms and recorded power  $P(i, j)$  at pixel  $(i, j)$ , and one without atoms and recorded power  $P_0(i, j)$ , we define the ratio of absorbed photons  $(P_0(i, j) - P(i, j))/P_0(i, j)$ . Note that here, we defined the domain of integration as the pixel size  $a^2$ , similarly to equation 2.7. Let's now define

$$R_{ph}(j) = \sum_i \frac{P_0(i, j) - P(i, j)}{P_0(i, j)} \quad (2.10)$$

the ratio of absorbed photons recorded on the camera along the elongated axis  $Oy$  (index  $j$ ) which is not problematic with respect to the imaging limitation. The integration along a pixel line in the transverse axis  $Ox$  (index  $i$ ) permits this reduction of dimensionality, which moreover allows to not account for the light diffraction along the short axis  $Ox$  [Arm+10]. Then, by inserting definition 2.7, one gets:

$$\begin{aligned} R_{ph}(j) &= \sum_i \frac{1}{P_0(i, j)} \iint_{pixel(i, j)} \left( I_0(x, y) - I(x, y) \right) dx dy \\ &= \sum_i \iint_{pixel(i, j)} \frac{I_0(x, y)}{P_0(i, j)} \left( 1 - \frac{I(x, y)}{I_0(x, y)} \right) dx dy \end{aligned} \quad (2.11)$$

Even if the object is small, the imaging light beam has to be large enough such that the light intensity is homogeneous over the surface of a pixel. In this case,  $P_0(i, j) =$

$a^2 I_0(x, y)$ . Then, by inserting the local column density  $\tilde{n}(x, y)$  defined in equation [2.6](#), one gets:

$$R_{ph}(j) = \sum_i \frac{1}{a^2} \int_{a_i}^{(a+1)^i} dx \int_{a_j}^{(a+1)^j} dy \left( 1 - \exp\left(-\sigma_0 \int n(x, y, z) dz\right) \right) \quad (2.12)$$

Far from the cloud of atoms, no photons are absorbed, such that the sum over the short axis  $\sum_i \int_{a_i}^{(a+1)^i} [\dots] dx$  can be extended to infinity  $\int_{\mathbb{R}} [\dots] dx$  where the ratio of absorbed photons is zero. Also, in our case, the gas is very elongated along axis Oy, and hence it is rather homogeneous over a pixel length along Oy, such that  $\int_{a_j}^{(a+1)^j} f[n(x, y, z)] dy \simeq a f[n(x, aj, z)]$ , where  $f$  can be any slow varying function of the atomic density  $n(x, y, z)$ . With these simplifications, equation [2.12](#) can be rewritten as:

$$R_{ph}(j) = \frac{1}{a} \int_{\mathbb{R}} \left( 1 - \exp(-\sigma_0 \tilde{n}(x, aj)) \right) dx \quad (2.13)$$

Equation [2.13](#) is our first equation relating the ratio of absorbed photons which is the actual data, with respect to the column density of atoms, which is what we want to infer. Until now, the following approximation have been made. First, the atomic gas is elongated enough along axis Oy so that the variations of the density profile along this axis are negligible along one pixel length. Also, we supposed that the light intensity of the imaging beam is homogeneous over the surface of a pixel, and, the diffraction of the probe light can be neglected over the depth of the sample along its propagation direction.

Now, let's parametrize the sub-resolution feature, which is the size of the cloud along the unresolved transverse axis. To do this, we introduce an ansatz on the local density of the gas, and it is relevant to use a gaussian ansatz for thermal gases:

$$\tilde{n}(x, aj) = e^{-\frac{x^2}{2\sigma_x^2}} \tilde{n}(0, aj) \quad (2.14)$$

where  $\sigma_x$  is the transverse size of the cloud, and  $\tilde{n}(0, aj)$  the peak column density along axis Oy. By inserting the gaussian ansatz in equation [2.13](#), and with change of variable  $u = x/\sigma_x$ , one gets:

$$\begin{aligned}
R_{ph}(j) &= \frac{\sigma_x}{a} \int_{\mathbb{R}} \left( 1 - \exp\left(-\sigma_0 \tilde{n}(0, aj) e^{-u^2/2}\right) \right) dx \\
&\equiv \frac{\sigma_x}{a} F(\sigma_0 \tilde{n}(0, aj))
\end{aligned} \tag{2.15}$$

which defines the transfer function  $F$ . This last equation relates the quantity  $R_{ph}(j)$  to the local density of atoms that we want to retrieve, parametrized by the size  $\sigma_x$ .  $F$  is monotonous, hence it can be inverted to have a direct reading of the local density:

$$\begin{aligned}
\tilde{n}(0, aj) &= \frac{1}{\sigma_0} F^{-1}\left(\frac{a}{\sigma_x} R_{ph}(j)\right) \\
&\equiv \frac{1}{\sigma_0} OD_{eff}(j)
\end{aligned} \tag{2.16}$$

This highlights that the expected local density is obtained from the establishment of an effective optical depth  $OD_{eff}(j)$ , dependent on the measurement  $R_{ph}(j)$ , and parametrized by the size  $\sigma_x$ . Actually, this is equivalent to the establishment of an effective absorption cross section  $\sigma_{eff}$  by the following transformation:

$$\tilde{n}(0, aj) = \frac{1}{\sigma_0} OD_{eff}(j) \Rightarrow \tilde{n}(0, aj) = \frac{1}{\sigma_{eff}} OD(j) \tag{2.17}$$

where  $OD = -\log P/P_0$  is the straight application of the Beer-Lamber law (see figure [2.1](#)), contrary to  $OD_{eff}$  which is inferred from our method. The expected local density of atoms is then equivalently inferred by introducing either an effective optical depth, or an effective absorption cross-section, both dependent on the measurement  $R_{ph}(j)$ , *i.e.* on the local density of atoms itself. In both cases, this correction is parametrized by the unknown size  $\sigma_x$ , hence a supplementary constraint is required.

### 2.2.2 Calibration of the non-linear correction

Several constraints can be used, typically the parameters defining the statistics of a thermal cloud, and here we choose an independent measurement of the number of atoms. A gas is prepared in the same conditions than the 1D expansion experiment and it is imaged after a time of flight, *i.e.* released along the three directions so that

it expands enough to be resolved and equation [2.6](#) can be used. In this case, the total number of atoms is obtained from a direct measurement of the optical depth as defined in equation [2.5](#):

$$N_{at}^{tof} = \frac{a^2}{\sigma_0} \sum_{i,j} OD^{3D}(i,j) \quad (2.18)$$

where the *tof* annotation refers to the independent measurement with a time of flight. Regarding the 1D expansion experiment, the total number of atoms can be computed from the column density  $\tilde{n}(0, aj)$  and transverse size  $\sigma_x$ , according to the gaussian ansatz [2.14](#), and using equation [2.16](#), the number of atoms finally reads:

$$N_{at} = \sqrt{2\pi}\sigma_x \frac{a}{\sigma_0} \sum_j F^{-1}\left(\frac{a}{\sigma_x} R_{ph}(j)\right) \quad (2.19)$$

Here, the pixel size  $a$  appears because the number of atoms is obtained from the discrete sum over pixels, which has to be rescaled to the physical pixel size. Equation [2.19](#) relates the unresolved transverse size  $\sigma_x$  to the measured number of missing photons, through the constrained number of atoms. Finally, the size  $\sigma_x$  that we measure is obtained by matching the number of atoms indendently measured with a time of flight and with a 1D expansion, which is done by solving:

$$N_{at}^{tof} - \sqrt{2\pi}\sigma_x \frac{a}{\sigma_0} \sum_j F^{-1}\left(\frac{a}{\sigma_x} R_{ph}(j)\right) = 0 \quad (2.20)$$

The establishment of this equation concludes the method to restore the density profiles from the distorted images of the atomic clouds. Note that the dependence on the atom-light absorption cross-section  $\sigma_0$  is the same for both derivations of the number of atoms, such that it is canceled from the cost function. Hence, the estimation of the size  $\sigma_x$  is independent of  $\sigma_0$ , which is an advantage because this method is then insensitive to fluctuations which could arise, for instance from optical pumping effects during the imaging.

## 2.3 Experimental demonstration

### 2.3.1 Production of degenerate Fermi gases expanding along one direction only

The gas is cooled by forced evaporation in our optical dipole trap as presented in chapter [1](#). The optical dipole trap (ODT) is made of two far red-detuned laser beams, one horizontal, and the other one makes a  $30^\circ$  angle with respect to gravity axis. After the gas has reached thermal equilibrium, we let the gas expand only in one direction by switching off the horizontal beam. The gas then falls along the mostly vertical beam. After a certain time of expansion along one dimension, the data is taken with absorption imaging, while the gas is still confined in the two perpendicular directions. The imaging setup has magnification 1 with an objective of focal length  $f = 150 \text{ mm}$  and diameter 2 inches, for a numerical aperture  $\text{NA}=0.08$ . The resulting diffraction limit is  $2\mu\text{m}$ , much lower than the size  $6.45 \times 6.45 \mu\text{m}$  of the square pixels of our camera, which is our ultimate resolution limit. Figure [2.2](#) shows absorption images of the channeled expansion for different times of channeling. This procedure was done for different final temperatures of the thermal gas before release. To measure the expected number of atoms, we use a second set of pictures which is actually a standard time of flight measurement. We let the gas expand in the three directions by turning off both ODT beams, then we take an absorption image. The 3D gas is prepared in the same conditions than the elongated gases, such that the number of atoms are the same in both images. Our imaging setup has magnification 1 and the pixels of the camera have dimension  $6.5 \mu\text{m} \times 6.5 \mu\text{m}$ .

### 2.3.2 Recovery of the unresolved transverse sizes $\sigma_x$ of elongated gases

For each image of the elongated gases, we retrieve the longitudinal profile of the ratio of absorbed photons defined in equation [2.10](#). Then assuming a size  $\sigma_x$ , we compute the corresponding number of atoms as defined in equation [2.19](#). It is possible to build a full curve by repeating this process for different values of  $\sigma_x$ , as shown on figure [2.3](#). In this figure, each one of the three curves corresponds to a single image, cooled to

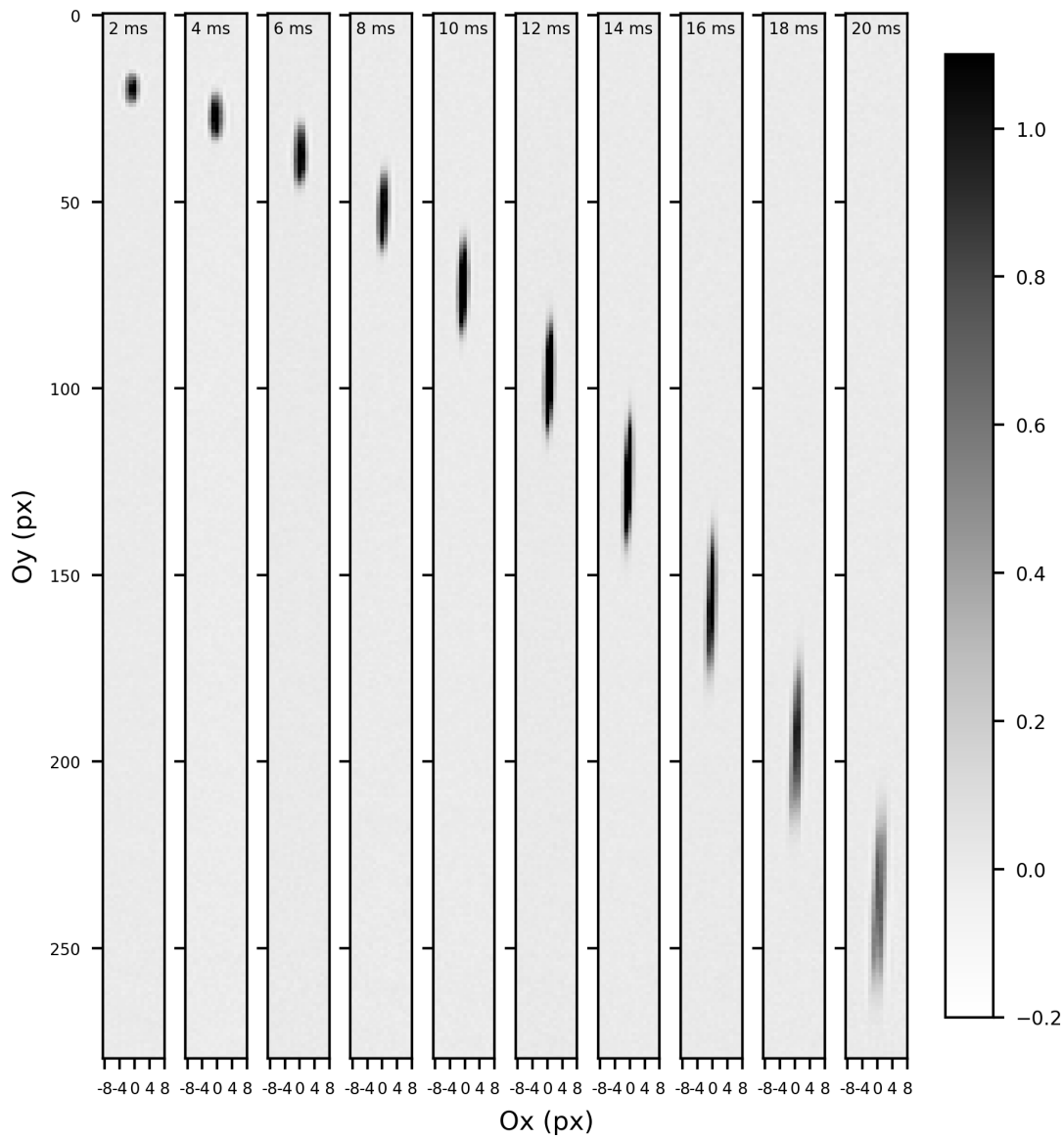


Figure 2.2: Absorption images of channeled expansion. The time of channeling before imaging is written at the top of each image. The horizontal and vertical axis are given in camera pixels scale, as captured during the experiment. The colorbar is the optical depth. The dimension of one pixel is  $6.5 \times 6.5 \mu m^2$  and the imaging setup has magnification 1. All these images belong to a same set of data with temperature  $T \simeq 0.35 T_F$ .

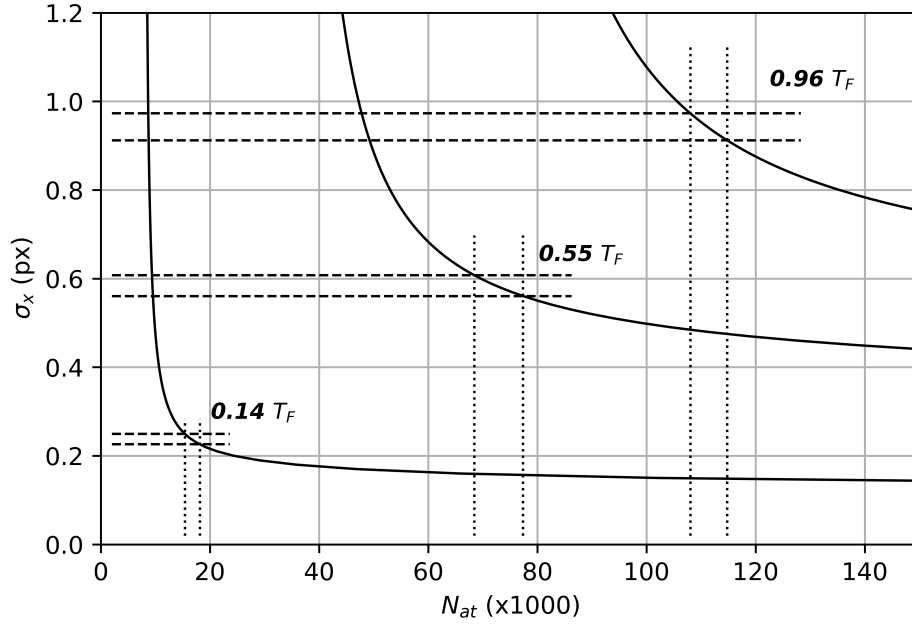


Figure 2.3: Size  $\sigma_x$ , in pixel units, of the elongated gas along the non resolved dimension  $O_x$ , with respect to the number of atoms, computed from the inverse of equation [2.19](#). Each curve indicates the analysis of a single experimental image of an elongated gas, for three different temperatures indicated in Fermi temperature units. The vertical dotted lines indicate the number of atoms measured from the images of 3D gases, with its uncertainty. The horizontal dashed lines indicate the corresponding size for the unresolved elongated gases.

the indicated degeneracy. The temperature and degeneracy are inferred from the 3D gases. Using the reference measurement of  $N_{at}^{tof}$  from the 3D time of flight images, and its associated uncertainty with shot to shot fluctuations, we get the corresponding transverse size  $\sigma_x$  and its confidence interval. This is pictured by the dashed lines on figure [2.3](#). We see here the principle of the analysis: for a given number of absorbed photons, more atoms means a smaller gas, and this is consistent with the shadowing effect described above.

The measured transverse sizes  $\sigma_x$  are reported in figure [2.4](#) as a function of the time of channeled expansion, for every temperatures after evaporation.

First we can see that  $\sigma_x$  doesn't vary much during the channeled expansion. For

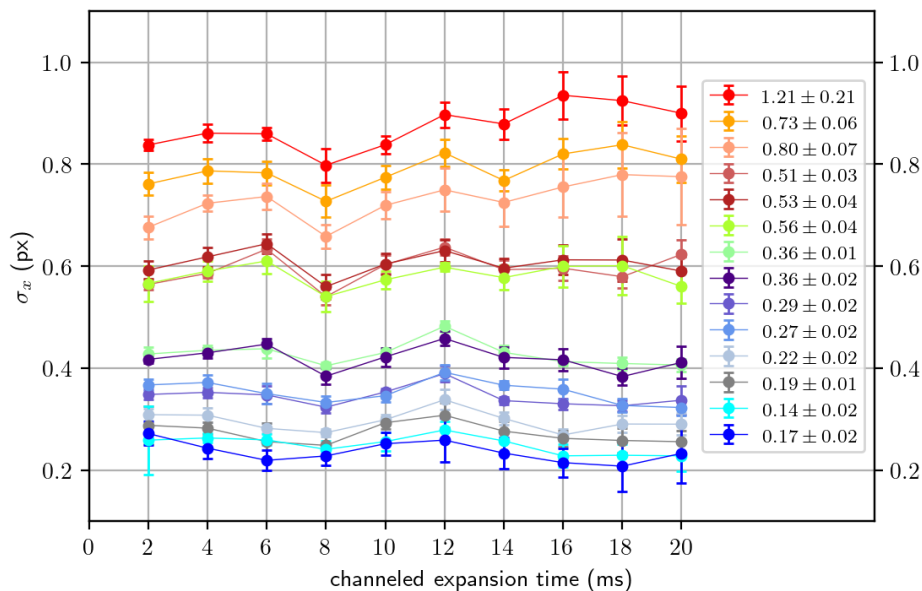


Figure 2.4: Transverse size  $\sigma_x$  in pixel units ( $1 \text{ px} = 6.45 \mu\text{m}$  with respect to the time of channeled expansion time, for different degeneracies  $T/T_F$ , indicated in the legend. Each point corresponds to a statistical average over nearly ten images. The errorbars contain both the confidence interval of the inferred  $\sigma_x$  for each image as well as the standard deviation over the different experimental realizations. The solid lines link the points of the same set of data, *i.e.* with same degeneracy, for visual comfort. The degeneracy is measured on the reference images with 3D time of flight.

instance, the size of gases with temperature  $T \simeq 0.5T_F$  vary within a  $0.6 \pm 0.05 \text{ px}$  window, which corresponds to nearly 10% variations, and colder gases vary as much if not less. However, the hottest gases at  $T \geq 0.7T_F$  have their transverse sizes  $\sigma_x$  somehow raised during the channeled expansion by nearly 10% to 15%. During the channeled expansion, the gas falls along nearly  $100 \mu\text{m}$  of the guiding beam, whose frequency for the transverse confinement evolves from 210 Hz at the initial position of the gas, to 145 Hz after 20 ms of channeling, according to our estimations. Atoms adiabatically follow the shape of the beam, due to the slowly varying Hamiltonian, and the transverse size should raise by 20%. We note the robustness of our method, considering that the measurement of the transverse sizes  $\sigma_x$  is stable with respect to the time of channeling which correspond to different elongations along  $Oy$ . Even at 2 ms of

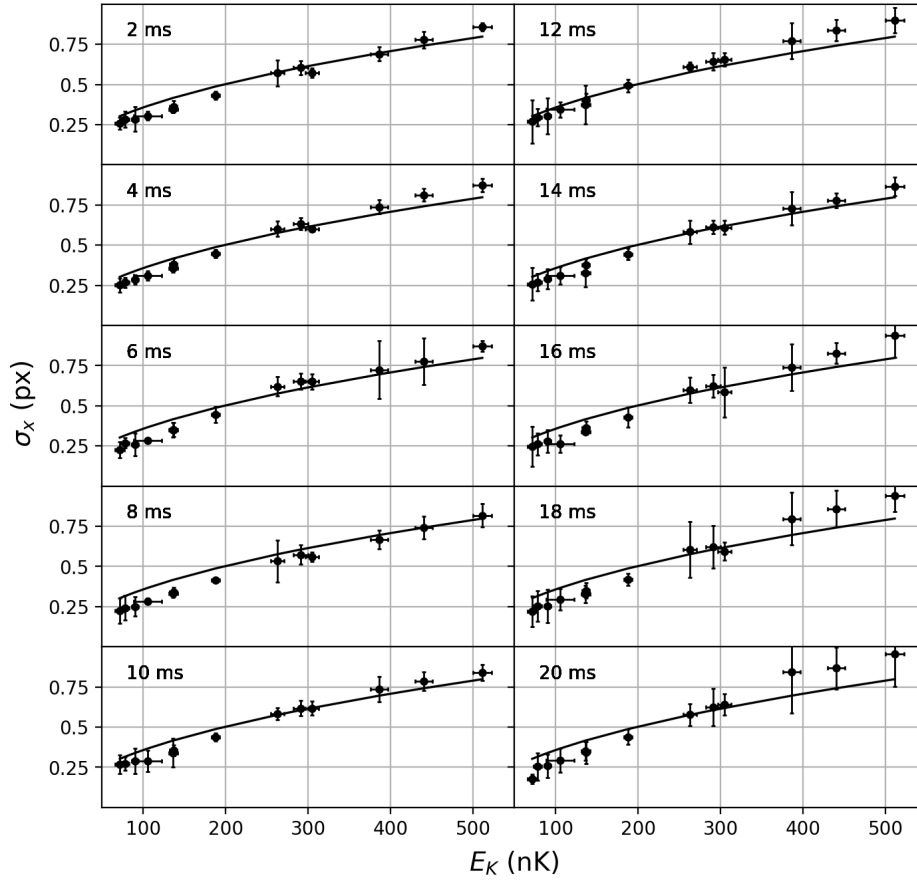


Figure 2.5: Transverse size  $\sigma_x$  with respect to the kinetic energy of the gas. Each box corresponds to a different position in the guiding beam, accordingly to the time of channeled expansion, which is written in the top left corner of each box. Each black dot corresponds to an average over ten images of the inferred transverse sizes. The associated errorbars contain both the confidence interval of the inferred  $\sigma_x$  for each image as well as the standard deviation over the different experimental realizations. The expected transverse size from equi-partition of energy is plotted as solid black line for each time of channeling.

channeling where the gas is smallest along  $Oy$  as shown on figure [2.2](#), the inferred sizes are consistent with the other measurements, which shows that the longitudinal profile varies smoothly enough with respect to the pixel size and the approximation made in equation [2.13](#) is correct.

The smallest measured size (gaussian rms) is as low as one fourth of a pixel, which corresponds to  $1.6 \mu\text{m}$  at the lowest measured temperatures in this experiment,  $T \simeq 30 \text{ nK}$  at  $T \simeq 0.15 T_F$ . This is smaller than the typical distortions introduced by diffraction of the imaging beam and out-of-focus measurements, and much smaller than our resolution limit imposed by the  $6.45 \mu\text{m}$  wide camera pixels.

To verify that our measurements of  $\sigma_x$  are consistent, we compare the result of our method to theoretical predictions. Because of equi-partition of energy, we expect that  $\frac{1}{2}m\omega^2\sigma_x^2 = E_K$ , where  $E_K \equiv \frac{1}{2}m \langle v_x \rangle^2$ , neglecting inter-atomic interactions. The kinetic energy can be measured from the reference images of gases expanding in 3D, and the trap frequency can be independently measured. It is then possible to have an independent prediction of the in-situ transverse size of our elongated gases, with no free parameter. The comparison between our measurement and the prediction is plotted on figure [2.5](#), independently for each time of channeling. At high temperatures, and long time of expansion, there is a tendency of overestimating  $\sigma_x$  with our method compared to the prediction, although both estimations remain in agreement within errorbars.

### 2.3.3 Recovery of the distorted longitudinal density profiles

We now are interested in the longitudinal density profile. I have shown in section [2.1.2](#) and [2.1.3](#) that absorption imaging distorts the local density of non resolved atomic clouds. In figure [2.1](#), it is shown that even if only one axis (Ox) is non-resolved, the density profile inferred from the Beer-Lambert law is wrong along the *assumed-resolved* axis (Oy). However, according to equation [2.15](#), it is now possible to properly infer  $\tilde{n}(0, a_j)$  with our method, once the transverse size has been measured. Comparing the recovered density profile with Boltzmann and Fermi predictions for thermal gases, at respectively  $T/T_F \simeq 1$  and  $T/T_F \ll 1$ , further confirms the validity of our method.

Figure [2.6](#), left, shows the longitudinal density profile recovered with our method, compared to the density profile directly inferred from the logarithm of the fraction of absorbed light on every pixel, as defined in equation [2.6](#). With  $\sigma_x$  known, our method gives  $\tilde{n}(0, a_j)$  which is the peak column density along the elongated axis in  $\text{atoms.m}^{-2}$

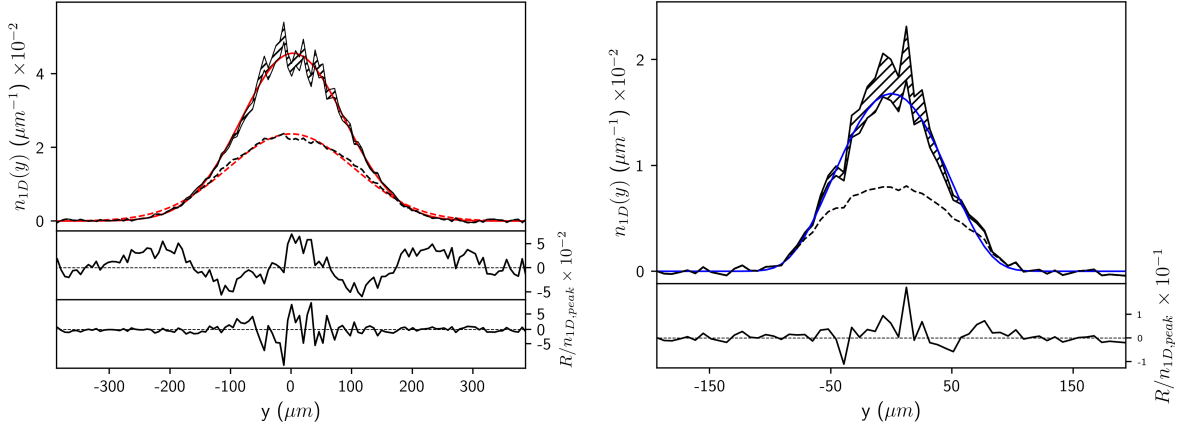


Figure 2.6: Left: Density profile along (Oy) for a hot thermal gas at  $T \simeq T_F$ . Left: in black dashed line, the integrated density profile obtained with equation 2.6, and in red dashed line the corresponding Boltzmann fit. The hashed region corresponds to recovered density with our method with the associated uncertainty, and the red solid line is the associated Boltzmann fit. Bottom: fit residuals, the top one corresponds to the dashed lines, while the bottom one corresponds to our method. Right: Density profile along (Oy) for a degenerate Fermi gas at  $T \simeq 0.15 T_F$ . The blue solid line is the predicted density profile for a Fermi degenerate gas, with no free parameters. The degeneracy, temperature, and trap frequencies are measured independently on the images of 3D expanding gases. The residuals on bottom figure show the agreement between the prediction and our method. For both left and right, the channeling time is 18 ms.

units. It is renormalized in  $\text{atoms.m}^{-1}$  to be comparable with the actual data which is the integrated density profile, *i.e.* for the recovered profile  $n_{1D}(y) = \sqrt{2\pi}\sigma_x\tilde{n}(0, y)$ . In this figure, the density profiles correspond to gases that have channeled during 18 ms, and we expect that they reflect the momentum distribution of the gas before starting their expansion, with initial temperature  $T \simeq T_F$ . At this temperature, the Boltzmann statistics still very well describe the momentum distribution of a thermal gas, and our fits are done with gaussian functions. While the density inferred from equation 2.6 deviates from the Boltzmann statistics, our method recovers a density profile in agreement with the expected statistics, as shown by the bottom fit residuals on figure 2.6, left.

Further verification is done on a degenerate Fermi gas. The recovered density is

compared to what is expected by Fermi statistics, with no free parameters. The result is shown on figure 2.6 right. Here, the prediction is the solid blue line, and the density measurement made with integrated Beer-Lambert law is the black dashed line, which is obviously wrong. The density profile recovered by our method is plotted as the hashed region, and it matches with the prediction, as shown by the residuals, plotted at the bottom.

Note that the channeled expansion is performed along a laser beam that makes an angle with the imaging plane (see appendix D), our measurement of the elongated gas is affected by parallax. Also, the divergence of the laser beam results in a position dependent force felt by the atoms as an anti-confinement. For the analysis shown in figure 2.6, the parallax and anticonfinement are compensated for with a single multiplicative correction parameter  $C$  to the cloud size for a given expansion time. More details for the analysis of the parallax and anticonfinement can be found in appendix D.

For both hot gas and degenerate gas, the residuals are small but there remains strong pixel to pixel density fluctuations after the correction, particularly at the lowest momenta. This is due to the non-linearity of the density dependent correction: at higher local densities, small variations of the light absorption result in strong variations of the density, because of the previously introduced shadowing effect.

To conclude, this demonstrates that with our method it is possible to measure the size of atomic clouds as low as one fourth of our resolution limit. This method also gives the possibility to recover density profiles initially distorted by pixelation, diffraction and out of focus imaging, associated with absorption imaging. Here, we used a gaussian ansatz on the cloud shape, and an independent measurement of the total number of atoms to calibrate the effective optical depth that let us infer the local density. Other ansatz are of course possible, however no unexpected features can be retrieved from this method, since different shapes can lead to the same number of absorbed photons. I also applied this method with a Fermi ansatz for the density distribution along the transverse axis. The procedure is exactly the same except that it necessitates independent calibration of the chemical potential and degeneracy, which is easily done from the reference images of 3D expanding gases, and the results are also in good agreement with different predictions. Note that although our method allows

to retrieve features below the imaging resolution, its fundamental limit is the imaging light wavelength  $\lambda$  as it sets the scattering cross section of light by the atoms. Finally, we expect that with this method, features smaller than the imaging resolution within clouds otherwise larger than the imaging resolution can be measured. For example, using the appropriate ansatz, it could be generalized to measure the size of vortex cores within a superfluid, that are typically below the imaging resolution, or other hydrodynamic structures, such as solitons.

## 2.4 Measurement attempt of the mean field interaction energy in a SU(10) degenerate Fermi gas

First motivated by the measurement of the mean-field interaction energy in  $SU(10)$  degenerate Fermi gas of fermionic  $^{87}\text{Sr}$  in the weakly interacting regime, we want to enhance the mean-field signal of an expanding degenerate gas by allowing the gas to expand along one direction only. As shown earlier in section [2.1.1](#) the release energy along one axis of a  $3D$  expansion is given by:

$$E_R^{3D} = \frac{1}{3}E_K + \frac{1}{3}E_{int} \tag{2.21}$$

and the release energy of the gases expanding along one direction only is given by:

$$E_R^{1D} = \frac{1}{3}E_K + E_{int} \tag{2.22}$$

which leads to a stronger impact from the interactions to the release energy than in  $3D$ . The release energy is inferred from the measurement of the RMS radius  $\sigma_y$  of the expanding clouds in ballistic expansion  $\sigma^2(t) = \sigma(0)^2 + a^2t^2$ , where  $a^2 = 2E_R/m$ . Regarding the  $1D$  expansion and the pixelated absorption images, the measurement of the RMS radius of the cloud can now be realized, after the recovery of the density profile of the elongated gases which is discussed in previous section. Figure [2.7](#), left, reports the measurement of the longitudinal size  $\sigma$  along Oy (see figure [2.1](#)) with respect to the time of expansion, both for the channeling gases and the gases released in  $3D$ , and for different degeneracies. Here, all the corrections have been applied for the channeling gases, *i.e.* the recovery of the density profiles, as well as accounting for the parallax and

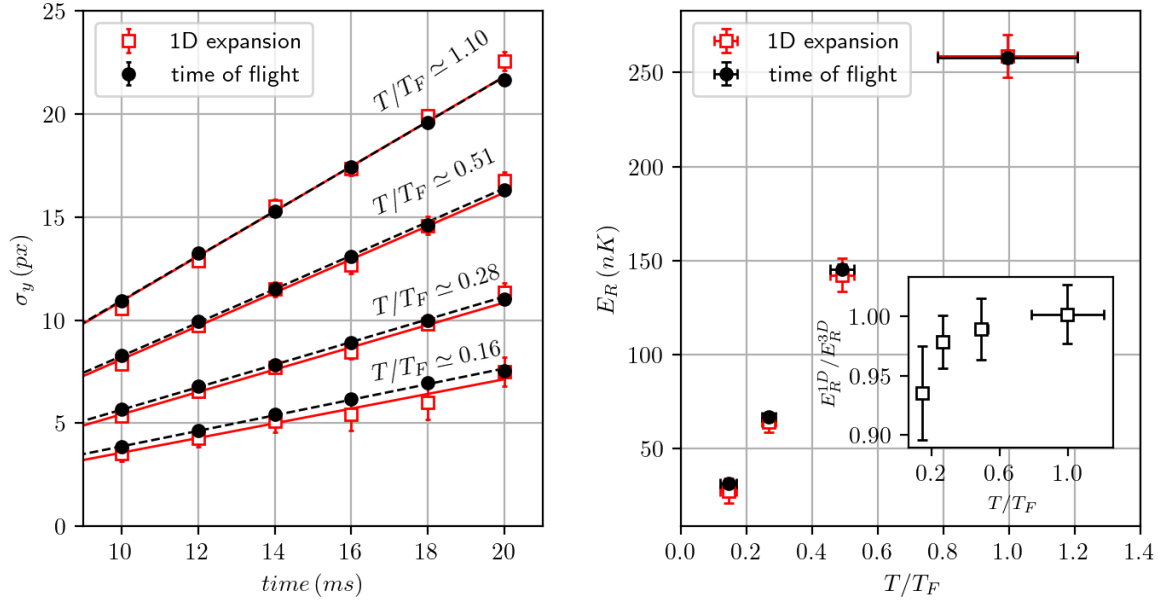


Figure 2.7: Measurement of the release energy of expanding gases. Left: RMS size  $\sigma_y$  in pixel unit ( $1 \text{ px} = 6.45 \mu\text{m}$ ) of the gases along the longitudinal axis  $Oy$ , with respect to the time of expansion. Dashed lines are ballistic fits  $\sigma(t)^2 = \sigma(0)^2 + a^2t^2$  for the expansion of the reference gases imaged after time of flight, and solid line for the 1D channeled expansions. Every  $\sigma_y$  of the channeled expansions are rescaled by a single multiplicative correction of the parallax and anticonfinement (see appendix D). Right: fitted release energies  $E_R$  from the ballistic expansion, with respect to  $T/T_F$ . In inset: ratio of the release energies  $E_R^{1D}/E_R^{3D}$ .

anti-confinement (see appendix D) with a single multiplicative correction parameter. The release energy is then inferred from the slope of the expansion, given that we measure the sizes after a long enough time so that  $\sigma(0)^2 \ll a^2t^2$ , and the result is reported on figure 2.7. The inset compares the release energies along the longitudinal axis  $Oy$  (see figure 2.1) for the 1D and 3D expansions, and it shows that  $E_R^{1D}$  is smaller than that of the 3D measurement for low  $T/T_F$ . This is not expected since the mean field interaction should significantly increase the release energy in 1D compared to 3D, particularly at the smallest temperatures.

We finally infer the kinetic energy and mean-field interaction energy which are

completely determined from the measurement of the release energies in 1D and 3D expansions,

$$\begin{aligned} E_{int} &= \frac{3}{2}(E_R^{1D} - E_R^{3D}) \\ E_K &= \frac{3}{2}(3E_R^{3D} - E_R^{1D}) \end{aligned} \quad (2.23)$$

and figure 2.8, (a) presents the result of our measurement of  $E_{int}/E_K$  with respect to  $T/T_F$ . Our result shows a decrease of the interaction energy at low  $T/T_F$ , which is not in agreement with the expected behavior. In the weakly interacting regime, the strength of the mean-field interactions for a SU(N) Fermi gas can be numerically computed from [MPS02]:

$$E_{int}^{SU(N)} = (N - 1) \frac{g}{4} \int d^3r n^2(r) \quad (2.24)$$

and

$$E_K = \int d^3p \frac{p^2}{2m} n(p) \quad (2.25)$$

and the prediction, shown on figure 2.8, (a), solid line, confirms that we expect a raise of  $E_{int}/E_k$  at low  $T/T_F$ .

The statistical noise of our result is as large as the signal we are looking for, and the tendency is in contradiction with the prediction. This result is not conclusive, and we suspect imperfect thermalization when the gases reach  $T < 0.5 T_F$ . This assumption is verified with an analysis of the aspect ratio of the gases expanding in 3D, as shown on figure 2.8 (b.1), with respect to the time of flight duration, for different degeneracies. A non-interacting Fermi gas with  $T \simeq 0.75 T_F$  has isotropic velocity distribution and the aspect ratio  $\sigma_x/\sigma_y$  of the expanding gas is 1 [BR97], as shown on figure 2.8, (b.1), similarly to a classical gas. Then, according to our measurement, the aspect ratio for a degenerate gas at  $T \simeq 0.17 T_F$  is inverted at  $tof \simeq 4$  ms and finally converges to approximately 1.12. This was observed in [Son+20] with approximately 50 000 atoms per spin state as a signature of the mean field interactions [OHa+02; PGS03; JPS04].

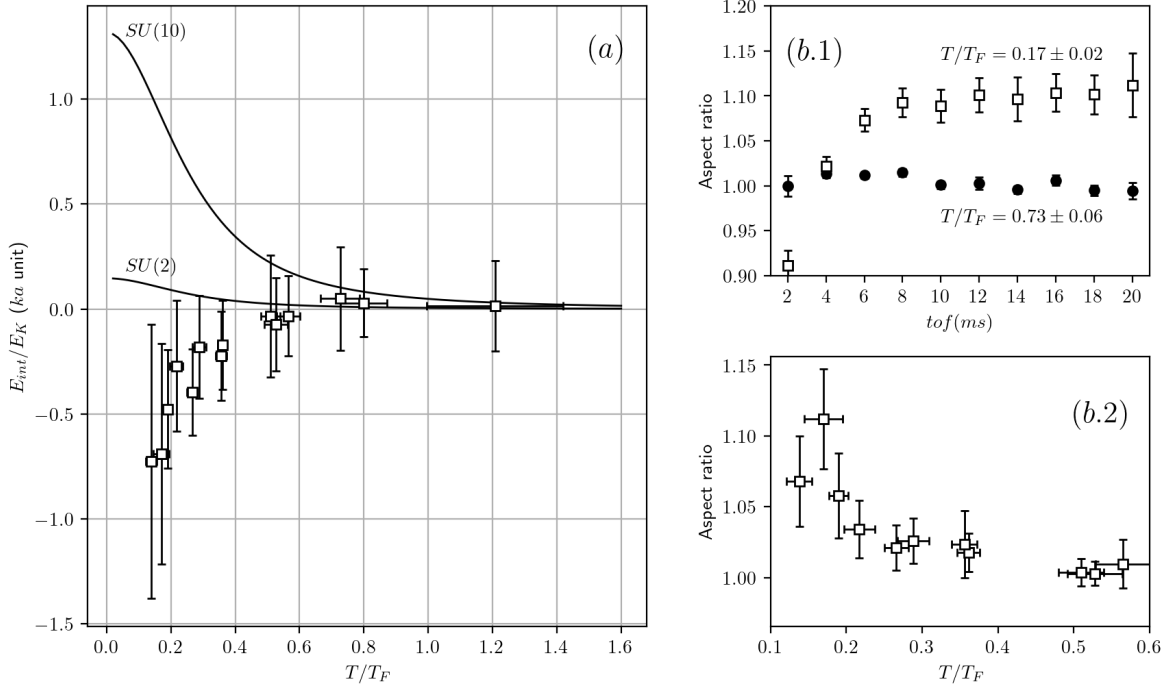


Figure 2.8: (a) Measurement attempt of the interaction energy with 1D channeled expansions, inferred from equations 2.23 and our measurement of the release energies presented on figure 2.7, in function of  $T/T_F$ . Solid lines show predictions of the mean field energy from numerical resolution of equations 2.24, 2.25. (b.1) Inversion of the aspect ratio  $\sigma_x/\sigma_y$  of the gases expanding in 3D with respect to the duration of the expansion and (b.2) increase of the aspect ratio with decreasing  $T/T_F$ . On figure (b.2), the aspect ratio is measured at fixed  $tof = 20$  ms.

However, from simulations based on MPS02, we predict that with approximately 2000 atoms per spin state in a trap of geometric mean frequency 160 Hz, which is our case, the aspect ratio shouldn't exceed 1%. Finally, figure 2.8, (b.2) shows our measurement of the aspect ratio as a function of  $T/T_F$  at fixed  $tof = 20$  ms, and it exceeds 1% for all measurements at  $T < 0.5 T_F$ . This indicates that in this data, thermalization is imperfect at the end of evaporation for the most degenerate gases, and no reliable measurement of the mean-field interaction energy could be realized.

## Chapter 3

# Preparation and measurement of the spin populations in a Fermi gas of $^{87}\text{Sr}$

The narrow intercombination line of strontium 87 offers ideal conditions for the realization of spin orbit coupling schemes [GD10; LJS11], with minimal spontaneous emission [CR14]. Associated with spin resolved transitions, it is possible to measure and manipulate the spin populations. For instance, a well established technique named Optical Stern-Gerlach (OSG) [Sle+92] makes use of the spin-dependent dipole force associated with the hyperfine structure of the intercombination line to spatially separate spin components of alkaline-earth like atoms. It has been demonstrated on both strontium [SGS11] and ytterbium [Tai+10], to measure the populations in each spin state. The ground state  $^1S_0$  of fermionic  $^{87}\text{Sr}$  has an electronic closed-shell *i.e.*  $J = 0$ , hence the electronic sensitivity to magnetic fields is zero, and there only remains the magnetic sensitivity of the nucleus which is as low as the electron to proton mass ratio relatively to the electronic g-factor. It is then not practical to use magnetic fields to manipulate the 10 degenerate ground spin states.

Excited triplet states such as  $^3P_1$  with non zero momentum have a much stronger magnetic susceptibility than the ground state  $^1S_0$ . Regarding  $^3P_1$  state with  $\Gamma/2\pi = 7.4$  kHz, the degeneracy lift of the excited spin states is easily larger than the linewidth: with g-factor  $g_J \simeq 0.27$ , on can reach MHz Zeeman shifts with modest magnetic fields

of a few Gauss. In this case, the resonances of the  $^1S_0 \leftrightarrow ^3P_1$  intercombination line acquire a spin dependence, which enables spin selective optical transitions. The number of spin components can then be tuned with standard optical pumping schemes [Tey+10; Pag+14; Son+20], further enabling the study of SU(N) many-body physics with tunable N. Although narrow MOT cooling may induce spontaneous polarization of a SU(N) Fermi gas, as demonstrated with erbium [Fri+12], specific schemes allow to selectively prepare polarized Fermi gases either with dissipative blast [He+20] only or associated with spin dependent light shifts [Son+20].

In this chapter, I first discuss our demonstrated method [Bat+20] to measure the nuclear spin populations with a spin orbit coupling scheme associated with the intercombination line [SGS11]. The robustness of our method is provided by adiabatic following of a quasi-dark state, ensuring minimal spontaneous emission. Using the strong difference of magnetic sensitivity of the coupled states, we selectively transfer, with a resonant passage, well defined momentum recoils to well defined spin states, with a simple retro-reflected laser beam. The overall efficiency is yet 85%, up to now limited by available light power. I will then show how we are able to tune the number of spin components in our Fermi gas of  $^{87}\text{Sr}$ . Using the high spin sensitivity of the excited state  $^3P_1$  associated with optical pumping [Tey+10; Oza+18; He+20], we prepare SU(N) fermi gas with tunable N, which leads to our preparation of a polarized Fermi sea with a spin selective blast. Finally, I estimate that the Fermi sea is polarized with  $90 \pm 10\%$  fidelity accounting for the overall efficiency of our detection scheme.

### 3.1 Measurement of the spin populations

This spin dependent momentum transfer scheme inherently relies on spin-orbit coupling (SOC) [GD10; LJS11] enabled by a polarization lattice. With a zeeman degeneracy lift of the  $^1S_0 \leftrightarrow ^3P_1, F = 11/2$  spin spin transitions, two highly saturating counter-propagating laser beams with same frequency and well defined  $\sigma_+$  and  $\sigma_-$  resonantly couple two selected ground spin states with an excited state, ensuring a strong spin sensitivity. The atoms in the selected spins are connected to a form a quasi-dark state  $|\Psi_C\rangle$ , ensuring reduced spontaneous emission. The dark state is adiabatically

rotated by ramping the frequency of the lasers, ensuring robustness. In the end, the final states have acquired exactly two momentum recoils by absorption of one photon from one beam and emission of one photon into the other beam. Ideally, the perfect correlation between the momentum and the polarization of the laser beams ensures that the two selected spins are diffracted in opposite directions, and after a time of flight, the diffracted spin states are separated from the rest of the cloud, and their populations can be measured with absorption imaging.

In this section, I first present our experimental demonstration of this scheme, and I will then discuss the adiabatic rotation of the quasi-dark state  $|\Psi_c\rangle$  in the dressed-states picture. With a focus on the possible spin sensitivity loss due to defects on the lasers polarization, we demonstrate the reliability of our measurement, which we verified on all the spins of the SU(10) ground state manifold. I will then show that our scheme can be generalized to simultaneously measure the populations of more than two spin states with a proper sequence of adiabatic rotations. Finally, we further increased the probability of success of the momentum transfer by improving the connection to the quasi-dark state  $|\Psi_c\rangle$ , which we practically do with a Blackman-like intensity window simultaneously to the frequency.

### 3.1.1 Experimental procedure

After preparing a degenerate Fermi gas (see chapter [1](#)), we first lift the degeneracy of the  $^3P_1, F = 11/2$  Zeeman sub-levels with a homogeneous magnetic field of amplitude  $|\mathbf{B}| = 16$  G, as shown on figure [3.1](#), (a). The excited spin states, with magnetic susceptibility 380 kHz/G are then separated by  $g_F\mu_B|\mathbf{B}| \simeq 6$  MHz, which is three orders of magnitude larger than the linewidth  $\Gamma_{^3P_1}/2\pi = 7.4$  kHz. The ground spin states are barely affected with magnetic susceptibility as low as 0.2 kHz/G [\[Boy07\]](#), [\[Bat+20\]](#). Here,  $g_F$  is the g-factor of the hyperfine state  $F = 11/2$ , and  $\mu_B$  the Bohr magneton. The  $^1S_0 \leftrightarrow ^3P_1, F = 11/2$  optical transitions are then spin resolved. Two highly saturating counter-propagating laser beams with same frequency and well defined polarizations  $\sigma_+$  and  $\sigma_-$  are turned on, shaping a polarization lattice, with  $I \simeq 1000I_{sat}$ ,  $I_{sat} \simeq 3\mu W/cm^2$ . For this, we use the vertical red MOT beams. Our measurement of the circularity of

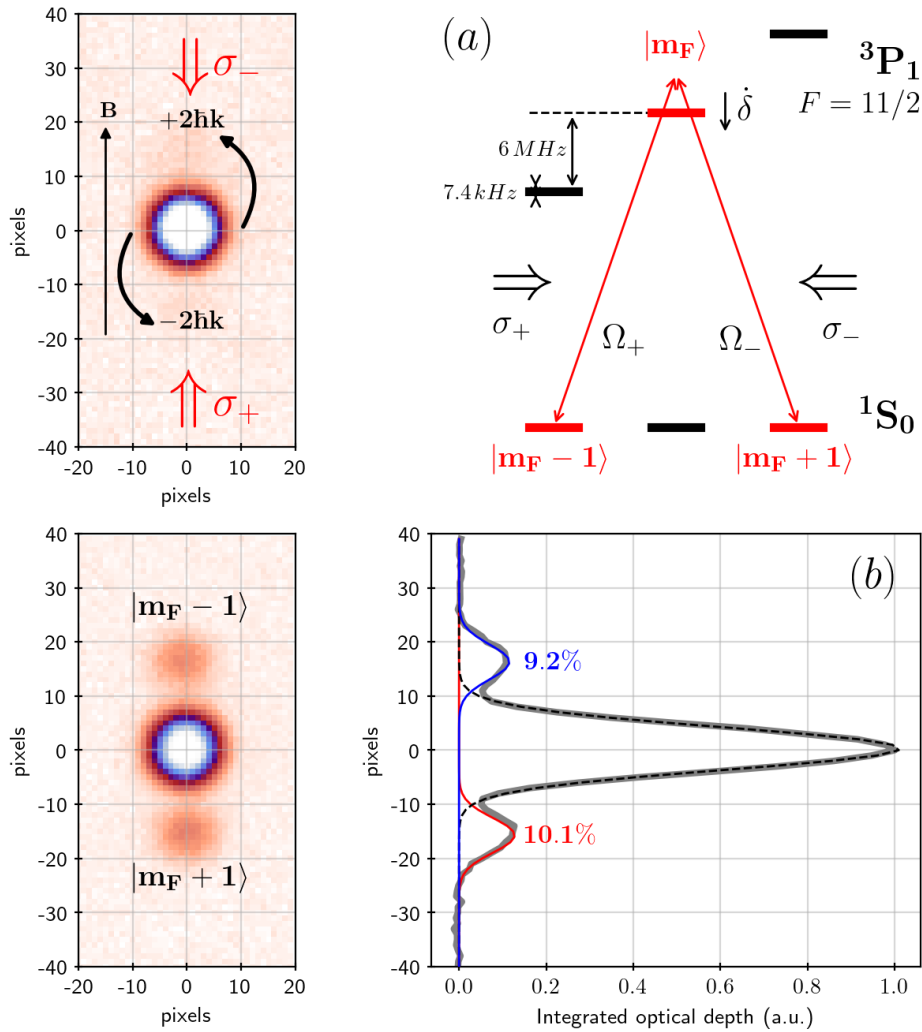


Figure 3.1: Spin dependent momentum transfer to measure the spin populations in a  $SU(N)$  degenerate gas. (a) The degeneracy of the hyperfine excited state  $^3P_1$ ,  $F = 11/2$  is lifted by  $6\text{ MHz}$  with a  $16\text{ G}$  homogeneous magnetic field, which is much larger than the  $7.4\text{ kHz}$  linewidth. Two counter-propagating laser beams with same frequency and well defined polarization  $\sigma_-$  and  $\sigma_+$  selectively couple two ground spin states  $|m_F - 1\rangle$  and  $|m_F + 1\rangle$  to the excited state  $|m_F\rangle$ . The frequency of the light excitation is ramped through resonance at rate  $\dot{\delta}$  to realize the momentum transfer. (b) Integrated optical depth, from absorption image, of the selected spin states  $|m_F \pm 1\rangle$  which are separated from the rest of the cloud after time of flight.

the laser beams is 99 % in intensity. With appropriate near-resonant frequency, two selected ground spin states  $|^1S_0, m_F - 1\rangle$  and  $|^1S_0, m_F + 1\rangle$  are coupled to the excited state  $|^3P_1, F = 11/2, m_F\rangle$ , defining an isolated three level system in  $\Lambda$  configuration, as shown in figure 3.1 (a). The magnetic field used to lift the degeneracy of the  $^1S_0 \leftrightarrow ^3P_1, F = 11/2$  spin spin transitions combined with optical couplings with well defined  $\sigma_{\pm}$  polarizations ensures the strong spin selectivity. Then, we perform a frequency sweep through the resonance from  $\delta \simeq +700$  kHz to  $\delta \simeq -700$  kHz during  $200 \mu\text{s}$ . Here,  $\delta = \omega - \omega_0$  is the detuning to the excited state. Atoms in  $|^1S_0, m_F - 1\rangle$  absorb one photon from the  $\sigma_+$  laser beam and re-emit one photon into the counter propagating  $\sigma_-$  laser beam, acquiring exactly two photon momentum recoils  $+2\hbar\vec{k}_R$ . The opposite happens for atoms initially in  $|^1S_0, m_F + 1\rangle$ , acquiring exactly minus two photon momentum recoils  $-2\hbar\vec{k}_R$ . During the momentum transfer, atoms are held against gravity with our horizontal beam for ODT. The selected spin states  $|^1S_0, m_F \mp 1\rangle$  with acquired  $\pm 2\hbar\vec{k}_R$  momentum recoils are then separated from the rest of the cloud after time of flight, and the populations in each spin state are measured from absorption images, as shown on figure 3.1, (b).

The momentum transfer is ensured by adiabatic following of a *quasi dark state*  $|\Psi_C\rangle$ . Its rotation from the initial state  $|m_F \mp 1, 0\hbar\vec{k}\rangle$  to the final state  $|m_F \pm 1, \pm 2\hbar\vec{k}\rangle$  is realized by the frequency ramp, which crosses the resonance with the excited state. I will now discuss the conditions for success of the adiabatic following of the quasi dark state and the associated reduced spontaneous emission, despite the resonant coupling.

### 3.1.2 Adiabatic following - Dressed-states picture

It is convenient to look at this three level system in  $\Lambda$  configuration in the dressed states picture [DC85]. The initial ground state  $|1\rangle = |^1S_0, m_F - 1, 0\hbar\vec{k}\rangle$  with approximately zero momentum is coupled to excited state  $|2\rangle = |^3P_1, F = 11/2, m_F, 1\hbar\vec{k}\rangle$  with one momentum recoil by  $\sigma_+$  excitation with associated rabi frequency  $\Omega_+$ . The excited state is coupled to the final ground state  $|3\rangle = |^1S_0, m_F + 1, 2\hbar\vec{k}\rangle$  with two momentum recoils by  $\sigma_-$  excitation with associated rabi frequency  $\Omega_-$ . In this dressed states basis  $\{|1\rangle, |2\rangle, |3\rangle\}$ , shown on figure 3.2, (a), the hamiltonian can be written as:

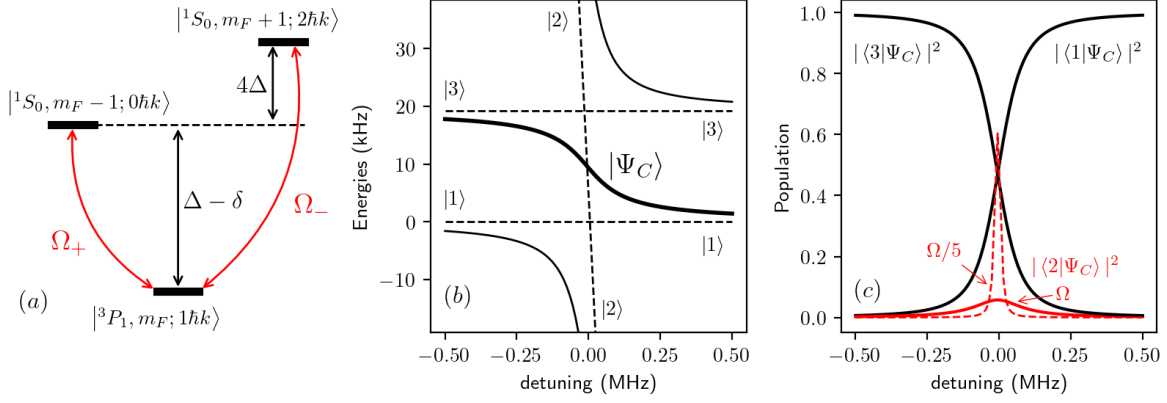


Figure 3.2: Dressed atom picture for the spin dependent momentum transfer scheme. (a): dressed states spectrum, where  $\Delta = \hbar k^2/2m$  is the photon recoil frequency,  $\delta = \omega - \omega_0$  is the detuning, and  $\Omega_{\pm}$  the rabi frequencies associated with  $\sigma_{\pm}$  excitations. (b): the dashed lines are the energies of the dressed states  $|1\rangle$ ,  $|2\rangle$ ,  $|3\rangle$ , and solid lines the eigen energies of hamiltonian defined in equation 3.1, with respect to the detuning  $\delta$ . Eigenstate  $|\Psi_C\rangle$  is defined in equation 3.2. (c):  $|\Psi_C\rangle$  populations along the three dressed states  $|1\rangle$ ,  $|2\rangle$ ,  $ket3$ . For figures (b) and (c), parameters used are  $\Delta = 4.8$  kHz and  $\Omega_{\pm} = 55$  kHz.

$$\hat{H}(\delta) = \hbar \begin{pmatrix} 0 & \Omega_+/2 & 0 \\ \Omega_+^*/2 & \delta - \Delta & \Omega_-/2 \\ 0 & \Omega_-^*/2 & 4\Delta \end{pmatrix} \quad (3.1)$$

where  $\delta = \omega - \omega_0$  is the light detuning with respect to the resonance with the excited state in this three spins manifold, and  $\Delta = \hbar k^2/2m$  is the recoil frequency. The light coupling between those three dressed states gives rise to three eigenstates, whose spectrum is shown on figure 3.2, (b). We are mainly interested in the eigenstate, here named  $|\Psi_C\rangle$ , that connects to initial state  $|1\rangle$  and final state  $|3\rangle$ . With first-order perturbative expansion  $\Delta \ll \Omega$  from hamiltonian 3.1 at  $\delta = 0$ , it can be shown that:

$$|\Psi_C(\delta = 0)\rangle = \frac{1}{\sqrt{\Omega_+^2 + \Omega_-^2}}(\Omega_- |1\rangle - \Omega_+ |3\rangle) - \frac{\Omega_+ \Omega_-}{\Omega^2} \frac{8\Delta}{\Omega} |2\rangle \quad (3.2)$$

The rate of spontaneous emission, inferred from the population in the excited state  $|\langle 2|\Psi_C\rangle|^2$ , reads:

$$\Gamma_{s.e.} \simeq \Gamma_{3P_1} (2\sqrt{2} \frac{\Delta}{\tilde{\Omega}})^2 \quad (3.3)$$

where  $\tilde{\Omega}^2 = \Omega_+ \Omega_-$ . With experimental parameters,  $\Omega_{\pm} / 2\pi \simeq CG_{\pm} 220$  kHz and  $\Delta / 2\pi \simeq 4.8$  kHz, where the  $CG_{\pm}$  are the Clebsch-Gordan coefficients associated with  $\sigma_{\pm}$  transitions. For a  $200 \mu s$  ramp duration, equation 3.3 gives an upper-bound of spontaneous emission between 15 % and 30 %, depending on the selected spins for the momentum transfer. Most importantly, equation 3.3 shows that spontaneous emission is reduced by the light excitation, and hence, stronger resonant coupling results in less light scattering.

Far from resonance when  $|\delta| \gg \Omega_{\pm}$ , the excited state can be eliminated, and the hamiltonian 3.1 is then reduced to:

$$\hat{H}(\delta) = \hbar \begin{pmatrix} 0 & \Omega_+^* \Omega_- / 2\delta \\ \Omega_+ \Omega_-^* / 2\delta & 4\Delta \end{pmatrix} \quad (3.4)$$

in  $|1\rangle, |3\rangle$  basis. In this perturbative regime, diagonalization of this hamiltonian shows that two eigen-states  $|+\rangle, |-\rangle$  read:

$$\begin{aligned} |+\rangle &\simeq |3\rangle + \frac{\Omega_+ \Omega_-}{4\delta\Delta} |1\rangle \\ |-\rangle &\simeq -|1\rangle + \frac{\Omega_+ \Omega_-}{4\delta\Delta} |3\rangle \end{aligned} \quad (3.5)$$

We want the atoms to connect to  $|\Psi_C\rangle$ . The phase relation between  $|1\rangle$  and  $|3\rangle$  imposes that for large positive detunings,  $|-\rangle \simeq |\Psi_C\rangle \simeq |1\rangle$  and for large negative detunings,  $|+\rangle \simeq |\Psi_C\rangle \simeq |3\rangle$ . Hence, the adiabatic connection to the dark-state is possible if the initial and final detunings  $|\delta_{i,f}|$  are large enough such that they respect the condition:

$$\frac{\Omega_+ \Omega_-}{4|\delta_{i,f}|\Delta} \ll 1 \quad (3.6)$$

so that the initial and final states are almost identical to  $|\Psi_C\rangle$ . Figure 3.2, (c), shows that  $|\langle 3|\Psi_C\rangle|^2 \simeq 1$  for  $\delta \ll 0$  and  $|\langle 1|\Psi_C\rangle|^2 \simeq 1$  for  $\delta \gg 0$ . Moreover, this

shows that the detuning has to be ramped from positive to negative such that the selected atoms initially at rest acquire two momentum recoils. With a detuning ramp in the other direction, it can be shown with the same method that atoms initially at rest follow a bright state which leads to the excited state and the momentum transfer fails.

*Adiabatic following* is ensured if the speed of rotation of  $|\Psi_C\rangle$  determined by the speed of the detuning ramp, is much lower than the coupling strength, which reads:

$$\dot{\delta} \ll \Omega^2 \tag{3.7}$$

This criterion can be understood in the frame of nuclear magnetic resonance. A spin in precession will stay colinear to a rotating magnetic field if the rotation speed is slow with respect to the larmor frequency, such that the axis of precession stays in phase with the magnetic field. This condition is analog to  $\dot{\delta} \ll \Omega^2$  regarding Raman adiabatic passage, so that the basis rotation is slow enough and the atoms stay in phase with the followed eigen-state rotating from one spin state to the other. The success of the adiabatic passage is ensured by fulfilling conditions [3.6](#) and [3.7](#).

*Transfer dynamics and spontaneous emission:* the dynamics of the transfer are compared to numerical simulations of the master equation including spontaneous emission. Figure [3.3](#) shows the experimental efficiency for the  $|-3/2, 0\hbar\vec{k}\rangle \rightarrow |1/2, 2\hbar\vec{k}\rangle$  momentum transfer (black dots), as a function of the duration of the detuning ramp. While the simulation is in agreement with our experiment and verifies that a  $200\ \mu\text{s}$  ramp duration fulfills the Landau-Zener condition for adiabatic following defined in equation [3.7](#), it also shows that spontaneous emission (red solid line) limits the efficiency of the transfer, compared to no spontaneous emission (black solid line). The probability of success of the adiabatic following as a function of the detuning sweep rate  $\dot{\delta}$  is finally compared to the Landau-Zener scaling (dashed-line on figure [3.3](#))  $P_{LZ}(\Omega_+) \times P_{LZ}(\Omega_-)$  [\[CH86\]](#) for the two-photons  $\Lambda$  scheme, resulting from the relative values of  $\Omega_+$ ,  $\Omega_-$ , and  $\Delta$ , where  $P_{LZ}$  is defined as:

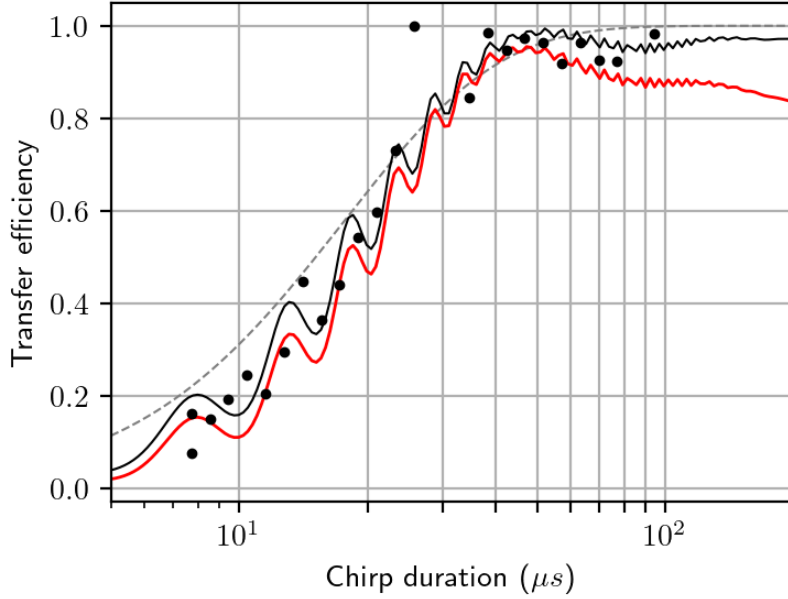


Figure 3.3: Efficiency of the adiabatic passage in function of the duration of the detuning ramp, for spin dependent momentum transfer from  $\left| -3/2, 0\hbar\vec{k} \right\rangle$  to  $\left| 1/2, 2\hbar\vec{k} \right\rangle$ , with a detuning ramp over  $1.4 \text{ MHz}$ , assuming an initial 10% population in  $-3/2$ . The experimental result (black dots) is compared to numerical simulations (solid lines) with no free parameters of the master equation including spontaneous emission (red), neglecting spontaneous emission (black), and to the Landau-Zener scaling (dashed line)  $P_{LZ}(\Omega_+) \times P_{LZ}(\Omega_-)$ .

$$P_{LZ}(\Omega) \simeq 1 - \exp\left(-2\pi \frac{\Omega^2}{4\delta}\right) \quad (3.8)$$

The lower Clebsch-Gordan thus gives the higher limit on the detuning sweep rate. If this limit is exceeded, different consequences arise depending on which arm of the momentum transfer has the lowest CG: associated with the first absorbed photon, atoms fail the transfer and stay at rest, while large spontaneous emission results from low CG associated with the second emitted photon.

At  $200 \mu\text{s}$ , approximately 10 to 15% atoms fail the coherent momentum transfer, according to both equation [3.3](#) and numerical simulation. Our experimental limit to

achieve better transfer efficiency is set by the light intensity, limited by the large waist of the MOT beams, as large as approximately 1 cm. An increase of the Rabi coupling by a factor 2 would reduce spontaneous emission to 5% and increase the efficiency of the coherent transfer up to 95%. This would require to increase the light intensity by a factor 4 and the width of the detuning ramp as much, according to the conditions for adiabatic transfer defined in equation 3.6. Ensuring spin selectivity requires then to increase the degeneracy lift of the excited state manifold  $^3P_1, F = 11/2$  by increasing the magnetic field to  $|\mathbf{B}| \simeq 60 \text{ G}$ . Although weakly sensitive, the zeeman lift of the ground state with susceptibility 185 Hz/G would then exceed the recoil energy associated with the momentum transfer. If not compensated for, for instance with a doppler shift associated with a short free fall in our vertical scheme, this would result in an asymmetry of the central frequency of the detuning ramp for the momentum transfer of selected  $|m_F - 1\rangle$  and  $|m_F + 1\rangle$  spin states.

### 3.1.3 Spin sensitivity

The spin sensitivity is ensured by the association of the degeneracy lift of the  $^1S_0 \leftrightarrow ^3P_1, F = 11/2$  spin transitions, to the well defined wavevectors  $\pm \vec{k}$  and  $\sigma \pm$  polarizations of the couplings. Hence, there are two possible sources of sensitivity loss, either from defects on the circularity of the laser beams polarization, or from misalignment of the counter-propagating laser beams and the magnetic field, which harms the correlation between the initial spin state and the direction of the momentum transfer. In the first case, spin states may be diffracted in the opposite direction to that assumed, while in the second case, the emergence of  $\pi$  couplings allows the diffraction to spin states that should not be diffracted. To estimate the consequences of the polarization defects, we consider that the Rabi frequency resulting from a circularity defect  $\varepsilon \simeq 0.1$  (measured 99% circularity in intensity) scales as  $\varepsilon\Omega$  and from a magnetic field misalignment  $\theta \simeq 6^\circ$  as  $\theta\Omega$ . A helpful approach is to consider separately the possible absorption processes for the unintended momentum transfers, and infer their probabilities of success from a Landau-Zener scaling  $P_{LZ}(\varepsilon\Omega)$  and  $P_{LZ}(\theta\Omega)$ , as defined in equation 3.8, with respective Rabi Frequencies. With a sweep rate satisfying 95% probability of success for the intended momentum transfer (with  $\varepsilon = 0$  and  $\theta = 0$ ), the unintended transfers

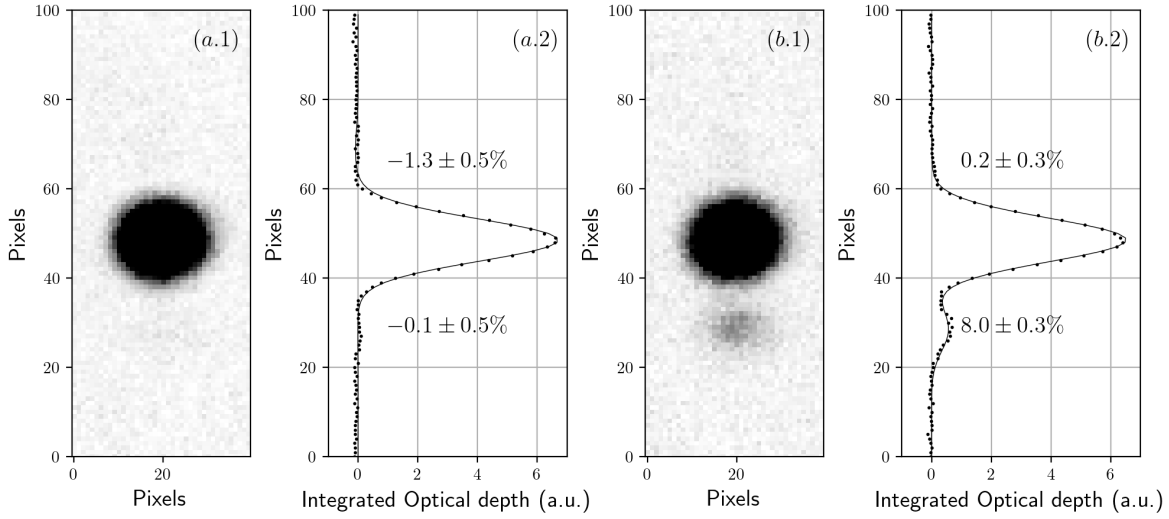


Figure 3.4: Measurement of the spin sensitivity with optical pumping prior to spin-dependent momentum transfer on the  $|1/2\rangle \leftrightarrow |-3/2\rangle$  diffraction line. (a): pumping of  $1/2$  and  $-3/2$  spin states to verify  $\pi$  defects in polarization. (b): pumping of  $-3/2$  only, to verify defects in circularity.

are reduced to approximately 3% accounting for the non zero polarization defects.

To verify the spin sensitivity, we use an optical pumping scheme to empty the populations of selected spin states (see section 3.2) prior to the momentum transfer. Then, we realize a momentum transfer targeting at the emptied spin states. If atoms are separated from the cloud after time of flight, they were initially populating non targeted spin states, and they have acquired momentum because of the polarization defects.

To evaluate the  $\pi$  defect associated with the alignment of the magnetic field, we empty the populations of both spin states  $1/2$  and  $-3/2$ , and we realize a momentum transfer on the associated  $|1/2\rangle \leftrightarrow |-3/2\rangle$  diffraction line. Then, we measure the atomic density at the expected locations of the separated clouds after time of flight, as shown on figure 3.4 (a.1), (a.2). The measured populations are zero, which is consistent with the prior pumping. Furthermore, no atoms from  $-1/2$  spin state are diffracted, which verifies that defects on  $\pi$  polarization can be neglected.

We also verify the quality of the circularity by selectively pumping one of the two

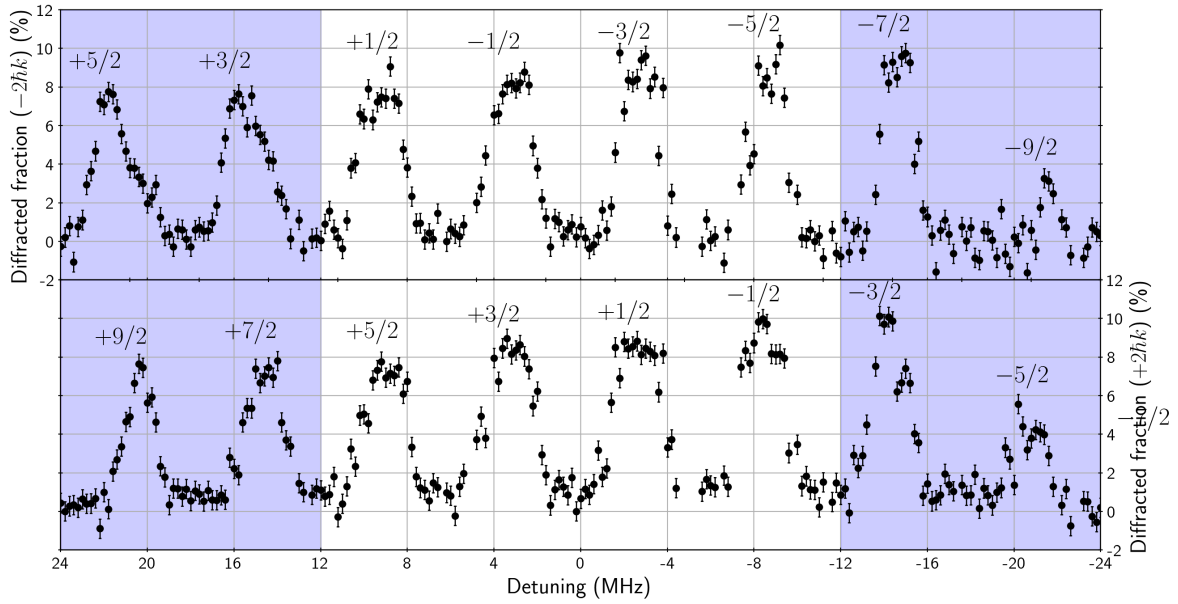


Figure 3.5: Spectrum for spin dependent momentum transfer over  $^1S_0$  manifold. Each point corresponds to diffracted fraction of atoms with respect to the central frequency of the detuning ramp which is 1.4 MHz wide, with duration  $330 \mu\text{s}$ . Top figure shows the lower diffracted cloud with  $-2\hbar k$  momentum transfer (see figure 3.1), while bottom figure shows upper diffracted cloud with associated  $+2\hbar k$  momentum transfer. The blue filled regions correspond to measurable asymmetry higher than 1 MHz in the optimal central frequency for the two diffracted spin populations.

targeted spin states prior to the diffraction measurement. Figure 3.4 (b.1), shows the measurement of the  $|1/2\rangle \leftrightarrow |-3/2\rangle$  diffraction line after pumping  $-3/2$ . The measurement of the populations, see figure (b.2), shows that one cloud only is separated from the rest of the atomic gas. This shows that the momentum acquired by targeted spin state  $1/2$  is well defined, and verifies that defects in circularity can be neglected. These two measurements hence verify our estimations on the  $\sigma_+$  and  $\pi$  polarization defects, and show that our spin sensitivity is robust.

### 3.1.4 Spin dependent momentum transfer in $\text{SU}(10)$ manifold

With a complete spectrum of the spin dependent momentum transfer over the  $\text{SU}(10)$  manifold of the  $^1S_0$  ground state, shown on figure 3.5, we find the optimal central

frequency of the detuning ramps and the corresponding measured spin populations  $N(m_F)$  for every spin state. A total of 8 diffraction lines are identified in this spectrum, each of them diffracting two spin states  $|m_F - 1\rangle$ ,  $|m_F + 1\rangle$ , in opposite directions. From the sum over all spin states of the diffracted atoms at optimal central frequencies, we infer that a total of approximately 85 % atoms are diffracted. This result is consistent with an average 10 to 15 % momentum transfer fail due to spontaneous emission, as discussed in [3.1.2](#), and that all spin states are equally populated with approximately 10 % atoms per spin state.

This estimation neglects the  $|-9/2\rangle \leftrightarrow |-5/2\rangle$  diffraction line, which peaks at 4 % diffracted atoms. We consider this measurement irregular because of two arguments. First, the non-repeatability of the measurement of the  $|-5/2\rangle$  population compared to the  $|-5/2\rangle \leftrightarrow |-1/2\rangle$  diffraction line shows an anomaly. Moreover, while the strong asymmetry in the Clebsch-Gordan associated with  $\sigma_+$  and  $\sigma_-$  couplings, see figure [3.6](#), for this diffraction line could explain a low efficiency of the momentum transfer, it is not observed in the  $|+9/2\rangle \leftrightarrow |+5/2\rangle$  diffraction line, which encounters the same asymmetry. Also, the measurement of the  $|+5/2\rangle$  spin population is repeatable compared to the  $|+5/2\rangle \leftrightarrow |+1/2\rangle$  line, showing that the asymmetry in Clebsch-Gordan coefficients is not responsible for the anomaly in the  $|-9/2\rangle \leftrightarrow |-5/2\rangle$  diffraction line. Hence, this measurement is not yet understood, but we suspect a lately spotted hardware failure (heating of direct digital synthesizers (DDS)) which can be responsible for the lowered efficiency and that has yet to be confirmed after repair. Until then, the sensitivity of the measure remains satisfying for a reliable estimation of the spin populations for all states but  $|-9/2\rangle$ .

*Asymmetric Clebsch-Gordan coefficients:* The diffraction line  $|+9/2\rangle \leftrightarrow |+5/2\rangle$  shows that a strong asymmetry in the Clebsch-Gordan coefficients (CG) associated with the two arms of the momentum transfer, here as high as  $CG_+/CG_- \simeq 6$ , is not detrimental to the sensitivity on the populations measurement, as long as the timescale for adiabatic passage is respected for the lowest CG. However, consequences arise regarding the optimal detuning ramp. The blue regions on figure [3.5](#) highlight the measured diffraction lines with strong asymmetry in the CGs. Here, we observe that the maximum

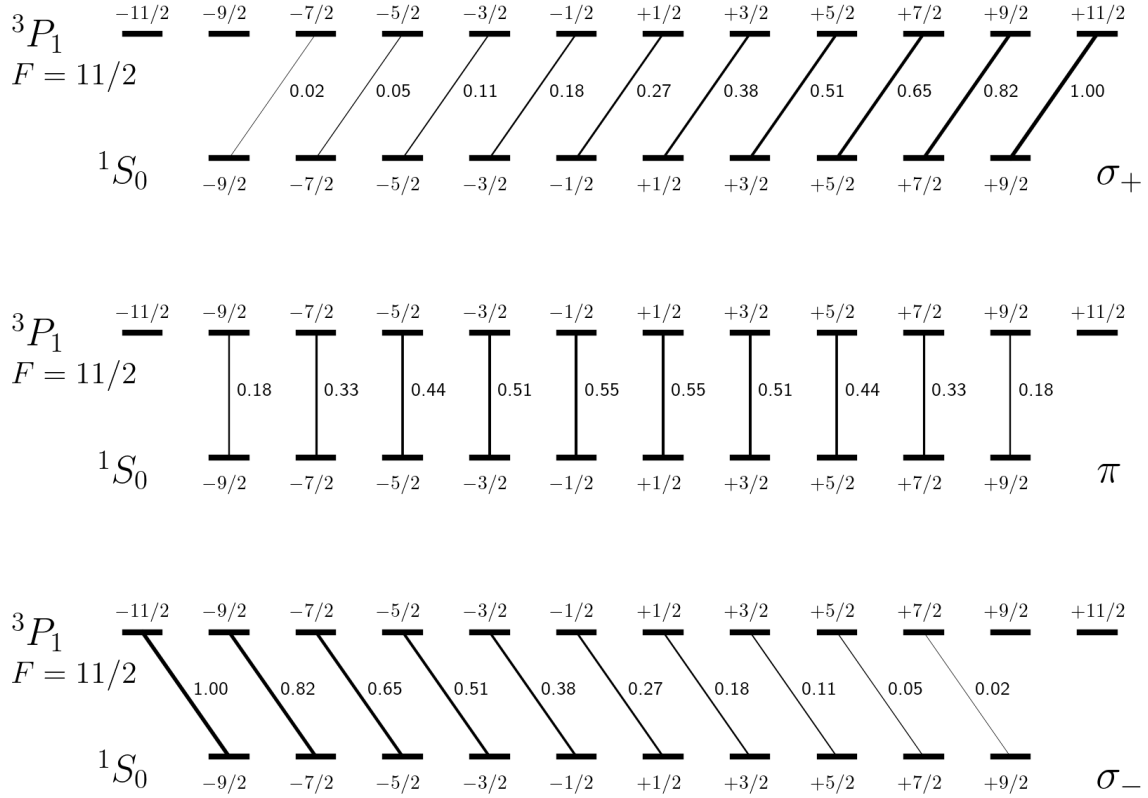


Figure 3.6: Clebsch Gordan coefficients squared associated with the  $^1S_0 \leftrightarrow ^3P_1, F = 11/2$  transitions. Top, transition associated with +1 orbital momentum, on middle 0 orbital momentum, and bottom -1 orbital momentum. The width of the lines are directly proportional to the Clebsch Gordan coefficients, which are noted squared aside each line.

efficiency of the momentum transfer for each of the two targeted spin states correspond to significantly different detunings. For instance, the optimal central frequencies for the diffraction of states  $|7/2\rangle$  and  $|3/2\rangle$  are approximately 14.5 MHz and 16 MHz, which is comparable to the width of the detuning ramp. Figure 3.7, (a.1) shows the strong asymmetry in the CGs in the  $\Lambda$  scheme associated with the  $|+9/2\rangle \leftrightarrow |+5/2\rangle$  diffraction line. The energy of the followed eigen-state, (red solid line on figures 3.7 (a.2) and (a.3)), is consequently displaced asymmetrically for each direction of the momentum transfer. This suggests that given the optimal center for the detuning ramp cannot be the same in both cases. Moreover, the  $|+9/2\rangle$  spin state with associated weak CG is in an electromagnetically induced transparency (EIT) [Fri+12] configuration, such that the *quasi-dark state*  $|\Psi_C\rangle$  is mostly along  $|+9/2\rangle$  at  $\delta = 0$ :

$$|\Psi_C\rangle = \frac{1}{\sqrt{\Omega_+^2 + \Omega_-^2}}(\Omega_- |+5/2\rangle - \Omega_+ |+9/2\rangle) \quad (3.9)$$

where  $\Omega_+/\Omega_- \simeq 6$ . This suggests that the rotation of  $|\Psi_C\rangle$  is either finished at  $\delta = 0$ , either not yet begun, and hence it cannot be center around the resonance. More precisely, equation 3.9 imposes that  $|\Psi_C\rangle$  rotates from  $|+9/2, 0\hbar\vec{k}\rangle$  to  $|+5/2, 2\hbar\vec{k}\rangle$  when  $\delta < 0$ , accounting for the positive to negative detunings ramp  $\dot{\delta} < 0$ , whereas the opposite rotation for the opposite momentum transfer from  $|+5/2, 0\hbar\vec{k}\rangle$  to  $|+9/2, 2\hbar\vec{k}\rangle$  occurs when  $\delta > 0$ . Figure 3.7, (a.4), shows that the central frequency of the detuning ramp for the adiabatic passage, that I here define as  $\delta_{center}$  so that  $|\Psi_C(\delta_{center})\rangle \simeq 1/\sqrt{2}(|m_F \mp 1\rangle - |m_F \pm 1\rangle)$ , is strongly shifted from the resonance  $\delta = 0$ . Regarding the  $|+9/2\rangle \leftrightarrow |+5/2\rangle$  diffraction line, The numerical computation with experimental parameters shown on figure 3.7, (a.4), shows the separation of the central frequency for each direction of the momentum transfer is 900 kHz, in agreement to the measured spectrum (see figure 3.5), and most importantly, it is almost as large as the detuning ramp which is 1.4 MHz. Hence, the adiabatic connexion of the initial and final spin states to the followed eigen-state  $|\Psi_C\rangle$  cannot be insured for both directions of the momentum transfer, which explains the asymmetry of the optimal central frequency for the detuning ramp.

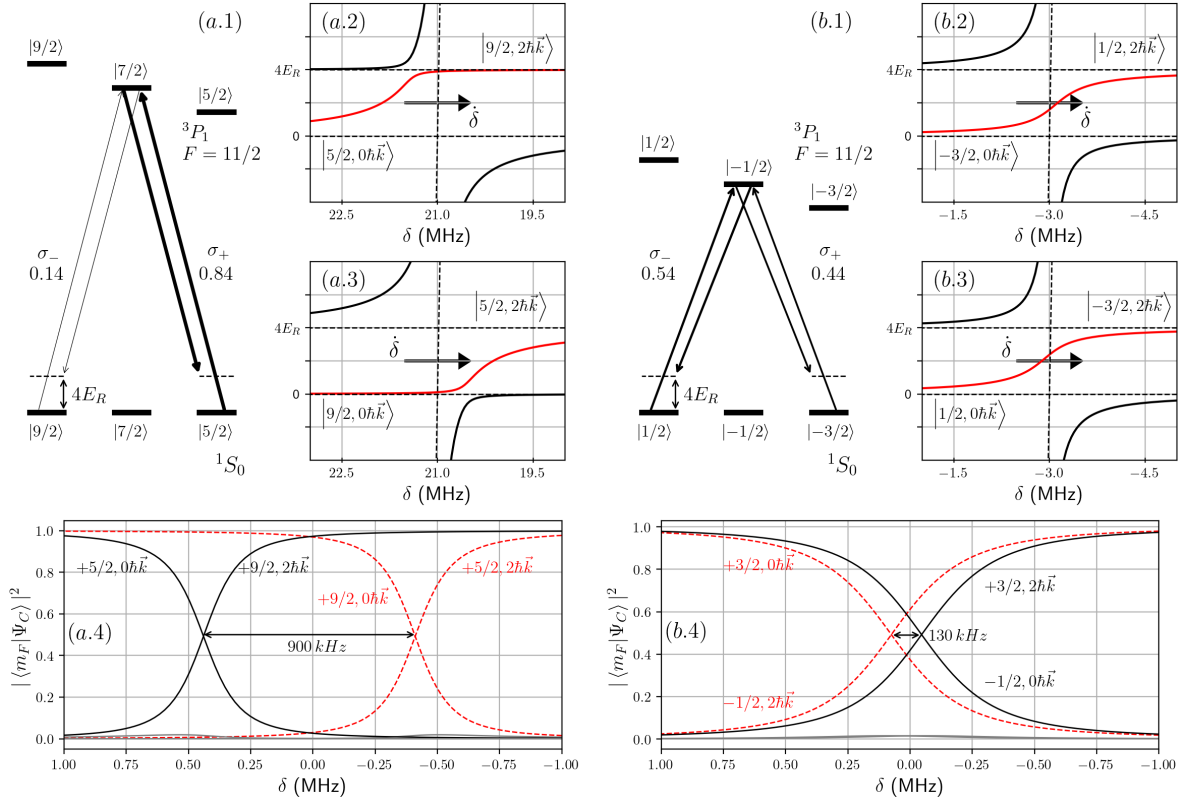


Figure 3.7: Focus on the asymmetry of the Clebsch-Gordan (CG) coefficients associated with the spin dependent momentum transfer. (a.1)  $\Lambda$  scheme for the  $|+9/2\rangle \leftrightarrow |+5/2\rangle$  transfer with strong asymmetric CGs, respectively 0.14 and 0.84. (a.2.3): Momentum transfer in the eigen-energies picture, from  $|+5/2, 0\hbar\vec{k}\rangle \rightarrow |+9/2, 2\hbar\vec{k}\rangle$  (a.2) and  $|+9/2, 0\hbar\vec{k}\rangle \rightarrow |+5/2, 2\hbar\vec{k}\rangle$  (a.3), with respect to the same detuning ramp. The energy displacement of the followed eigen-state  $|\Psi_C\rangle$  (red solid line) with respect to the dressed states (dashed lines) is highly asymmetric around the central frequency of the detuning ramp, as a result of the CGs asymmetry. (b) Momentum transfer for the  $|+1/2\rangle \leftrightarrow |-3/2\rangle$  line with approximately equal CGs, respectively 0.54 and 0.44. (a.4) and (b.4): projections of  $|\Psi_C\rangle$  along the dressed-states for each momentum transfer, as a function of  $\delta$ , here centered around the resonance with the zeeman shifted excited state.

This feature can be compared to the case  $\Omega_- \simeq \Omega_+$  where the followed eigen-state is in a balanced superposition of the two spin states  $|\Psi_C\rangle \simeq 1/\sqrt{2}(|1\rangle - |3\rangle)$ , at resonance

$\delta = 0$ . In this case, the central frequency of the rotation is obviously close enough to the resonance such that both directions of the momentum transfer are efficient for the same detuning ramp of 1.4 MHz. Figure 3.7, (b), shows that for the  $|+1/2\rangle \leftrightarrow |-3/2\rangle$  diffraction line with balanced CGs 0.54 and 0.44, the energy displacement of  $|\Psi_C\rangle$  is negligible over the detuning ramp, and the separation of central frequencies for each direction of the transfer is only 10% of the detuning ramp. Hence, both directions of the momentum transfer are optimally realized with the same detuning ramp.

### 3.1.5 Simultaneous measurement of four spin populations

We demonstrated a generalization of our scheme to simultaneously measure more than two spin populations. Figure 3.8 shows an experimental measurement of four spin populations,  $-7/2$ ,  $-3/2$ ,  $+1/2$ , and  $+5/2$ , with a single realization. This is done by transferring four different momenta to each one of the selected spin states, respectively  $+2\hbar\vec{k}$ ,  $+4\hbar\vec{k}$ ,  $-4\hbar\vec{k}$ , and  $-2\hbar\vec{k}$ , such that they are all separated after time of flight. For this measurement, we realize a sequence of three adiabatic passages, shown on figure 3.8, (a). The first passage on diffraction line  $|-3/2\rangle \leftrightarrow |+1/2\rangle$  is the same as introduced before:

$$\begin{aligned} |-3/2, 0\hbar\vec{k}\rangle &\rightarrow |+1/2, +2\hbar\vec{k}\rangle \\ |+1/2, 0\hbar\vec{k}\rangle &\rightarrow |-3/2, -2\hbar\vec{k}\rangle \end{aligned} \quad (3.10)$$

while the second passage  $|+1/2\rangle \leftrightarrow |+5/2\rangle$  transfers two more momentum recoils to the final states of the first passage:

$$\begin{aligned} |+1/2, +2\hbar\vec{k}\rangle &\rightarrow |+5/2, +4\hbar\vec{k}\rangle \\ |+5/2, 0\hbar\vec{k}\rangle &\rightarrow |+1/2, -2\hbar\vec{k}\rangle \end{aligned} \quad (3.11)$$

as well as the third passage on diffraction line  $|-7/2\rangle \leftrightarrow |-3/2\rangle$ :

$$\begin{aligned} |-3/2, -2\hbar\vec{k}\rangle &\rightarrow |-7/2, -4\hbar\vec{k}\rangle \\ |-7/2, 0\hbar\vec{k}\rangle &\rightarrow |-3/2, +2\hbar\vec{k}\rangle \end{aligned} \quad (3.12)$$

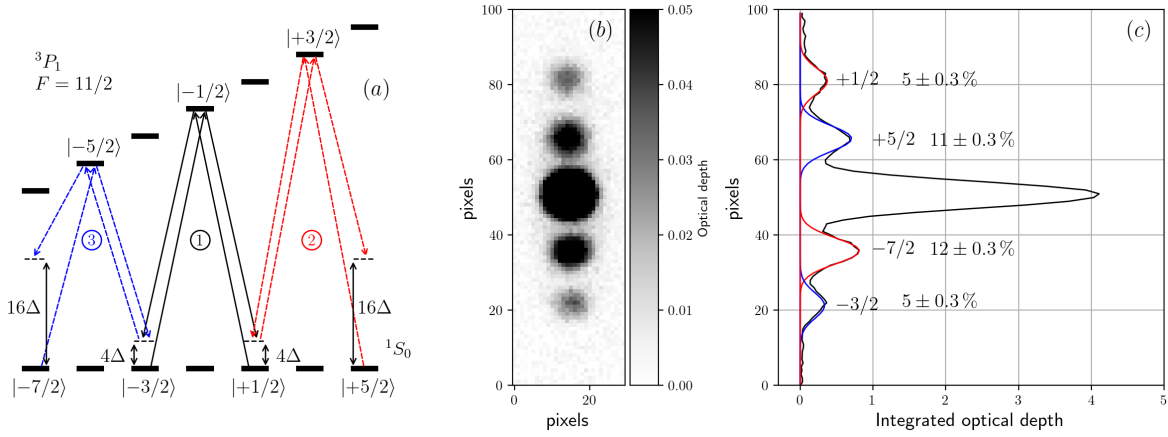


Figure 3.8: Simultaneous measurement of four spin populations with the spin dependent momentum transfer scheme. (a) Sequence of adiabatic passages. The second and third passages transfer two momentum recoils to the final states of the first passage, such that they final states have acquired a total of four momentum recoils, with associated recoil frequency  $16\Delta$ . (b) Absorption image after time of flight of the four diffracted spin states. (c) Integrated optical depth from the absorption image (b) to measure the spin populations. The red and blue solid lines are fits of the diffracted atomic clouds with a Boltzmann distribution.

From absorption images of the diffracted spin states, we measure the number of atoms in each selected spin state, as shown on figures [3.8](#), (b) and (c). The first observation is that the population of atoms which have experienced two adiabatic passages, *i.e.*  $|+1/2\rangle$  and  $| -3/2\rangle$  is weaker than the populations associated with  $\pm 2\hbar\vec{k}$  recoils. Obviously, the probability of success of two consecutive adiabatic passages, which scales as the product of each individual probability of success, is lower than for one single passage. Moreover, the eigen-state  $|\Psi_C\rangle$  associated with the transfer to the final states with acquired four recoil momenta and 16 recoil energy must have a larger rate of spontaneous emission according to equation [3.9](#), further reducing the probability of success of the second adiabatic passage. Hence, diffracted clouds at  $\pm 2\hbar\vec{k}$  are contaminated by the populations that failed passage to  $\pm 4\hbar\vec{k}$ .

Although having limited efficiency, this measurement that can yet be optimized demonstrates the possibility to simultaneously measure the populations and associated

resolved momentum distributions of four different spin states. Further improvements may enable the simultaneous measurement of the populations of the ten spin states, matching the performances of OSG [SGS11; Tai+10].

### 3.1.6 Intensity window for improved adiabaticity

While the realization of an efficient adiabatic passage requires a slow enough rotation of the eigen-basis with respect to the coupling intensities, the initial and final parameters of the passage have to be chosen so that atoms properly connect to the eigen-state of interest  $|\Psi_C\rangle$ . In the case of the spin dependent momentum transfer, those conditions, defined in equations 3.6 and 3.7, are written as:

$$\dot{\delta} \ll \Omega^2 \quad (3.13)$$

$$|\delta_{i,f}| \gg \frac{\Omega^2}{4\Delta} \quad (3.14)$$

In the ideal case, respecting both conditions can be done with a very slow sweep rate and a large detuning ramp. While the speed is limited by processes realized at longer time scales such as unintended momentum transfers from polarization defects, and spontaneous emission, the span of the detuning ramp is limited by the neighboring resonances. With  $\Omega/2\pi = 220$  kHz and  $\Delta/2\pi = 4.8$  kHz, the detuning ramp should start much farther than approximately 1.5 MHz from the resonance, accounting for the CGs, while the excited spin states are separated by 6 MHz. Hence, preserving spin selectivity with a narrower detuning ramp is preferable, and it is actually not incompatible with a proper connection to the eigen-state of interest, which can be done by slowly increasing the Rabi coupling.

In the spin-dependent momentum transfer picture, the basis rotation is induced by the variation of the detuning. However, a variation of the Rabi coupling rotates the basis as well, starting from the atomic states at zero coupling. Consequently, a slow increase of the Rabi coupling at the beginning of the ramp, and slow decrease at the end, maximizes the connection of the atoms to  $|\Psi_C\rangle$ . We increased the efficiency of the adiabatic passage by approximately 5%, as shown on figure 3.9 by superimposing an intensity window over the detuning ramp. We compare the measurement of the

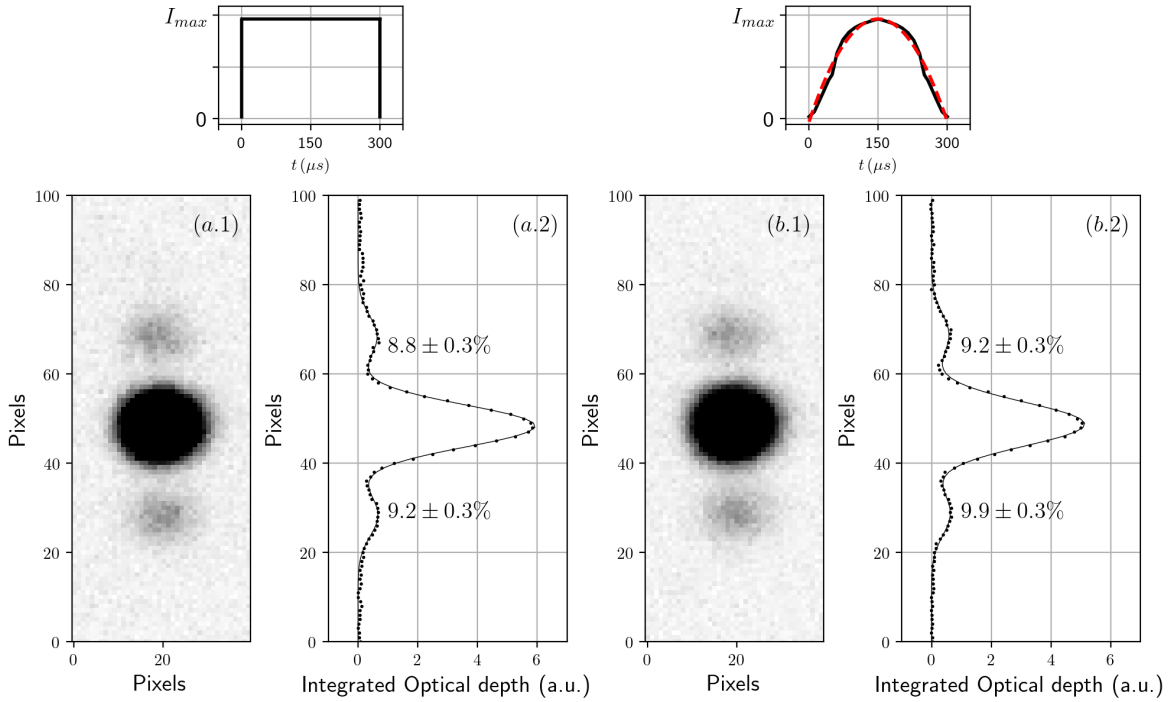


Figure 3.9: Intensity window to enhance the efficiency of the adiabatic following. (a)  $|1/2\rangle \leftrightarrow |-3/2\rangle$  diffraction line with squared intensity window, and (b) with an inverted parabolic intensity window. The intensity ramps are shown on the upper insets, the black solid is the measured intensity during the frequency ramp, the red dashed line is an inverted parabola  $\propto -(t - t_0)^2/\Delta t^2$  with  $\Delta t = 36\mu\text{s}$ . Each image (a.1) and (b.1) are averages over 7 measurements.

populations of the diffracted clouds with a squared intensity ramp, shown on figure (a), and with a smoothed intensity ramp, shown on figure (b), which practically corresponds to an inverted parabola. Averaged over 7 measurements for each case, we measure that the efficiency of the momentum transfer is then increased by approximately 5%, confirming the improvement on the connection to the followed eigenstate.

In this section I presented our method to selectively measure the population in every spin state of the  $^1S_0$  manifold with a spin dependent momentum transfer scheme. This tool permits us to monitor manipulation schemes of the spin populations that I present in the next section, and which we ultimately use to prepare polarized Fermi seas of

$^{87}\text{Sr}$ .

## 3.2 Selective preparation of polarized Fermi sea of $^{87}\text{Sr}$

We apply a magnetic field to produce a Zeeman degeneracy lift of the  $^3P_1, F = 11/2$  Zeeman states. We thus can resonantly couple a selected ground spin state to an excited state with a pulse of light with well defined  $\sigma_-$  polarization to realize spin selective optical pumpings [Tey+10; Pag+14; Oza+18; Son+20]. First, I discuss our method to empty the population of one spin state and the associated heating, and then the preparation of two components Fermi mixtures. Finally, I will show how we can prepare polarized Fermi seas with this method.

### 3.2.1 Optical pumping

#### Experimental procedure

After loading the optical dipole trap, and before forced evaporation (see chapter [1]), we lift the degeneracy of the  $^3P_1, F = 11/2$  Zeeman sub-levels with a homogeneous magnetic field of amplitude  $|\mathbf{B}| = 6.8\text{ G}$ , as shown on figure [3.10], top. The excited spin states, with magnetic susceptibility  $380\text{ kHz/G}$  are then separated by  $g_F\mu_B|\mathbf{B}| \simeq 2.6\text{ MHz}$ . The  $^1S_0 \leftrightarrow ^3P_1, F = 11/2$  optical transitions are spin resolved, and we pulse a strongly saturating laser beam,  $I \simeq 70I_{sat}$  with  $I_{sat} \simeq 3\mu\text{W/cm}^2$ , with well defined polarization  $\sigma_-$ , resonant with a  $|^1S_0, m_F\rangle \leftrightarrow |^3P_1, m_F - 1\rangle$  transition, to pump the population out of the targeted  $|m_F\rangle$  spin state. Figure [3.10], middle, shows the depletion of the each pumped spin population, measured with the spin dependent momentum transfer scheme, with respect to the frequency of the pump, with pulse duration 30 ms. This spectrum lets us infer the resonance of every  $|^1S_0, m_F\rangle \leftrightarrow |^3P_1, m_F - 1\rangle$  transition with a Lorentz fit:

$$L(f) = N_0 \left( 1 - \frac{1}{1 + \left(\frac{f-f_0}{\Gamma/2}\right)^2} \right) \quad (3.15)$$

of the populations depletion. Here,  $y_0$  is the baseline,  $f$  the frequency of the pump

and  $f_0$  the resonance. The measured resonances  $f_0$  are reported on figure 3.10, bottom, for every spin state, as well as the width of the depletion. The resonances are separated by 2.6 MHz which is in agreement with the expected Zeeman degeneracy lift with magnetic field  $|\mathbf{B}| = 6.8 \text{ G}$ .

This measurement shows that we are able to empty the population of any selected spin state of the ground state manifold with a pulse of well polarized  $\sigma_-$  light at appropriate frequency. Due to spontaneous emission, the population of the targeted  $|m_F\rangle$  spin state is transferred to  $|m_F - 1\rangle$  and  $|m_F - 2\rangle$  spin states, and the emission of one spontaneous emission with  $\pi$  or  $\sigma_+$  polarization is enough to flip the spin of the atom. Once an atom populates a new spin state, it will not see the excitation anymore because of the degeneracy lift and the light polarization, and thus will remain stable in the new spin state. Note that the  $\sigma_-$  excitation on  $-9/2$  is cyclic, such that atoms in  $|^3P_1, F = 11/2, m_F = -11/2\rangle$  cannot de-excite anywhere but back on  $-9/2$ . Note that transferring this spin population would require to reverse the magnetic field.

### Frequency and polarization sensitivity

While experiencing Rabi oscillations between the ground and the excited nuclear spin states, an atom has a probability to spontaneously emit a photon with random polarization and relax to any of the connected ground states, and the excitation has to be applied for a long enough duration such that the probability of spontaneous emission increases and the spin flip is realized. Figure 3.11 reports our measurements of the  $+9/2$ ,  $+7/2$ ,  $-1/2$ , and  $-7/2$ , spin population depletion (black dots, indicated at bottom right corner of each figure) with respect to the duration of the  $\sigma_-$  light pulse. The population depletions are fit with exponential decays  $\exp(-t/\tau)$  (dashed lines) and the inferred decay times  $\tau$  are all in the order of one millisecond (written at bottom left corner of each figure). The data is compared to numerical time integration of the Lindblad equation shown by the solid black lines, accounting for possible detuning and circularity defect that will be discussed in the following.

*Frequency sensitivity:* in the saturating regime  $I \simeq 70 I_{sat}$ , one would expect that the rate of spontaneous emission governs the timescale of optical pumping, which would

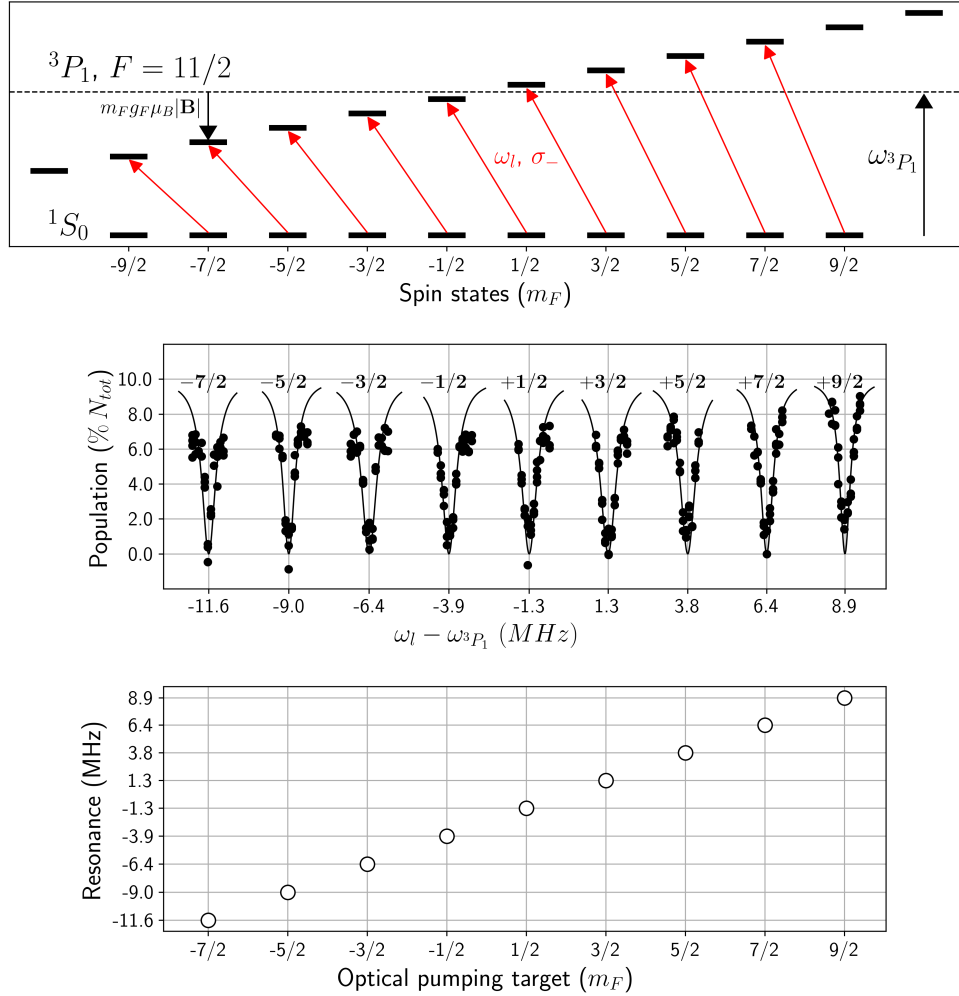


Figure 3.10: Experimental population transfer within the nuclear ground spin states manifold. Top: optical pumping scheme with  $\sigma_-$  resonant coupling, where  $\omega_{3P_1}$  is the  $^3P_1, F = 11/2 \leftrightarrow ^1S_0$  resonance for all spin states without magnetic field. Middle: spectroscopy for  $\sigma_-$  excitation in the saturating regime for all spin states. The depletion of the population of each spin is measured with respect to the frequency of the pump. The black solid line is a lorentzian fit as defined in [3.15](#) to measure the optical pumping resonance  $\omega_{op}$ , assuming 10% initial population. Bottom: resonances (black circles) for every nuclear spin states.

be  $(\Gamma_{3P_1}/2)^{-1}$ , *i.e.* tens of microseconds for  $\Gamma_{3P_1} = 7.4\text{kHz}$ , which is much faster than our measurement. This scaling is correct in the case  $\Omega \gg \Gamma, \delta$  such that the

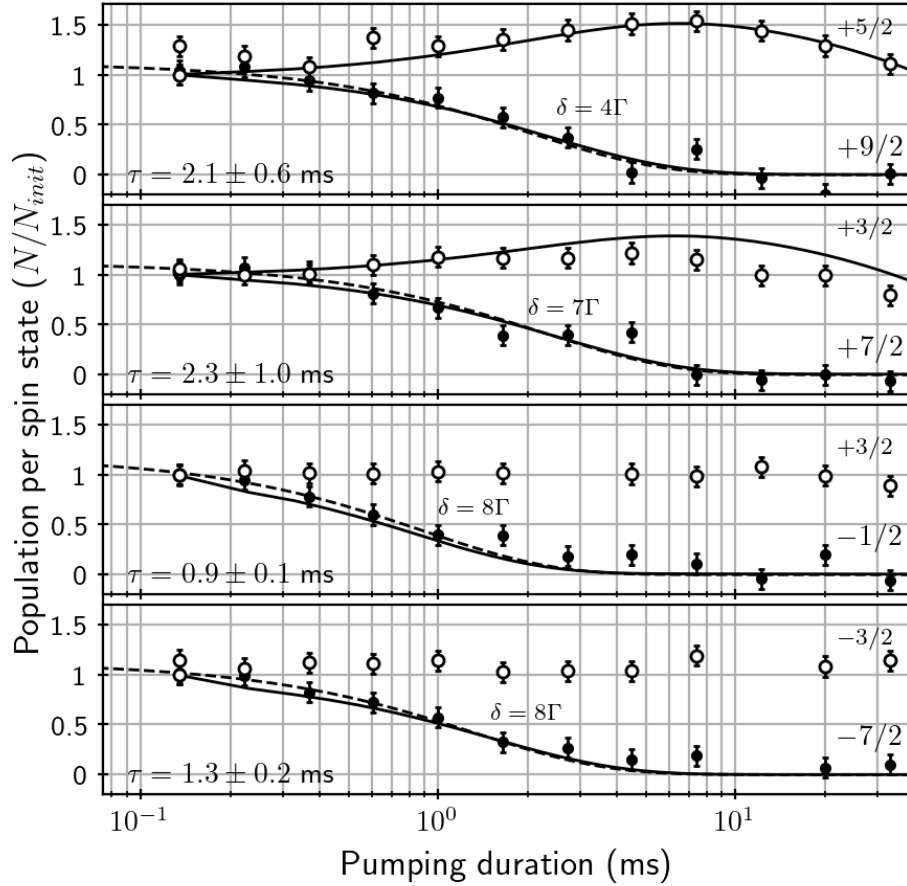


Figure 3.11: Spin populations depletion with respect to the duration of the  $\sigma_-$  light pulse. We measure the number of atoms remaining in the target spin state (black dots), respectively  $+9/2$ ,  $+7/2$ ,  $-1/2$ , and  $-7/2$ , from top to bottom figure, and the associated spins with the spin-dependent momentum transfer scheme, respectively  $+5/2$ ,  $+3/2$ ,  $+3/2$ ,  $-3/2$  (white dots). Each spin population depletion is fit with an exponential decay  $\exp(-t/\tau)$  (dashed line), and the fitted decay time  $\tau$  is noted on the bottom left corner of each figure. Black solid lines: numerical integration of the Lindblad equation with experimental parameter  $I = 70 I_{sat}$  accounting for a global perturbative defect in light circularity ( $2.5 \times 10^{-3} \times I$ ) for all spin states, and tunable detuning.

probability for each atom to populate the excited state is close to  $1/2$ . However, if the light excitation is detuned from resonance, the amplitude of the Rabi oscillation is reduced, hence is the population of the excited state, which reads in the rotating wave

approximation (RWA) [MS99]:

$$P_e = \frac{1}{2} \frac{s}{1+s} \quad (3.16)$$

where  $s$  is the saturation parameter defined as:

$$s = \frac{2\Omega^2}{\Gamma^2 + 4\delta^2} \quad (3.17)$$

The radiative decay time in the non-resonant case can be directly inferred, and it reads, in units of the resonant radiative decay time:

$$\frac{\tau(\delta)}{\tau_0} = 1 + \left( \frac{2\delta}{\Gamma'} \right)^2 \quad (3.18)$$

where  $\Gamma' = \Gamma_{3P_1} \sqrt{1 + CG^2 I/I_{sat}}$  is the power broadened linewidth of the transition, with associated Clebsch-Gordan (CG), and  $\tau_0 \simeq 70 \mu\text{s}$ . If considering the depletion of  $m_F = +9/2$ , with  $I \simeq 70 I_{sat}$  and  $CG \simeq 0.135$ , a detuning  $\delta = 4\Gamma_{3P_1}$  increases the decay rate to approximately 2.2 ms, which is in good agreement with the measured decay time, and numerical time integration of the Lindblad equation, accounting for the detuning, confirms this result, as shown by black solid lines on figure 3.11. The increase of decay time of the pumping of the other spin states  $+7/2$ ,  $-1/2$ , and  $-7/2$ , is similarly explained with respective detunings  $7\Gamma_{3P_1}$ ,  $8\Gamma_{3P_1}$ , and  $8\Gamma_{3P_1}$ . Regarding our measurement, those detunings are relevant since we calibrated the optimal pumping frequency with a  $100 \text{ kHz} \simeq 13\Gamma_{3P_1}/2\pi$  step. This also confirms that pumping is robust against frequency drifts which only extends the duration of the light pulse to a few milliseconds, and hence can be easily compensated for. Another possibility is to sweep the frequency of the optical pumping, and this gives the same results than extended pulse durations.

*Polarization sensitivity:* the number of atoms are measured with the spin-dependent momentum transfer scheme, hence a second spin population is measured simultaneously, as shown by the white dots (indicated top right corner of each figure). The pumping of spin states  $+9/2$  and  $+7/2$  are measured with the diffraction lines  $+9/2 \leftrightarrow +5/2$  and  $+7/2 \leftrightarrow +3/2$ , which means that one of the two final states is measured simultaneously

with the depletion of initial state. However, the pumping of spin states  $-1/2$  and  $-7/2$  are measured with the diffraction lines  $-1/2 \leftrightarrow +3/2$  and  $-7/2 \leftrightarrow -3/2$ , and the second measured state cannot be a final state of  $\sigma_-$  optical puming, and the measurement of these populations, which is stable all over the duration of the pulse, confirms the robustness in spin sensitivity.

The first two measurements show that the populations of  $+5/2$  and  $+3/2$  are increased simultaneously with the depletion of  $+9/2$  and  $+7/2$ , respectively, which is expected for optical pumping. However, for longer pulse duration, higher than 10 ms, the populations of final states  $+5/2$  and  $+3/2$  start decreasing. In our case, we explain this decay by the imperfection of the circularity of the light. Let's consider the pumping of  $+9/2$  with  $\sigma_-$  excitation. A negligible fraction of  $\sigma_+$  light is enough to excite  $+5/2$ , and in a two level picture, the associated rate of spontaneous emission reads:

$$\Gamma_{se} = \Gamma_{3P_1} \frac{s}{2} \quad (3.19)$$

where  $s \ll 1$  is defined in [3.17](#), accounting for the polarization defect  $\varepsilon$  along  $\sigma_+$  so that:

$$\Omega^2 = \frac{\Gamma^2}{2} \varepsilon^2 \frac{I}{I_{sat}} \quad (3.20)$$

and a defect as small as  $\varepsilon^2 = 2.5 \times 10^{-3}$ , *i.e.*  $I_{\sigma_+}/I_{\sigma_-} = \varepsilon^2$ , which is hardly measurable with a powermeter, is enough to be responsible for a depletion of the  $+5/2$  population with associated decay time  $\tau \simeq 12.5$  ms. On figure [3.11](#), the time integration of the Lindblad equation, shown by the black solid lines, accounts for this circularity defect  $\varepsilon^2 = 2.5 \times 10^{-3}$ , and is enough to explain the population depletion of  $+5/2$  and  $+3/2$  that we measure, as small as it is. This shows that pumping is very sensitive to the polarization, indeed a 1% defect in intensity, 5 times larger than we infer, would be enough to lower the decay time of  $|+5/2\rangle$  to 3 ms, and would break the spin sensitivity at our time scales. It is then critical that the polarization is optimized on the *non-depletion* of  $m_F - 2$  population for  $\sigma_-$  optical pumping.

Another possible explanation would be that these states are also excited by the  $\sigma_-$

pulse, but the 2.6 MHz Zeeman degeneracy lift of the excited states ensures the spin selectivity, and the verified equation [3.18](#) confirms that with such a detuning as large as the degeneracy lift, the associated decay time is as large as hundreds of milliseconds, which would not be observable on the measured time scales. Note that a defect in  $\pi$  polarization could not explain the depletion of spin states  $|+5/2\rangle$  and  $|+3/2\rangle$  because of the Zeeman degeneracy lift, and considering the non-zero  $\sigma_+$  defect, the stationary state of the three coupled ground states would obviously have non zero population in the target state. Even if we don't reach a stationary state, as shown by the populations of  $+5/3$  and  $+3/2$ , our measurement shows that the target state is completely depleted, which shows that a defect in  $\pi$  polarization is completely negligible, and this confirms a good alignment of the magnetic field with the propagation of the light.

### Associated heating

Since this scheme relies on spontaneous emission, the atoms obviously heat during the process. When experiencing the Rabi oscillations, atoms can relax to any of the connected ground states, including the initial state. This means that the atoms may need to emit more than one spontaneous photon before changing spin state. The probabilities for relaxation are exactly the square of the Clebsch-Gordan coefficients (CG), which are defined as  $C_{j_1q_1, j_2q_2}^{kq} = \langle j_1q_1, j_2q_2 | kq \rangle$ , where  $|j_1q_1\rangle = |^3P_1, F = 11/2, m_{F_e}\rangle$  and  $|kq\rangle = |^1S_0, F = 9/2, m_{F_i}\rangle$ . For each spontaneously emitted photon, let's define

$$p_{fail} = C_{m_{F_e}, 1-1}^{m_{F_i}}^2 \quad (3.21)$$

the probability for the atom to relax in the initial state, and

$$p_{success} = 1 - p_{fail} \quad (3.22)$$

the probability to relax in one of the two possible final states. This is a binomial process, with associated probabilities for success  $p_{success}$  and fail  $p_{fail}$ , and then the average number of tries for first success, here changing spin population, is simply  $1/p_{success}$ , which is exactly the average number of spontaneously emitted photon needed to change spin population  $\langle N_{sp.em.} \rangle = 1/p_{success}$ .

Let's now discuss the heating associated with optical pumping and resulting from the multiple momentum exchanges, say  $n$ , between an atom and the photons from the light excitation. An isolated atom at rest realizes a Brownian motion in the momentum space, consequently to the  $n$  consecutive momentum recoils acquired with the absorption - spontaneous emission process. It results in an acceleration along the light propagation with acquired  $n^2 E_R$  1D kinetic energy, where  $E_R = \hbar^2 k^2 / 2m$  is the recoil energy, and a three dimensional diffusion in momentum resulting from the spontaneously emitted photons with acquired  $n E_R$  3D kinetic energy. Let's quickly give a proof of this well known result. The momentum variation  $\delta \vec{k}$  associated with multiple processes of one absorption of a photon from the excitation with momentum  $\hbar \vec{k}_L$  and one spontaneous emission with momentum  $\hbar \vec{k}_{se,i}$  and random direction  $i$  reads:

$$\delta \vec{k} = n \vec{k}_L + \sum_{i=1}^n \vec{k}_{se,i} \quad (3.23)$$

Regarding this energetic consideration, the relevant quantity is the momentum spread, which reads as the quadratic momentum variation averaged over the realizations:

$$\begin{aligned} \langle \delta \vec{k}^2 \rangle &= \langle n^2 k_L^2 + \left( \sum_{i=1}^n \vec{k}_{se,i} \right)^2 + 2n \sum_{i=1}^n \vec{k}_{se,i} \cdot \vec{k}_L \rangle \\ &= n^2 \langle k_L^2 \rangle + n \langle k_{se}^2 \rangle \end{aligned} \quad (3.24)$$

This results from the independence between the absorption and emission process, so that the momentum of the absorbed photon is not correlated with the momentum of the spontaneous photon, and  $\langle \vec{k}_L \cdot \vec{k}_{se} \rangle = \langle \vec{k}_L \rangle \cdot \langle \vec{k}_{se} \rangle$ . Similarly, every spontaneous emission is independant so that  $\langle \vec{k}_{se,i} \cdot \vec{k}_{se,j} \rangle = \langle \vec{k}_{se,i} \rangle \cdot \langle \vec{k}_{se,j} \rangle$ . Since the momentum of spontaneously emitted photons is random,  $\langle \vec{k}_{se} \rangle = \vec{0}$ , which cancels both products. Now, the recoil energy  $E_R = \hbar^2 k_R^2 / 2/m$  associated with the intercombination line can be inserted to define the average energy acquired:

$$\langle \delta E \rangle = n^2 E_R + n E_R \quad (3.25)$$

which shows the quadratic dependence on  $n$  of the energy acquired from the 1D acceleration and the linear dependence on  $n$  of the 3D momentum diffusion resulting from the spontaneous emission.

In our experiment, the decay time associated with optical pumping of a spin state is approximately between 1 and 2 ms (see figure 3.11), while the collision rate is slightly lower than 1 collision per atom per millisecond. Considering that the gas necessitates several collisions to thermalize, and the pumping duration is smaller than the dipole trap period, it is then reasonable to consider that an atom is approximately isolated when it is pumped into another spin state. The estimated average energy acquired by the atom is:

$$\langle \delta E \rangle = n^2 E_R + n E_R \quad (3.26)$$

The associated heating for a 3D thermal gas in a harmonic trap with total energy  $E_{tot} = 3k_B T$  finally reads:

$$\delta T = \frac{1}{3} n(n+1) T_R \quad (3.27)$$

Where the recoil temperature associated with the intercombination line of  $^{87}\text{Sr}$  is  $T_R = E_R/k_B = 230$  nK. Considering that the heating associated with one spin flip is redistributed to the whole gas after thermalization, the heating associated with the total depletion of a spin population can finally be predicted from:

$$\delta T = \frac{N_i}{N_{tot}} \frac{1}{3} n(n+1) T_R \quad (3.28)$$

where  $N_i$  is the initial number of atoms in the pumped spin state and  $N_{tot}$  the total number of atoms in the gas, and  $n = 1/p_{success}$  the average number of spontaneous emissions needed to change spin population, where  $p_{success}$  is defined in equation 3.22. For instance, considering that the gas is initially unpolarized with 10% atoms per spin state, atoms in  $-3/2$  have 0.5 probability to change spin state, so that emptying the population of  $-3/2$  heats the gas by approximately 115 nK. Note that the populations of the low negative  $m_F$  spin states, with strong CGs associated with  $\sigma_-$  relaxation, see

figure 3.6, need to experience more spontaneous emission than the positive spin states to be transferred, for instance  $-3/2$  spins are heated twice as much as  $9/2$ .

Optical pumping is best realized on a hot gas in a deep trap, rather than on an ultra-cold gas in a shallow trap which would consequently strongly heat the atoms and might blast them out of the trap. For this reason, the spin populations are emptied just after loading the dipole trap which is  $90\mu\text{K}$  deep, while the gas is unpolarized with approximately 10% atoms per spin state (see section 3.1) at  $7.2\mu\text{K}$  (see section 1.1.6 of chapter 1). In this case, the heating associated with the pumping of one spin population is hardly measurable.

### 3.2.2 Controlling the number of spin components from 1 to 10

In the previous section, I presented our method to empty the population of a  $m_F$  spin state and transfer it to  $m_F - 1$  and  $m_F - 2$ . I will now explain how we can tune the number of spin components in the Fermi gas of  $^{87}\text{Sr}$  from 10 to 1. To prepare a selective spin mixture, we rely on the pure polarization of the laser, such that consecutive spin states can be emptied in descending  $m_F$  order, while never bringing back atoms in previously emptied spin states. Considering the preparation of a Fermi gas with 2 spin components with initially all 10 spin states populated, we sequentially empty all  $m_F$  states with decreasing  $m_F$ , but one spin state that we voluntarily skip, say  $-5/2$ , and  $-9/2$  that cannot be pumped with  $\sigma_-$  excitation, so that all spin states are emptied, but  $-5/2$  and  $-9/2$ .

Figure 3.12 shows absorption image after time of flight of a  $\text{SU}(2)$   $^{87}\text{Sr}$  thermal gas (right) after a pumping sequence to prepare a  $\{-9/2, -1/2\}$  mixture, and a  $\text{SU}(10)$  gas (left) with no prior optical pumping. We compare the temperature of the gas after the pumping sequence and after allowing for 500 ms thermalization, to the initial temperature of the gas prior to pumping, as well as the number of atoms. The increase of temperature is reported on figure 3.12, (a), for the  $\{-9/2, -1/2\}$  preparation, as well as other preparations,  $\{-9/2, 3/2\}$ ,  $\{-9/2, -3/2\}$ , and  $\{-9/2, -7/2\}$ . We measure an increase of  $1\mu\text{K}$  after thermalization of the  $\{-9/2, -7/2\}$  preparation, and smaller

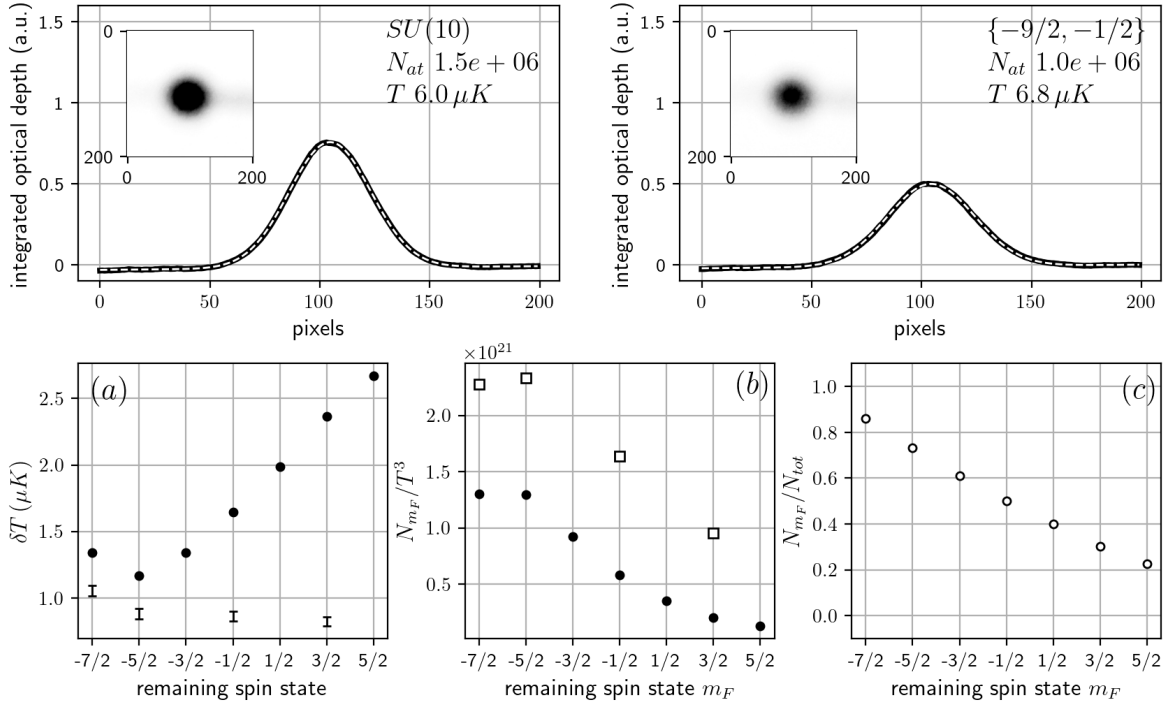


Figure 3.12: Measurement of the heating and atom loss associated with the preparation of a 2 component Fermi gas of  $^{87}\text{Sr}$  with a pumping sequence. Top figures, absorption images after time of flight of a  $SU(10)$  gas (left) and  $SU(2)$  gas with remaining  $-9/2$  and  $-1/2$  spin states. The number of atoms and temperatures and inferred from a Gaussian fit (white dashed line) of the integrated optical depths (black solid lines). (a): heating of  $\delta T = T_{SU(10)} - T_{SU(2)}$ , inferred from a simulated pumping sequence (black dots), neglecting evaporation, and measurement with associated fit uncertainty. (b) density of the remaining spin component, here defined as  $\propto N_{m_F}/T^3$ , inferred from a simulation (black dots) and measurement (empty squares), where the population in  $m_F$  is inferred from the measured number of atoms and the predicted population balance after the pumping sequence. (c) Prediction of the ratio of atoms in  $m_F$  after preparation of a  $-9/2, m_F$  two component gas, using Clebsch-Gordan coefficients.

increase of approximately 800 nK for the other preparations, and it is compared to simulations of the associated pumping sequences using only the Clebsch-Gordan coefficients, and equations [3.22](#) and [3.28](#). Our measurement shows that heating is less spin dependent contrary to the prediction and moreover it is generally lower. A possible explanation is that during thermalization, the two component gas continues evapora-

tion, attenuating the heating from the pumping sequence, and our measurement of the number of atoms  $N_{at}^{SU(2)} \simeq 10^6$  for all preparations confirms that one third of the atoms are lost after thermalization. We assume that thermalization is homogeneous for all spin states, and that there is no spin exchange due to the  $SU(N)$  symmetry of the collision properties [Gor+10]. Then, the population in the remaining  $m_F$  component can be inferred from the total number of atoms measured and the predicted population imbalance after the pumping sequence, shown on figure 3.12, (c). This way, we deduce the density of atoms in the remaining  $m_F$  component, as shown on figure 3.12, (b).

On figure 3.13, we compare the final state of several gases after evaporation, depending on spins mixture preparation prior to evaporation. The initial mixtures are either a  $SU(10)$  gas with no optical pumping prior to evaporation, or a  $SU(2)$  gas prepared in  $\{-9/2, -7/2\}$ ,  $\{-9/2, -3/2\}$ ,  $\{-9/2, -1/2\}$ , or  $\{-9/2, +3/2\}$  (these preparations are the ones discussed on figure 3.12). After the evaporations, all realized from initial trap frequency 330 Hz ramped down to 85 Hz during 5 seconds, we compare the densities and degeneracies of each preparation, accounting for the predicted balance of the population, see figure 3.12.

This measurement first shows that a  $SU(10)$  gas of  $^{87}\text{Sr}$  has four times more atoms than a  $SU(2)$ , and thermalizes at a temperature lower by 20 %, for this evaporation depth. Accounting for the fact that initially  $SU(10)$  gas has approximately 30 % more atoms, this shows that relatively more atoms are evaporated in  $SU(2)$  preparations. This is consistent with previous observations that the collision rate of a  $SU(2)$  gas is lowered compared to that one of a  $SU(10)$  gas [Son+20]. However, accounting for the number of atoms per spin state, the phase space density  $N_{m_f}/T^3$  of the most populated spin state of the  $SU(2)$  preparations  $\{-9/2, -7/2\}$  and  $\{-9/2, -5/2\}$  is equal to that one of the  $SU(10)$  preparation, as well as the degeneracy  $T/T_F$ . The  $\{-9/2, -1/2\}$  and  $\{-9/2, 3/2\}$  preparations, with less atoms in the selected spin states, are consequently less degenerate. This shows that the manipulation of the spins populations is viable for the preparation of ultra cold gases of  $^{87}\text{Sr}$  with tunable  $N$ . Moreover, we are not interested into the choice of the spin mixture regarding the latter study of the Heisenberg model in enlarged  $SU(N)$  symmetry, since the collision properties of  $^{87}\text{Sr}$  do not depend on the spin states. It is then reasonable to select the most favorable spin mixture

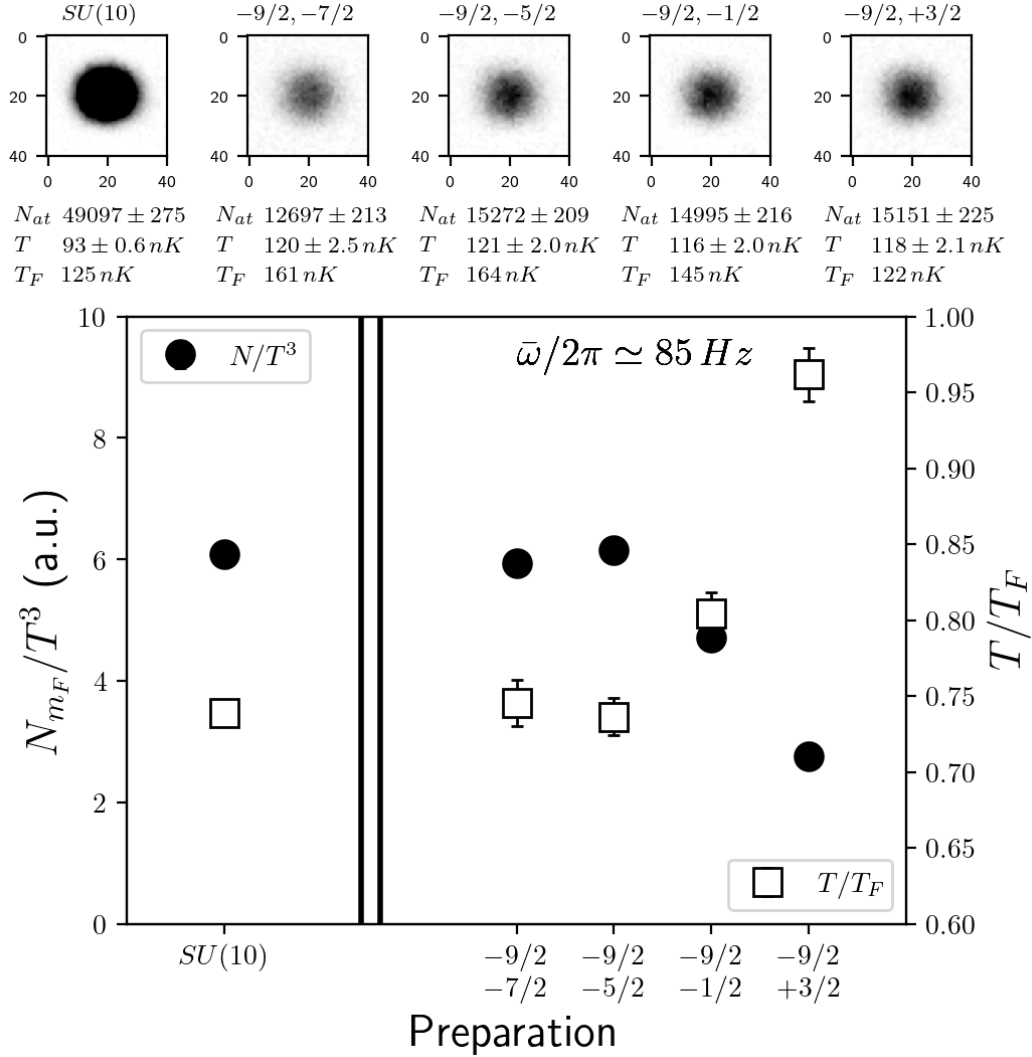


Figure 3.13: Final state of different spin mixtures after evaporation. Top: absorption images after 12 milliseconds of time of flight of the different mixtures, SU(10) on left, and SU(2) preparations. From the measured number of atoms and temperatures, we infer the density per spin state  $N_{m_F}/T^3$  for each preparation, and degeneracy  $T/T_F$ , using predicted populations per spin states. The final trap frequency of evaporation is indicated at top right corner.

regarding only the production of degenerate gases.

*Collision rate for unbalanced mixtures.* The preparation of the SU(2) mixtures induces populations imbalances between the remaining spin states. It is then interesting to investigate the consequences regarding the efficiency of evaporation, that depends on collisions. Symmetry rules forbid s-wave collisions between two identical fermions, so that collisions are inhibited in the degenerate regime and the efficiency of the evaporation decreases when  $T \rightarrow 0$  [DeS+10]. In case of population imbalance between the colliding fermions, the collision rate per atom will be lowered for the most populated spin state,  $m_F$  in our case. Indeed, the less populated has more partners to collide with, and Pauli exclusion principle forbids collisions for which the arrival state is already occupied by a fermion of the same specie, so that at thermal equilibrium between the two spin states, the most populated state has more occupied states in the arrival state for the collision, inhibiting the probability for this collision. It is possible to numerically predict the inhibition of collisions due to a population imbalance in a two components fermi mixture. The collision rate of two colliding species  $\alpha$  and  $\beta$  can be computed thanks to the collisional integral [LRW96; Geh+03]:

$$\begin{aligned} \rho(\varepsilon_4)\dot{f}_\alpha(\varepsilon_4) &= \frac{M\sigma}{\pi^2\hbar^3} \int_0^\infty d\varepsilon_1 d\varepsilon_2 d\varepsilon_3 \rho(\varepsilon_{min}) \delta(d\varepsilon_1 + d\varepsilon_2 - d\varepsilon_3 - d\varepsilon_4) \\ &\quad (1 - f_\alpha(\varepsilon_1))(1 - f_\beta(\varepsilon_2))f_\alpha(\varepsilon_3)f_\beta(\varepsilon_4) \end{aligned} \quad (3.29)$$

$$\Gamma_{coll}^{\alpha\beta} N_\alpha = \int_0^\infty d\varepsilon_4 \rho(\varepsilon_4) \dot{f}_\alpha(\varepsilon_4)$$

where  $M$  is the mass,  $\sigma = 4\pi a_s^2$  the low energy s-wave collisions cross-section with  $a_s$  the scattering length, and  $\hbar$  the reduced Planck constant.  $\rho(\varepsilon) = \varepsilon^2/2(\hbar\bar{\omega})^3$  stands for the density of states, in a harmonic trap of geometric mean frequency  $\omega$ . The Pauli exclusion principle is taken into account by the  $(1 - f(\varepsilon))$  *non-occupation* number, where  $f(\varepsilon)$  is the Fermi-Dirac occupation number:

$$f_{FD}(\varepsilon, T, \mu) = \frac{1}{e^{\beta(\varepsilon - \mu)} + 1} \quad (3.30)$$

Here,  $\beta = 1/k_B T$  and the chemical potential  $\mu$  is defined as the Fermi energy at zero temperature  $\mu(T = 0) = \varepsilon_F = k_B T_F$ ,  $T_F$  the Fermi temperature. When solving equation [3.29], it is important to take into account the fact that the two unbalanced

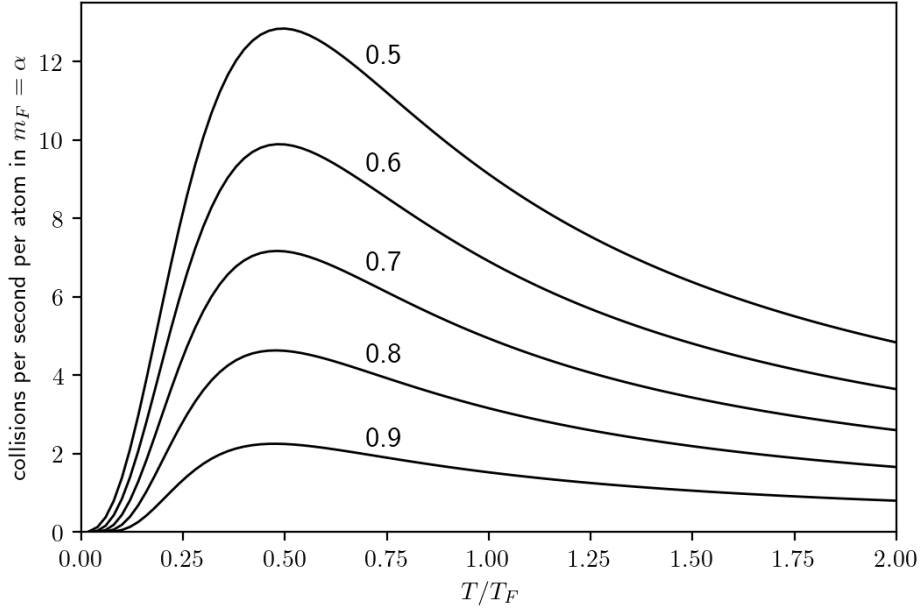


Figure 3.14: Inhibition of the collision rate per atom for unbalanced populations in the two colliding Fermi components  $\alpha$  and  $\beta$ . The numbers above each curve indicates the ratio of atoms  $p_\alpha$  in the considered state  $\alpha$  with respect to the total number of atoms  $N_{tot} = N_\alpha + N_\beta$ , i.e.  $N_\alpha = p_\alpha N_{tot}$ . The calculation has been made for trap frequency  $\bar{\omega} = 120$  Hz and  $N_{tot} = 10^5$ , representative of our trap after after evaporation.

populations have different Fermi energy  $\varepsilon_{F\alpha} = \hbar\bar{\omega}(6N_\alpha)^{1/3}$  and hence Fermi temperature and chemical potential. So the occupation numbers  $f_\alpha$  and  $f_\beta$  are not the same for the two species. The details for the computation can be found in appendix [A](#). In figure [3.14](#) are presented different collision rates per atom in state  $m_{F_{sel}}$  with respect to  $T/T_{F\alpha}$  and populations inbalance, for fixed  $N_{tot}$  and  $\bar{\omega}$ . If the two spin states are equally populated,  $N_\alpha = N_\beta = N_{tot}/2$ , then collision rate per atom is maximal, and the forced evaporation efficiency optimal. Then if the state  $m_{F_{sel}}$  starts to be more populated, i.e.  $p_\alpha = N_\alpha/N_{tot} > p_\beta$ , the collision rate drops quickly, from -20% for  $p_\alpha = 0.6$  with respect to equally populated states ( $p_\alpha = p_\beta = 0.5$ ) to approximately -80% for  $p_\alpha = 0.9$ .

This shows that unbalanced mixtures suffer from inhibition of the collisions, which results in a less efficient evaporation. This is consistent with our measurement of the

number of atoms after evaporation presented on figure 3.13, which indicates that the most unbalanced mixture  $\{-9/2, -7/2\}$  is slightly lower than the other  $\text{SU}(2)$  preparations. However, it is not significant, as  $T/T_F$  is smaller. Regarding the preparation of  $\text{SU}(2)$  degenerate Fermi gases with forced evaporation, the best mixtures are hence  $-9/2$  with either  $-7/2$  or  $-5/2$ , according to our measurement.

A spin mixture with more than two components can be prepared exactly the same way, except that another  $m_F$  spin has to be skipped during the pumping sequence. Note that the preparation of the Fermi gas with tunable number of spin components is realized in the deep dipole trap prior to evaporation because of the heating associated with optical pumping, so it is mandatory to keep at least two spin components to authorize forced-evaporation assisted by s-wave collisions. For this reason, our preparations of polarized Fermi seas have to be done after evaporation, which I will now discuss.

### 3.2.3 Spin purification to prepare a polarized Fermi sea

To prepare a polarized Fermi sea from a two components degenerate Fermi gas, we selectively blast one spin state out of the trap after evaporation. This is done by realizing our optical pumping scheme on spin state  $-9/2$ , *i.e.* with a long pulse of saturating  $\sigma_-$  light resonant with the  $|^1S_0, -9/2\rangle \leftrightarrow |^3P_1, F = 11/2, -11/2\rangle$  transition. This transition is cyclic, and atoms absorb photons from the laser and emit spontaneous photons until they acquire enough energy to leave trap. Then, there remains only the other spin state and the Fermi gas is spin polarized.

Figure 3.15 shows our experimental realization of the blast to prepare a polarized Fermi gas in  $m_F = -1/2$ , from an evaporated gas previously prepared in a  $-9/2, -1/2$  spins mixture with optical pumping. Right figure shows absorption images of the  $|-1/2\rangle \leftrightarrow |+3/2\rangle$  diffraction line, with respect to the duration of the  $\sigma_-$  pulse, and the corresponding longitudinal integrated optical depths are superimposed for each blast duration. The population in the non diffracted cloud, which corresponds to atoms in  $-9/2$ , and centered on pixel 30, is progressively reduced with longer pulses until it reaches a minimum while the population in  $-1/2$  seems not affected, and the absence of a second

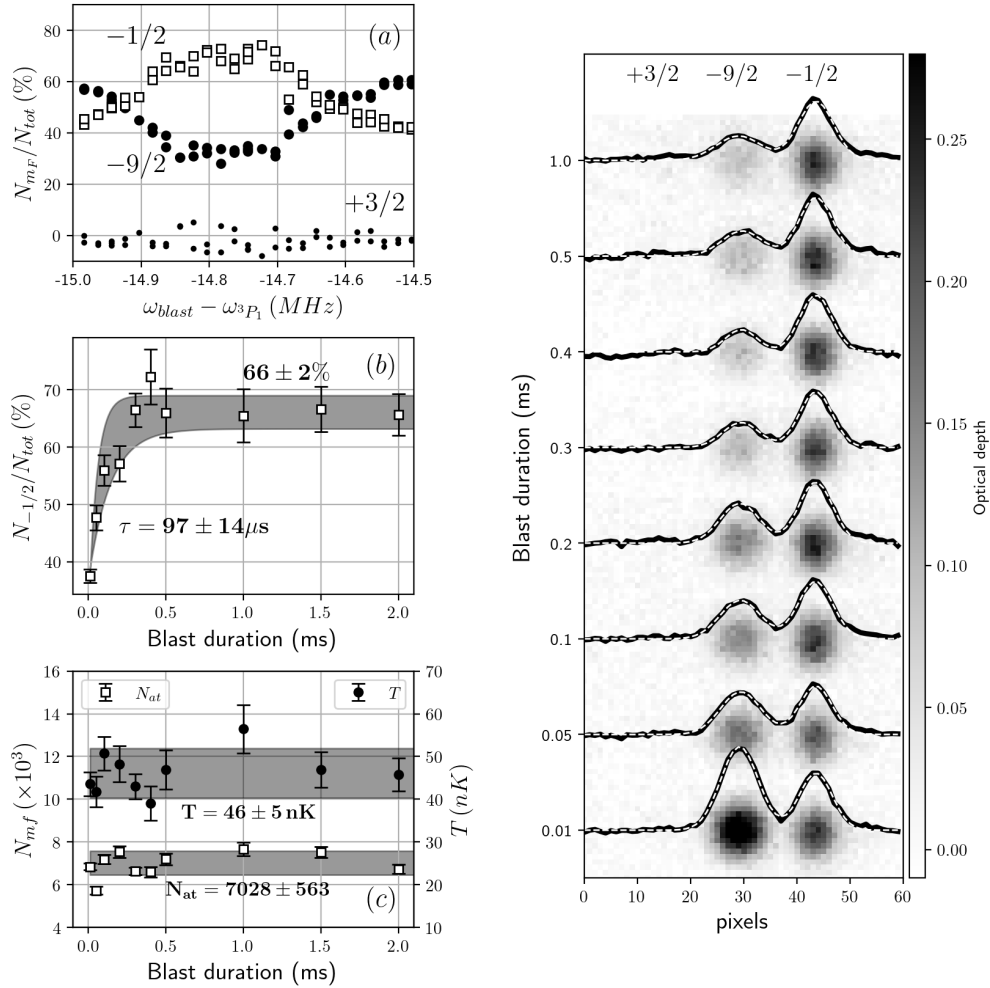


Figure 3.15: Preparation of a polarized Fermi gas in  $m_F = -1/2$  by blasting atoms in  $m_F = -9/2$  out of a two components trapped Fermi gas. (a) Depletion of the  $-9/2$  population, and relative increase of the  $-1/2$  population, with respect to the frequency of the blast with fixed duration 5 ms. (b) Ratio of atoms in  $m_F = -1/2$  with respect to the blast duration. It is fit with an exponential decay of the  $-9/2$  population  $e^{-t/\tau}$ , with fitted decay time  $\tau = 97 \pm 14 \mu s$ , and the ratio of atoms in  $-1/2$  saturates at approximately 66% in this measurement. (c) Measured number of atoms and temperature of the diffracted cloud associated with  $-1/2$  population, with respect to the duration of the blast. Right figure: absorption images of the  $|-1/2\rangle \leftrightarrow |+3/2\rangle$  diffraction line, with respect to the duration of the resonant blast with saturating  $\sigma_-$  excitation,  $I \simeq 70 I_{sat}$ , used for the measurements on figures (b) and (c).

diffracted cloud confirms that the population in  $+3/2$  is zero. From this measurement, we infer the ratio of atoms in  $-1/2$  with respect to the blast duration, shown on figure (b), which raises consequently to the exponential decay of the population in  $-9/2$ , with fitted decay time  $\tau = 97 \pm 14 \mu\text{s}$ . We observe here that the population in  $-1/2$  saturates close to 70 %, and this is also observed on a scan of the optimal frequency of the blast with 5 ms of pulse, shown on figure (a), with a plateau of the depletion in  $-9/2$  over 150 kHz of scan. This poor efficiency of the blast was due to a hardware failure damaging the efficiency of the spin-dependent momentum transfer, so that atoms in  $-1/2$  were not diffracted for this specific data. This failure was later corrected.

Nevertheless, our measurement shows that during the blast of atoms in  $-9/2$ , atoms in  $-1/2$  remain unaffected, as the diffracted cloud has an approximately constant number of atoms, and the temperature remains stable compared to the temperature of the initial gas  $T_i \simeq 45 \text{ nK}$ , as shown on figure 3.15, (c). This is consistent with the fitted decay rate  $\gamma = 1/\tau \simeq 2\pi \times 1.5 \text{ kHz}$  of the  $-9/2$  population, which is much higher than the collision rate and the trap frequency. Atoms in  $-9/2$  leave the trap before colliding with atoms in  $-1/2$ , and the Zeeman degeneracy lift of the excited state ensures that there is no possible light scattering from atoms in  $-1/2$  on those timescales.

### 3.2.4 Polarized Fermi sea

We measure the fidelity of our preparation of a polarized Fermi sea of  $^{87}\text{Sr}$  in  $m_F = -7/2$ , by measuring the number of atoms in every spin state with the spin-dependent momentum transfer scheme. Figure 3.16 shows the results of our preparation with absorption images of each diffraction line (see section 3.1.4). From the diffraction line  $|-7/2\rangle \leftrightarrow |-3/2\rangle$  (see (a)), we measure  $75 \pm 3\%$  diffracted atoms from  $-7/2$ .

The signal in the non diffracted cloud, in both the absorption image (top) and the integrated optical depth (a), shows that atoms at rest prior to the momentum transfer, at the center of the gas, are better diffracted than atoms with non zero velocity away from the center. This is a systematic effect that leads to an underestimate of the number of atoms from  $-7/2$ . The feature is taken into account in figure (b). The inset shows the velocity dependence of the efficiency of the momentum transfer, which is inferred from

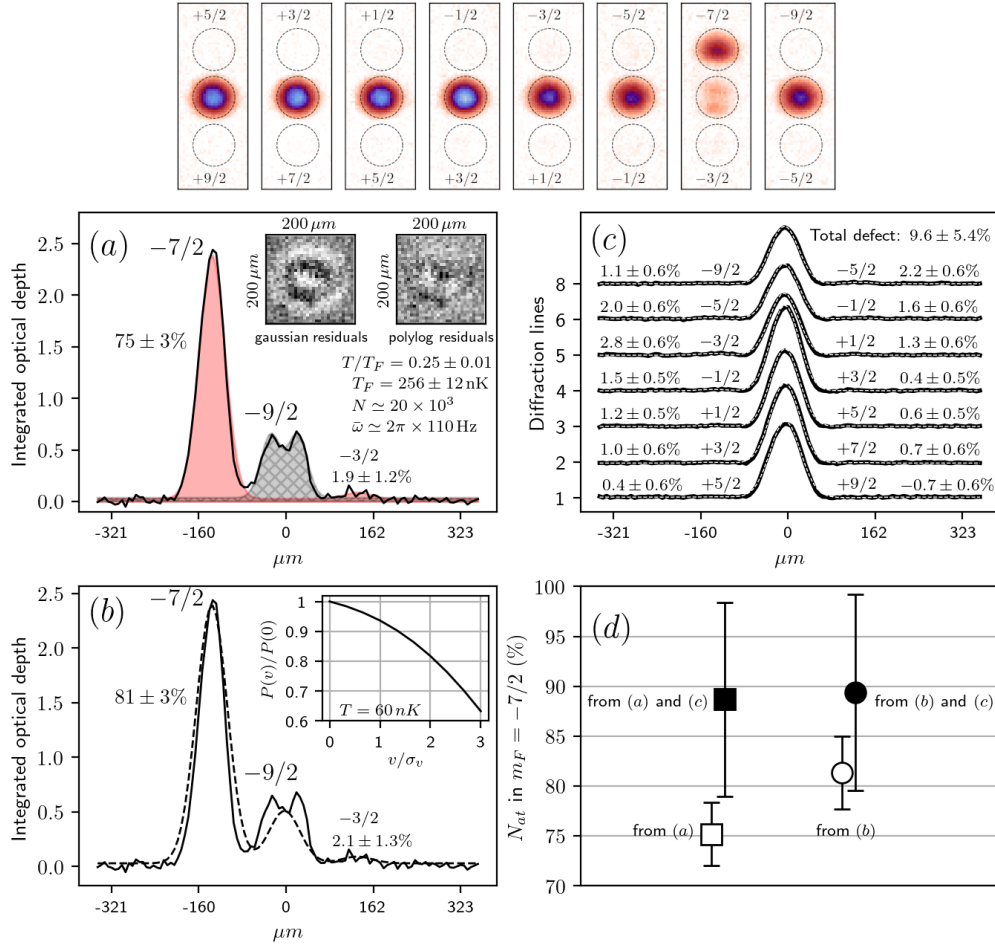


Figure 3.16: Measurement of the spin polarization after preparation of a polarized Fermi sea in  $m_F = -7/2$ . Top: absorption images of each diffraction line, the labels correspond to the spins expected at location indicated by the dashed circles. (a) Fit of the  $|-7/2\rangle \leftrightarrow |-3/2\rangle$  diffraction line (solid line) with the sum of gaussian distributions. Inset: residuals of thermal (left) and degenerate (right) fits of a non diffracted polarized Fermi sea. (b) Expected density profile (dashed-line), accounting for the velocity  $v$  dependent efficiency  $P(v)$  of the spin-dependent momentum transfer (see inset). (c) Integrated optical depths of the other diffraction lines with indicated fraction of diffracted atoms. (d) Measured number of atoms in  $-7/2$  (empty square), accounting for the velocity dependent efficiency (empty circle), and calibrated by the total fraction of diffracted atoms (filled square and circle).

numerical integration of hamiltonian [3.1](#) accounting for an opposite doppler shift on the  $\sigma_+$  and  $\sigma_-$  photons. The number of atoms in  $-7/2$  is then measured by accounting only for atoms at rest, *i.e.* the peak density of the diffracted cloud, and the density at  $v = 0$  for the non diffracted cloud. On figure (b), the dashed line indicates the expected density profile by neglecting the velocity dependence. With this correction, we infer  $81 \pm 3\%$  diffracted atoms from  $-7/2$ . These two results are finally calibrated by taking into accounts the atoms detected in the other spin states (see figure (c)), and we find  $89.5 \pm 10\%$ . Figure (d) reports the result of our measurements: accounting only for the detected atoms in  $-7/2$  (empty square), with the correction of the velocity sensitivity (empty circle), and calibrated by the efficiency of the diffraction measurement (respectively filled square and circle).

Finally, the degeneracy of the gas is measured from a non diffracted gas prepared in the same conditions, with a fit of the absorption images with a degenerate density distribution [KZ08](#) (see residuals and fit result in inset of figure [3.16](#), (a)), and we measure  $T \simeq 0.25 T_F$ ,  $T_F \simeq 250$  nK with approximately 20 000 atoms.

This finally shows that we are able to prepare a degenerate polarized Fermi gas of  $^{87}\text{Sr}$  at  $T/T_F \simeq 0.25$  with  $20 \times 10^3$  atoms, and we estimate that  $89.5 \pm 10\%$  atoms are in the same spin state  $|-7/2\rangle$ . Therefore our measurement is compatible with a 99% SU(1) degenerate Fermi gas.

# Chapter 4

## Coherent manipulation of the nuclear spin states of $^{87}\text{Sr}$

The ground state  $^1S_0$  of fermionic  $^{87}\text{Sr}$  has an electronic closed-shell. As mentioned in chapter 3, it is not practical to use magnetic fields to manipulate the 10 degenerate ground spin states. In the prospect of studying the Heisenberg model in enlarged  $\text{SU}(N)$  symmetry, we rely on spin-orbit coupling and spin resolved Raman transitions to coherently probe and manipulate the spins with light. To do this, we take advantage of spin dependent light shifts.

The bosonic isotopes of strontium have zero nuclear spin and  $J=0$  in the ground state, and hence no hyperfine structure. However, one of the most interesting properties of fermionic  $^{87}\text{Sr}$  is the hyperfine coupling between total momentum  $J$  and the large nuclear spin  $I = 9/2$  in excited states. For instance, the excited state  $^3P_1$  with non-zero momentum  $J$  is split into 3 hyperfine states  $F = 7/2, 9/2, 11/2$ , which are all separated by more than 1 GHz. These three hyperfine states are highly resolved compared to the narrow linewidth  $\Gamma/2\pi = 7.4\text{ kHz}$  of the optical transitions. Therefore, the dynamic polarizability associated with the intercombination line can acquire a significant and tunable spin dependence [Shi+15], so called tensor polarizability [MOR86], with low spontaneous emission. While experiments for optical lattice clocks take specific care of minimizing spin dependent light shifts [Boy07; Lud08] on alkaline earth species to prevent perturbations on the clock frequencies, degenerate gases experiments can take

advantage of the tensor polarizability. It has been demonstrated on both strontium [SGS11] and ytterbium [Tai+10] that spin components can be separated using conservative spin dependent forces, enhancing the study potential of many-body physics in enlarged  $\text{SU}(N)$  symmetry [CHU09; Gor+10; Tai+12].

In our experiment, we use a *dressing* laser beam that realizes spin dependent light shifts associated with the intercombination line of  $^{87}\text{Sr}$ , so that the degeneracy of Raman transitions within the ground state spin manifold is lifted. Then, we selectively and coherently flip chosen nuclear spin states with two photon Raman process, with one photon from the *dressing beam*, and a one photon from another laser, that I call *Raman beam* in this chapter, and whose frequency is adiabatically swept through the selected Raman resonance. Designed as a dipolar optical lattices, the spin dependent light shifts are then associated with a spatial selectivity that can be tailored at the optical wavelength scale. Therefore, the Raman process acquire a site dependence, that can be used to prepare, and detect, spin textures into lattices. In the prospect of the realization of a quantum simulator for Heisenberg model, this scheme enables the possibility to probe long range spin ordering, and to detect spin entanglement [Tai+20; Sun+21].

The basics of the tensor polarizability and the derivation of the quadratic light shift, as well as the associated scattering rate, are well known results that are first recalled in this chapter. We measured the quadratic light shift with Raman spectroscopy, and results are compared to predictions. Then, I show how we manipulate the ground spin states, taking advantage of the tensor polarizability to engineer spin selective adiabatic passages within the 10 spins ground state manifold of  $^{87}\text{Sr}$ . Finally I discuss the short-term prospect of associating spatial selectivity to the spin dependent light shift, to prepare spin textures into lattices with site dependent adiabatic passages.

## 4.1 Degeneracy lift associated with spin dependent light shift

### 4.1.1 Tensor dynamic polarizability

The rotational invariance of AC Stark shift can be broken for atoms which have fine and hyperfine structures, and in this case, the polarizability can acquire a dependence on the zeeman sub-levels  $m_F$ . Here, I will focus on the main steps to summarize the derivation of the irreducible tensor components of the atomic polarizability  $\alpha$  in order to expand the spin-dependant light shifts in terms of a scalar component, independent on  $m_F$ , a vector component, linearly dependent on  $m_F$ , and a tensor component, quadratically dependent on  $m_F$ . This well-known result can already be found in several publications and pedagogical contents. [MOR86; Ovs+06; Shi+15]. A clear and interesting introduction to the angular momentum algebra and spherical tensors can be found in [Wal21], which are explicitly used for the following derivations.

The interaction between the atom electric dipole  $\hat{\mathbf{D}}$  and the classic monochromatic light field  $\mathbf{E}$  of angular frequency  $\omega_l$ ,  $\mathbf{E} = \frac{1}{2}\boldsymbol{\epsilon}|\mathbf{E}|e^{i(\omega_l t - \phi)} + c.c.$ , is described by the electric dipole potential operator  $\hat{U}_{dip}$ :

$$\hat{U}_{dip} = -\frac{1}{4}\hat{\alpha}|\mathbf{E}|^2 \quad (4.1)$$

where  $\alpha$  is the polarizability operator. We are interested in the magnetic dependence of the polarizability  $\langle m_1 | \hat{\alpha} | m_2 \rangle$ , where  $|m_1\rangle$  and  $|m_2\rangle$  are Zeeman sub-levels of the ground state  $^1S_0$ . In second order perturbation theory,  $\alpha$  reads:

$$\hat{\alpha} = \frac{1}{\hbar} \sum_{|\phi'\rangle} \frac{\boldsymbol{\epsilon}^* \cdot \hat{\mathbf{D}} |\phi'\rangle \langle \phi' | \boldsymbol{\epsilon} \cdot \hat{\mathbf{D}}}{\omega_{\phi'} - \omega_l} + \frac{\boldsymbol{\epsilon} \cdot \hat{\mathbf{D}} |\phi'\rangle \langle \phi' | \boldsymbol{\epsilon}^* \cdot \hat{\mathbf{D}}}{\omega_{\phi'} + \omega_l} \quad (4.2)$$

where  $\hbar$  is the reduced Planck constant. Here,  $|\phi'\rangle = |n'L'S'J'F'm'\rangle$  are the excited states, and  $\boldsymbol{\epsilon}$  is the polarization of the electric field. In the spherical basis of unit vectors  $\mathbf{u}_q^*$ , defined as  $\mathbf{u}_{\pm 1} = \mp(\mathbf{x} \pm i\mathbf{y})/\sqrt{2}$ ,  $\mathbf{u}_0 = \mathbf{z}$ , with  $\mathbf{u}_q = (-1)^q \mathbf{u}_{-q}^*$ , the electric dipole operator  $\hat{\mathbf{D}} = -e\hat{\mathbf{R}}$  can be expanded as a linear combination of spherical harmonics

$\mathcal{Y}_l^m$  [Wal21]:

$$\hat{\mathbf{D}} = \sum_q -e|\mathbf{r}|\sqrt{\frac{4\pi}{3}}\mathcal{Y}_1^q\mathbf{u}_q^* \quad (4.3)$$

This is enough to show that  $\hat{\mathbf{D}}$  is a spherical tensor  $T^k$  of rank  $k = 1$ , with three standard components  $T_{kq}$ ,  $q = 0, \pm 1$ . It is then possible to apply the Wigner-Eckart theorem on the electric dipoles  $D_1(|m_1\rangle, |\phi'\rangle) = \langle m_1 | \epsilon^* \cdot \hat{\mathbf{D}} | \phi'\rangle$  and  $D_2(|\phi'\rangle, |m_2\rangle) = \langle \phi' | \epsilon \cdot \hat{\mathbf{D}} | m_2\rangle$ :

$$\begin{aligned} D_1(m_1, \phi') &= \sum_{q_1} (\epsilon^* \cdot \mathbf{u}_{q_1}^*) (-1)^{F_1 - m_1} \langle F_1 || D || F' \rangle \begin{pmatrix} F_1 & 1 & F' \\ -m_1 & q_1 & m' \end{pmatrix} \\ D_2(\phi', m_2) &= \sum_{q_2} (\epsilon \cdot \mathbf{u}_{q_2}^*) (-1)^{F_2 - 1 + m'} \langle F' || D || F_2 \rangle \begin{pmatrix} F_2 & 1 & F' \\ m_2 & q_2 & -m' \end{pmatrix} \end{aligned} \quad (4.4)$$

where the angular dependence is contained into the Wigner-3j symbols. Here,  $F_i$  and  $F'$  are the hyperfine states associated with the  $|m_i\rangle$ ,  $i = 1, 2$ , Zeeman sub-levels and the excited state  $|\phi'\rangle$ . The double bar matrix elements  $\langle F_1 || D || F' \rangle$  and  $\langle F' || D || F_2 \rangle$  are the reduced dipole matrix elements which do not depend on  $m_1$ ,  $m_2$  or  $m'$ .

The product of the two spherical tensors  $D_1$  and  $D_2$  of rank  $k_1$  and  $k_2$  can be expanded as the sum of irreducible tensor operators of integer ranks  $|k_1 - k_2| \leq k \leq k_1 + k_2$ . This can be done either by expanding the product of Wigner-3j symbols over  $m'$  using sum rules for angular momentum, or by identically expanding the product of the two uncoupled spherical tensors in a direct sum of irreducible tensors [Wal21]. Practically, these irreducible tensor operators have rank  $k = 0, 1, 2$  in the case of the combination of two electric dipole operators. The result of the expansion takes the simple form [MOR86; Ovs+06; Shi+15]:

$$\langle m_1 | \hat{\alpha} | m_2 \rangle = \sum_{k=0}^2 \alpha_k(\omega_l) \sum_{q=-k}^k (-1)^q \mathcal{C}_{Fm_2, kq}^{Fm_1} \{\epsilon \otimes \epsilon^*\}_{kq} \quad (4.5)$$

where  $\{\epsilon \otimes \epsilon^*\}_{kq} = \sum \mathcal{C}_{1q_1, 1q_2}^{kq} \epsilon_{q_1} \epsilon_{q_2}^*$  [MOR86], and  $\epsilon_q = \mathbf{u}_q^* \cdot \epsilon$ . Here,  $q_1$  and  $q_2$  are the projections in the spherical basis of the standard components of the electric dipole operator, as defined in equation 4.3. The  $\mathcal{C}$  symbols are the Clebsch-Gordan coefficients

defined as  $\mathcal{C}_{j_1 q_1, j_2 q_2}^{kq} = \langle j_1 q_1, j_2 q_2 | kq \rangle$ . This approach allows to isolate the contributions from the different physical components. Indeed, the polarization dependence is entirely contained in the tensor  $\{\boldsymbol{\epsilon} \otimes \boldsymbol{\epsilon}^*\}_{kq}$ , the magnetic dependence in the Clebsch-Gordan coefficient  $\mathcal{C}_{F m_2, kq}^{F m_1}$ , and the light angular frequency in the tensor component  $\alpha_k(\omega_l)$  of the dynamic polarizability, which reads [MOR86; Ovs+06; Shi+15]:

$$\alpha_k(\omega_l) = \frac{1}{\hbar} \sqrt{\frac{2k+1}{2F+1}} \sum_{n'} \sum_{F'=F-1}^{F+1} (-1)^{k-F-F'} \left( \frac{1}{\omega_{\phi'} - \omega_l} + \frac{(-1)^k}{\omega_{\phi'} + \omega_l} \right) \left\{ \begin{matrix} F & F & k \\ 1 & 1 & F' \end{matrix} \right\} |\langle nF || D || n'F' \rangle|^2 \quad (4.6)$$

where the bracket symbols are the Wigner-6j symbols. Two useful examples with purely polarized light illustrate the efficiency of this approach.

If the light is  $\pi$  (linearly) polarized, such that  $\boldsymbol{\epsilon} = \mathbf{u}_0^* = \boldsymbol{\epsilon}^*$ , then  $\{\boldsymbol{\epsilon} \otimes \boldsymbol{\epsilon}^*\}_{kq}$  is non zero only if  $q = 0$ . In this case the momentum conservation rules impose  $m_1 = m_2 = m$ , which makes sense for purely polarized light, and parity rules impose that  $k$  is even, else  $\mathcal{C}_{10,10}^{k0} = 0$ . Thus, the polarizability matrix elements can be written as following [MOR86; Shi+15]:

$$\langle m | \hat{\alpha} | m \rangle \Big|_{\pi} = \mathcal{C}_{F m 0 0}^{F m} \mathcal{C}_{10 10}^{00} \alpha_0(\omega_l) + \mathcal{C}_{F m 2 0}^{F m} \mathcal{C}_{10 10}^{20} \alpha_2(\omega_l) \quad (4.7)$$

$$\langle m | \hat{\alpha} | m \rangle \Big|_{\pi} = -\frac{1}{\sqrt{3}} \alpha_0(\omega_l) - \sqrt{\frac{2}{3}} \frac{3m^2 - F(F+1)}{\sqrt{F(F+1)(2F-1)(2F+3)}} \alpha_2(\omega_l) \quad (4.8)$$

The polarizability matrix elements are now reduced to a sum of two terms, as seen on the right hand side. The first term is independent of the magnetic sub-levels, depending only on the scalar component of the dynamic polarizability, while the second term is quadratically dependent on the magnetic sublevels. This first result shows that if the tensor component of rank 2  $\alpha_2(\omega_l)$  is non zero, then the dynamic polarizability acquires a dependence in the magnetic sub-levels, and for pure  $\pi$  polarized electric field, this dependence is quadratic.

If the light is  $\sigma_{\pm}$  (circularly) polarized, such that  $\boldsymbol{\epsilon} = \mathbf{u}_{\pm 1}^*$ , i.e.  $\boldsymbol{\epsilon}_{\pm 1}^* = -\boldsymbol{\epsilon}_{\mp 1}$ , then again  $\{\boldsymbol{\epsilon} \otimes \boldsymbol{\epsilon}^*\}_{kq}$  is non zero only if  $q = 0$ , and momentum conservation rules impose

$m_1 = m_2 = m$ . But  $k$  only needs to respect triangle inequality in  $\mathcal{C}_{1\pm 1, 1\mp 1}^{k0}$ , such that rank 1 irreducible tensor of polarizability expansion is not obviously zero. In this case, the polarizability matrix elements read:

$$\langle m | \hat{\alpha} | m \rangle \Big|_{\sigma_{\pm}} = \mathcal{C}_{Fm00}^{Fm} \mathcal{C}_{1\pm 1, 1\mp 1}^{00} \alpha_0(\omega_l) + \mathcal{C}_{Fm10}^{Fm} \mathcal{C}_{1\pm 1, 1\mp 1}^{10} \alpha_0(\omega_l) + \mathcal{C}_{Fm20}^{Fm} \mathcal{C}_{1\pm 1, 1\mp 1}^{20} \alpha_2(\omega_l) \quad (4.9)$$

$$\langle m | \hat{\alpha} | m \rangle \Big|_{\sigma_{\pm}} = \frac{1}{\sqrt{3}} \alpha_0(\omega_l) \mp \alpha_1(\omega_l) m \frac{1}{\sqrt{2F(F+1)}} + \frac{1}{2} \sqrt{\frac{2}{3}} \frac{3m^2 - F(F+1)}{\sqrt{F(F+1)(2F-1)(2F+3)}} \alpha_2(\omega_l) \quad (4.10)$$

Finally, let's consider an electric field with mixed polarizations, for instance  $\pi + \sigma_+$ , *i.e.*  $\boldsymbol{\epsilon} = (\mathbf{u}_0^* + \mathbf{u}_+^*)\sqrt{2}$  and  $\boldsymbol{\epsilon}^* = (\mathbf{u}_0 - \mathbf{u}_-)\sqrt{2}$ . In this case,  $\{\boldsymbol{\epsilon} \otimes \boldsymbol{\epsilon}^*\}_{kq}$  can be non zero for all four possible 2 photon process involving  $\pi$  and  $\sigma_+$  photons, which corresponds to  $(q_1, q_2)$  pairs  $(0, 0)$ ,  $(1, -1)$ ,  $(1, 0)$  and  $(0, -1)$ . The two first possibilities correspond to absorption and reemission of a photon with same polarization, which is exactly the two first introduced examples with pure polarized light. However, the  $(1, 0)$  and  $(0, -1)$  pairs respectively correspond to absorption of a  $\pi(\sigma_+)$  photon and reemission of a  $\sigma_+(\pi)$  photon. This coupling is actually a Raman two photon coupling, which is non diagonal in the Zeeman sub-levels basis and hence involves a basis rotation. The tensor polarizability acquires non diagonal components  $\langle m-1 | \hat{\alpha} | m \rangle$  for  $(q_1 = 1, q_2 = 0)$  and  $\langle m+1 | \hat{\alpha} | m \rangle$  for  $(q_1 = 0, q_2 = -1)$ , and selection rules respectively impose that  $q = 1$  or  $q = -1$  and hence  $k > 0$ . Finally, the new non-diagonal matrix elements of the tensor polarizability read:

$$\langle m-1 | \hat{\alpha} | m \rangle \Big|_{\pi+\sigma_+} = (\mathcal{C}_{Fm11}^{Fm-1} \mathcal{C}_{11,10}^{11} \alpha_1(\omega_l) + \mathcal{C}_{Fm21}^{Fm-1} \mathcal{C}_{11,10}^{21} \alpha_2(\omega_l))/2 \quad (4.11)$$

$$\langle m+1 | \hat{\alpha} | m \rangle \Big|_{\pi+\sigma_+} = (\mathcal{C}_{Fm1-1}^{Fm+1} \mathcal{C}_{10,1-1}^{1-1} \alpha_1(\omega_l) + \mathcal{C}_{Fm2-1}^{Fm+1} \mathcal{C}_{10,1-1}^{2-1} \alpha_2(\omega_l))/2 \quad (4.12)$$

Tensor polarizability is then completely defined from equations [4.7](#), [4.9](#), [4.11](#), and [4.12](#). Note that a factor 1/2 has to be added to the diagonal elements when summing

the  $\pi, \pi$  and  $\sigma_+, \sigma_+$  contributions, which comes from the  $1/\sqrt{2}$  normalization of the unit polarization of the electric field.

This shows that the polarizability matrix elements can be completely defined by Clebsch-Gordan coefficients and three parameters, which are commonly defined as the scalar  $\alpha_S$ , vector  $\alpha_V$  and tensor  $\alpha_T$  irreducible components of the polarizability, and usually obtained by rescaling  $\alpha_0, \alpha_1, \alpha_2$  [MOR86; Shi+15]:

$$\begin{aligned}\alpha_S &= \alpha_0 \frac{1}{\sqrt{3}} \\ \alpha_V &= \alpha_1 \sqrt{\frac{2F}{F+1}} \\ \alpha_T &= \alpha_2 \sqrt{\frac{2F(2F-1)}{3(F+1)(2F+3)}}\end{aligned}\tag{4.13}$$

One has to know the transition strength  $D_{\phi\phi'}^2 = |\langle nF || D || n'F' \rangle|^2$  to fully compute the dynamic polarizability. Extensive research on the characterization of the transition rates for atomic spectra has yielded an affluent database on atomic spectroscopy, for instance [SN10] and more recently [HS22] regarding strontium 87. It is then possible to determine the transition strength element from the transition angular frequencies  $\omega_{\phi\phi'}$ , oscillator strengths  $f_{\phi\phi'}$  [Lud08] and transition rates  $\Gamma_{\phi\phi'}$ :

$$\begin{aligned}\Gamma_{\phi\phi'} &= \frac{\omega_{\phi\phi'}^3}{3\pi\hbar\epsilon_0 c^3} D_{\phi\phi'}^2 \\ f_{\phi\phi'} &= \frac{2}{3} \omega_{\phi\phi'}^3 \frac{m}{\hbar e^2} D_{\phi\phi'}^2\end{aligned}\tag{4.14}$$

where  $m$  and  $e$  are the electron mass and charge.

### 4.1.2 Scattering rate

The scattering of photons can be modeled by the absorption of a photon from the laser field with angular frequency  $\omega_L$ , and the spontaneous emission of another photon. This two photon process connects to the continuum energy many-fold, which can be described by the Fermi golden rule to derive the scattering rate:

$$\Gamma_{m_i \rightarrow m_j} = \frac{2\pi}{\hbar} |\langle m_j | \hat{W} | m_i \rangle|^2 \rho(E = \hbar\omega_L) \quad (4.15)$$

where  $\hat{W}$  is the coupling between the ground states  $|m_i\rangle$  and  $|m_j\rangle$  with energies  $E_{m_j} = E_{m_i}$ , and  $\rho(E)$  the density of states of energy  $E$ . If the excited state connecting  $|m_i\rangle$  and  $|m_j\rangle$  is weakly populated, then the two photon effective coupling  $\hat{W}$  reads in second order perturbation theory:

$$\hat{W} = \frac{1}{2} |\mathbf{E}_L| |\mathbf{E}_v| \frac{1}{\hbar} \sum_{|\phi'\rangle} \frac{\boldsymbol{\epsilon}_v^* \cdot \hat{\mathbf{D}} |\phi'\rangle \langle \phi'| \boldsymbol{\epsilon}_L \cdot \hat{\mathbf{D}}}{\omega_{\phi'} - \omega_L} + \frac{\boldsymbol{\epsilon}_v \cdot \hat{\mathbf{D}} |\phi'\rangle \langle \phi'| \boldsymbol{\epsilon}_L^* \cdot \hat{\mathbf{D}}}{\omega_{\phi'} + \omega_L} \quad (4.16)$$

Here,  $\mathbf{E}_v(\mathbf{E}_L)$  stands for the electric field of the vacuum (laser) of polarization  $\boldsymbol{\epsilon}_v$  ( $\boldsymbol{\epsilon}_L$ ). Note that here we consider that the polarization of the excitation is  $\pi$ , so that the polarization of the spontaneous photon is well defined for a considered arrival state  $m_j$ . Injecting the effective two photon coupling into Fermi golden rule finally gives, after neglecting the anti-resonant term:

$$\Gamma_{m_i \rightarrow m_j} = \frac{3\pi\epsilon_0 \hbar c^3}{\omega^3} \frac{|\mathbf{E}_L|^2}{4} \frac{\Gamma_{nat}^2}{\hbar^2} \left| \sum_{|\phi'\rangle} \frac{(2F' + 1)}{\omega_{\phi'} - \omega_L} \begin{pmatrix} F & 1 & F' \\ m_j & m' - m_j & -m' \end{pmatrix} \begin{pmatrix} F & 1 & F' \\ m_i & 0 & -m' \end{pmatrix} \right|^2 \quad (4.17)$$

which can be rewritten with the Clebsch-Gordan coefficients

$$\Gamma_{m_i \rightarrow m_j} = \frac{3\pi\epsilon_0 \hbar c^3}{\omega^3} \frac{|\mathbf{E}_L|^2}{4} \frac{\Gamma_{nat}^2}{\hbar^2} \left| \sum_{|\phi'\rangle} \frac{\mathcal{C}_{Fm_j, 1m' - m_j}^{F'm'} \mathcal{C}_{Fm_i, 10}^{F'm'}}{\omega_{\phi'} - \omega_L} \right|^2 \quad (4.18)$$

This result for the scattering rate associated with small population of the excited state is actually known as the Kramers-Heisenberg formula [\[RF99\]](#). In our case, the polarisation of the laser electric field is pure  $\pi$ , *i.e.*  $\boldsymbol{\epsilon}_L = \mathbf{u}_0$ , and  $\Gamma_{nat}$  is the inverse life time of the excited states  $|\phi'\rangle$ .

The decay to the final state depends on the polarisation of the spontaneous emitted photon, such that the total scattering rate  $\Gamma_i = \sum_j \Gamma_{i \rightarrow j}$  from the initial spin state  $|m_i\rangle$  can be decomposed over the scattering to the three possible final states  $|m_i\rangle$  ( $|m_i \pm 1\rangle$ ) for a  $\pi$  ( $\sigma_{\mp}$ ) emitted photon. Scattering rate of  $m_F = +3/2$  for each polarization of the

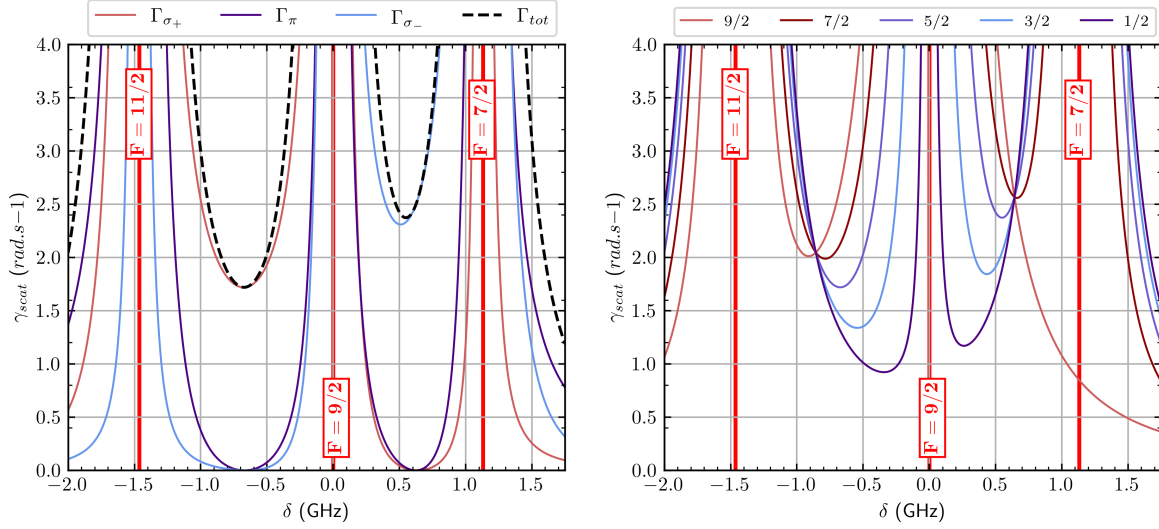


Figure 4.1: Calculated scattering rate as a function of the light frequency spanned within the hyperfine structure  $F=7/2, 9/2, 11/2$  of the  $^1S_0 \leftrightarrow ^3P_1$  transition. The scattering rate is calculated using experimental light parameters, which is a 6 mW gaussian laser beam with a waist of  $180 \mu\text{m}$  and polarization  $\pi$ . Left: scattering rate from  $m_F = +3/2$ , for each polarization of the spontaneously emitted photon, in dashed lines. The total scattering rate is plotted in solid black line. Right: total scattering rate for each zeeman sub-level. Here, only positive spin states are represented because  $\Gamma_{tot}$  is symmetric in  $m_F$ . On both figures, the red vertical solid lines are the hyperfine resonances.

spontaneous photon is plotted on figure 4.1, left, as well as the resulting total scattering rate. In this figure, the calculation is made with a  $\pi$  polarized light excitation, and the intercombination line  $^1S_0 \leftrightarrow ^3P_1, F = 9/2$  only is considered for the calculation.

As expected, the spin dependent scattering rate is maximum closer to resonance. There exist detuning values  $\delta$  such that the scattering process towards a specific final state, *i.e.* emitted photon polarisation, is canceled, as it can be seen when the scattering rate reaches zero. The sum over the hyperfine states  $F' = 7/2, F' = 9/2$ , and  $F' = 11/2$ , accounts for the different paths through those excited states leading from the initial state to the final state, and the probability for a scattering event to happen results from the interference between these different possible paths. This can be seen in equation

(4.18) from the sum over the excited states of  $\mathcal{C}_j\mathcal{C}_i/\delta$  which can be zero for specific  $\delta$ , depending on the coupling strengths  $\mathcal{C}_j\mathcal{C}_i$ , *i.e.* on  $|m_j\rangle$  and  $|m_i\rangle$ . However, this doesn't mean that the light scattering is canceled. Indeed, the total light scattering accounts for all possible scattering paths.

Since the polarization of the excitation is well defined, the final states associated with scattering are distinguishable and there are no interferences involved into the total scattering from one  $m_F$ , *i.e.*  $\Gamma_i = \sum_j \Gamma_{i \rightarrow j}$ . The total light scattering from each spin state is plotted on figure 4.1, right, and it can be seen that indeed it is never zero for any frequency of the light excitation.

### 4.1.3 Tensor light shift associated with the intercombination line

Tensor light shifts can be easily computed numerically from equation 4.5, given that the transition strength defined in equation 4.14 is known. If the transition is not closed, *e.g.* if the lower state has fine or hyperfine structure, then the branching ratios of the transitions have to be taken into account [Lud08; Shi+15]. Regarding the intercombination line of  $^{87}\text{Sr}$ , the excited state  $^3P_1$  can decay only to the ground state  $^1S_0$ . Hence, the radiative decay rate of the excited state  $\Gamma_{^3P_1}$  gives the  $L - L'$  transition strength:

$$\Gamma_{^3P_1} = \frac{\omega_0^3}{3\pi\hbar\epsilon_0c^3} D_{L,L'}^2 \quad (4.19)$$

where  $L = 0$  and  $L' = 1$ . Here, the hyperfine structure is not accounted for, and the branching ratios are needed to write the transition strength in the hyperfine coupled basis [MS99; Wal21]:

$$D_{F,F'}^2 = (2L' + 1)(2F + 1)(2F' + 1)(2J + 1)(2J' + 1) \begin{Bmatrix} J' & 1 & J \\ L & S & L' \end{Bmatrix} \begin{Bmatrix} F' & 1 & F \\ J & I & J' \end{Bmatrix} D_{L,L'}^2 \quad (4.20)$$

and it finally reads:

$$|\langle F || D || F' \rangle|^2 = \Gamma_{^3P_1} \frac{3\pi\hbar\epsilon_0c^3}{\omega_0^3} (2L'+1)(2F+1)(2F'+1)(2J+1)(2J'+1) \begin{Bmatrix} J' & 1 & J \\ L & S & L' \end{Bmatrix} \begin{Bmatrix} F' & 1 & F \\ J & I & J' \end{Bmatrix} \quad (4.21)$$

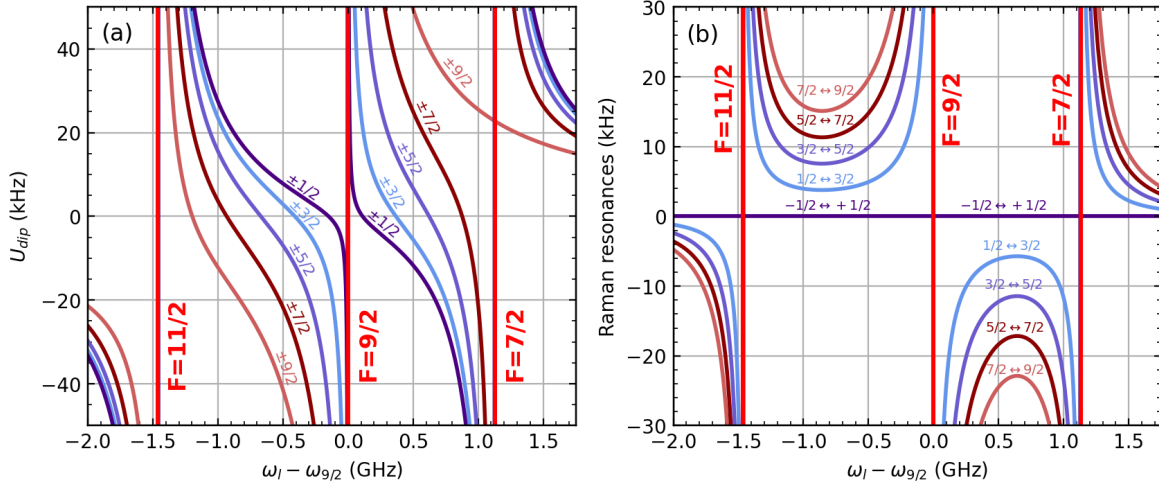


Figure 4.2: (a) Calculated light shifts as a function of the light frequency spanned within the hyperfine structure  $F=7/2, 9/2, 11/2$  of the  $^1S_0 \leftrightarrow ^3P_1$  transition, for each spin state of the ground state manifold. The  $m_F$  spin states are noted above the corresponding solid lines. The spin dependent light shift is calculated using experimental light parameters, which is a 6 mW gaussian laser beam with a waist of  $180 \mu\text{m}$  and polarization  $\pi$ . (b) Degeneracy lift of the  $m_F \leftrightarrow m_F \pm 1$  Raman resonances within the ground state manifold, computed as  $U_{dip}(m_F) - U_{dip}(m_F \pm 1)$ . The corresponding spin states are noted above the curves. On both figures, the red vertical solid lines are the hyperfine resonances.

Now, the tensor polarizability associated with the intercombination line can be computed for a defined polarization of the electric field, from equations [4.5](#), [4.6](#) and [4.21](#). Figure [4.2](#) (a) shows a numerical computation of spin dependent light shifts within the ground state manifold  $^1S_0$  with  $\pi$  light, with respect to the detuning to the  $^1S_0 \leftrightarrow ^3P_1, F = 9/2$  transition, within second order perturbation theory. Because the approximation  $\delta \gg \Gamma_{3P_1}$  has been made, the calculated light shifts diverge close to the resonance with each hyperfine state. However, it is interesting to see that for every spin state, the dipole force goes from attractive to positive, when the light frequency goes from the  $F = 9/2$  to  $F = 11/2$  resonance. Moreover, a light detuned at approximately  $-700$  MHz from  $F = 9/2$  highlights the spin dependence of the dipole potential, where half the spins are attracted and the other half expelled by the potential. Practically, figure [4.2](#) (a) shows that with those parameters, it is possible to expell all spin states

but  $+9/2$  and  $-9/2$  with  $\omega_l - \omega_{9/2} \simeq -1.1$  GHz, effectively preparing a  $\text{SU}(2)$   $^{87}\text{Sr}$  gas, similarly to [Son+20]. The opposite can also be realized by setting the light frequency at  $\omega_l - \omega_{9/2} \simeq +1$  GHz, preparing a  $\text{SU}(8)$  gas. The resulting energy splits between the  $m_F$  ground states are plotted with respect to the angular frequency of the light on figure 4.2 (b). The energy differences are rather uniform when the light frequency is tuned in the middle of two hyperfine states, while close to resonance the spectral resolution diverges for all the  $|m_F\rangle \leftrightarrow |m_F + 1\rangle$  opened gaps.

Most importantly, we see here that because of the spin-dependent light shift, the ground state manifold acquires spectrally resolved  $|m_F\rangle \leftrightarrow |m_F \pm 1\rangle$  transitions. With only a scalar or linear dependence on the Zeeman sub-levels, all the transitions would be resonant. This means that only thanks to the quadratic spin dependence of the tensor light shift, two photon Raman transitions can be used to selectively couple two ground spins states. For pure  $\pi$  polarized light, this lifted degeneracy can be easily written as :

$$\alpha(m_F + 1) - \alpha(m_F) = \frac{-3\alpha_T}{F(2F - 1)}(2m_F + 1) \quad (4.22)$$

according to equations 4.8 and 4.13, where  $\alpha(m_F) = \langle m_F | \hat{\alpha} | m_F \rangle$ . Hence, a quadratic spin dependent light shift results in linear spin dependent  $|m_F\rangle \leftrightarrow |m_F \pm 1\rangle$  Raman resonances. Increasing the spectral resolution of the Raman resonances by tuning the light close to resonance also increases the scattering rate as shown in figure 4.1, not only heating the atoms but also enhancing spin relaxation and decoherence. It should be noticed that close to the  $F = 9/2$  resonance, stretched states have highest polarizability, resulting in maximal light scattering and energy shifts for these spin states, while close to the  $F = 11/2$  resonance, the minimally magnetic spins, *i.e.* minimal  $|m_F|$ , are the most shifted and scattering spin states. The competition between light shift and light scattering thus has non trivial spin dependence. This competition can be looked at by comparing the energy difference between two successive spin states, to the mean of the scattering rate of these two states. The ratio of these two quantities is plotted in figure 4.3, and it shows that optimal light frequency tuning might exist to maximize the degeneracy light while minimizing scattering rate, and this result highly depends

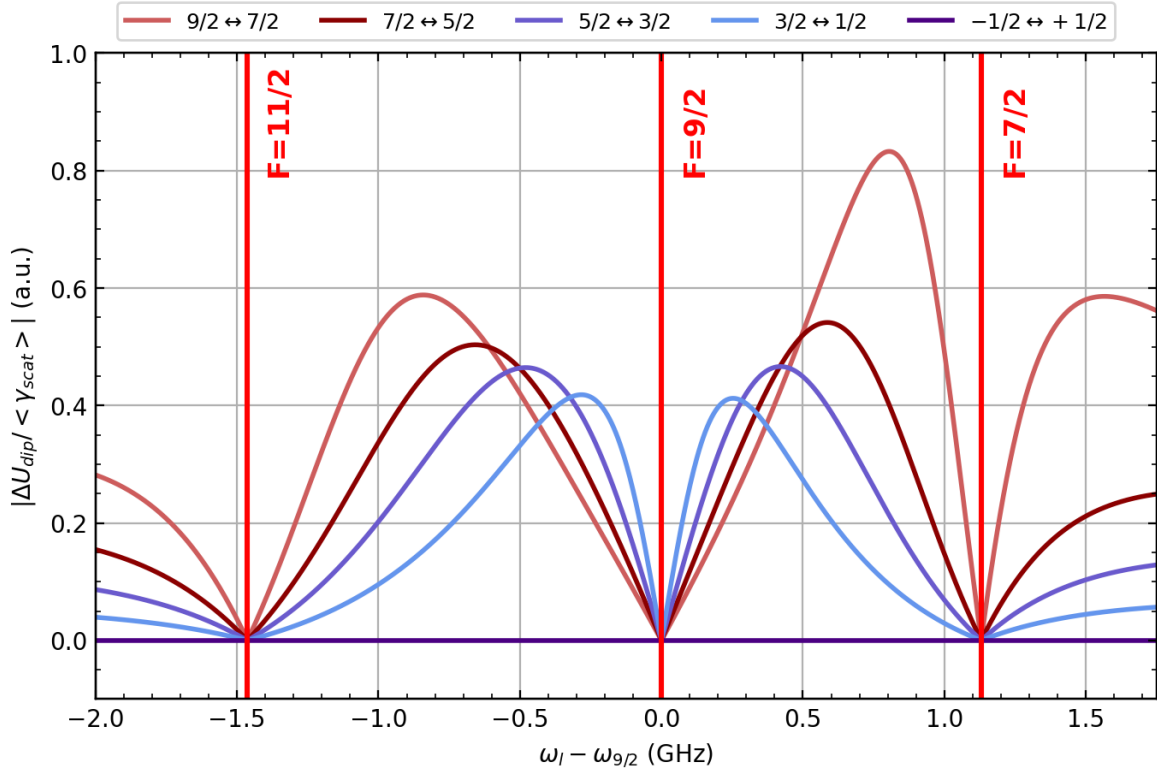


Figure 4.3: Calculated degeneracy lift of Raman resonances within the  $^1S_0$  manifold, over spin dependent scattering rate, computed as the mean over the two connected spin states, as a function of the frequency of near resonant light field spanned within the hyperfine structure of the  $^3P_1$  state. The red vertical solid lines are the hyperfine resonances. This calculation is made with our experimental parameters

on the spin-spin transitions. This has non negligible consequences on the choices of experimental schemes to realize spin swaps by efficient adiabatic passages.

The predictions for the tensor light shift associated with the intercombination line of  $^{87}\text{Sr}$  are well characterized, as well as for the associated scattering rate. We are now interested in the experimental realization and measurements of the tensor light shifts associated with the intercombination line of  $^{87}\text{Sr}$ .

## 4.2 Engineering the degeneracy lift of $^{87}\text{Sr}$ ground state manifold

### 4.2.1 Experimental design

To realize spin dependent light shifts on the experiment, we use a dedicated laser setup presented in figure [4.4](#). The laser head is made of a diode with extended cavity, and it is beat-locked onto our Master red laser. By setting the frequency for the beat signal, it is possible to tune the frequency of the laser beam within a 1 GHz wide frequency window centered on the  $F = 9/2$  hyperfine resonance. For the experiment, we use two double pass acousto-optical modulators, such that we can tune independently the frequencies of two laser beams. The RF frequencies for the two AOMs derive from two direct digital synthesizers (DDS) which share the same clock and are therefore phase coherent. The first one is used to realize the spin dependent light shift, which I will call *dressing beam* for simplicity. The second beam is used to flip the spins with a two photon process together with the first beam, and I will call this laser beam *Raman beam*. Before interacting with the atoms, the dressing and Raman beams are superimposed with a beam-splitter, and the outgoing electric fields of the two beams are orthogonal. The quantization axis can be chosen collinear with the dressing beam wave vector, such that in this frame the electric field of the Raman laser is  $\sigma_+ + \sigma_-$  polarized. To do this, we set the power of the Raman beam one thousand time weaker than the dressing beam. This way, it is possible to realize well defined  $|m_F\rangle \leftrightarrow |m_F \pm 1\rangle$  two photon Raman transitions with one  $\pi$  photon from the dressing beam, and one  $\sigma_{\pm}$  photon from the Raman beam. The Raman beam has the same waist than the dressing beam, *i.e.*  $180\ \mu\text{m}$ , at the location of the atoms. In this case, the relative intensities are equal to the relative powers.

### 4.2.2 Measurement of the spin dependent light shifts

We characterize the spin-dependent light shift by measuring the energy difference between two consecutive spins of the ground state manifold. This is done with a Raman spectroscopy after the tensor light shift is turned on, and our measurement shows that the resonances are separated by a quadratic light shift.

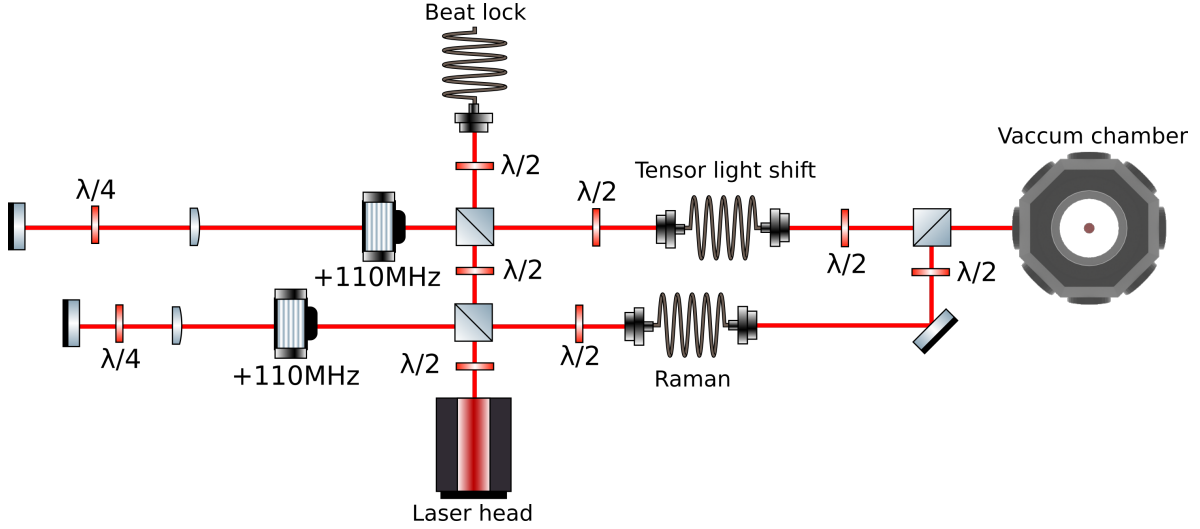


Figure 4.4: Dedicated laser setup for the spin dependent light shift and spin selective spin flips. This scheme is simplified for easy reading, only the main components are presented. Two acousto-optical modulators (AOM) in double passe configuration are used to independently tune the frequencies of the dressing beam and the Raman beam. A third path is used for beat lock onto the Master laser. The Raman and dressing beam are finally recombined before the vacuum chamber.

The measurement proceeds as follows. The gas is prepared in a spin polarized state, as presented in section 3.2.3 of chapter 3, after forced evaporation. Then, the homogeneous magnetic field is slowly rotated such that it is aligned with the linear polarization of the electric field of the dressing beam. This way, the polarization of the light is well defined and it is purely  $\pi$ . Then, the dressing beam is slowly turned to its maximum power  $P = 6 \text{ mW}$  within 2 ms. Now, the degeneracy of the ground state is lifted by the quadratic light shift. We then rely on Raman spectroscopy to find the  $|m_F\rangle \leftrightarrow |m_F \pm 1\rangle$  resonances by pulsing the Raman laser beam at different frequencies. The power of the Raman beam is set as low as possible, here  $5 \mu\text{W}$ , in order to narrow the measurement of the resonances, and the time of pulse at fixed frequency long enough, here 10 ms, to maximize the frequency resolution of the Raman spectroscopy.

The result of the experiment is shown on figure 4.5. Atoms are initially in  $m_F = -5/2$ , and the Raman detuning is scanned to find the  $|-5/2\rangle \leftrightarrow |-3/2\rangle$  and  $|-5/2\rangle \leftrightarrow$

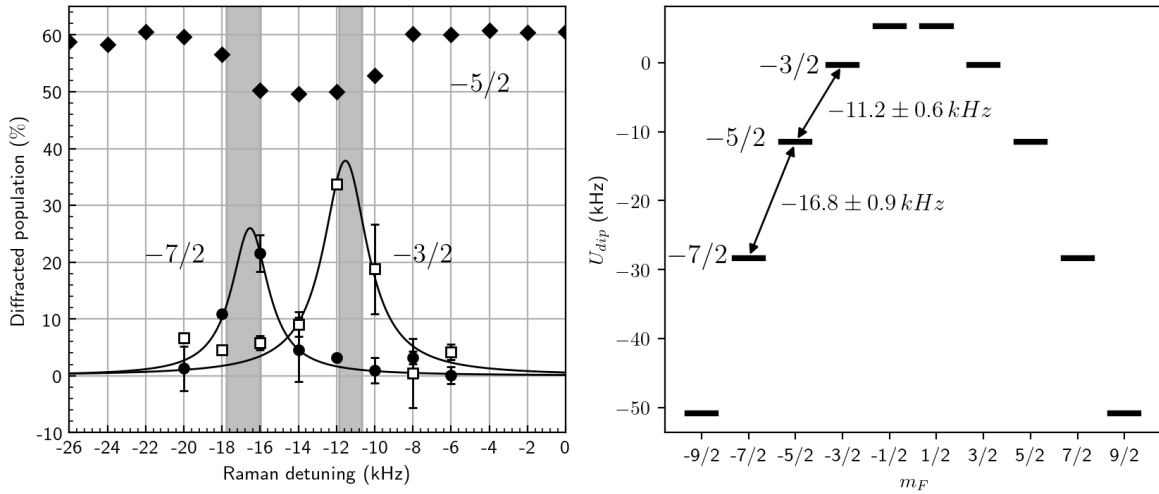


Figure 4.5: Left: Raman spectroscopy of the  $|-5/2\rangle \leftrightarrow |-5/2 \pm 1\rangle$  resonances, after degeneracy lift with quadratic light shift. Atoms are initially in  $m_F = -5/2$ , and the population transfer to  $m_F = -7/2$  and  $m_F = -3/2$  are measured with spin-dependent momentum transfer (see chapter 3). The solid lines are fits of each resonance with Lorentz functions (see equation 4.23). In this experiment, the dressing beam has measured power 6 mW and waist  $185 \pm 5 \mu\text{m}$  at the location of the polarized fermi sea, and the Raman beam has measured power  $5 \mu\text{W}$  and same waist. The filled regions correspond to the resonances prediction with experimental parameters and associated uncertainty on the waist  $185 \pm 5 \mu\text{m}$ . Right: calculated degeneracy lift of the ground state manifold with experimental parameters, and the two photon Raman transitions correspond to the ones measured.

$|-7/2\rangle$  resonances. The populations of the coupled spin states after the pulse are measured with the spin dependent momentum transfer technique presented on chapter 3. The populations are fitted with Lorentz functions:

$$L(f, A, f_0, \Gamma) = \frac{A}{1 + \left(\frac{f-f_0}{\Gamma/2}\right)^2} \quad (4.23)$$

and their centers  $f_0$  is found at  $-11.5 \pm 0.3 \text{ kHz}$  for the  $|-5/2\rangle \leftrightarrow |-3/2\rangle$  resonance and  $-16.5 \pm 0.3 \text{ kHz}$  for the  $|-5/2\rangle \leftrightarrow |-7/2\rangle$  resonance. This measurement confirms that the energy difference between two consecutive spin states is as expected for a quadratic light shift, see equation 4.22.

This result is compared to numerical prediction with experimental parameters, including the uncertainty on the waist measurement  $180 \pm 5 \mu\text{m}$ , which is shown as the filled region on the same figure, for each resonance. The computation predicts compatible resonances,  $-11.2 \pm 0.6 \text{ kHz}$  for the  $|-5/2\rangle \leftrightarrow |-3/2\rangle$  transition and  $-16.80 \pm 0.9 \text{ kHz}$  for the  $|-5/2\rangle \leftrightarrow |-7/2\rangle$  transition. The uncertainty comes only from the measurement of waist of the dressing beam. The degeneracy lift of the ground state manifold, numerically calculated, is plotted on figure 4.5, right, where we can see both the quadratic light shift, as well as the spin dependence of the energy gaps between two consecutive spin states. The whole spectrum is numerically computed with experimental parameters, as it can easily be inferred from the measurement of  $\alpha_T$ .

### 4.2.3 Measurement of the scattering rate

We are interested in the light scattering associated with the spin dependent light shift, as it is a limitation to the conservative spin manipulations. On the experiment, the scattering rate is characterized by measuring the heating rate associated with the spin dependent light shift. After preparing a cold gas of strontium with ten spin components, the dipole trap is recompressed to its maximum depth  $U_{dip} \simeq 65 \mu\text{K}$  and either the dressing beam or the Raman are pulsed, with detuning  $\Delta = -400 \text{ MHz}$  from the  $^3P_1, F = 9/2$  hyperfine state, and with respective powers  $P_D = 6 \text{ mW}$  and  $P_R = 6 \text{ mW}$ . Atoms acquire  $kT$  of heating energy during the light pulse, and the deep trap with  $U_{dip} \gg kT$  ensures that they don't leave the trap, so that all the energy acquired by the uncoherent scattering events is maintained into the gas. For each duration of pulse, the temperature of the gas is then measured after a time of flight, and the result of the experiment is shown on figure 4.6, left. It is compared to a witness heating rate measurement, which is done by realizing the same sequence without ever turning on the dressing nor the Raman beam, and that I call here *residual heating*. We suppose that this heating is due to mechanical vibrations of the optical dipole trap in which atoms are trapped during the measurement. Right figure shows the heating slope after removing the residual heating signal, and the heating rate associated with the spin dependent light shift is measured between  $220 \pm 10 \text{ nK.s}^{-1}.\text{mW}^{-1}$  and  $255 \pm 12 \text{ nK.s}^{-1}.\text{mW}^{-1}$  from the dressing beam and Raman beam respectively, assuming the same waist. Note that

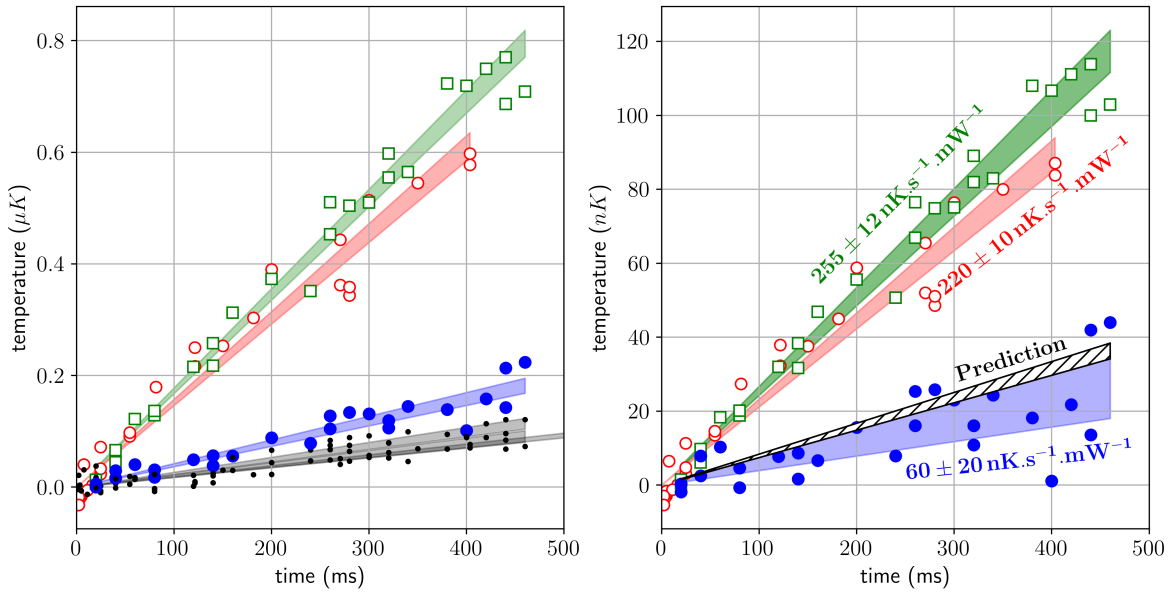


Figure 4.6: Measurement of the heating rate associated with the spin dependent light shift. For this measure, the detuning is set at  $\Delta = -400$  MHz from the  $^3P_1, F = 9/2$  hyperfine state. The heating rate of the Raman (empty squares) and dressing (empty dots) beams are compared to the residual heating (black dots), and to the same measurement after spectral mode filtering of the laser (blue filled dots). Left figure shows the straight measure of the gas temperature, with  $P_R = 6$  mW,  $P_D = 6$  mW and  $P_{cav} = 2.5$  mW. Right figure shows the same data normalized to the respective beam powers, and the slope of the residual heating has been removed. The prediction (hatched region) is computed according to equation [4.26](#) with waist  $185 \pm 5$   $\mu\text{m}$ .

the uncertainty doesn't take into account the power and waists measurements of the laser beams, only the fit covariance is given. Since the trap is recompressed, atoms are hot and dense enough such that the collision rate is much bigger than the scattering rate, so we can assume that the gas is always at equilibrium, hence the scattering rate can be inferred from heating rate as follows.

When an atom scatters photons, a two step process happens. The atom absorbs the photon of momentum  $\hbar\vec{k}_1$  from the coherent laser beam, then randomly emits another photon of momentum  $\hbar\vec{k}_2$  in any direction. The exchange of momenta between the atoms and the photons after a scattering event can be written as  $\delta\vec{p} = \hbar\vec{k}_2 - \hbar\vec{k}_1$ .

Assuming that the trapped 3D gas is at equilibrium  $\langle \vec{\delta p} \rangle = 0$  with temperature  $T$ , and no other process can be responsible for energy variations, then the time evolution of the kinetic energy of the gas  $E_K = 3k_B T/2$ , where  $k_B$  is the Boltzmann constant, is only due to the exchange of momenta  $\vec{\delta p}$  happening at rate  $\gamma_{scatt}$ , and it reads

$$\frac{dE_K}{dt} = \gamma_{scatt} \frac{\langle \delta p^2 \rangle}{2m} \Leftrightarrow \frac{3}{2} \frac{dk_B T}{dt} = \gamma_{scatt} \frac{\langle \delta p^2 \rangle}{2m} \quad (4.24)$$

where  $m$  is the mass of an atom. The spontaneous emission of a photon with random momentum  $\langle \vec{k}_{se} \rangle = 0$  implies that the absorption-emission processes are independent  $\langle \vec{k}_1 \vec{k}_2 \rangle = \langle \vec{k}_1 \rangle \langle \vec{k}_2 \rangle = 0$ , such that  $\langle \delta p^2 \rangle = 2(\hbar k_R)^2$  where  $\hbar k_R$  is the recoil momentum of a 689 nm photon. Therefore, the heating rate associated with the light scattering reads:

$$\frac{dk_B T}{dt} = \frac{2}{3} \gamma_{scat} E_R \quad (4.25)$$

where  $E_R = \hbar^2 k^2 / 2m$  is the recoil energy of a photon absorbed or emitted by a strontium atom. Finally the scattering rate can be deduced from the heating rate that is experimentally measured:

$$\gamma_{scat} = \frac{3}{2} \frac{d}{dt} \left( \frac{k_B T}{E_R} \right) \quad (4.26)$$

From the measured heating, we infer a scattering rate  $1.4 \pm 0.06 \text{ s}^{-1}$  for the Raman beam and  $1.7 \pm 0.08 \text{ s}^{-1}$  for the dressing beam, per 1 mW, *i.e.* approximately  $2.9 \text{ W/cm}^2$ . With the experimental parameters, the prediction of the scattering rate from equation [4.18](#), averaged over the 10 spin states, gives  $\langle \gamma_{scatt} \rangle_{m_F} \simeq 0.54 \text{ s}^{-1}$ , which is three times lower than our measurement. We explain our measurement of enlarged scattering by spectral imperfections of the diode generating the laser beam, resulting in amplified spontaneous emission (ASE) [\[SGS13\]](#).

To circumvent this issue, we added a Fabry-Perot cavity to our setup. After filtering the spectral mode of the laser diode, we measure a heating rate lowered to  $60 \pm 20 \text{ nK.s}^{-1} \cdot \text{mW}^{-1}$ , as shown on [4.6](#), corresponding to scattering rate  $0.39 \pm 0.12 \text{ s}^{-1} \cdot \text{mW}^{-1}$ . This result is in agreement with the prediction at the upper limit of

the uncertainty, which embeds only the fit covariance. This measurement is enough to show that the spectral mode of the laser is broadened, and after cavity filtering, the scattering rate associated with the tensor light shift is properly understood and predicted. Note that the cavity was not further used because of instability issues, and is presently being upgraded for persistent use.

#### 4.2.4 Spin depolarization

Our setup to engineer the spin dependent light shifts involves spin dependent couplings, notably the dressing beam and the quantization field. Hence, attention has to be paid to possible second order spin-spin couplings, which would allow spin rotations, and in the case of a polarized Fermi sea, result in depolarization. For instance, the electric-dipole operator resulting from the interaction of atoms with a dressing beam with not pure  $\pi$  polarization allows  $|m_F\rangle \leftrightarrow |m_F \pm 1\rangle$  couplings, as shown in equations [4.11](#) and [4.12](#). In this case, the spin eigenbasis is  $\text{SU}(N)$  rotated and the definition of the new eigenstates is not trivial, which is unwanted for proper understanding of our schemes.

To avoid these complications, it is possible to physically rotate the magnetic field such that the polarization of the electric field of dressing beam is well defined and purely  $\pi$ ,  $\sigma_+$  or  $\sigma_-$ . Is it particularly true if the dressing beam is linearly polarized and the magnetic field aligned with the direction of the polarization and in this case, the eigenstates are the same with or without dressing beam. In our experiment, we optimized the alignment of the magnetic field with the  $\pi$  polarized electric field as follows: we prepare a polarized Fermi sea, and for each rotation of the quantization field the dressing beam is pulsed at maximum power, then we measure the number of atoms remaining in the initial spin state.

### 4.3 Selective global manipulation of the spin states

In this section, I present our scheme to selectively and coherently flip the ground spin states of strontium 87. After lifting the degeneracy of the ground state manifold with a quadratic light shift, we take advantage of the resolved  $|m_F\rangle \leftrightarrow |m_F \pm 1\rangle$  transitions

to engineer selective adiabatic passages. With minimal spontaneous emission, we flip the spin of the atoms from their initial state to a well determined final spin state. With a measurement of the spin populations we infer 80% efficiency for the preliminary experiments. We finally compare our results with simulations.

### 4.3.1 Scheme overview

In our setup, the spin flips are induced by two photon adiabatic Raman passages. One photon of the Raman process comes from the dressing beam, with  $\pi$  polarization, while the second photon comes from the Raman beam, with either  $\sigma_+$  or  $\sigma_-$  polarization. Raman transitions can be engineered either with  $\pi + \sigma_-$  photons, or with  $\pi + \sigma_+$  photons, as presented on figure 4.7. Because of the quadratic degeneracy lift and selection rules, only one of the two polarizations of the Raman beam crosses a Raman resonance for one Raman detuning  $\delta = \omega_D - \omega_R$ . Hence, for each Raman transition, it is possible to choose either  $\pi + \sigma_+$  or  $\pi + \sigma_-$  two photon transition. Since we usually work with negative spin states because of our optical pumping scheme (see chapter 3), and since Clebsch-Gordan coefficients associated with  $\sigma_-$  transitions are stronger for negative spin states, we focus on the  $\pi + \sigma_-$  case only. Indeed, stronger Rabi couplings allow faster passages, which means that the time needed to engineer spin flips is lowered compared to typical time for light scattering, which is strongly favorable in presence of noise. In this case, the Raman resonances are crossed for  $\delta > 0$  for negative spin states and  $\delta < 0$  for positive spin states, as shown on figure 4.7.

### 4.3.2 Spectrum of the Raman transitions in the $^1S_0$ manifold

Now, I will discuss adiabatic passages in  $\Lambda$  scheme in the large spin states manifold. Let's consider the ground state manifold of  $^{87}\text{Sr}$  and its 10 spin states, coupled to two photon fields  $\mathbf{E}_\pi$ ,  $\mathbf{E}_{\sigma_-}$  with  $\pi$  and  $\sigma_-$  polarizations. To write the associated Hamiltonian, it is convenient to define the dressed state basis  $|m_F + n\rangle \equiv |m_F + n, N_\pi - n, N_\sigma + n\rangle$ , where  $N_\pi$  ( $N_\sigma$ ) is the number of photons in the field  $\mathbf{E}_\pi$  ( $\mathbf{E}_{\sigma_-}$ ), and  $n$  is integer. Each spin state  $|m_F\rangle$  is connected to  $|m_F \pm 1\rangle$  states by the  $\pi + \sigma_-$  two photon Raman process, with associated Raman detuning  $\delta = \omega_\pi - \omega_{\sigma_-}$ . Hence, in the absence of the quadratic degeneracy lift, each dressed state  $|m_F + n\rangle$  has energy  $n\delta$ .

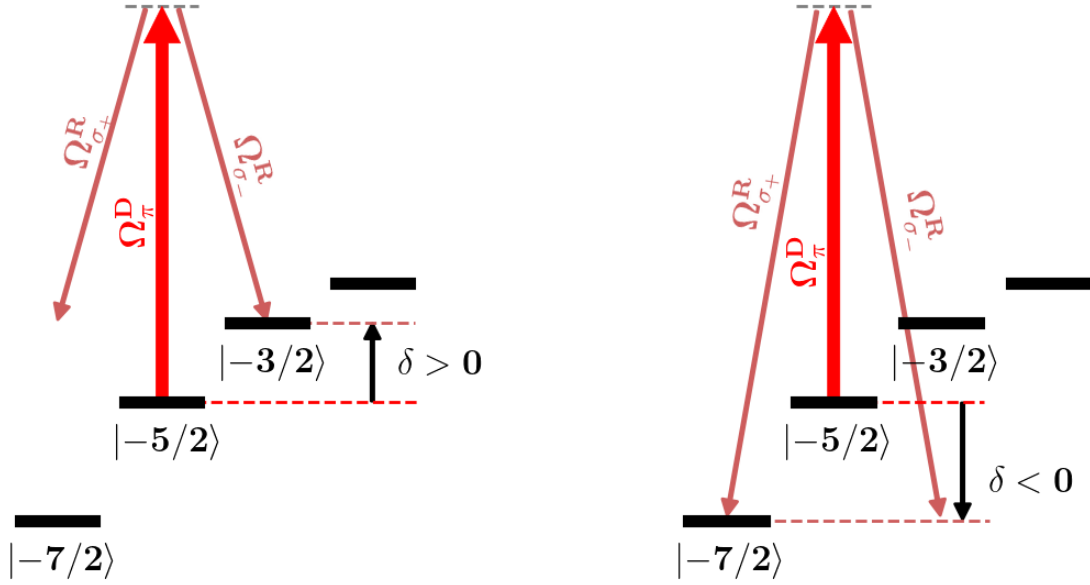


Figure 4.7: Scheme of Raman two photon couplings within the spin states manifold after quadratic degeneracy lift, within  $m_F < 0$  spin states. R and D letters above Rabi frequencies stand for Raman beam,  $\sigma_+ + \sigma_-$  polarized, and Dressing beam,  $\pi$  polarized. Left: positive detuning  $\delta = \omega_D - \omega_R > 0$ , such that negative spin states are coupled with  $\pi + \sigma_-$  photons. Right: negative detuning  $\delta = \omega_D - \omega_R < 0$ , such that negative spin states are coupled with  $\pi + \sigma_+$  photons.

Then, the off-diagonal couplings of the dressed Hamiltonian are effective two photon Raman couplings which can be computed from second order perturbation theory:

$$\frac{\hbar \Omega_{m_{F1}}^{m_{F2}}}{2} = |\mathbf{E}_{\pi}| |\mathbf{E}_{\sigma_-}| \sum_{|e\rangle} \frac{\langle m_{F2} | \boldsymbol{\epsilon}_{\pi}^* \cdot \hat{\mathbf{D}} | e \rangle \langle e | \boldsymbol{\epsilon}_{\sigma_-} \cdot \hat{\mathbf{D}} | m_{F1} \rangle}{\Delta_e} \quad (4.27)$$

where  $\Delta_e \simeq \omega_e - \omega_{\pi} \simeq \omega_e - \omega_{\sigma_-}$ . This approximation holds since the Raman detuning is in the order of the  $kHz$ , while the detuning from the excited state is in the  $MHz$  range. After applying the Wigner-Eckart theorem, the summed terms  $\mu_{m_F, e} = \langle e | \boldsymbol{\epsilon} \cdot \hat{\mathbf{D}} | m_F \rangle$  can be written as:

$$\mu_{m_F, e} = (-1)^{1+L'+S+J+J'+I-m'_F} \begin{pmatrix} F & 1 & F' \\ m_F & q & -m'_F \end{pmatrix} D_{F, F'} \quad (4.28)$$

where  $'$  symbol stands for the excited state  $|e\rangle$ , and  $D_{F, F'}$  has been defined in

equation [4.21](#) with branching ratios. The effective two photon Raman couplings are then completely defined for any  $|m_F\rangle \leftrightarrow |m_F \pm 1\rangle$  transition.

Taking into account the quadratic degeneracy lift of the ground state manifold by  $\mathbf{E}_\pi$  as a diagonal operator  $\langle m_F | \hat{H}_q | m_F \rangle = -1/4 \langle m_F | \hat{\alpha} | m_F \rangle |\mathbf{E}_\pi|^2$ , where  $\langle m_F | \hat{\alpha} | m_F \rangle$  is defined in equation [4.8](#), the effective tridiagonal hamiltonian in the dressed state basis finally reads:

$$\hat{H}(\delta) = \frac{\hbar}{2} \begin{pmatrix} -9\delta & \Omega_{-9/2}^{-7/2} & 0 & \dots & 0 & 0 & 0 \\ \Omega_{-9/2}^{-7/2*} & -7\delta & \Omega_{-7/2}^{-5/2} & \dots & 0 & 0 & 0 \\ 0 & \Omega_{-7/2}^{-5/2*} & -5\delta & \ddots & 0 & 0 & 0 \\ \vdots & \vdots & \ddots & \ddots & \ddots & \vdots & \vdots \\ 0 & 0 & 0 & \ddots & 5\delta & \Omega_{5/2}^{7/2} & 0 \\ 0 & 0 & 0 & \dots & \Omega_{5/2}^{7/2*} & 7\delta & \Omega_{7/2}^{9/2} \\ 0 & 0 & 0 & \dots & 0 & \Omega_{7/2}^{9/2*} & 9\delta \end{pmatrix} + \hat{H}_q \quad (4.29)$$

This approach to write the effective hamiltonian gives the same result as obtained with the standard components of the tensor polarizability in the case of an electric field with polarizations  $\pi + \sigma_-$  treated in section [4.1.1](#), with amplitudes  $|\mathbf{E}_\pi|$  and  $|\mathbf{E}_{\sigma_-}|$ . The spectrum of hamiltonian [4.29](#), giving the energy crossings and hence light induced spin-spin transitions, can be obtained by direct diagonalization. The result of the diagonalization, is plotted in figure [4.8](#), and it is calculated with experimental parameters (see caption).

The spectrum within  $m_F < 0$  manifold only is shown here for better visibility. This spectrum shows that the energy crossings between  $|m_F\rangle$  and  $|m_F \pm 1\rangle$  states are avoided, authorizing two photon transitions, and those are the transitions that we use to selectively flip the spins. The insets of figure [4.8](#) show that crossings between  $|m_F\rangle$  and  $|m_F \pm 2\rangle$  states are also avoided, authorizing transitions involving the exchange of four photons. To make sure that the four photon transitions do not damage the selectivity of the spin flips that we realize with the two photon transitions, it is relevant to investigate on the relative strength of the two process.

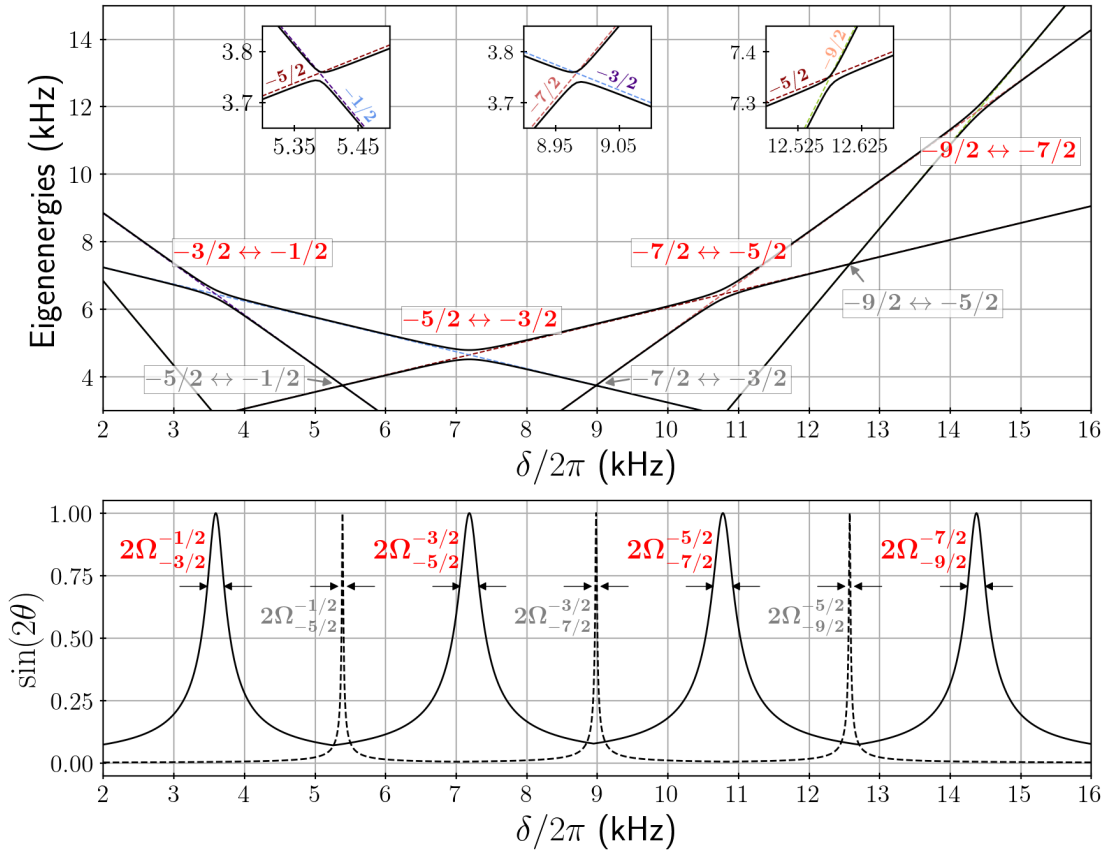


Figure 4.8: Spectrum of Hamiltonian defined in equation [4.29](#) with  $\pi + \sigma_-$  two photon couplings, with respect to Raman detuning  $\delta$ . For this computation, experimental parameters are used: detuning of the dressing beam  $\Delta/2\pi = -700$  MHz from the hyperfine state  $^3P_1, F = 9/2$  and intensity  $I_D \simeq 9.3$  W/cm $^2$ , and much lower intensity of the Raman beam  $I_R \simeq 5.1$  mW/cm $^2$ . Top: eigenenergies with respect to Raman detuning  $\delta = \omega_\pi - \omega_{\sigma_-}$ , where the solid lines are the eigenenergies, while the dashed lines indicate the energy of the dressed states. Two photon transitions are annotated in red, and four photon transitions are annotated in grey. Upper insets zoom in respective four photon transitions. Bottom : states mixing, defined in [4.30](#) as a function of the two photon Raman detuning  $\delta$ . The solid (dashed) line indicates two (four) photon transitions, and the respective Rabi couplings, defined in equation [4.27](#) ([4.32](#)) are given by the half width at  $1/\sqrt{2}$  of the states mixing.

The strength of the transitions, given by the Rabi frequency  $\Omega$ , can be graphically evaluated by the size of the gap at the avoided crossings, and figure [4.8](#), top, indicate

the the two photon transitions are stronger. It is also convenient to look at the states mixing [MS99]:

$$\sin(2\theta) = \frac{\Omega^2}{\sqrt{\Omega^2 + (\delta - \omega_R)^2}} \quad (4.30)$$

as a function of the detuning  $\delta - \omega_R$  with respect to the resonance  $\omega_R$  of the considered transition. The states mixing is shown on figure 4.8, bottom, for every resonances. Here,  $\theta$  is the mixing angle [MS99; FIM05], which defines the coherent superposition of the atom  $|\Psi\rangle$  over the two spin states  $|m_F\rangle$  and  $|m'_F\rangle$  involved into the transition, which can read:

$$|\Psi\rangle = \cos(\theta) |m_F\rangle + \sin(\theta) |m'_F\rangle \quad (4.31)$$

At resonance  $\delta - \omega_R = 0$ , the states mixing is maximal  $\sin(2\theta) = 1$ , *i.e.*  $|\Psi\rangle = (|m_F\rangle + |m'_F\rangle)/\sqrt{2}$ . The half-width of the resonances at  $\sin(2\theta)/\sqrt{2}$ , for both two and four photons transitions, is then given by the Rabi frequency  $\Omega$ , and 4.8, bottom, illustrates again that with the experimental parameters, the two photon transitions are much stronger than the four photon transitions.

From the dressed states point of view, which is schemed on figure 4.9, the four photon transitions are very similar to standard two photon Raman transitions. At resonance, the effective coupling between  $|m_F\rangle$  and  $|m_F \pm 2\rangle$  is simply  $\Omega_4 = \Omega_2^* \Omega_2 / 2\Delta$ , where  $\Delta = \delta - (\varepsilon_{m_{F+1}} - \varepsilon_{m_F})$  is the detuning with respect to the intermediate state, which is actually the detuning to the two photon transition. Hence, the effective four photon couplings read:

$$\Omega_{m_F}^{m_F+2} = \frac{\Omega_{m_F}^{m_F+1} \Omega_{m_F+1}^{m_F+2}}{2\Delta} \quad (4.32)$$

At resonance with the four photon transition,  $\delta = (\varepsilon_{m_{F+2}} - \varepsilon_{m_F})/2$ . Hence,  $\Delta$  is simply the difference between with the four photon and two photon resonances. It is very interesting to note here that both resonances depend on the quadratic light shift which is proportional to the intensity of the dressing beam, and then  $\Delta \propto I_D$ . Since the two photon Rabi couplings are proportional to  $\sqrt{I_D I_R}$ , then  $\Omega_{m_F}^{m_F+2} \propto I_R$ , which

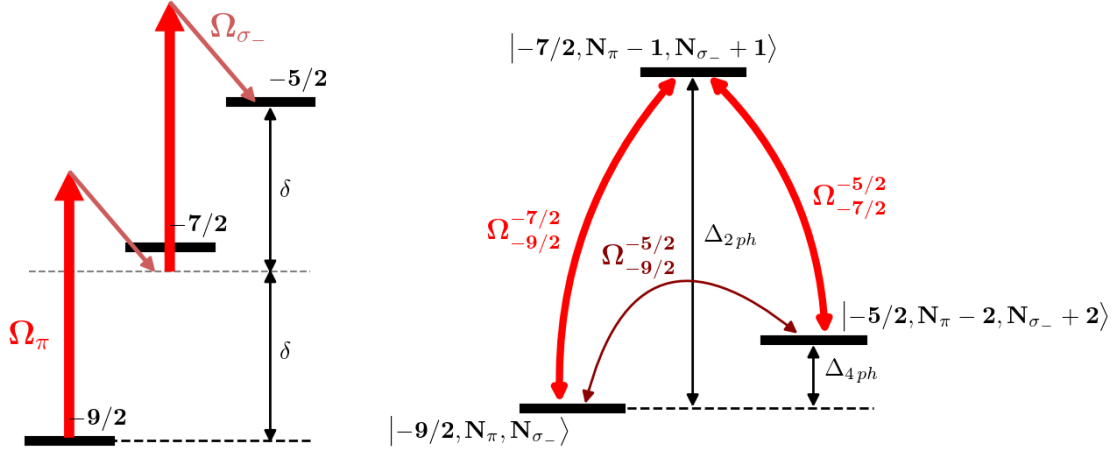


Figure 4.9: Four photon transitions in the dressed states point of view. Left: energy levels with quadratic degeneracy lift, and example of a four photon transition with associated resonance  $(\varepsilon_{-5/2} - \varepsilon_{-9/2})/2$  and Raman detuning  $\delta$ . Right: dressed state picture of 2 and 4 photons couplings, where  $\Delta_{2ph} = \delta - (\varepsilon_{-7/2} - \varepsilon_{-9/2})$  is the detuning with respect to the 2 photons transition, and  $\Delta_{4ph} = 2\delta - (\varepsilon_{-5/2} - \varepsilon_{-9/2})$  to the 4 photons transition.  $N_\pi$  and  $N_{\sigma_-}$  are the number of photons in respective photon fields  $E_\pi$  and  $E_{\sigma_-}$ .

first shows that the four photon transitions are much weaker than the two photon. And most importantly, the relative strength of the effective couplings finally scale as:

$$\frac{\Omega_4}{\Omega_2} \propto \sqrt{\frac{I_R}{I_D}} \quad (4.33)$$

This shows that the relative strength of the four photon couplings is strongly reduced with an appropriate setting of the Raman and dressing beams intensities. In this example shown on figure 4.8, the laser intensity into the Raman beam is 500 times smaller than that of the dressing beam. It is sufficient to strongly displace the eigenenergies, enabling the avoided crossing that we use for adiabatic passages, while the relative strength of the four photon couplings is as low as  $\Omega_4/\Omega_2 \simeq 5\%$ .

Note that all this derivation is done in the  $|\mathbf{E}_\pi| \gg |\mathbf{E}_{\sigma_-}|$  regime. In the opposite case, where the dressing beam is  $\sigma_-$  polarized and the Raman beam  $\pi$  polarized, the

degeneracy lift of the ground state manifold should be derived for a  $\sigma_-$  excitation, as presented in [4.1.1](#), with the main difference that the polarizability acquires a linear dependence in  $m_F$ . Regarding the Raman transitions, it has no consequences, and hence the previous estimation of the relative strength of the two photon and four photon couplings remains valid.

In the intermediate regime  $I_D \simeq I_R$ , the tensor polarizability accounts for the combination of the two laser and associated polarizations, and the ground state manifold is rotated from the  $|m_F\rangle \leftrightarrow |m_F \pm 1\rangle$  couplings defined in equations [4.11](#) and [4.12](#) as presented in section [4.1.1](#). This means that spin flips can be better realized with a STIRAP sequence [\[BVS15\]](#); [\[Vit+01\]](#); [\[MSB96\]](#), *i.e.* a sequence of pulses sequence by varying the laser intensities with respect to time rather than the Raman detuning.

In our experiment, we manipulate the spins in the  $|\mathbf{E}_\pi| \gg |\mathbf{E}_{\sigma_-}|$  regime that we considered here, and this is the case that I will also consider in the following discussions.

### 4.3.3 Engineering selective spin flips

In the frame presented on figure [4.8](#), a selected spin can be flipped to a target spin with adiabatic passage by ramping the Raman detuning through the corresponding Raman resonance. With proper parameters to center the ramp on the resonance and with initial and final detunings such that no other resonances are crossed, the success of the adiabatic passage presents no difficulty. However, it is possible to take advantage of the conditions for adiabatic passage to facilitate experimental engineering of the spin flips. Indeed, I have shown in the previous section that, accordingly to equation [4.33](#), the relative strength of the four photon couplings can be dramatically minimized by lowering the power of the Raman beam or increasing the power of the Dressing beam. Regarding adiabatic passages, a four photon transition has much lower probability of success than a two photon transition considering a fixed duration of ramp of the Raman detuning. It is then possible to engineer a spin flip with a ramp crossing multiple four photon transitions.

To realize selective spin flips on the experiment, we first prepare a spin polarized gas in spin state  $m_F = -7/2$ , as presented in section [3.2.3](#) of chapter [3](#). Then, the

magnetic field is slowly rotated such that it is aligned with the linear polarization of the electric field of the dressing beam. This way, the polarization of the light is well defined and it is purely linear. Then, the dressing beam,  $\pi$  polarized, is slowly turned to its maximum intensity  $I_D \simeq 9.3 \text{ W/cm}^2$  within 2 ms, with detuning  $\Delta = -700 \text{ MHz}$  from the  $^3P_1, F = 9/2$  hyperfine state. Now, the degeneracy of the ground state  $^1S_0$  is lifted by the quadratic light shift, and the spin-spin transitions are well resolved. At this step, the experiment is ready for adiabatic passage.

After slowly turning on the Raman beam up to  $I_R \simeq 5.1 \text{ mW/cm}^2$  within 2.5 ms, ensuring smooth connection to the eigenstates (see annexe C), the frequency of the Raman beam is ramped such that the Raman detuning  $\delta = \omega_\pi - \omega_{\sigma_-}$  is spanned from 5 KHz to 13 kHz, for different durations of the frequency ramp. Then, the Raman beam is turned off within 2.5 ms, and the populations in the spin states are measured with the spin dependent momentum transfer scheme (see chapter 3). The result of this spin flip experiment is presented on figure 4.10, left. The top figure shows the frequency ramp through the Raman resonances, and the bottom figures shows the measurement of the spin populations, which are shown as round dots with associated errorbars and rescaled by the 80 % efficiency of the populations measurement, for different durations of the detuning ramp. Note that not all atoms are detected during the populations measurement. This is shown by the total percentage of detected atoms in gray dots in bottom plots of figure 4.10, which is not constantly 100 % and even goes as low as 80 %.

Initially, approximately 90 % atoms are in  $-7/2$  and 10 % in  $-5/2$ . For fast ramps, atoms remain in the initial state  $-7/2$  and all transitions fail. For slow enough ramp with duration  $\simeq 20 \text{ ms}$ , 80 % spins have flipped to  $-5/2$ , while the population in  $-3/2$  has raised to 10 %, and approximately 10 % atoms remain in  $-7/2$ . To evaluate the efficiency of the adiabatic passage, it is convenient to realize a back passage. From the final state of the forth passage, the same procedure is done with a reversed ramp from  $\delta = 13 \text{ kHz}$  to  $\delta = 5 \text{ kHz}$ , and the Raman beam is turned off between the two passages. The back passage is shown on right figures. For slow enough ramp with duration  $\simeq 20 \text{ ms}$ , we detect 60 % atoms in  $-7/2$ , and nearly 10 % atoms are in both  $-5/2$  and  $-3/2$ . With this experiment, we infer that approximately 65 % out of the 90 % atoms initially in  $-7/2$  have successfully realized the back and forth adiabatic passage, which

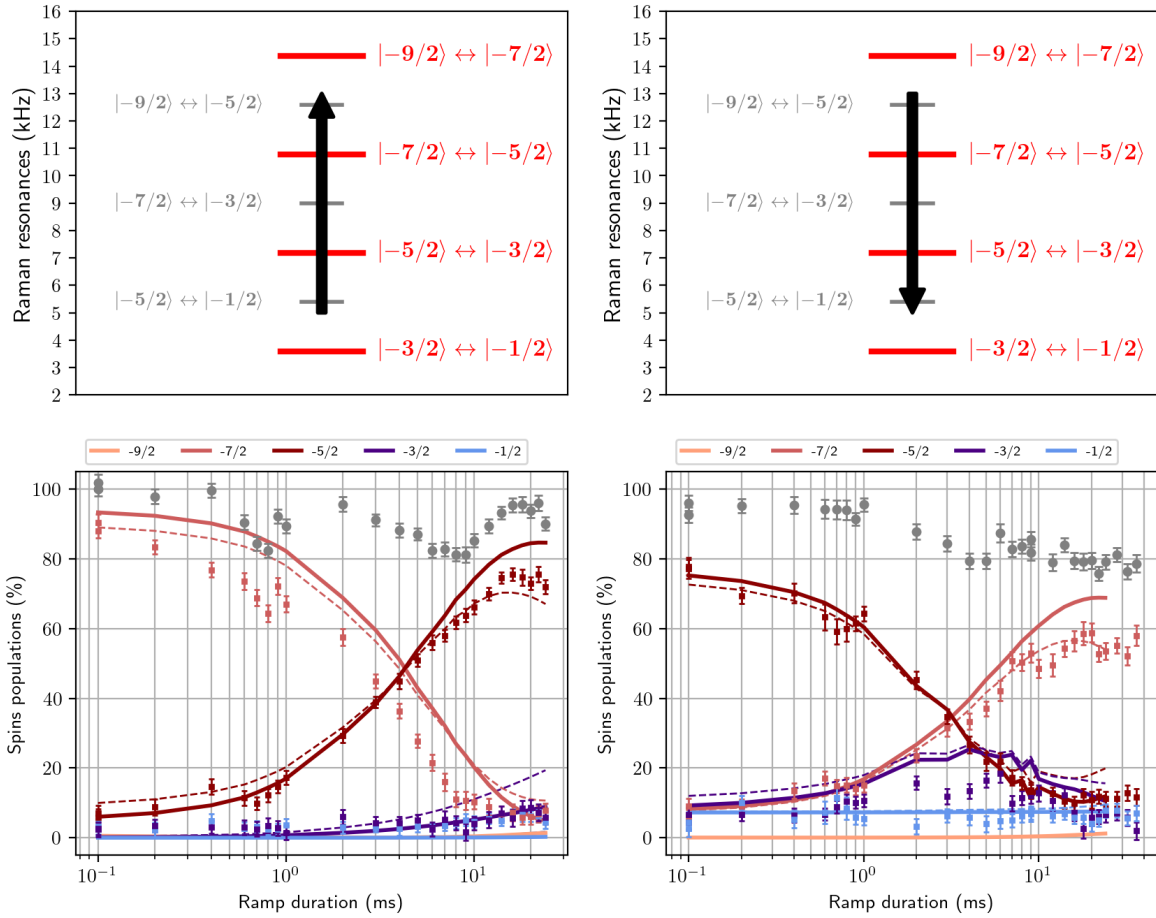


Figure 4.10: Experimental back and forth adiabatic passages from  $-7/2$  to  $-5/2$ , with  $\Delta = -700$  MHz,  $I_D \simeq 9.3$  W/cm<sup>2</sup>, and  $I_R \simeq 5.1$  mW/cm<sup>2</sup>. Left: forth passage from  $-7/2$  to  $-5/2$  with ramp of the Raman detuning  $\delta = \omega_\pi - \omega_{\sigma_-}$  from 5 kHz to 13 kHz. Right: consecutive back passage from  $-5/2$  to  $-7/2$  with ramp of the Raman detuning from 13 kHz to 5 kHz. The Raman beam is turned off between the two passages. Ramps through the spectrum of the two and four photon transitions are shown on top figures. The measured populations, with associated errorbars and rescaled by the 20% efficiency of the measurement, in the different spin states are shown in bottom figures, with respect to the duration of the ramp. The gray large points correspond to the total percentage of measured atoms. On both figures, solid and dashed lines are results from time integration of the Lindblad equation, including respectively predicted scattering rate and four times the predicted scattering rate.

results in 80 % efficiency for a one way adiabatic spin transfer. This experiment verifies the applicability, and robustness, of this adiabatic spin transfer scheme. Even if the detuning ramp crosses multiple two and four photon resonances, there is an optimal duration of the frequency ramp such that the four photon transitions are avoided while the adiabatic followings are ensured for two photon transitions. With proper choice of the direction of the frequency ramp, it is then possible to ensure a reliable selectivity on the spin transfer  $|m_F\rangle \leftrightarrow |m_F \pm 1\rangle$ , depending only on the initial spin state.

The result of the experiment is compared to numerical time integration of Lindblad equation [Man20]:

$$\frac{d\hat{\rho}}{dt} = \frac{1}{i\hbar}[\hat{H}, \hat{\rho}] + \sum_k \gamma_k \left( \hat{L}i_k \hat{\rho} \hat{L}i_k^\dagger - \frac{1}{2} \{ \hat{L}i_k \hat{L}i_k^\dagger, \hat{\rho} \} \right) \quad (4.34)$$

where the hamiltonian is defined in equation 4.29,  $\hat{\rho}$  is the density matrix, and the  $\hat{L}i_k$ 's are the jump operators, *i.e.*  $|m_{Fi}\rangle \langle m_{Ff}|$  projectors [DCM92] for  $m_{Fi} \rightarrow m_{Ff}$  transitions, associated with rate  $\gamma_k$ . Here,  $\{A, B\} = AB + BA$  is the anticommutator operator for  $A$  and  $B$ . The sum runs over all the possible spin projections, in our case set by Raman scattering defined in equation 4.18. Note that the elastic Rayleigh scattering  $\Gamma_{m_F \rightarrow m_F}$  is taken into account, even if it doesn't change the spin state, as it is a source of spin decoherence and hence it can decrease the efficiency of the coherent adiabatic passage. Also, no atom loss is considered here, since the measured heating rate is low enough so that the atoms cannot be blasted from the trap, according to our measurement presented on figure 4.6.

The prediction with experimental parameters (intensities and detuning) and no other adjustable parameter is plotted on figure 4.10, bottom left and right, as thick solid line, and it shows that the efficiency of the adiabatic passage should be significantly higher than measured, as high as 95 %. Because the measurement of the scattering rate showed that it is much higher than predicted (see section 4.2.3), it is relevant to artificially enlarge the scattering rate as high as measured to compare prediction with the spin flip measurement. This is shown by the thin dashed line on 4.10, bottom left and right, where the scattering rate is four times higher than predicted, according

to the measurement. While the expected populations in  $-7/2$  and  $-3/2$  are higher by a few percents to what is measured, this second simulation seems to be in good agreement with the experimental results, accounting for the non 100 % total percentage of detected atoms. Hence, this simulation shows that our experiment is only limited by spontaneous emission due to the enlarged light scattering, that can be corrected by filtering the spectral mode of the laser with a Fabry-Perot cavity. Then, we expect that the adiabatic passage scheme to selectively flip spin state should reach 90 % efficiency. Note that a cavity has been set and used to measure the scattering rate (see section 4.2.3), however its sensitivity to vibrations has prevented us from using it for a spin flip experiment. The cavity is presently being upgraded for future use.

## 4.4 Site selective adiabatic passage to prepare spin textures - Outlook

Previous experiments have demonstrated experimental realizations of patterns of atoms selectively placed at the sites of optical lattices, using an optical super lattice [Pei+03], or site selective light shifts [Gri+06]. More recently, experiments have shown that patterns can be assembled atom by atom using optical tweezers [Bar+16; Kum+18]. In this section, I present our scheme to prepare alternate spin textures [Li+16]. Using a spin dependent optical super-lattice [Man+03; Hei+20] and a homogeneous Raman laser, we will selectively flip half the spins of a single component band insulator.

### 4.4.1 General Idea

Starting from a polarized Fermi gas loaded in the ground band of a 2D lattice, half the spins are selectively flipped to prepare a Neel order [Sun+21], *i.e.* an alternate pattern of up and down spins, as shown on figure 4.11. This is done with a space dependent tensor light shift [Hei+20] which varies at the micrometer scale, and it is engineered by retro-reflecting the laser beam responsible for the spin dependent light shifts. Since the resonances of the lifted spin spin Raman transitions are proportionnal to the local laser intensity, it is possible to realize a chirp of Raman detuning that crosses the resonances at sites with maximal depth of the spin dependent potential only, using

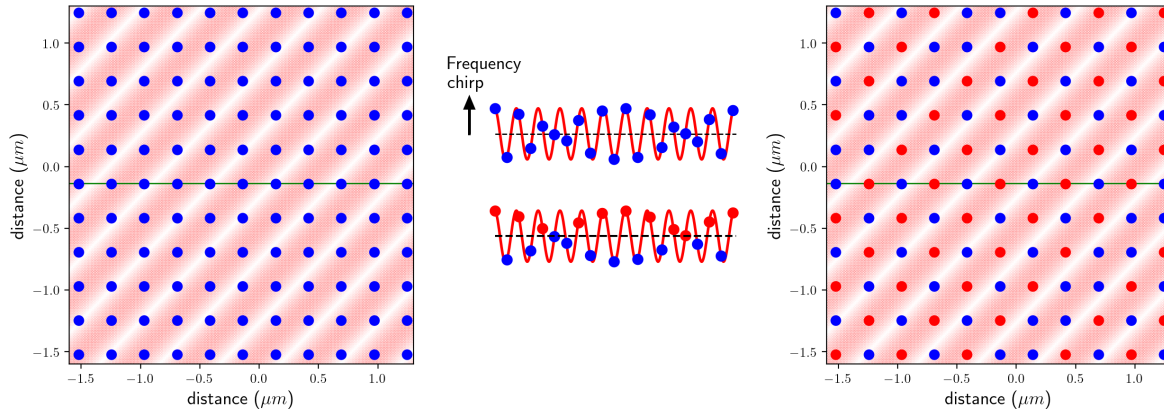


Figure 4.11: Scheme for writing spin textures. Left: the spin dependent lattice (red background) is superimposed to a 2D spin polarized lattice. A cut of the potential (horizontal green solid line) is presented on the middle figure. Middle: spin dependent potential (red solid line) along an eigenaxis of the 2D lattice. Each spin (blue dots) localized at the sites of the 2D lattice (x axis) feels a different light shift which is proportional to the light intensity (yaxis). The chirp of the raman detuning is shown by the black arrow and crosses the Raman resonances (see figure 4.10) of the maximally shifted sites only, which are flipped from blue spin to red spin. The resulting spin texture is shown on right figure.

an homogeneous Raman beam. Then, our demonstrated scheme to coherently flip the nuclear spin states acquires a well defined site dependence, enabling the possibility to handwrite a predictable spin texture.

#### 4.4.2 Geometry of the lattices

The geometry of the laser setup used to engineer the spin dependent lattice is presented on figure 4.12. The dressing beam at 689 nm is retro-reflected to shape a 1D lattice, that I will call for simplicity *dressing* lattice, and the azimuthal angle between the dressing beam and the 532 nm beams is  $45^\circ$ , such that the dressing lattice is along the diagonals of the 2D trapping lattice. With elevation angle  $16^\circ$ , the projection of the dressing lattice on the 2D layers has site spacing  $a_{689} \simeq 360$  nm, which is smaller by less than 10% than the diagonal of the 2D lattice  $a_{532}\sqrt{2} \simeq 390$  nm (*i.e.* the distance between neighbours at  $45^\circ$  of the main lattice axis). Neglecting the 10% difference in first

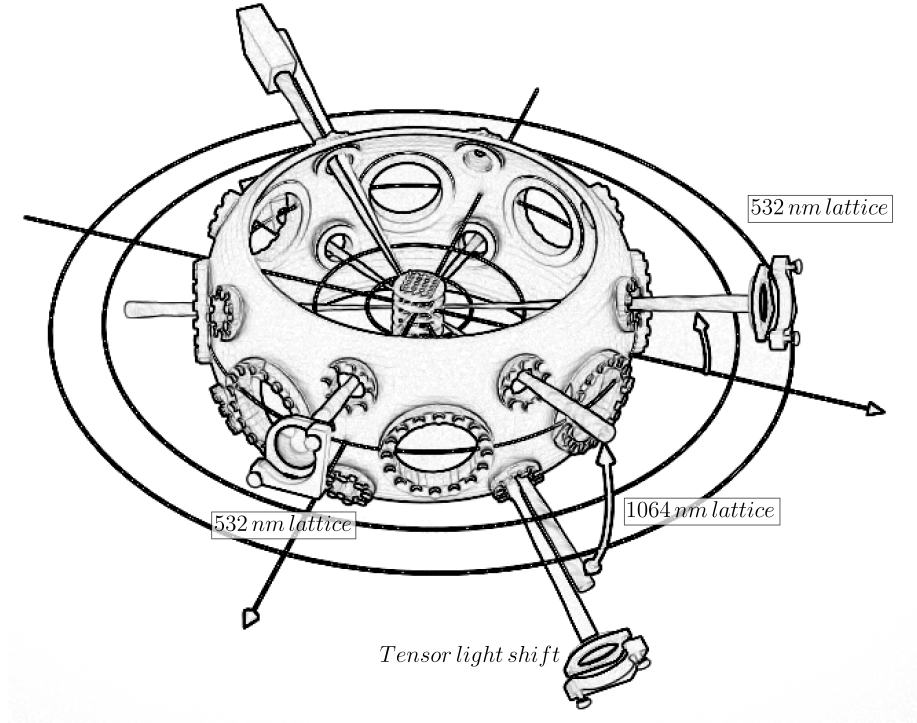


Figure 4.12: Experimental design of the setup for lattices. The retro-reflected 1D spin dependent lattice is nearly colinear with one arm of the 1064 nm lattice, with azimuthal angle  $45^\circ$  with each arm of the 2D lattice at 532 nm and  $16^\circ$  elevation angle.

approximation (see figure 4.13, (a)), it means that the spin dependent light shift is maximum one out of two diagonals of the 2D lattice, and hence the depth of the spin dependent potential would alternate along an eigen-axis of the 2D lattice. In this case, a chirp of a Raman detuning crossing only the maximally shifted resonances to flip half the spins would realize exactly a Neel order. If considering the 10% difference, Figure 4.13 (b.1) shows that trapped atoms actually see 11 sites periodic pattern of alternate maximum and minimum depth of the spin dependent potential. This pattern has maximum contrast at the center over about 7 sites and is blurred at the edges over about 4 sites, and this results in alternate pattern for the Raman resonances between higher and lower frequencies, see figure 4.13 (b.2), over 11 sites.

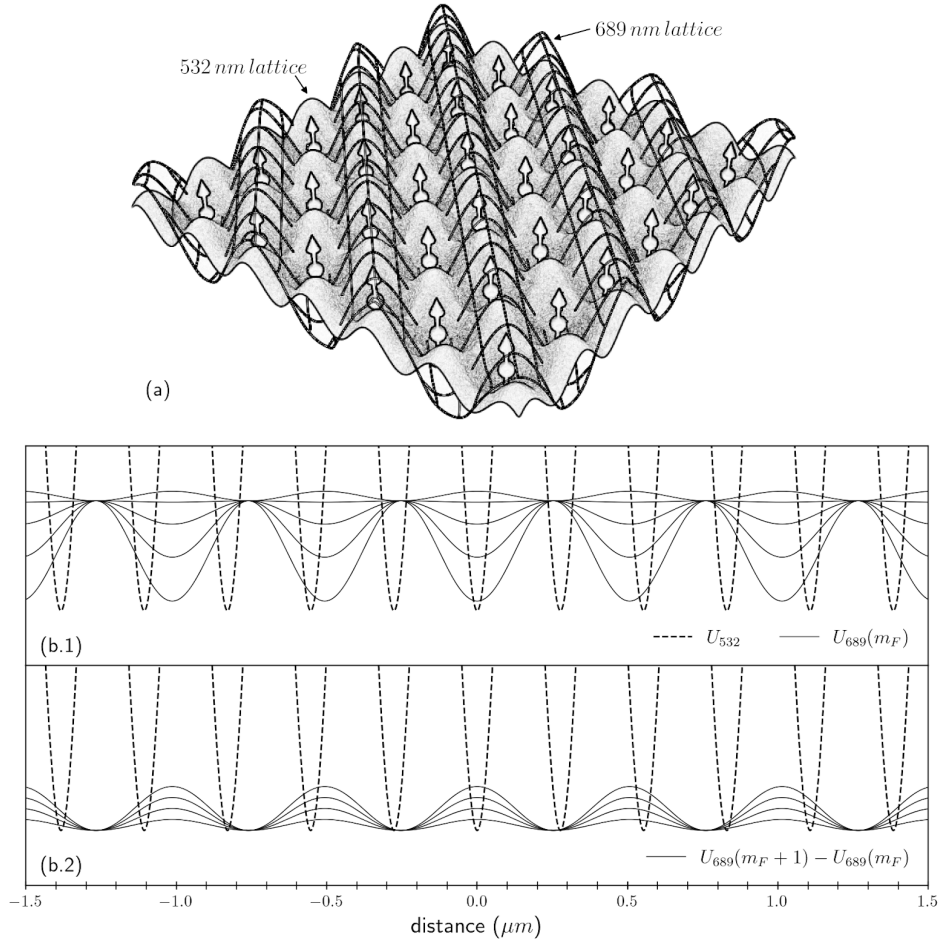


Figure 4.13: Spatial and spin dependence of the tensor light shift associated with the intercombination line. (a) The eigenaxis of the 689 nm 1D lattice is along the diagonal of the trapping 2D lattice, considering  $a_{689} = a_{532}\sqrt{2}$ . (b.1) Considering the experimental situation with sites spacing  $a_{689} \simeq 360$  nm, which is 90 % of the diagonal of the 2D lattice, this is the projection along one eigenaxis of the 2D square lattice at 532 nm of the trapping (dashed lines) and spin dependent (solid lines) potentials, for each spin state. (b.2) Projection along one eigenaxis of the 2D square lattice of the raman resonances defined as  $U_{689}(m_F) - U_{689}(m_F + 1)$ , where  $U$  is the dipole potential.

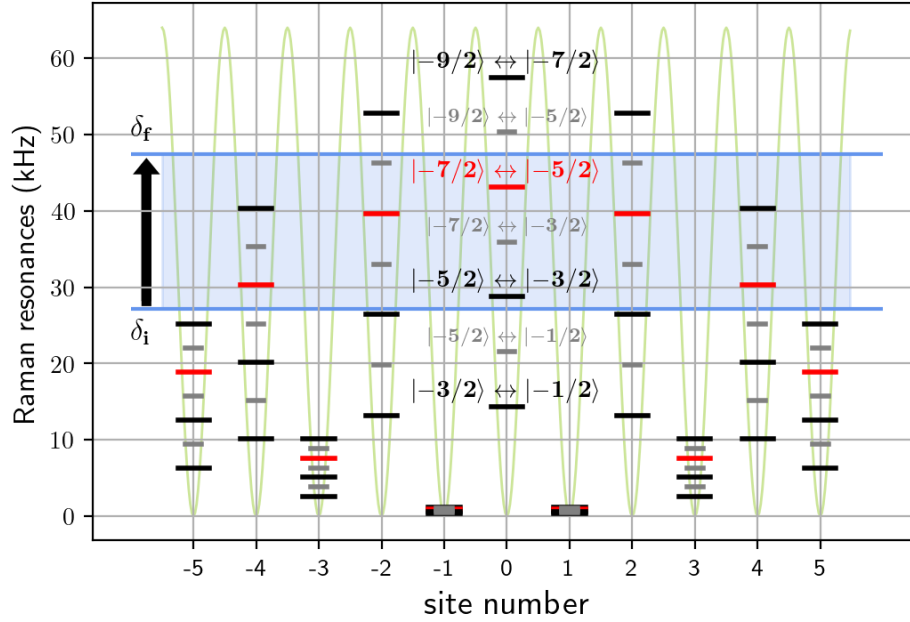


Figure 4.14: Site dependent Raman resonances. The 532 nm lattice is sketched as the green solid line, and the target two photon  $| -7/2 \rangle \leftrightarrow | -5/2 \rangle$  transition (Red) is sketched for each site, as well as the other Raman resonances subtitled at the central site. The ramp of Raman detuning from  $\delta_i$  to  $\delta_f$ , sketched by the black arrow, crosses the resonance one over two sites only, as shown by the blue filled region. The initial frequency is chosen as 90 % of the less shifted  $| -7/2 \rangle \leftrightarrow | -5/2 \rangle$  resonance among selected sites, and the final frequency as 110 % of the most shifted resonance, which corresponds to the lattice depth.

### 4.4.3 Site dependent Raman resonances

The Raman resonances of the spin spin transitions, with acquired site dependence, are presented on figure [4.14](#) along 11 sites of an eigen-axis of the 2D lattice at 532 nm. The Raman resonances, proportional to the local intensity of the dressing lattice, are then site resolved.

One every two sites, say odd sites, the resonances are maximally shifted, so that chirp of the Raman detuning with appropriate initial and final frequencies can cross the resonance of a target two photon resonance on these sites only, while it is not crossed on the other half sites, say even sites. This way, it is possible to realize an adiabatic spin

flip on the odd sites, while atoms at the even sites are not affected by the frequency chirp. It is pictured by the black arrow between an initial  $\delta_i$  and final  $\delta_f$  detunings, and  $\delta_i$  is chosen such that the  $|-9/2\rangle \leftrightarrow |-7/2\rangle$  two photon resonances of the avoided sites are not crossed by the ramp, for instance on sites -5 and 5 on figure [4.14](#).

#### 4.4.4 Predicted texture writing

The frequency chirp presented on figure [4.14](#) is simulated by numerical integration of the Lindblad equation defined in equation [4.34](#) for each one of the 11 sites, and the result is shown on figure [4.15](#). For this simulation, the intensities are  $I_D \simeq 11 \text{ W/cm}^2$  and  $I_R \simeq 6 \text{ mW/cm}^2$ , where  $I_D$  ( $I_R$ ) is the intensity of the dressing (Raman) beam, with detuning  $\Delta = -700 \text{ MHz}$  from the excited hyperfine state  $|^3P_1, F = 9/2\rangle$ . The Raman detuning  $\delta = \omega_D - \omega_R$  is ramped from 63% to 110% of the maximally shifted  $|-7/2\rangle \leftrightarrow |-5/2\rangle$  target resonance (site 0 of figure [4.14](#)) during 5 ms. The amplitude of the Raman beam is ramped up (down) during 2.5 ms before (after) the frequency ramp, as shown by the red filled background, to improve the connection to the followed eigenstates. The left column, considering predicted spontaneous emission, shows the spins populations dynamics during a transfer from the initial spin state  $-7/2$  to the final spin state  $-5/2$ . Sites with deeper tensor light shift ( $U_{dip}/U_{max} > 0.5$ ) are flipped with 90% chance of success, while the avoided sites ( $U_{dip}/U_{max} < 0.5$ ) have less than 3% chance of success, and on this 11 sites sample, the fidelity of the spin texture writing, here defined as the average of the final  $-5/2$  populations in target sites and final  $-7/2$  in avoided sites, can be estimated as high as 97%. If taking into account the measured spontaneous emission which is four times higher than the prediction (see section [4.2.3](#)), the result of the simulation is shown on the right figure, and the estimated fidelity of the spin texture writing is lowered to 85%.

The conditions for adiabatic passage have to be carefully looked at for every site. Indeed, the spin dependent light shift is not the same for all selected sites, and hence the Landau-Zener (LZ) condition for adiabatic following (see appendix [C](#)) varies accordingly. It is therefore important to focus on the site dependence of the adiabatic following. First, let's recall that the Landau-Zener probability of success for an adia-

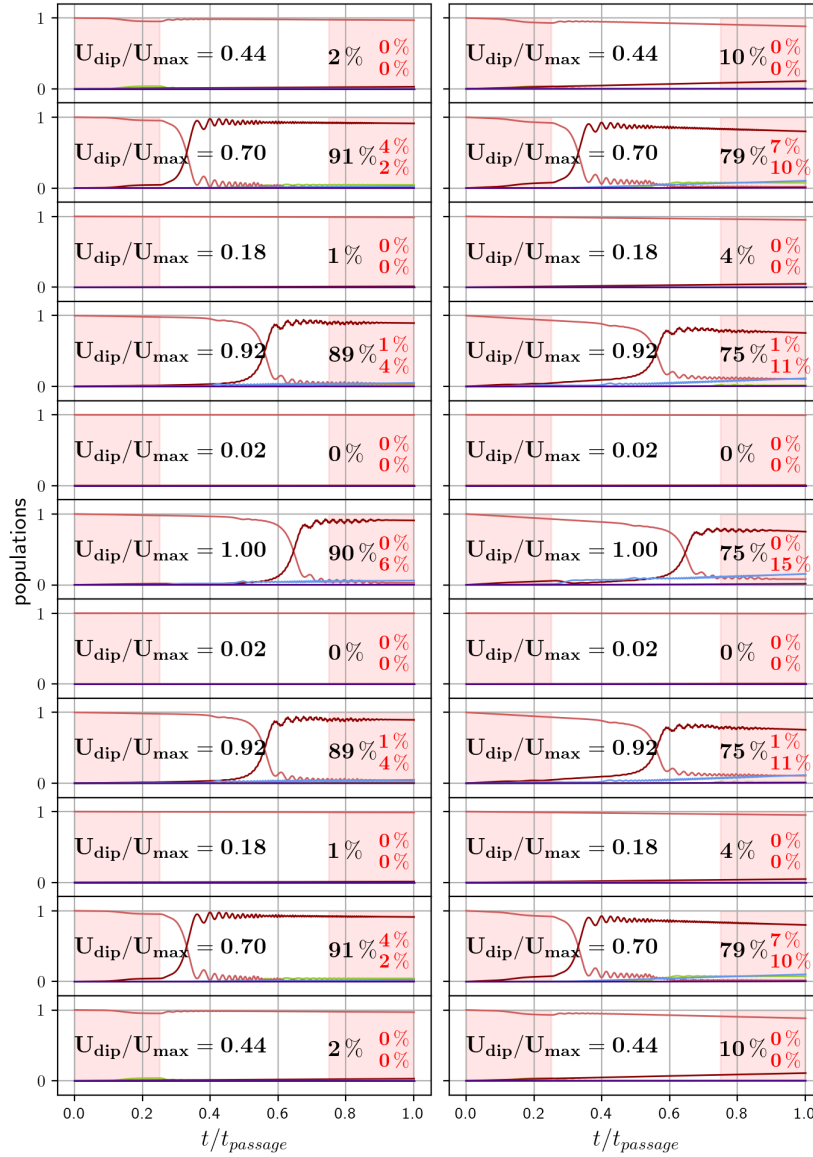


Figure 4.15: Simulation of the frequency chirp presented on figure 4.14 with numerical integration of the Lindblad equation (4.34) for each one of the 11 sites, to flip spins from  $-7/2$  to  $-5/2$ . The success of passage is indicated in big black font, and the final populations in  $-9/2$  and  $-3/2$  are indicated in small red font. The simulation parameters are detailed in section 4.4.4. In left column, the simulation is realized with predicted scattering rate, while right column takes into account measured scattering which is four times larger.

batic following is defined as:

$$P_{LZ}(\Omega^2, \dot{\delta}) = 1 - \exp\left(-2\pi \frac{\Omega^2}{4\dot{\delta}}\right) \quad (4.35)$$

where  $\Omega^2$  is the coupling strength and  $\dot{\delta}$  is the speed of the detuning ramp. Considering that the intensity of the Raman beam is homogeneous over the whole lattice, and that the detuning ramp is linear in time, then the chance of success is lowered at sites with lower spin dependent light shift, since  $\Omega^2 \propto I_D$ . However, the scattering rate associated with the tensor light shift is obviously higher at sites with stronger intensity of the dressing lattice. Finally, the probability of success for four photon transitions does not depend on the depth of the tensor light shift. This means that there exists optimal conditions for adiabatic passage, which corresponds to a chirp duration slow enough to maximize the relative chance of success of the targeted two photon transitions on the less shifted sites with respect to the avoided four photon transitions, and fast enough to minimize spontaneous emission on the most shifted sites.

## Chapter 5

# 2D Fermi gases in the lowest band of a low recoil 1D lattice

The objective of our experiment is to realize a Fermi Hubbard model with 2D lattices [BDZ08; GB17]. Such experiments require the preparation of ultra cold Fermi gases, that are trapped into the lowest Bloch band of optical lattices with minimal entropy [MD11]. Practically, it requires to circumvent the difficulties associated with the manipulation of ultra cold gases of fermions [Ess10]. For instance, atoms are typically cooled to quantum degeneracy with forced evaporation assisted by collisions [GWO00; LRW96], that are inhibited for ultra-cold fermions [DeS+10]. Yet, active research on the Fermi Hubbard Model led to the realization of numerous quantum simulators, typically using alkali fermions such as potassium 40 [Sch+08; Che+15; Dre+17] or lithium 6 [Gre+16; Bol+16; Par+16]. Regarding alkali atoms, Feshbach resonances [Chi+10] can be used to tune the scattering length  $a_s$ , which helps prepare ultra-cold gases, and at the realization of isentropic transformations assisted by collisions, such as lattice loading. Inside lattices, entropy can be further reduced, for instance with Raman side band cooling [Ham+98; GWO00; Ker+00; Tho+13], or by filtering of atoms populating the excited bands [Arn+19].

In our experiment, ultra cold strontium 87 shall be trapped in a 3D optical lattice, that is made of the combination of a 1D lattice with large site spacing [Huc+09] and negligible tunneling, with a 2D lattice where the spin dynamics takes place (see chapter

1). The 1D lattice, that is first loaded, has site spacing  $2\mu m$ , so that prior to the loading the gas extends over approximately 8 sites. The large spacing of the lattice permits that the inter site tunneling is inhibited with moderate lattice depths of a few tens of  $kHz$ . From this geometry, we prepare several independent 2D Fermi gases that are vertically stacked. The 2D gases shall next be adiabatically loaded in a 2D square lattice to prepare several band insulators [Leb+18] that do not interact with each other. This chapter is dedicated to the loading of the lowest band of the 1D lattice.

*Chapter summary:* first, I will discuss a critical limit set by the Pauli exclusion principle at the loading of the lowest band only of the 1D lattice with large site spacing. The Fermi energy of the 2D gases cannot exceed the lattice band gap, which limits the number of atoms that can be loaded. However, in practice, the Fermi momentum of our evaporated gases exceed the recoil momentum of the lattice, so that atoms connect to excited bands when turning on the lattice. In this case, loading the lowest band of the lattice requires a quasi-static transformation assisted by s-wave collisions [Ess10].

Then, I will present our loading experiment. I will describe two attempts to do so. In the first, the gas is initially prepared at very low temperature, by strong evaporation in the dimple. I show that we are able to load the 1D lattice with 93(2)% atoms into the lowest band, using a Boltzmann approximation and a global analysis over the entire cloud distributed in a few layers. It is even possible to extract information that depends on the layers of the 2D lattice. From the Fermi statistics, I estimate the chemical potential of each layer, as well as the temperature, based on an independent measurement of the distribution of atoms between the layers.

Using this method, I find that the 2D gases have negative chemical potentials, indicating that they are not degenerate, and the inferred probability of occupation of the lowest band is the same than the classical analysis. A comparison with the initial thermal state of the gas prior to the loading shows that the high probability of occupation of the lowest band is enabled by a deep evaporation prior to the lattice loading, until our lower limit yet of measurable temperature  $T = 5 \pm 5 nK$  into the dipole trap with approximately 5000 atoms. However, the degeneracy of the loaded gases are higher than expected for an isentropic loading. Hence, this measurement shows the quasi-static behavior failed, and it suggests that the collisions were not sufficient. This study

serves as a guideline for a preliminary result.

In a second attempt, improved adiabaticity is shown by holding sufficient dipole trap compression prior to the loading into the lattice, ensuring sufficiently high collision rate. This way, we are able to produce 4 independent 2D degenerate SU(10) Fermi gases with  $\mu/\varepsilon_F \geq 0.4$  and approximately 99 % atoms into the lowest band.

## 5.1 Limit to the atom number for fermions in the lowest band

In our experiment, the site spacing of our 1D lattice is  $a \simeq 2 \mu\text{m}$  with associated recoil momentum  $k_R = \pi/a$ . In this case, the recoil energy  $E_R = \hbar^2 k_R^2 / 2m$  is as low as  $E_R \simeq k_B \times 7 \text{ nK} \simeq \text{h} \times 150 \text{ Hz}$ , which is much lower than in typical retroreflected optical lattices. Consequently, the site to site tunneling  $t \sim \exp\left(-2\sqrt{V_0/E_R}\right)$  [BDZ08] is negligible for a lattice depth  $V_0$  of a few tens of kHz, and in our experiment we measure  $V_0 \simeq 1800 E_R$  (see chapter [1]), so that the motional degree of freedom along the lattice eigen axis is practically frozen. The phase space is then restrained to the *on-site* 2D motion, with associated phase-space cell  $d^2 r d^2 p / h^2$ , and to the band excitation  $n$ . Assuming that only the lowest band  $n = 0$  is populated, every site of the 1D lattice is reduced to 2D dimensionality  $(r, p) = (r_x, r_y, p_x, p_y)$ .

In the  $T = 0 \text{ K}$  limit, fermions occupy all energy states below the Fermi energy, and for non zero temperature, higher energy states are accessible. This sets a critical limit to the number of atoms that can be loaded into the lowest band of a 1D lattice. Assuming that the transverse confinement of the lattice sites can be approximated to harmonic traps of frequency  $\omega_\perp$ , and that the tunneling is negligible, the limit reads

$$\varepsilon_F - \varepsilon_0 = \hbar\omega_\perp(2N)^{1/2} < \hbar\omega_\parallel \quad (5.1)$$

where  $\hbar\omega_\parallel = 2\sqrt{V_0 E_R}$  is the lattice band gap, and  $\varepsilon_0$  the energy of the lowest band. This result can be shown by derivating the Fermi energy  $\varepsilon_F$  of a gas trapped into a 3D harmonic trap, tightly confined along one direction only and with zero band excitation (see appendix [A]). It is simply the Fermi energy of a 2D gas shifted by the energy of

the lowest band. In our experiment,  $\hbar\omega_{\parallel} \simeq 12$  kHz and  $\hbar\omega_{\perp} \simeq 80$  Hz, so that the Fermi energy is lower than the energy of the first excited band only if  $N < 10\,000$  atoms per spin state. If the transverse harmonic confinement can be adjusted without changing the lattice depth, for instance by using a combination of a red and blue detuned dipole traps, the maximum number of atoms in the lowest band can be practically adjusted [Sch+08].

## 5.2 Adiabatic loading of the lowest band : collision requirements

Typically, lattice loading requires adiabaticity in the single particle sense. It relies on the adiabatic theorem that implies that atoms follow the eigenstates of the time dependent Hamiltonian if it is modified sufficiently slowly [Den+02]. This way, an atom in a plane wave state  $k_{atom}$  evolves into a Bloch state, that will be the ground state if  $k_{atom} < k_R$ . The momentum recoil  $k_R = \pi/a$  of the lattice defines the limit of the first Brillouin zone (FBZ), and momenta exceeding the FBZ connect to the excited bands of the lattice. In the case of a Fermi gas, the loading of the lowest band only thus implies, in the single particle limit, that  $k_F < \pi/a$ . In our case, the recoil energy  $E_R \simeq k_B \times 7$  nK  $\simeq h \times 150$  Hz is much lower than in typical retroreflected optical lattices, and this is cause for concern. First, cooling a thermal gas of strontium 87 fermions in this limit is difficult as collisions are inhibited by Pauli blocking at deep evaporation stages [DeS+10], and closed shell strontium 87 atoms do not benefit from Feshbach resonances to favorably tune the collision rate. Second, even if we did, the average distance between atoms would scale as the site spacing  $a$ . In the prospect of next loading a 2D lattice with site spacing  $a/8$  (see chapter 1) to realize a band insulator, such low densities are not favorable. Therefore, the idea of adiabatic following at the single particle level is not fruitful. Fortunately, there is also the possibility to be quasi-static in the thermodynamic sens, if collisions are allowed, and this approach is typically used to prepare Mott insulators [CHU09; Fuk+09; Jör+08].

This second possibility for loading the ground band of the lattice relies on collisions, which means that the adiabaticity of the process is not an eigenstate following which

relies on single particle physics, but an adiabatic process in the sense of remaining at thermal equilibrium relying on s-wave collisions [Ess10]. Furthermore, this many-body transformation requires a mixture of fermionic species. When the lattice is turned on, the initial thermal state of the transformation is a 3D gas in a 3D harmonic trap with Fermi energy  $\varepsilon_F^{3D} \propto \hbar(\omega_\perp^2 \omega_\parallel)^{1/3} \gg \hbar\omega_\parallel$ , where  $\hbar\omega_\parallel$  is the band gap of the lattice. Hence, atoms populate excited bands. When the depth of the lattice is increased, the band gap increases faster than the Fermi energy, and collision assisted relaxation permits to empty the band excitations. In the final thermal state, the gas can be 2D only if  $\varepsilon_F^{2D} < \varepsilon_1$ , as discussed in the previous section, where  $\varepsilon_F^{2D} = \hbar\omega_\perp(2N)^{1/2}$  is the 2D Fermi energy and  $\varepsilon_1 = \hbar\omega_\parallel$  the excitation energy of the first vibrational state. Therefore, the lattice loading can be seen as an adiabatic trap compression assisted by collisions along the 1D lattice eigen-axis so that  $\omega_\parallel \gg \omega_\perp$ , which permits a dimensionality cross-over from 3D to 2D.

While the single-particle approach is limited by  $\varepsilon_F < E_R$ , the collision assisted loading of the lowest band is limited by  $\varepsilon_F < \varepsilon_1$ , where  $\varepsilon_1 \gg E_R$ . Hence, loading the lowest band of the lattice with a mixture of fermions allowing for s-wave collisions permits to produce much more dense 2D gases. However, the adiabaticity criterion is very different between the two schemes. In the single-particle approach, which can be realized with only one fermionic species, the timescale associated with the lattice depth variations is in the order of a ms for band gaps in the order of 1 kHz, which is more favorable than the timescale associated with the inter atomic collisions, that require a mixture of fermionic species, and that is in the order of the hundreds of ms for degenerate Fermi gases of strontium.

### 5.3 Loading experiments and measurement of the band populations with a Boltzmann approximation

In this section, I present our protocole to produce a 2D Fermi gas of  $^{87}\text{Sr}$ . From time of flight absorption images of the loaded gases, the kinetic energy of the gas expanding

transversally to the lattice eigen axis is used as a thermometer, and the probability of occupation of the lowest band  $r_0$ , that I will refer to as loading efficiency, is inferred from a Boltzmann approximation. While the kinetic energy along the lattice eigen axis converges to that one of the lowest Wannier state and the temperature of the gas decreases, the aspect ratio measured on the time of flight images increases, indicating that the Fermi gas reaches the 2D regime. Our measurement shows that we are able to produce 2D gases with 93(2) % atoms into the lowest band of the 1D lattice.

*Experimental procedure:* we produce a spin mixture  $m_F = +9/2, -5/2, -9/2$  of  $^{87}\text{Sr}$  with a sequence of spin selective optical pumping, as presented in chapter [3](#), and the relative populations are respectively nearly 10%, 70% and 20% due to the sequence of the mixture preparation (see section [3.2.2](#)). The gas is cooled by forced evaporation, with final number of atoms  $N_{at}$  and degeneracy  $T/T_{FODT}$  tunable with respect to the final depth of the 3D optical dipole trap. Then, the 1D lattice is slowly ramped up in two steps. First, while the collision rate per atom is as low as approximately  $\gamma_{col} \simeq 3 \text{ s}^{-1}$ , inhibited by the Pauli exclusion principle after reaching low  $T/T_{FODT}$ , the lattice is slowly turned on from zero depth to  $V_0 \simeq 270 E_R$ , *i.e.*  $h \times 40 \text{ kHz}$ , in 600 ms. During this stage, the gas is split in different layers of the 1D lattice as pictured on figure [5.1](#), and for such depth, the tunneling is negligible. Here we assume that the gases in every layer remain at thermal equilibrium, and it is discussed later in section [5.4.2](#). Then in a second stage, the lattice is ramped up to its maximal depth  $V_0 \simeq 1780 E_R$ , *i.e.* 255 kHz, in 600 ms. The measurement of the depth of the low recoil lattice is presented in section [1.2.1](#), and at full depth, the band gap  $\hbar\omega_{\parallel} = 2\sqrt{V_0 E_R}$  is 12 kHz. During this stage, the optical dipole trap is slowly turned off such that the geometry of the trap is completely determined by the lattice laser. After loading the lattice, there is 250 ms hold time. Then, the lattice is abruptly shut off and the atoms are imaged with absorption imaging after a time of flight of 10 ms. The result of the experiment is shown on figure [5.2](#).

After time of flight of the loaded gas, the imaged densities, shown on figure [5.2](#), (a.1) and (a.2) for different number of atoms and respective final depth of the dipole trap, are analysed in the classical approximation, and fitted with Gaussian distributions. The

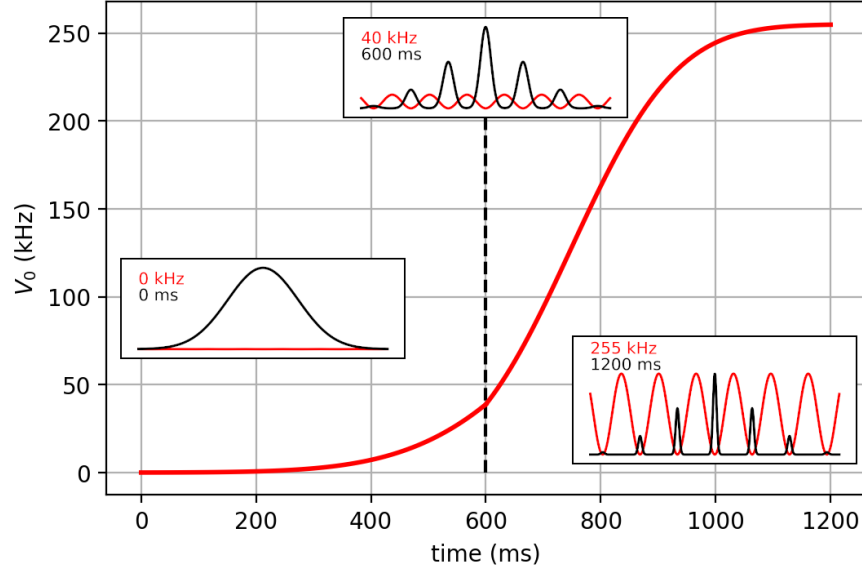


Figure 5.1: Depth of the lattice with respect to the time of ramp. The loading is done in two stages, split by the dashed line on the plot at  $V_0 \simeq 40 \text{ kHz}$ . The insets are illustrations of the loading at different stages, the black curve is the density and the red curve is the 1D lattice potential. At 0 ms, the lattice is off and the gas is bulk, at 40 kHz the lattice depth is deep enough such that the thermal gas is split into different 2D layers, at 255 kHz the depth is maximal and the atoms shall occupy the ground band only, *i.e.* the lowest Wannier state, with a Gaussian density distribution.

kinetic energy  $\langle E_k \rangle = \langle p^2 \rangle / 2m = k_B T / 2$  measured along  $O_r$ , *i.e.* along the 2D layers, is presented on figure 5.2, (b), empty squares, as a function of the number of atoms. Assuming that the gas is at thermal equilibrium, we use the measurement of the momentum distribution  $\langle p_r^2 \rangle$  as a thermometer for this experiment, the temperature drops linearly with respect to the number of atoms, from approximately 450 nK to 200 nK in this data. The momentum distribution measured along  $O_z$ , *i.e.* along the lattice eigenaxis, (filled circles on figure 5.2), converges towards that one of Wannier state of the lowest band with momentum spread  $\Delta p^2 / 2m = \hbar \omega_{\parallel} / 2$  (dashed line). Atoms in the lowest Wannier state of the lattice have their momentum distribution defined by the harmonic oscillator length only: considering the Heisenberg uncertainty principle  $\Delta x \Delta p = \hbar / 2$ , where  $\Delta x = a_{ho} / \sqrt{2}$  for the lowest Wannier state, then  $\Delta p^2 = m \hbar \omega_{\parallel} / 4$ . It shows that obviously, fewer atoms occupy excited bands for deeper evaporations prior

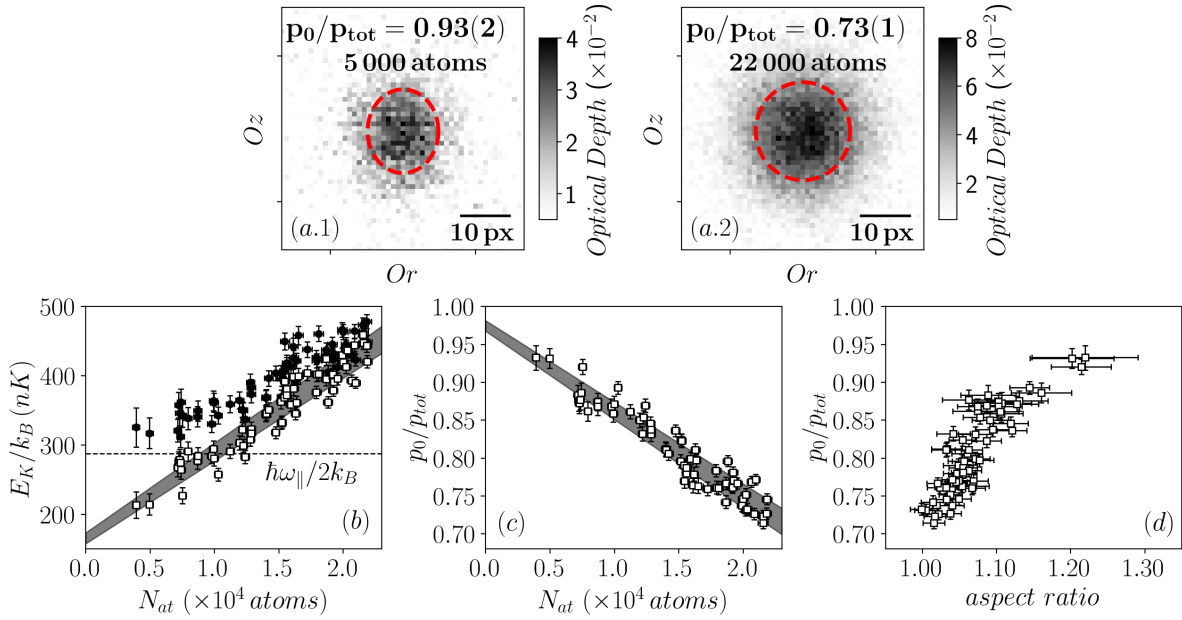


Figure 5.2: Classical analysis from *tof* images, with 10 *ms* time of flight. (a.1) and (a.2): Absorption images of gases with respectively 93(2) % and 73(1) % atoms in the lowest band, with indicated RMS radius in red dashed line. (b) Kinetic energy, along *Or*, *i.e.* along the 2D layers (empty squares), and along *Oz*, *i.e.* along the lattice eigenaxis (filled circle), as a function of the number of atoms. The horizontal dashed line indicates the kinetic energy of the lowest Wannier state. (c), probability of occupation of the lowest band  $p_0/p_{tot}$ , as a function of the number of atoms. (d) probability of occupation of the lowest band as a function of the aspect ratio  $\sigma_z/\sigma_r$ . On (b) and (c), the grey filled slope are linear fits, filled at  $\pm 1\sigma$  fit uncertainty.

to the loading.

From the measurement of the temperature of the gas loaded into the 1D lattice, we infer the bands populations from the Boltzmann factor:

$$p_n(T) = e^{-\varepsilon/k_B T} \quad (5.2)$$

and the probability of occupation of the band  $n$  is defined as  $p_n/Z$  where  $Z$  is the partition function. For a given temperature, it is defined in the canonical ensemble as  $Z(T) = \sum_n p_n(T) = p_{tot}$ . The probability of occupation of the lowest band in this

classical approximation  $r_0|_C$ , that I here define as the efficiency of the loading:

$$r_0|_C = p_0(T)/p_{tot} \quad (5.3)$$

is shown on figure 5.2, (c), as a function of the number of loaded atoms  $N_{at}$ . We are able to load up to 93(2) % atoms into the lowest band of the 1D lattice, with approximately 5000 atoms.

The aspect ratio of the loaded gas is compared to the inferred  $p_0/p_{tot}$  on figure 5.2, (d), which shows the strong correlation,  $C = 0.85$ , between the two quantities. Indeed, the lower bound of the momentum distribution  $\langle p_z^2 \rangle$  along the eigen axis of the lattice is the momentum spread of the lowest Wannier state. Considering a gas cold enough so that all excited bands are empty, which reads with the Boltzmann factors

$$e^{-(\varepsilon_1 - \varepsilon_0)/k_B T} \ll 1 \iff k_B T \ll \varepsilon_1 - \varepsilon_0 = \hbar\omega_{\parallel} \quad (5.4)$$

the kinetic energy within the 2D layers decreases as much as the temperature while it remains constant along the lattice eigen axis. Hence, the increase of the aspect ratio is a good signature that the band excitation degree of freedom is vanishing and the gas reaches a 2D regime.

This measurement shows that we are able to produce 2D gases of strontium 87 with 93(2) % atoms into the lowest band. However, this classical approach doesn't account for the Fermi statistics. Differently populated sites have different chemical potentials, and hence different probabilities of occupation of the lowest band. Indeed, with sites spacing  $a = 2 \mu m$ , the atomic cloud extends over a few sites only, where  $a_{ho} \simeq 1 \mu m$  prior to the loading, and the tunneling rapidly decays when the lattice depth is increased so that the populations are not redistributed between the sites. An accurate description of the loaded gases then requires to consider different chemical potentials at every site, and it cannot be accounted for in the classical analysis of the time of flight images since the density of a classical gas does not depend on the chemical potential. Hence, I will now discuss a semi-classical approach that I use to accurately describe the thermal state of degenerate fermions loaded in several layers of a low recoil 1D lattice with a

non uniform distribution of the number of atoms.

## 5.4 Band populations in the semi classical approximation for a 2D gas of Fermions

In this section, I first derive the analytic equations from the Fermi statistics that permit to infer the probability of occupation of the lowest band of a deep 1D lattice. Accounting for the non uniform population in every site of the 1D lattice, I derive a formula that relates the chemical potentials of every site, to the relative populations. The fitting function used to analyse absorption images after time of flight of the Fermi gas trapped into the 1D lattice is then derived, accounting for the several layers with different number of atoms.

### 5.4.1 Derivation of the number of atoms in each band

In the following derivations, I consider that the sites of the 1D lattice are 2D harmonic oscillators with quasi-classical phase space cells  $d^2r d^2p/h^2$ . In the deep 1D lattice approximation, with  $V_0 \simeq 1800E_R \gg E_R$ , the bands of the lattice are considered as vibrational states of a quantized harmonic oscillator [BDZ08] with degree of freedom  $n$ , which I will next consider equivalently. In this case, the Hamiltonian with no interactions reads

$$H_n(r, p) = \frac{p^2}{2m} + \frac{1}{2}m\omega_{\perp}^2 r^2 + (n + \frac{1}{2})\hbar\omega_{\parallel} \quad (5.5)$$

This hamiltonian is separable, such that the in plane physics and axial quantized physics can be treated separately, and  $\varepsilon_n(r, p) = \varepsilon_{2D}(r, p) + \varepsilon_n$ , where  $\varepsilon_n = (n+1/2)\hbar\omega_{\parallel}$ , and the associated Fermi Dirac occupation number reads

$$f_n(r, p) = \frac{1}{\exp(\beta(\varepsilon_{2D}(r, p) + \varepsilon_n - \mu)) + 1} \quad (5.6)$$

The band energies  $\varepsilon_n$  can be injected into the chemical potential  $\mu_n = \mu - \varepsilon_n$ , which is a similar approach to the Thomas-Fermi approximation [GPS08], here associated to the vibrational degree of freedom of the quantized harmonic oscillator. In this case,

#### 147.4. Band populations in the semi classical approximation for a 2D gas of Fermions

the phase space density of each band  $n$  is the same except that the chemical potential is shifted by exactly the energy of the band. It is then possible to directly derive the density  $n(r)$  as the sum of 2D densities over all populated bands:

$$n(r) = \sum_n n_{2D}(r, \mu_n) \quad (5.7)$$

where  $n_{2D}(r, \mu_n)$  is the *local* density of each vibrational state  $n$ :

$$n_{2D}(r, \mu_n) = \frac{-1}{\Lambda_{DB}^2} Li_1(-e^{\beta(\mu_n - V(r))}) \quad (5.8)$$

It is calculated by integrating the phase space density over the 2D momentum (see appendix [A](#)), and using the definition of polylogarithm for the integral of the Fermi Dirac distribution at  $T \neq 0$ , according to equation [A.18](#). The number of atoms  $N_n$  in the band  $n$  is then computed by integrating the density according to the integration rule for the polylogarithm:

$$N_n(T, \mu_n) = - \left( \frac{k_B T}{\hbar \omega_{\perp}} \right)^2 Li_2(-e^{\beta \mu_n}) \quad (5.9)$$

The probability of occupation of the lowest band  $n_0$  is then:

$$r_0(T, \mu) = \frac{N_0}{\sum_n N_n} \quad (5.10)$$

This is consistent with the fact that occupation of energy states is defined by the Fermi Dirac distribution, as a function of the temperature and chemical potential. The numerical result of equation [5.10](#) is presented on figure [5.3](#). Obviously, the probability of occupation of the lowest band increases at lower temperature, as the occupation number of high energy states is lower than at high temperature. Moreover, for any fixed temperature, a lower chemical potential implies a higher fraction of atoms in the ground band. Let's focus on the  $T = 0 K$  regime where the chemical potential is the Fermi energy, which is pictured as the thick dashed line on figure [5.3](#). Until Fermi energy  $\varepsilon_F$  reaches the energy of the first excited band, pictured as the filled region at  $\varepsilon = \frac{3}{2} \hbar \omega_{\parallel}$ , all atoms occupy energy states lower than  $\varepsilon_F$ , which is the ground band

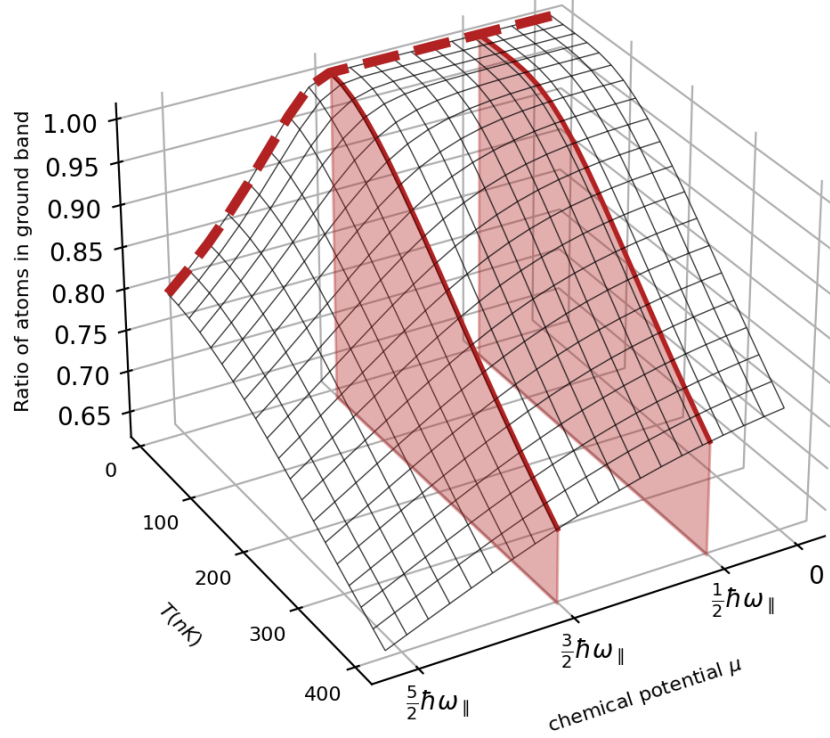


Figure 5.3: Ratio of atoms in the ground band of the 1D lattice, with respect to the temperature  $T$  and the chemical potential  $\mu$ . The red fills indicate the energy of the first two vibrational states at  $\varepsilon_0 = \hbar\omega_{\parallel}/2$  and  $\varepsilon_1 = 3\hbar\omega_{\parallel}/2$ . The chemical potential read at  $T = 0$  is the Fermi energy, and the ratio of atoms in the first band at  $T = 0$  with respect to the Fermi energy is plotted in dashed line. The ratio has been computed with equation 5.10 by taking into account the populations into the first 10 vibrational states. Here,  $\mu > 0$ , assuming that the gas is degenerate with  $T/T_F < 0.6$ .

only, and  $r_0 = 1$ . As soon as  $\varepsilon_F \geq \varepsilon_1$  atoms can populate the first excited band. As introduced in section 5.1, this sets a limit in the maximum number of atoms  $N_{max}$  that can populate the ground band only, such that  $\varepsilon_F \leq \varepsilon_1$ . Using the definition of  $\varepsilon_F$  from equation 5.1, this limit reads

$$N_{max} = \frac{1}{2} \left( \frac{\hbar\omega_{\parallel}}{\hbar\omega_{\perp}} \right)^2 \quad (5.11)$$

Regarding the experiment this limit is very important. Considering there are 25% atoms in the most populated 2D layer, where  $\omega_{\perp}/2\pi \simeq 80 \text{ Hz}$  and  $\omega_{\parallel}/2\pi \simeq 12 \text{ kHz}$ , then the 1D lattice could not be loaded with a gas which has initially more than approximately 10 000 atoms per spin state and per lattice site at  $T = 0 \text{ K}$  if we want the first band only to be populated in order to prepare a 2D gas. Obviously, the  $T = 0 \text{ K}$  limit can't be reached. At  $T \neq 0 \text{ K}$ , the wings of the Fermi Dirac distribution are enlarged, such that probability of occupation of the first excited states is enlarged and the chemical potential has to be lowered, hence the number of atoms, in order to maintain a high  $r_0$ .

### 5.4.2 Accounting for multiple layers in the lattice

The site spacing  $a$  of the 1D lattice is approximately  $2 \mu\text{m}$ , which means that the gas can extend over several sites just before loading the 1D lattice. In our experiment, we measure the number of atoms in each site with a magnification of the loaded lattice (see section 1.2.1 of chapter 1), and the result is recalled on figure 5.4. Our measurement shows that approximately 8 sites are significantly loaded with different populations. To account for this feature to measure the number of atoms in each band, I assume the following assertions.

First, the recoil momentum associated with the lattice  $k_R = \pi/a$  is very low, as a consequence of the large site spacing, and therefore the tunneling  $t \propto \exp\left(-2\sqrt{V_0/E_R}\right)$  [BDZ08] rapidly vanishes when the lattice depth  $V_0$  is increased, up to  $V_0 \simeq 1800E_R$  in our experiment. Hence, the inter layer coupling is negligible and we do not assume inter layer equilibrium. It is then possible to assign a different chemical potential to each site  $i$ , according to a local chemical potential of the gas binned around site  $i$ , making use of the local density approximation (LDA). This means that each layer of the 1D lattice must have a different degeneracy, chemical potential, and entropy per particle, depending on the number of atoms  $N_i$  which have been initially loaded in each lattice site  $i$ .

Then, before loading the lattice, the initial gas is at thermal equilibrium, with a

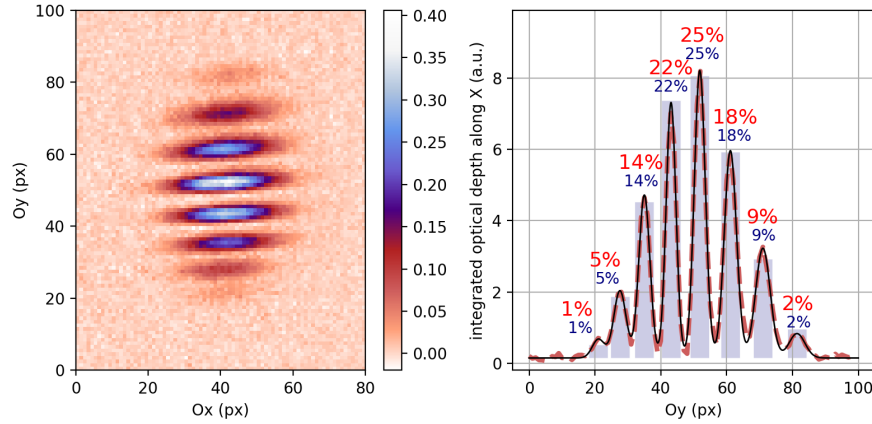


Figure 5.4: Magnification of the sites of the 1D lattice using the quantum magnifier scheme [Ast+21] along the vertical axis. Left: experimental absorption image of the magnification of the sites. The color bar represents the optical depth. Right: fit of the integrated optical depth to measure the populations into the different 2D layers. The relative population measured in each layer is noted as a percentage above each peak picturing a layer, in red, big font. The bins represent a guess of the populations with respect to the size  $\sigma$  of the initial gas and the sites spacing  $a$  of the lattice. Here,  $\sigma \simeq 3.1 \mu m$  and  $a \simeq 2 \mu m$ . The relative population guessed in each layer is noted as a percentage above each peak picturing a layer, in dark blue, small font

well defined temperature. Temperature is an intensive thermodynamic quantity, such that when the gas is separated into the different sites, each fraction of the gas must have the same temperature, since the potential is the same for each fraction of the gas. Then the lattice depth is slowly increased, and assuming that the trap curvature is negligible over a few sites of the lattice (8 in our case), the adiabatic theorem for dipole trap compression  $T/\omega = T'\omega'$  holds, and the compression is the same at each site. Therefore, the temperature is the same in every site of the deep 1D lattice.

Now I use these assertions to define the chemical potential for each site. Each site, or 2D layer, is independent and at thermal equilibrium, so that the relation between the number of atoms and chemical potential defined in equation 5.9 can be used independently for each layer. Since the temperature and confinement frequency are the same in each layer, it possible to link the chemical potential of two layer  $i$  and  $j$  with respect to the ratio of the number atoms only:

$$Li_2(-e^{\beta\mu_i}) = \frac{N_i}{N_j} Li_2(-e^{\beta\mu_j}) \quad (5.12)$$

With the distribution of atoms into the different layers known, that can be measured with the magnification of the lattice sites, all the chemical potentials are then inferred from a single free parameter  $\mu_0$ , and it is then possible to determine all of the thermodynamic and statistical quantities of the independent gases loaded in several 2D layers of the 1D lattice.

### 5.4.3 Fit function with time of flight imaging

Let's now derive the fitting function to measure the thermodynamics quantities from the expanded density after time of flight, assuming that the mean-field energy can be neglected and that ballistic expansion is a good approximation. From this measurement, it is then possible to infer the bands populations in every site of the 1D lattice. It is an application of the fitting functions for the imaged densities of expanding Fermi gases [KZ08; DeM01] to the Hamiltonian defined in [5.5], accounting for the vibrational degree of freedom  $n$  and the different 2D layers  $i$ .

The Hamiltonian [5.5] is separable, and the expansion during the time of flight can be treated separately along the layers and along the axis of the lattice.

First, along the lattice eigen-axis, atoms occupy the localized Wannier states, which expand as the harmonic oscillator eigenstates in the deep-lattice approximation. Assuming that most atoms are in the lowest Wannier state, the momentum distribution along the lattice eigenaxis can be considered Gaussian as a first-order approximation.

Then, along the 2D layers, we want to derive the expansion of the density of atoms defined in equation [5.8]. Let's consider a single layer first. The expanded density  $n(r, t)$  after time of flight of duration  $t$  is derived from the initial phase space density distribution  $f_n(r_0, p_0)$  in the trap, respecting energy conservation so that  $r(t) = r_0 + p_0 t/m$ :

$$\begin{aligned}
n_{tof}(r, t) &= \sum_n \int d^2 r_0 \int \frac{d^2 p_0}{h^2} f_n(r_0, p_0) \delta(r - (r_0 + p_0 t/m)) \\
&= \frac{2mk_B T}{h^2 b^2} \sum_n \int d^2 q \frac{-1}{e^{q^2/z} - 1}
\end{aligned} \tag{5.13}$$

where  $b^2(t) = 1 + \bar{\omega}^2 t^2$  is the scaling factor [KSS96; CD96], and the change of variable  $q^2 = \beta b^2 p_0^2 / 2m$  has been made. Here,  $z = \beta(\mu_n - V(r)/b^2(t))$ , where  $\varepsilon_n$  is the excitation energy of band  $n$ . Using the formula for the integration of the polylogarithm, the 2D density after time of flight reads:

$$n_{tof}(r, t) = \frac{-1}{\Lambda_{DB}^2 b^2(t)} \sum_n Li_1(-e^{\beta(\mu - \varepsilon_n)} e^{-\beta V(r)/b^2(t)}) \tag{5.14}$$

In our experiment, we image by the side of the 1D lattice, *i.e.* along one of the axis of the 2D confinement. The integrated density profile along the imaging axis is then:

$$n_{tof}^{integrated}(x, t) = \frac{-2\pi a_{ho}^2}{\Lambda_{DB}^3 b(t)} \sum_n Li_{3/2}(-e^{\beta(\mu - \varepsilon_n)} e^{-\beta V(x)/b^2(t)}) \tag{5.15}$$

which depends on the free parameters  $(\omega_\perp, \omega_\parallel, T, \mu)$ . The depth of the lattice can be measured independently (see section 1.2.1 of chapter 1), so that the lattice band gap  $\hbar\omega_\parallel$  is known. Moreover, the harmonic confinement of frequency  $\omega_\perp/2\pi$  within the 2D layers can be inferred from a measurement of the size of the gaussian laser beams. Accounting for the different 2D layers  $i$ , the fit function used on time of flight images of gas loaded in the 1D lattice is then:

$$n_{tof}^{integrated}(x, T, \mu_0) = \sum_i n_{tof,i}^{integrated}(x, T, \mu_i) \tag{5.16}$$

where

$$n_{tof,i}^{integrated}(x, T, \mu_i) = \frac{-2\pi a_{ho}^2(\omega_\perp)}{\Lambda_{DB}^3(T, \omega_\perp) b(\omega_\perp)} \sum_n Li_{3/2}(-e^{\beta(\mu_i - \varepsilon_n(\omega_\parallel))} e^{-\beta V(x, \omega_\perp)/b^2(\omega_\perp)}) \tag{5.17}$$

with free parameters  $T$  and  $\mu_0$ , and the other  $\mu_i$ 's are inferred from  $\mu_0$  using equation 5.12 and the relative number of atoms in every layer, that is measured independently.

This concludes the derivation of the fit function with the semi-classical approach, and now, it can be applied to our data.

## 5.5 Semi-classical measurement of the bands populations of several independent 2D layers

In this section, I present the application of the semi-classical approach to analyse the time of flight images of the gases loaded in the 1D lattice. The procedure of loading is detailed in section 5.3. The gases are loaded after evaporation, and the initial temperature, number of atoms, and degeneracy, before loading the lattice, are set by tuning the depth of dipole trap prior to the loading. The gas are released 250 ms after loading, and imaged with absorption imaging after 10 ms time of flight. Using the semi-classical analysis, I show that we are able to prepare several independent 2D Fermi gases with 93(2) % atoms in the lowest band of the 1D lattice, which is the same result than the classical analysis, and the measurement of the chemical potentials further shows that the 2D gases are not degenerate with  $\mu < 0$ . Then I will discuss the efficiency of the loading as a function of the evaporation depth. With deep evaporation, our experiment reaches its lower limit of measurable temperatures  $5 \pm 5$  nK, and the efficiency of the loading of the lowest band is further improved by pursuing the evaporation.

### 5.5.1 Analysis of a single image

To apply the semi-classical analysis, I assume that the temperature is well defined and equal in all the sites, and that the inter-site tunneling is negligible. Moreover, the distribution of atoms in the sites of the lattice is well known, with 8 populated sites, from the magnification measurement (see figure 5.4). The fit function 5.16 can then be used to measure the temperature  $T$  and a reference chemical potential  $\mu_0$ , that I attribute to the most populated site. The chemical potentials of all other sites can then be inferred from equation 5.12. Note that the three spins mixture is accounted for by considering three independent population distributions in every layer, that are weighted by the relative populations in every spin state. The chemical population of each spin state in every layer is then inferred from equation 5.12. The fitted chemical potential is

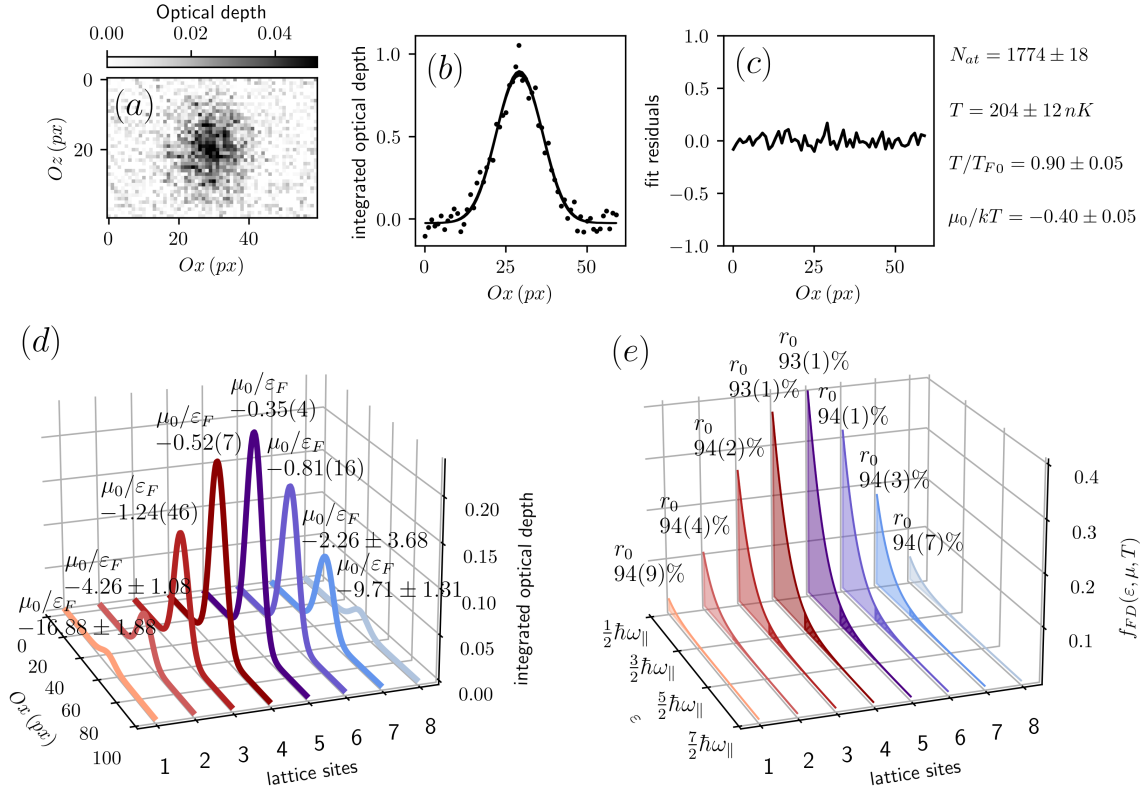


Figure 5.5: Semi classical analysis of time of flight absorption images of a gas loaded in several sites of a deep 1D lattice. (a) Absorption image (b) Integrated optical depth along the lattice eigenaxis  $Oz$  (dots) and result of the fit using equation 5.16 (solid line). (c) Fit residuals, and measured temperature  $T$  and 2D chemical potential  $\mu_0 = \mu - \varepsilon_0$  of the most populated layer for this image. (d) Artificial split of the optical depths of every site, and associated *local* chemical potential inferred from  $\mu_0$ . (e) Fermi Dirac occupation number  $f_{FD}(\varepsilon, \mu, T)$  for every site. The energy axis is in bang gap  $\hbar\omega_{\parallel}$  units, and the population of the lowest band is indicated above each site.

that of the most populated spin in the most populated layer, from which the chemical potentials for the different spin states in the different layers are deduced.

The fit function 5.16 can be used with two free parameters only,  $T$  and  $\mu_0$ . The parameters  $T$ ,  $\mu_0$ ,  $\omega_{\perp}$ , and  $\omega_{\parallel}$ , are highly correlated, so that the fit uncertainty is strongly increased if all parameters are free. It is then convenient to infer  $\omega_{\parallel}$  and  $\omega_{\perp}$

from independent measurements, so that they are fixed and the uncertainty of the fits is drastically reduced.

The band gap  $\hbar\omega_{\parallel} = 2\sqrt{V_0 E_R}$  is directly infered from the measurement of the depth  $V_0$  of the 1D lattice (see chapter [1](#)). In this run,  $V_0 \simeq h \times 255$  kHz, which sets the associated band gap frequency to  $\omega_{\parallel}/2\pi \simeq 12$  kHz. The radial confinement within each layer of the 1D lattice can be approximated as a harmonic potential in the bottom of the sites:

$$V_0 e^{-2r^2/w^2} \Big|_{r \rightarrow 0} \simeq V_0 \left(1 - 2\frac{r^2}{w^2}\right) \simeq V_0 + \frac{1}{2}m\omega_r^2 r^2 \quad (5.18)$$

where  $w$  is the waist of the laser beam. Hence, the radial frequency  $\omega_r$  can be directly infered from the depth  $V_0$  and waist  $w$  as:

$$\omega_{x,y}^2 \simeq \frac{4|V_0|}{mw_{x,y}^2} \quad (5.19)$$

In our experiment,  $|V_0| \simeq 255$  kHz, and the measured waists are  $w_x \simeq 170$   $\mu$ m and  $w_y \simeq 105$   $\mu$ m. The geometric mean of the radial frequency  $\omega_{\perp}^2 = \omega_x \omega_y$  is then:

$$\frac{\omega_{\perp}}{2\pi} \simeq 80 \text{ Hz} \quad (5.20)$$

For the analysis,  $\omega_{\perp}$  and  $\omega_{\parallel}$  are then fixed to the respective values  $2\pi \times 80$  Hz and  $2\pi \times 12$  kHz.

The result of the semi-classical analysis of a time of flight absorption image is presented on figure [5.5](#). The optical depth, shown on (a), is integrated along the eigen axis of the lattice (Oz), and it is fit using the fit function [5.16](#). For this gas, the measured temperature is  $T = 210 \pm 14$  nK, and the measurement of the chemical potential of the most populated layer  $\mu_0/k_B T = -0.40(5)$  is then used to infer the chemical potential of the other layers using relation [5.12](#). Figure [5.5](#), (d), shows an artificial split of the sites and their respective chemical potentials. The thermodynamics properties are known in every site, and the Fermi Dirac occupation number  $f_{FD}$  is well determined, and it is plotted on figure (e). The band populations can be infered from equation [5.9](#), and the probability of occupation of the lowest band  $r_0$ , defined in equation [5.10](#), here measured  $r_0 = 93 \pm 1\%$ , is shown on figure (e) for every site.

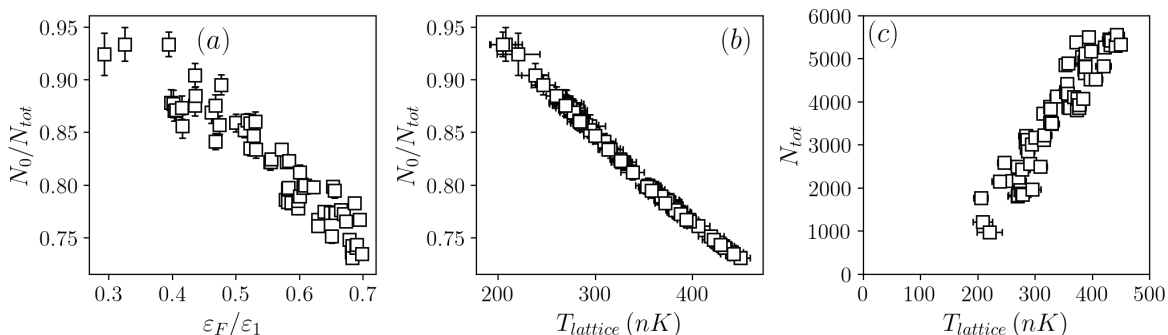


Figure 5.6: (a) Population in the lowest band as a function of the Fermi energy  $\varepsilon_F$  in units of the energy of the first excited band  $\varepsilon_1 = 3/2\hbar\omega_{\parallel}$ , into the most populated layer. (b) Population in the lowest band as a function of the measured temperature into the lattice. (c) Number of atoms into the most populated layer as a function of the temperature.

This result shows that it is possible to infer the thermodynamic properties of independent sites of the 1D lattice with the distribution of atoms known, even if they are not distinguishable on a single absorption image, assuming a uniform adiabatic compression in every site and negligible tunneling. With this method, we measure that we are able to prepare a set of independent 2D Fermi gases with  $r_0 > 90\%$  that can be analysed simultaneously. The semi-classical analysis is made easier with independent measurements of the lattice depth, and the harmonic confinement within each site. Note that here the signal to noise ratio (SNR) of the integrated density profile is slightly lower than 10. With a better SNR, the independent measurements on the lattice geometry should not be required to have significant measurements.

The joint measurement of the chemical potential of the most populated layer  $\mu_0/k_B T = -0.40(5)$  and temperature  $T \simeq 210$  nK gives a measurement of the Fermi energy, which is lower than the energy of the first excited vibrational state  $\varepsilon_F/\varepsilon_1 \simeq 0.3$ , where  $\varepsilon_1/k_B \simeq 870$  nK. Hence, the population of the lowest band is not saturated by the number of atoms, and assuming thermal equilibrium, the residual band excitations are then due to the non zero temperature. Figure 5.6, (a) shows the increase of  $r_0 = N_0/N_{tot}$  as a function of the Fermi energy  $\varepsilon_F$ , which approximately amounts to the number of atoms, and (b) as a function of the temperature  $T$  into the lattice. This measurement shows

that our production of multiple 2D degenerate gases with best  $r_0 \simeq 93(1)\%$  is due as much to a reduced number of atoms, *i.e.* chemical potential, as to a low temperature.

*Comparison with the classical analysis:* both the classical and semi-classical provide the same measurement of the probability of occupation of the lowest band, and this shows that the degeneracy of the 2D gas is not sufficient for the density to significantly deviate from a Gaussian distribution. This is further confirmed by the measurement of negative chemical potentials. However, the semi-classical approach provides an accurate description of the loading of several independent 2D Fermi gases which are not uniformly populated, and this approach can be applied on further degenerate gases. Moreover, the chemical potentials and degeneracies of every layer can be measured from a single absorption image, with the distribution of atoms known.

### 5.5.2 Systematic study as a function of the evaporation depth, for SU(3) and SU(10) gases

The efficiency of the lattice loading with a three spins mixture with populations 10%, 20% and 70%, and an equipopulated SU(10) gas, are here compared as a function of the evaporation depth prior to the loading, read as the geometric mean frequency of the dipole trap  $\bar{\omega}$ . It is inferred from an independent calibration of the trap geometry. Note that in this study, the evaporation approaches spilling, so that the estimation of  $\bar{\omega}$  is uncertain. Hence, *the value of  $\bar{\omega}$  has to be read with caution*, and its use only intends to give a reading of the depth of the evaporation, else than the numeric command that we use on our experiment.

The probability of occupation of the lowest band is plotted on figure 5.7 (a), as a function of  $\bar{\omega}$  at the end of the evaporation, and the tendency is a regular increase towards 100% for both mixtures, however a slight increase of the slope can be observed for  $\bar{\omega}/2\pi < 50$  Hz. In this measurement, the efficiency of loading with a SU(10) gas is larger by approximately a multiplicative factor 1.05. Figure 5.7 (b), and (c), respectively show the number of atoms in a single spin state, here the most populated of the SU(3) preparation, and temperature of the gases prior to the loading as a function of

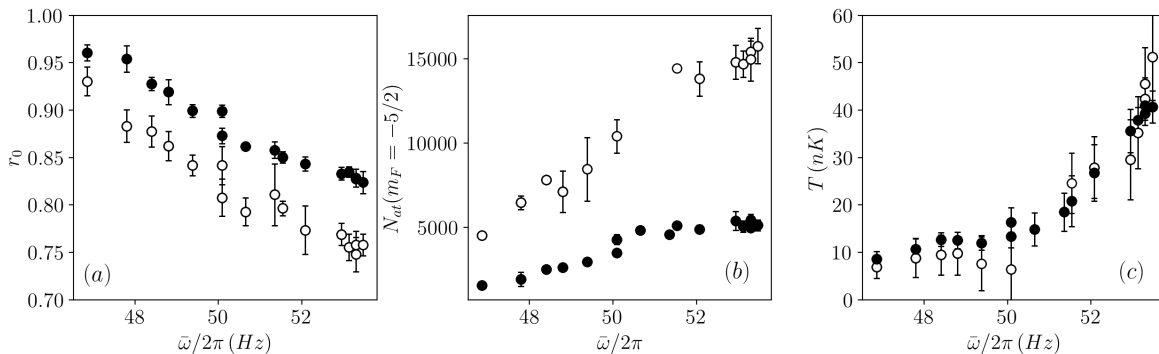


Figure 5.7: SU(3) (empty squares) and SU(10) (filled circles) loading of the lowest band as a function of the evaporation depth. (a) Probability of occupation of the lowest band  $r_0$  as a function of the geometric mean frequency  $\bar{\omega}$  of the dipole trap, which is inferred from independent measurements. (b) Number of atoms  $N_{at}$  in  $m_F = -5/2$ , into the dipole trap before loading as a function of  $\bar{\omega}$ . It represents 70% of the total number of atoms into the SU(3) gas, and 10% into the equipopulated SU(10) gas. (c) Temperature of the gas before loading as a function of  $\bar{\omega}$ .

$\bar{\omega}$ . Ultra-cold temperatures  $T \simeq 10$  nK are reached from  $\bar{\omega}/2\pi \simeq 50$  Hz, and further evaporation results in atom depletion only. These measurements show that deep evaporation prior to the lattice loading increases the probability of occupation of the lowest band after loading, and this is associated with very low initial temperatures as well as low chemical potentials.

On figure [5.8](#), the degeneracy of the 2D gas  $T/T_F$  after loading is compared to the depth of evaporation, for both SU(3) and SU(10) gases. In both cases, the measurement shows that deeper evaporation prior to the loading doesn't permit to produce more degenerate 2D gases. A possible explanation is that in this experiment, we reach very low temperatures at the end of the evaporation by reducing simultaneously the horizontal and vertical confinements of the dipole trap, which reduces significantly the collision rate. Consequently, when the lattice is turned on, adiabatic following of the lattice depth compression is made very difficult, which is already challenging for degenerate fermions due to Pauli blocking.

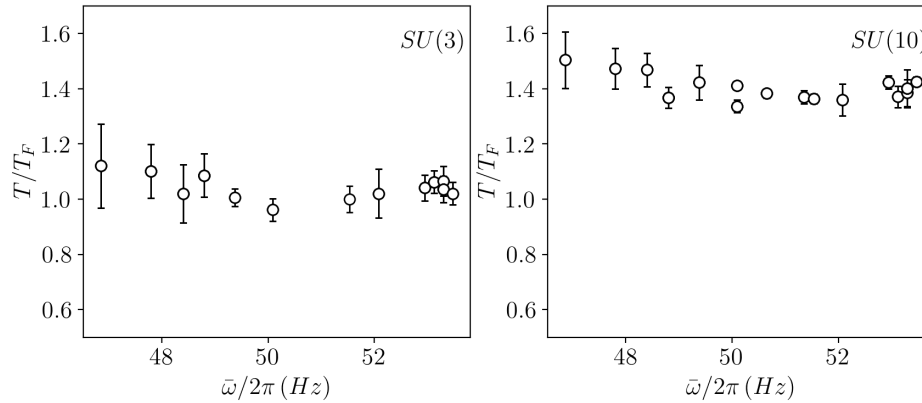


Figure 5.8: Degeneracy  $T/T_F$  for SU(3) (left) and SU(10) (right) gases after loading of the lowest band as a function of the evaporation depth.

### 5.5.3 Preparation of degenerate Fermi 2D gases with improved adiabaticity

To enhance the loading efficiency, we experienced two modifications to the previous protocole.

First, we compensated for the low collision rate when the lattice depth is increased. Closed shell  $^{87}\text{Sr}$  atoms do not benefit from Feshbach resonances to tune the interaction strength. Hence, we rather hold a strong transverse harmonic confinement compared to the previous experiment, with the vertical laser beam of the optical dipole trap (ODT), that propagates mostly along the lattice eigenaxis. In the previous experiment, its power was lowered to reach deep evaporation, until the transverse frequency  $\omega_{\perp}^{ODT}$  reached approximately  $2\pi \times 30$  Hz, and it is now held at approximately  $2\pi \times 85$  Hz.

Second, the lattice depth is increased to only  $h \times 70$  kHz in 500 ms, which reduces the band gap from  $\omega_{\parallel} \simeq 2\pi \times 12$  kHz to  $\omega_{\parallel} \simeq 2\pi \times 6.4$  kHz. Consequently, the transverse harmonic confinement of the lattice is also reduced. However, the vertical ODT beam is not turned off, and the total transverse frequency after loading is now approximately  $\omega_{\perp} \simeq 2\pi \times 95$  Hz.

The result of the lattice loading with a SU(10) gas of 12000 atoms initially at  $T \lesssim 20$  nK and  $T/T_F \gtrsim 0.15$  is shown on figure [5.9](#). With this preparation, the



periments indicate that it is much more favorable to hold sufficiently high harmonic confinement for isentropic transformations with degenerate alkaline-earth fermions, than to reach ultra deep evaporation where collisions are strongly inhibited. Also, the final depth of the lattice can be an important parameter that has to be investigated. Further systematic study for this protocole is planned.

## 5.6 Conclusion and outlook

In this chapter, I have shown the production of several independent 2D Fermi gases of  $^{87}\text{Sr}$  atoms with populations ranging from 1 000 to 1 700 atoms in a three spins mixture with relative populations 10%, 70% and 20%. In a first set of experiments, the probability of loading of the lowest band of the 1D lattice is 93(2)% with a band gap  $\omega_{\parallel} = 2\pi \times 12$  kHz and Fermi energy  $\varepsilon_F$  one third of the energy of the first excited band. Improved adiabaticity is shown in a second experiment by holding sufficient dipole trap compression prior to the loading into less deep lattice. This way, we are able to produce 4 independent 2D degenerate SU(10) Fermi gases with  $\mu_0/\varepsilon_F \geq 0.4$  and approximately 99% atoms into the lowest band. This preparation will be the starting point for the loading of 2D lattices to realize a SU(1) band insulator. The 2D gases shall be adiabatically loaded in a 2D square lattices to prepare several non interacting band insulators [Leb+18]. The independent 2D Fermi gases can be later used as independent realizations of a same experiment in a 2D geometry [Fel+11], similarly to wire arrays experiments [Gre+01; Par+04].



# Conclusion

In this thesis, I reviewed my contributions to the various protocols required for the realization of the 2D Fermi-Hubbard model with enlarged  $SU(N)$  symmetry with strontium 87. These key protocols are now sufficient to reach the short term objectives of the experiment, *i.e.* an adiabatic following to the lowest energy states of a  $SU(2)$  quantum magnet, with a full control and monitoring over the spin dynamics in 2D lattices that will provide a first demonstration of super-exchange dynamics on our experiment.

## Summary

In chapter 2, I presented our method to measure local densities with absorption imaging of objects smaller than the resolution limit of our imaging setup. I have shown that the fast variations of the local density are averaged over the resolution limit, and this results in non-linear errors on the imaged density. This correction is demonstrated on elongated Fermi gases, from which we infer the unresolved transverse size, as small as one fourth of our imaging resolution limit. The density profile along the longitudinal axis, distorted by the non linear error, is also recovered with our method. This work was first motivated by an experiment to measure the enhanced mean-field interaction in the weakly interacting regime of a  $SU(10)$  degenerate Fermi gas. For this, we wanted to further enhance the mean-field signal with a 1D expansion, *i.e.* by allowing the gas to expand along direction axis only, so that the full mean-field energy is converted to kinetic energy into this axis only. Although this investigation was not conclusive due to thermalization failure, it yielded the establishment of the demonstrated method, which was required for the analysis of the tightly confined gas expanding in 1D.

In the last chapter, I have shown that we can prepare 2D Fermi seas with  $\mu/\varepsilon_F \geq$

0.4 and approximately 99% atoms in the lowest band of the 1D lattice. With spin selective blast, the Fermi gases will next be polarized, as demonstrated in chapter 3, and adiabatically loaded in the 2D square lattices to prepare several band insulators with a single spin component.

In chapter 4, I demonstrated a method to selectively flip the nuclear spins of strontium 87 with Raman adiabatic passages and a tensor light shift associated with the intercombination line, with actual approximately 80% efficiency. Next, using a spin dependent optical superlattice realized by simply retroreflecting the tensor light shift beam, a Néel spin order shall be written from the band insulators, with approximately 97% fidelity according to my simulations. It will then be possible to adiabatically approach the regime where many-body physics are driven by super-exchange interactions, by slowly reducing the depth of the spin dependent superlattice.

The alternate magnetization along the quantization axis will be measured by first reversing the texture writing protocole, then measuring the spin populations as demonstrated in chapter 3. The dynamics of the spin ordering, that shall deviate from the initial preparation, will provide a first measurement of the super-exchange dynamics.

## Short-term prospects

The spin correlations, that can result effectively in squeezing of the alternate magnetization, will be detected using the same spin dependent optical superlattice. However, this measurement requires supplementary implements, not discussed in this thesis, and yet to be investigated. The squeezing detection requires a measurement of the variance of the alternate magnetization associated with the SU(2) rotation generators  $\hat{S}_x$ ,  $\hat{S}_y$ , and  $\hat{S}_z$ . Practically, these rotations will be engineered with  $\pi/2$  light pulses, which notably require a stabilization of the intensity of the laser realizing the tensor light shift.

Moreover, the detection of quantum correlations require to reduce the detection noises and fluctuations as close as possible to the standard quantum limit (SQL) [Ala22]. For this, the implementation of a high resolution imaging system with diffraction limit  $1.25 \mu\text{m}$  and reduced noise sensitivity is ongoing. Note that the ground state of strontium 87 with zero angular momentum is very weakly sensitive to magnetic fields, which

is a strong advantage for minimal systematic noise on the measurement of quantum correlations.

Also, the current setup is planned to include a 2D spin independent superlattice at 1064 nm. It will permit to isolate 2x2 clusters on the 2D lattice at 532 nm, to prepare local singlet states. By reducing the depth of the superlattice, either abruptly or slowly, this setup will provide an original measurement of the dynamics from local to global correlations.

## Improvement suggestions

I would like to propose some easy implements that could improve the detection efficiency of the spin populations and facilitate statistical measurements of the spin correlations, as last contribution.

In chapter 3, I have discussed the limitation of our method to measure the spin populations, which is almost entirely due to the laser intensity. In our experiment, we use the retroflected vertical MOT beam to realize the measurement, which has a very large waist of approximately 1 cm and approximately 8 mW power. I suggest to use a dedicated laser setup with a beam of much smaller waist. For instance, a waist of  $100\ \mu\text{m}$  with only  $80\ \mu\text{W}$  power would increase the light intensity by two orders of magnitude, which would significantly increase the efficiency of measurement of the spin populations to approximately 99 %, and hence increase the reliability of the detection of quantum correlations. Furthermore, the simultaneous measurement of multiple spin populations, currently limited by the efficiency of a single adiabatic passage, would be facilitated.

Using a dedicated laser setup, it is possible to change the direction of the momentum transfer, which is presently along the 1D lattice eigen axis. I suggest that the momentum transfer should be orthogonal to the lattice eigen axis. In chapter 1, I demonstrated that we are able to spatially separate the sites of the 1D lattice with the quantum magnifier method. Combined with an orthogonal spin dependent momentum transfer, it would be possible to simultaneously measure the spin populations of every layer in

a single shot. Furthermore, I demonstrated in chapter 5 that we are able to prepare at least 4 independent degenerate 2D gases, that are good candidates to prepare Mott insulators. Hence, it would be possible to realize at least 4 independent experiments, simultaneously measurable.

Considering the required statistical measurements to detect quantum correlations close to the SQL, such a setup would permit to both critically enhance the reliability of the spin populations measurement, and dramatically reduce the average time per experiment to approximately 5 s.

## Outlook

This experiment is designed to study  $SU(N)$  quantum magnetism with strontium 87. The ongoing demonstration of the method to prepare spin textures in  $SU(2)$  is easily generalized to  $SU(N)$ ,  $N > 2$ , by realizing consecutive spin flips. Very interesting investigations will then be lead on the growth of correlations, with tunable  $N$ . For instance, frustrated spin ordering is expected [HGR09], and this experiment will offer a unique platform for this study in square lattices with  $N$  as high as 10.

Taking advantage of enhanced large-spin Pomeranchuk cooling [Tai+12], this experiment shall produce strongly correlated 2D spin ensembles. With a control on the filling factor, a possible implementation of the fermionic t-J model [And87] can be considered, in  $SU(2)$  symmetry, and possibly generalized, in enlarged  $SU(N)$  symmetry, with tunable  $N$ .

Remarkably, this experiment makes use of protocols, notably the artificial magnetic field, very similar to the ones used to implement topological lattices. Accounting for the lattice geometry, and the spatially dependent spin orbit coupling associated with the intercombination line, already implemented on the experiment, artificial gauge fields could be engineered [Sch+20].

# Appendix A

## Basic theory for d-dimensional Fermi gases in harmonic traps

### A.1 Density of states and Fermi energy

Let's consider a shallow d-dimensional (1D, 2D or 3D) harmonic trap. In the semi-classical limit  $k_B T \ll \hbar\bar{\omega}$ , the Hamiltonian reads

$$H(r, p) = \sum_{i=1}^d \frac{1}{2} m \omega_i^2 r_i^2 + \frac{p_i^2}{2m} \quad (\text{A.1})$$

The density of states is then derived from Thomas-Fermi rule, which reads in the semi-classical limit

$$\rho(\varepsilon) = \int \frac{d^d r d^d p}{h^d} \delta(\varepsilon - H(r, p)) \quad (\text{A.2})$$

$$\rho(\varepsilon) = \frac{1}{(d-1)!} \frac{\varepsilon^{d-1}}{(\hbar\bar{\omega})^d} \quad (\text{A.3})$$

From the density of states, it is then possible to derive the number of atoms with integration over the density of states and Fermi-Dirac occupation number  $f_{FD}$

$$N = \int_0^\infty d\varepsilon \rho(\varepsilon) f_{FD}(\varepsilon, \mu, T) \quad (\text{A.4})$$

at  $T = 0 K$ , fermions condensate in the energy states lower than the Fermi energy which is defined as  $\varepsilon_F = \mu|_{T=0}$ , such that the Fermi-Dirac distribution reduces to the heaviside distribution and the number of atoms becomes

$$N = \int_0^{\varepsilon_F} d\varepsilon \rho(\varepsilon) \quad (\text{A.5})$$

Using the definition of the density of states [A.3](#), the d-dimension Fermi energy can be computed directly, with respect to the number of atoms and mean trap frequency  $\bar{\omega} = (\prod_i \omega_i)^{1/d}$

$$\varepsilon_F = \hbar \bar{\omega} (d! N)^{1/d} \quad (\text{A.6})$$

On lower dimensions, the density of states is lowered, such that for a fixed number of atoms, fermions have to occupy higher energy states, and thus the Fermi energy is increased, and this is embedded in the  $N^{1/d}$  scaling of the Fermi energy.

### A.1.1 3D harmonic trap tightly confined along one direction only

In the following derivation, I consider a gas trapped into a 3D harmonic trap tightly confined along one direction only. The transverse shallow confinement is a shallow 2D harmonic trap with associated phase-space cell  $d^2 r d^2 p / h^2$ , and the tight confinement is a quantized harmonic trap with associated degree of freedom  $n$ , the band excitations. In this case, the Hamiltonian with no interactions reads

$$H_n(r, p) = \frac{p^2}{2m} + \frac{1}{2} m \omega_{\perp}^2 r^2 + (n + \frac{1}{2}) \hbar \omega_{\parallel} \quad (\text{A.7})$$

This hamiltonian is separable, such that the in plane physics and axial quantized physics can be treated separately. In this geometry, the density of states  $\rho(\varepsilon)$  of the 2D harmonic confinements within each site of the lattice reads:

$$\rho(\varepsilon) = \sum_n \int \frac{d^2 r d^2 p}{h^2} \delta(\varepsilon - (\varepsilon_{2D}(r, p) + \varepsilon_n)) \quad (\text{A.8})$$

Picturing  $\varepsilon - \varepsilon_n$  as a shift of the 0 energy state, where  $\varepsilon_n = (n + 1/2) \hbar \omega_{\parallel}$ , it amounts to assign an independent 2D density of state  $\rho_n$  for each energy band  $\varepsilon_n$ :

$$\rho_n(\varepsilon) = \frac{\varepsilon - \varepsilon_n}{(\hbar\omega_\perp)^2} \quad (\text{A.9})$$

and then the total density of states is the sum over all bands:

$$\rho(\varepsilon) = \sum_n \frac{\varepsilon - \varepsilon_n}{(\hbar\omega_\perp)^2} \quad (\text{A.10})$$

One can consider the *local* density of states as defined in equation [A.9](#) for each band, so that the number of atoms in each band  $n$  can be computed as follows:

$$N_n = \int_{\varepsilon_n}^{\varepsilon_{n+1} - \delta\varepsilon} d\varepsilon \rho_n(\varepsilon) f_n(\varepsilon, \mu, T) \quad (\text{A.11})$$

where the Fermi-Dirac occupation number  $f_n(\varepsilon, \mu, T)$  is defined as

$$f_n(\varepsilon, \mu, T) = \frac{1}{\exp(\beta(\varepsilon_{2D}(r, p) + \varepsilon_n - \mu)) + 1} \quad (\text{A.12})$$

In the  $T = 0$  limit of a 2D Fermi gas with  $\varepsilon_F < \varepsilon_1$ , the number of atoms into the lowest band is then inferred from

$$N \Big|_{T=0} = \int_{\varepsilon_0}^{\varepsilon_F} d\varepsilon \rho_0(\varepsilon) f_{FD}(\varepsilon, \mu, T) \quad (\text{A.13})$$

and by replacing  $\rho_0$  by its expression given in equation [A.9](#) and  $f_{FD}|_{T=0}$  by the heaviside distribution, the Fermi energy reads

$$\varepsilon_F = \hbar\omega_\perp (2N)^{1/2} + \varepsilon_0 \quad (\text{A.14})$$

This result shows that by taking into account the vertical confinement which allows to engineer a 2D Fermi gas by populating the ground band only of a 1D lattice, the 3D Fermi energy is simply the Fermi energy of the gas living in a 2D layer, *c.f.* equation [A.6](#), shifted by the energy of the ground band.

## A.2 Density and chemical potential, exact derivation in the semi-classical regime

The in-situ density of a Fermi gas is obtained from momentum integration the Fermi-Dirac phase space density

$$n(r) = \int \frac{d^d p}{h^d} f(r, p) \quad (\text{A.15})$$

where  $d$  is the dimensionality. To derive this integral with the Fermi-Dirac distribution, it requires to use the polylogarithm functions, which can be defined as follows [KZ08](#):

$$Li_n(z) = \frac{1}{\pi^n} \int d^{2n} q \frac{1}{e^{q^2/z} - 1} \quad (\text{A.16})$$

$$\int_{-\infty}^{+\infty} dx Li_n(ze^{-x^2}) = \sqrt{\pi} Li_{n+\frac{1}{2}}(z)$$

Equation [A.15](#) has to be rewritten in order to apply the definition of the polylogarithm integral. This is easily done by isolating the kinetic energy  $p^2/2m$  and multiplying by  $-1$ :

$$n(r) = - \int \frac{d^n p}{h^n} \left[ \frac{e^{\beta p^2/2m}}{-e^{\beta(\mu-V(r))}} - 1 \right]^{-1} \quad (\text{A.17})$$

with change of variable  $y^2 = \beta p^2/2m$  and replacing  $n = d/2$ , the identification with polylogarithm is straightforward and the density reads:

$$n(r) = \frac{-1}{\Lambda_{DB}^d} Li_{d/2}(-e^{\beta(\mu-V(r))}) \quad (\text{A.18})$$

where  $\Lambda_{DB} = h/\sqrt{2\pi m k_B T}$  is the DeBroglie wavelength. It is interesting to see here that the fugacity  $q = \beta\mu$  defines the shape of the cloud, while the potential  $\beta V(r) = \frac{1}{2}m\omega r^2$  defines the size of the cloud. Indeed, the fugacity is an homogeneous prefactor to the potential term in the highly non linear polylogarithm function, which distorts the density profile defined by  $\beta V(r) = \frac{1}{2}m\omega r^2$ , for high positive values when

$\mu/\varepsilon_F \rightarrow 1$  and  $T/T_F \rightarrow 0$ . On the other hand, the phase space density tends to a gaussian distribution for a Boltzmann gas if  $\mu/k_B T \rightarrow -\infty$ .

The number of atoms of atoms can then be computed through integration successive integrations of the density and use of the polylogarithm integration defined in equation [A.16](#):

$$N_d = - \left( \frac{k_B T}{\hbar \bar{\omega}} \right)^d Li_d(-e^{\beta \mu_d}) \quad (\text{A.19})$$

This result is important because it directly shows how the number of atoms is linked to the temperature, the trap, and the chemical potential. This makes sens because the chemical potential is the energy cost to add a new particle to the degenerate gas, whose energy and degeneracy is defined by the trap, the temperature, and the number of atoms. Finally, the chemical potential can be derived from equation [A.3](#) by injecting the definition of Fermi energy [A.6](#).

$$Li_d(-e^{\beta \mu_d}) = d! \left( \frac{T}{T_F} \right)^d \quad (\text{A.20})$$

This derivation requires to invert the polylogarithm, which can easily be done numerically with an interpolation. Note that this result shows that the fugacity only depends on the degeneracy of the Fermi gas and on the dimensionality.

### A.3 Thermodynamics and entropy, derivation in the semi-classical regime

In a statistical ensemble at equilibrium, thermodynamics are defined from the first principle of thermodynamics:

$$dU = \partial_S U dS + \partial_V U dV + \partial_N U dN \quad (\text{A.21})$$

where the thermodynamic potential  $U$  is the internal energy for an isolated system. Conjugated thermodynamic quantities  $(\mu, N)$ ,  $(S, T)$  and  $(p, V)$  can be seen as canonical variables connected by the thermodynamic potential  $U$ . In this picture, one quantity

is a generalized force  $\vec{F}$  deriving from the thermodynamic potential  $U$ , through its derivative from a generalized displacement  $\vec{X}$ , *i.e.*  $\vec{F} = -\nabla_{\vec{X}}U$ . This is embedded in the well known definitions

$$\begin{aligned} T &= \partial_S U \\ p &= -\partial_V U \\ \mu &= \partial_N U \end{aligned} \tag{A.22}$$

The choice of the thermodynamic ensemble doesn't actually change the average values of the thermodynamic quantities [Hua87], but working in the proper ensemble is mandatory to derive the fluctuations. For instance, a gas of ultra-cold atoms in a dipole trap is an isolated system, so it requires that the fluctuations are derived in the micro-canonical ensemble. In our case, we are mainly interested at the average values. For this reason, I will next derive entropy and chemical potential in the grand-canonical ensemble, which is more convenient regarding the study of degenerate fermions. (the chemical potential is properly defined by the degeneracy of the gas, the temperature is properly defined by the cooling procedure (MOT then evaporative cooling (open system here), need to explain it briefly). In the grand-canonical ensemble, the thermodynamic potential is the free energy of Landau  $J = U - TS - \mu N$ . In this ensemble, the first principle of thermodynamics becomes:

$$dJ = \partial_T J dT + \partial_V J dV + \partial_\mu J d\mu \tag{A.23}$$

The chemical potential  $\mu$  and entropy  $S$  can then defined from the free energy of Landau as

$$\begin{aligned} S &= -\partial_T J|_{\mu, V} \\ N &= -\partial_\mu J|_{T, V} \end{aligned} \tag{A.24}$$

Those relations are convenient for fermions in the grand canonical ensemble since  $J$  is well defined for degenerate gases, with respect to the number of occupations  $f_{FD}$ . In the semi-classical limit for fermions, the grand potential reads:

$$J = -k_B T \int d\varepsilon \rho(\varepsilon) \log(1 - f_{FD}(\varepsilon, \mu, T)) \quad (\text{A.25})$$

The density of states can be replaced by equation [A.3](#), and after injecting the Fermi energy derived in equation [A.6](#), one gets

$$J_d = -N k_B T d \int \frac{d\varepsilon}{\varepsilon_F} \left(\frac{\varepsilon}{\varepsilon_F}\right)^{d-1} \log(1 - f_{FD}(\varepsilon, \mu, T)). \quad (\text{A.26})$$

It is then convenient to rewrite all energies in Fermi energy units  $\varepsilon/\varepsilon_F$ , as well as temperature in Fermi temperature units  $T/T_F$ . This permits to have a universal reading of the results with respect to a single variable  $T/T_F$  which can be read as the degeneracy of the Fermi gas. Also, the chemical potential expressed in Fermi energy units gives in a direct reading of the degeneracy, since  $\varepsilon_F \equiv \mu|_{T=0}$ , such that  $\mu/\varepsilon_F$  has to saturate to 1 at low temperature. This makes sens because all low energy states are occupied and the energy cost to add a new particle converges to the Fermi energy. Hence, reading the saturation of  $\mu/\varepsilon_F$  gives a direct reading on the energy states occupation. This can be convenient for instance when looking at the sites occupation of the ground band of a lattice. If the Fermi energy is lower than the first excited band, a saturating chemical potential indicates that the occupation number tends to 1 per site. For those reasons, I strongly recommend students to get used to be working on normalized units, such as  $T/T_F$  and  $\varepsilon/\varepsilon_F$  in this case. And more practicaly, it makes the derivations easier.

In normalized units, the Fermi-Dirac distribution is simply rewritten as follows:

$$\begin{aligned} f_{FD}(\varepsilon, \mu, T) &= \frac{1}{e^{\beta(\varepsilon-\mu)} + 1} \\ &= \left[ \exp\left(\frac{1}{T/T_F} \left(\frac{\varepsilon}{\varepsilon_F} - \frac{\mu}{\varepsilon_F}\right)\right) + 1 \right]^{-1} \end{aligned} \quad (\text{A.27})$$

and then with a change of variable  $x = \varepsilon/\varepsilon_F$ , the free energy of Landau can be defined in Fermi energy units, with respect to the degeneracy  $T/T_F$ :

$$\frac{J}{\varepsilon_F} (T/T_F) = -N \frac{T}{T_F} d \int dx x^{d-1} \log\left(1 + \exp\left(-\frac{1}{T/T_F} \left(x - \frac{\mu_d}{\varepsilon_F}\right)\right)\right) \quad (\text{A.28})$$

This equation might look complicated but it is in fact very simple since it depends only on the number of atoms  $N$  and the degeneracy  $T/T_F$ , such that  $J$  can be simply written as

$$\frac{J}{\varepsilon_F}(T/T_F) = -NI(T/T_F) \quad (\text{A.29})$$

where the integral  $I$  depends only on  $T/T_F$ .

$$I(T/T_F) = \frac{T}{T_F} d \int dx x^{d-1} \log\left(1 + \exp\left(-\frac{1}{T/T_F}\left(x - \frac{\mu_d}{\varepsilon_F}\right)\right)\right) \quad (\text{A.30})$$

Using definition [A.24](#), the entropy per particle can be finally calculated by derivating  $I(T/T_F)$  with respect to  $T/T_F$ :

$$\frac{S}{N} = k_B \left[ \frac{\partial I(T/T_F)}{\partial (T/T_F)} \right]_{\mu} \quad (\text{A.31})$$

The entropy per particle can then be computed numerically. In order to have a numerical result in the semi-classical regime with no further approximation, the chemical potential can be computed by using equation [A.20](#). Note that  $\mu/\varepsilon_F = \beta\mu\frac{T}{T_F}$ .

## A.4 Thermodynamics, entropy and chemical potential, degenerate approximations

Previous derivations allow to compute the chemical potential and entropy per particle numerically, but it can be interesting to derive analytic formulas for better insight. In the degenerate regime, the so called Sommerfeld expansion or low temperature expansion is commonly used to approximate integrals dependent on the Fermi Dirac distribution function.

$$\begin{aligned} I &= \int_0^{\infty} d\varepsilon h(\varepsilon) f_{FD}(\varepsilon, \mu, T) \\ &= H(\mu) + \frac{\pi^2}{6} (k_B T)^2 h'(\mu) + \mathcal{O}(k_B T^2) \end{aligned} \quad (\text{A.32})$$

where  $H$  is a primitive of  $h$  and  $h'$  its derivative. To take advantage of the low temperature expansion, it is convenient to use the grand potential definition in equation [A.25](#) without injecting the Fermi energy expression:

$$J = -\frac{k_B T}{(d-1)!(\hbar\bar{\omega})^d} \int d\varepsilon \varepsilon^{d-1} \log(1 - f_{FD}(\varepsilon, \mu, T)) \quad (\text{A.33})$$

First integrating by part  $\varepsilon^{d-1}$  and  $\ln(1 + e^{-\beta(\varepsilon-\mu)})$ , the Sommerfield expansion for the free energy of Landau reads in a  $d$ -dimensional harmonic trap reads:

$$J(\mu, T) = -\frac{\mu^{d+1}}{(d+1)!(\hbar\bar{\omega})^d} \left(1 + \frac{\pi^2}{6} d(d+1) \left(\frac{k_B T}{\mu}\right)^2 + \mathcal{O}(k_B T^2)\right) \quad (\text{A.34})$$

The derivation of entropy  $S$  is then straightforward by directly derivating  $J$  with respect to  $T$ :

$$\frac{S}{N} = d \frac{\pi^2}{3} k_B \frac{T}{T_F} \quad (\text{A.35})$$

The chemical potential is obtained by first computing the number of atoms by derivating  $J$  with respect to  $\mu$

$$N = \frac{\mu^d}{d!(\hbar\bar{\omega})^d} \left(1 + d(d-1) \frac{\pi^2}{6} \left(\frac{k_B T}{\mu}\right)^2\right) \quad (\text{A.36})$$

Then by injecting the  $d$ -dimensional Fermi energy equation [A.6](#), and by using a low temperature approximation  $k_B T/\mu \simeq T/T_F \ll 1$ , the chemical potential finally reads [BR97](#):

$$\frac{\mu}{\varepsilon_F} \simeq \left(1 - (d-1) \frac{\pi^2}{6} \left(\frac{T}{T_F}\right)^2\right) \quad (\text{A.37})$$

The analytic formulas obtained for entropy in equation [A.35](#) and chemical potential in equation [A.37](#) are interesting because they show that for stronger degeneracy, *i.e.* when  $T/T_F \rightarrow 0$ , Fermi gas in low dimension tend to condensate faster than in a higher dimension. This can be seen from the chemical potential that saturates faster to 1 for fixed  $T/T_F$  in low dimension, which means that the low energy states, which have indeed lower density in lower dimension as shown by equation [A.3](#), are faster saturated. The resulting entropy is then obviously lower. The numerical results shown in figures

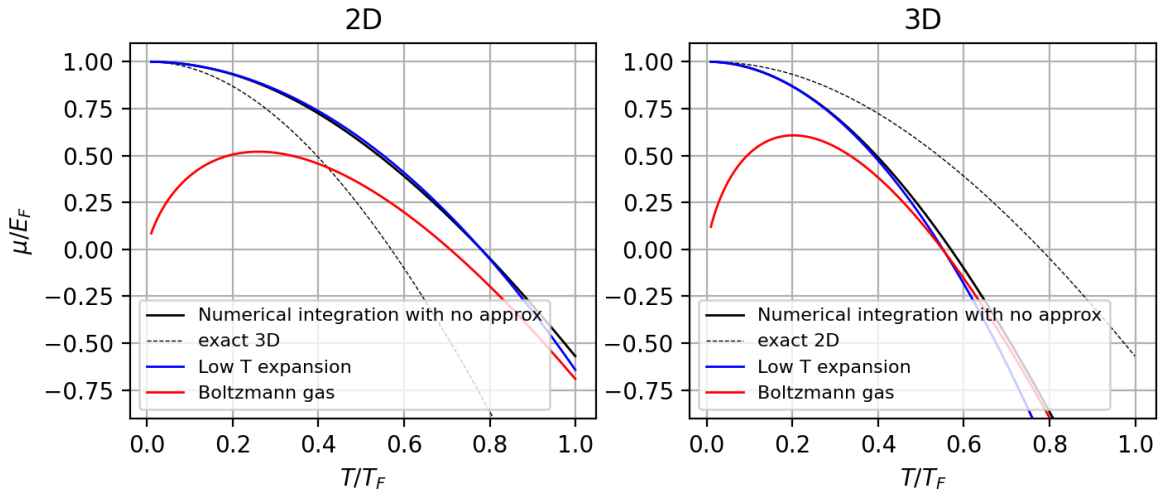


Figure A.1: 2D and 3D Chemical potential for degenerate fermi gases. Comparison between low and high temperature analytic approximations with numerical resolution.

[A.1](#) and [A.2](#) compare the analytical results for low temperature expansion with the numerical computation of the exact solution in the semi-classical regime. First, they show that the low temperature approximation reach about 10% error from  $T/T_F \simeq 1$

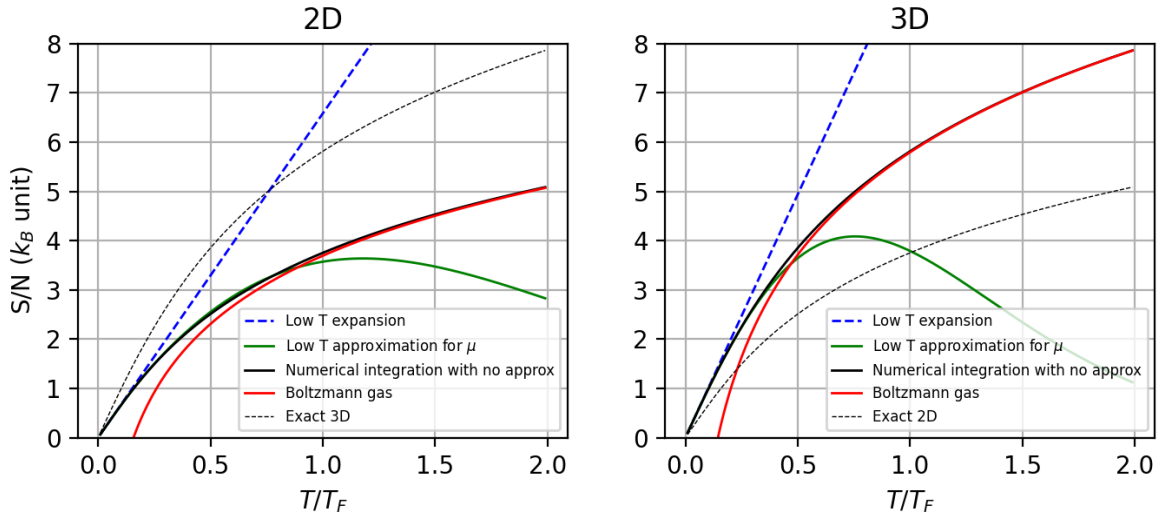


Figure A.2: 2D and 3D entropy for degenerate fermi gases. Comparison between low and high temperature analytic approximations with numerical resolution.

for 2D gases while the same error is already reached for  $T/T_F \simeq 0.5$  for 3D gases. This is consistent with the fact that in low dimension, Fermi gases condense faster because of the lower density of states, and hence the degeneracy in the sense of  $\mu/\varepsilon_F \rightarrow 1$  is reached faster for low dimension gases, such that the low temperature expansion holds better at higher  $T/T_F$  in 2D than in 3D.

## A.5 Thermodynamics, entropy and chemical potential, classical gas approximations

Finally, it can be interesting to have a glance at the high temperature approximations to bring more insight into the intermediate state from classical to degenerate gas for fermions. Indeed, the condensation of fermions is not a phase transition contrary to bosons, and there is no critical point to define that fermions reach a degenerate state. Hence, it can be convenient to compare the classical gas approximation with the fermi regime in order to better characterize the emergence of degeneracy, when the Boltzmann description doesn't hold anymore.

To derive the average thermodynamic quantities for a Boltzmann gas, it is convenient to work in the canonical ensemble. The relevant thermodynamic potential is the free energy  $F$  defined as:

$$F = E - TS \tag{A.38}$$

where the constraint over the entropy is released with respect to an isolated system. In this case, the first principle of thermodynamic reads:

$$dF = \partial_T F dT + \partial_V F dV + \partial_N F dN \tag{A.39}$$

The averages of  $S$  and  $\mu$  are then derived from the free energy with respect to the conjugated variables  $T$  and  $N$ :

$$\begin{aligned} S &= -\partial_T F \\ \mu &= -\partial_N F \end{aligned} \tag{A.40}$$

The free energy is computed from the total number of configurations of the system of  $N$  particles  $Z_N$ , also called the partition function.

$$F = -k_B T \log(Z_N) \quad (\text{A.41})$$

The partition function for  $N$  indiscernable particles is directly related to the partition function for 1 particle  $Z$  by  $Z_N = Z^N/N!$ , where

$$\begin{aligned} Z &= \int \frac{d^d r d^d p}{h^d} e^{-\beta H(r,p)} \\ &= \left( \frac{k_B T}{\hbar \bar{\omega}} \right)^d \end{aligned} \quad (\text{A.42})$$

The entropy  $S$  and chemical potential  $\mu$  can then be derived from the free energy, and in the classical approximation they read [\[BR97\]](#):

$$\begin{aligned} \frac{S}{N} &= k_B \left( d + 1 + \log \left( d! \left( \frac{T}{T_F} \right)^d \right) \right) \\ \frac{\mu}{\varepsilon_F} &= -\frac{T}{T_F} \log \left( d! \left( \frac{T}{T_F} \right)^d \right) \end{aligned} \quad (\text{A.43})$$

The analytical result for the Boltzmann gas in d-dimension are plotted in figures [A.1](#) and [A.2](#) and compared to the derivation in the degenerate regime. For low dimensional gas, it is clear that the Boltzmann description doesn't hold for  $T/T_F < 1$ . For 3D gases, it is possible to identify a smooth transition from the Boltzmann to the Fermi description at  $T/T_F \simeq 0.5$ , which corresponds to a transition from negative to positive values for  $\mu/\varepsilon_F$ , and  $S/N \simeq 4$ .

# Appendix B

## Basic theory for optical lattices

### B.1 Eigenstates and energy bands

Let's consider a periodic 1D dipole trap  $V_a(x) = V_0 \sin^2(k_L x)$ , of period  $a$  such that  $V_a(x + a) = V_a(x)$ , where  $k_L = \pi/a$  is the recoil momentum of the lattice and  $V_0$  the depth of the trap, resulting from the interference pattern of a retroflected far off detuned laser beam. The hamiltonian reads:

$$H(x, p) = \frac{p^2}{2m} + V_a(x) \quad (\text{B.1})$$

Since this hamiltonian is invariant by spatial translation, the Bloch theorem can be applied, such that the eigenstates of this hamiltonian are bloch states

$$\psi_q(x) = u_q(x)e^{iqx} \quad (\text{B.2})$$

where the quasi-momentum is a quantum number in the reciprocal space used to define each bloch state, and  $u_q$  are defined as periodic functions such that  $u_q(x + a) = u_q(x)$ . It is convenient to rewrite the hamiltonian according to the bloch states definition for diagonalization:

$$\begin{aligned} e^{iqx} \left[ \frac{(p + \hbar q)^2}{2m} + V_a(x) \right] u_{nq}(x) &= \varepsilon_n(q) u_{nq}(x) e^{iqx} \\ \left[ \frac{(p + \hbar q)^2}{2m} + V_a(x) \right] u_{nq}(x) &= \varepsilon_n(q) u_{nq}(x) \end{aligned} \quad (\text{B.3})$$

where the relation  $p(e^{iqx}u_q(x)) = e^{iqx}(p + \hbar q)u_q(x)$  has been used. The discrete index  $n$  stands for each eigenvector of the eigen sub space corresponding to a single value of the real valued quasi-momentum  $q$ . We can see here that the spectrum of the hamiltonian is completely determined by the functions  $u_q$ . It is then relevant to decompose the a-periodic  $u_q$  functions on the plane wave basis as a Fourier sum:

$$u_q(x) = \sum_{j=-\infty}^{\infty} C_j(q)e^{2i\pi jx/a} \quad (\text{B.4})$$

where  $j$  indicates the Fourier component along the plane wave of momentum  $|2jk_L\rangle$ . The periodic potential can be rewritten as follows

$$V_a(x) = V_0/2 - V_0/4(e^{2ik_Lx} + e^{-2ik_Lx}) \quad (\text{B.5})$$

By injecting the fourrier decomposition of the  $u_q$  functions and the linearised potential  $V_a(x)$  into equation [B.3](#), we obtain the equation used to compute the spectrum of the Hamiltonian:

$$\left( \left(2j - \frac{q}{k_L}\right)^2 + \frac{V_0}{2E_R} \right) C_j(q) - \frac{V_0}{4E_R} \left( C_{j-1}(q) + C_{j+1}(q) \right) = \frac{\varepsilon_n(q)}{E_R} C_j \quad (\text{B.6})$$

where  $E_R = \hbar^2 k_L^2 / 2m$  is the recoil energy of the lattice. The spectrum is defined with respect to two variables, discrete  $n$  standing for the energy levels and continuous  $q$  standing for the quasi-momentum. We can clearly see here that lattice potential couples plane waves  $|2jk_L\rangle$  to  $|2((j \pm 1)k_L)\rangle$ , which corresponds to an absorption of one photon and emission of one counter-propagating photon into the lattice photons modes. It is important to note here that the bloch states are periodic with respect to the quasi-momentum  $q$ , which periodicity which is exactly twice the recoil momentum  $k_L$  in the case of simple lattices such as this case. Hence, a  $2k_L$  translation in the Bravais lattice doesn't change the state of the particle. For this reason, the spectrum of the hamiltonian has to be defined over one period of the Bravais lattice, which has a width  $\delta q = 2k_L$ . It is then convenient to define a momentum space  $[-k_L; k_L]$ , which is the so-called the First Brillouin zone, where the eigen states and eigen energies are properly defined. Equation [B.6](#) can be numerically computed. The result is plotted on

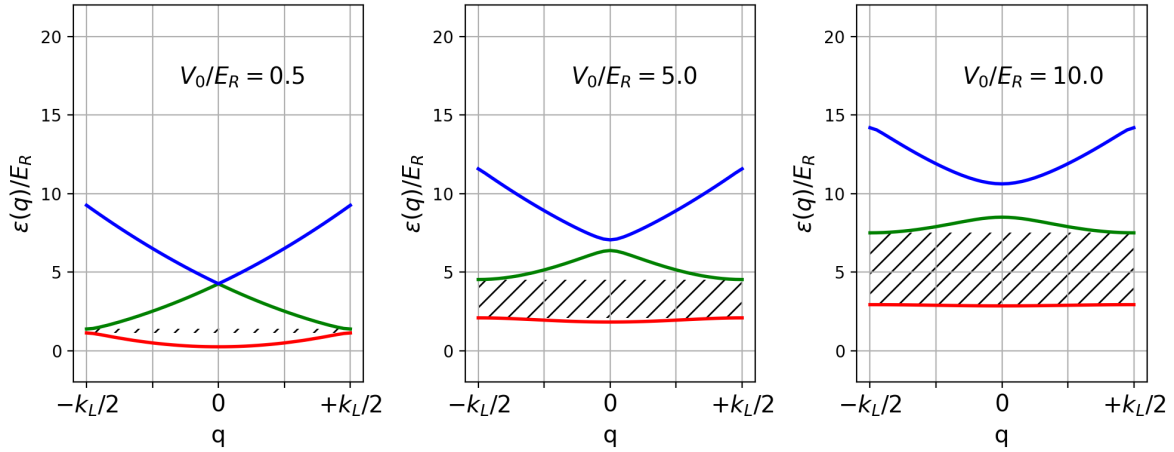


Figure B.1: Band structure computed from equation [B.6](#) in a 1D lattice for different depth  $V_0$ . Energies are in  $E_R$  recoil units. The hatched region represent the gap between bands  $n=0$  and  $n=1$ .

figure [B.1](#). Energy bands are flattened in deep lattices, and this is mostly visible on the ground band  $n = 0$ . The energy difference between the ground band and the first excited band  $\varepsilon_{bg} = \min(\varepsilon_1(q)) - \max(\varepsilon_0(q))$  where bg stands for band gap increases with the depth of the lattice, as shown by the hatched region. The band gap opens in the border of the FBZ where the two bands are degenerate at  $V_0 = 0$ , *i.e.*  $q = \pm k_L$ , such that actually  $\varepsilon_{bg} = \varepsilon_1(\pm k_L) - \varepsilon_0(\pm k_L)$ . In the shallow lattice regime, the coupling between plane waves  $j \leftrightarrow j \pm 1$  which is ensured by the lattice potential with strength  $-V_0/4$ , as shown in equation [B.6](#) can be reduced to first order, such that the hamiltonian developed in equation [B.6](#) reduces to:

$$H = \begin{pmatrix} E_R + V_0/2 & -V_0/4 \\ -V_0/4 & E_R + V_0/2 \end{pmatrix} \quad (\text{B.7})$$

The diagonalisation of this hamiltonian allows to compute the band gap in the shallow lattice regime:

$$\varepsilon_{bg} = \frac{V_0}{2} \quad (\text{B.8})$$

## B.2 Adiabatic lattice loading with fermions

On ultra-cold atoms experiment with lattices, we typically want to study the lowest energy states of the system by loading only the ground band. This is done by first cooling a gas to degeneracy, until the temperature is close to  $T = 0 K$ . In this regime, the momentum distribution peaks around  $\hbar k = 0$ , and the atoms lay in the lowest energy states. In this low energy states, if the momentum distribution doesn't exceed the lattice recoil, then the atomic wave function maps on the ground Bloch states only. By ramping up the lattice depth slower than the coupling between the bands, which can be considered as the band gap, atoms follow the ground Bloch states and remain on the ground band. The condition on the initial momentum distribution, can be quickly shown as follows.

Let's first consider the condition on initial momentum distribution for loading the ground band only. The atomic wave function expands over the eigenstates of the lattice as:

$$|\Phi\rangle = \sum_n \int_{-k_L}^{k_L} dq \langle n, q | \Phi \rangle |n, q\rangle \quad (\text{B.9})$$

where  $|n, q\rangle$  are the Bloch states  $\psi_{n,q}(x) = u_{n,q}(x)e^{iqx}$  in the momentum basis. From equation [B.4](#), the decomposition of the Bloch states over the plane wave basis reads:

$$|n, q\rangle = \sum_j C_j(q) |q + 2jk_L\rangle \quad (\text{B.10})$$

The atomic wave function can then be rewritten in the plane wave basis with a relation de fermeture

$$|\Phi\rangle = \sum_n \int_{-k_L}^{k_L} dq \sum_j C_j^*(q) \langle q + 2jk_L | \Phi \rangle |n, q\rangle \quad (\text{B.11})$$

If we consider the  $V_0 = 0$  case, then the Bloch states are simply plane waves, such that  $|n, q\rangle = |q + 2nk_L\rangle$  and then the atomic wave function reduces to:

$$|\Phi\rangle \Big|_{V_0=0} = \sum_n \int_{-k_L}^{k_L} dq \langle q + 2nk_L | \Phi \rangle |n, q\rangle \quad (\text{B.12})$$

Here we can clearly read that if the momentum distribution of the atoms exceeds the first Brillouin zone, then the projection of the atomic wave function on excited bands  $n \neq 0$  is non zero. Adiabatic following relies on the fact that the initial state of the atom is colinear to the followed eigenstate. Hence, if excited bands are initially populated, it is not possible that after loading atoms lay on the ground band only. Then the momentum distribution of the initial atomic wave function has to not exceed the first Brillouin zone.

In the case of bosons, even at non zero temperature, Bose-Einstein condensation ensures that atoms are all in the lowest momentum state corresponding to  $q = 0, n = 0$  and hence loading the ground band of the lattice presents no difficulty. Regarding fermions, the chemical potential and temperature define the momentum distribution. At  $T = 0 K$ , atoms occupy all momentum states  $k < k_F$  where  $\hbar k_F$  is the Fermi momentum. This means that to ensure adiabatic loading of the ground band of a lattice,  $k_F$  has to be lower than  $k_L$ , giving an upper limit on the number of atoms that can be loaded in the ground band. If the temperature is non zero, then the momentum distribution acquires wings and the characterization of bands occupation is no more trivial. This discussion is developed in section 6.4.



# Appendix C

## Adiabatic passages in $\Lambda$ scheme

Optical or radio-frequency (RF) pulses are commonly used to swap the populations of the two coupled quantum states. These schemes rely on the control of Rabi oscillations, requiring a perfect stabilization of the strength of the couplings as well as the duration of the pulse. The advantage of adiabatic passages over pulses is their robustness against experimental fluctuations, *e.g.* of laser frequencies and amplitudes. While a Raman pulse would require a timed pulse to swap the populations between two spin states, an adiabatic passage requires a time dependent transformation fulfilling the so-called Landau-Zener condition. These conditions can be accurately described and quantified in the dressed-states basis of atom-light interaction. First I will summarize the conditions for adiabatic passage in a three level scheme with 2 photons coupling. Then I will extend the scheme for a 3 spin states manifold.

### C.1 Two ground states

Let's first consider two degenerate ground states  $|g_1\rangle$ ,  $|g_2\rangle$ , and an excited state  $|e\rangle$ . Two photon fields  $\mathbf{E}_1$ ,  $\mathbf{E}_2$  of angular frequency  $\omega_1$ ,  $\omega_2$  couple the ground and excited states as following :

$$\begin{aligned}\hbar\Omega_1 &= -\langle e|\hat{\mathbf{D}}\cdot\mathbf{E}_1|g_1\rangle \\ \hbar\Omega_2 &= -\langle e|\hat{\mathbf{D}}\cdot\mathbf{E}_2|g_2\rangle\end{aligned}\tag{C.1}$$

where  $\Omega_1$  and  $\Omega_2$  are the Rabi frequencies, and  $\hbar = \frac{h}{2\pi}$  the reduced planck constant.

The scheme for this three level system is shown on figure [C.1](#), left. If both photons are sufficiently detuned from the  $|g_1\rangle \leftrightarrow |e\rangle$  and  $|g_2\rangle \leftrightarrow |e\rangle$  resonance  $\omega_0$ , the excited state can be ruled out using second order perturbation. In the dressed states basis  $\{|\tilde{g}_1\rangle, |\tilde{g}_2\rangle\}$ , the effective hamiltonian can then be written as :

$$\hat{H}_{eff}(\delta) = \frac{\hbar}{2} \begin{pmatrix} \delta & \Omega \\ \Omega^* & -\delta \end{pmatrix} \quad (\text{C.2})$$

where  $\Omega = \Omega_1\Omega_2^*/\Delta_e$  is the effective two-photons coupling between  $|\tilde{g}_1\rangle$  and  $|\tilde{g}_2\rangle$ , while  $\delta = \omega_2 - \omega_1$  is the detuning between the the angular frequencies of two photons from the fields  $\mathbf{E}_1$  and  $\mathbf{E}_2$ .  $\Delta_e$  stands for the detuning  $\omega_0 - \omega_1 \simeq \omega_0 - \omega_2$ . The spectrum of the effective hamiltonian is obtained by direct diagonalization. Figure [C.1](#), middle, shows the energies of eigenstates  $|+\rangle, |-\rangle$ , which read:

$$\begin{aligned} E_{|-\rangle}(\delta) &= -\frac{\hbar}{2}\sqrt{\Omega^2 + \delta^2} \\ E_{|+\rangle}(\delta) &= +\frac{\hbar}{2}\sqrt{\Omega^2 + \delta^2} \end{aligned} \quad (\text{C.3})$$

with respect to the Raman detuning  $\delta$ . Far of the Raman resonance  $\delta = 0$ , *i.e.* when  $\delta \ll \Omega$ , the eigenstate  $|-\rangle$  ( $|+\rangle$ ) is colinear to the dressed state  $|\tilde{g}_1\rangle$  ( $|\tilde{g}_2\rangle$ ), which corresponds to the bare atomic state  $|g_1\rangle$  ( $|g_2\rangle$ ), as shown on figure [C.1](#), right. When ramping up the frequency of  $\omega_2$ , the detuning  $\delta$  between the two photons gets closer to zero and so to the Raman resonance, where the effective coupling  $\Omega$  lifts the degeneracy by exactly  $\Omega$  at resonance.

To realize an adiabatic passage, atoms in state  $|\psi\rangle$  can be prepared in  $|g_1\rangle$ , which is colinear to  $|-\rangle$  far of Raman resonance,  $\delta \ll \Omega$ . If the rate of the detuning ramp is slow enough with respect to the avoided crossing, *i.e.*  $\dot{\delta} \ll \Omega^2$ , then the state  $|\psi\rangle$  adiabatically follows the eigenstate  $|-\rangle$  all along the ramp. Far of the other side of the Raman resonance, toward the right of figure [C.1](#), right, the dressed state  $|-\rangle$  is now colinear to  $|g_2\rangle$ , so is  $|\psi\rangle$ . The population has then been transfer from  $|g_1\rangle$  to  $|g_2\rangle$ . The occupation probabilities, initially at  $|\langle g_1|\psi\rangle|^2 = 1$ , swap at the Raman resonance such that  $|\langle g_2|\psi\rangle|^2 = 1$  at the end of the passage.

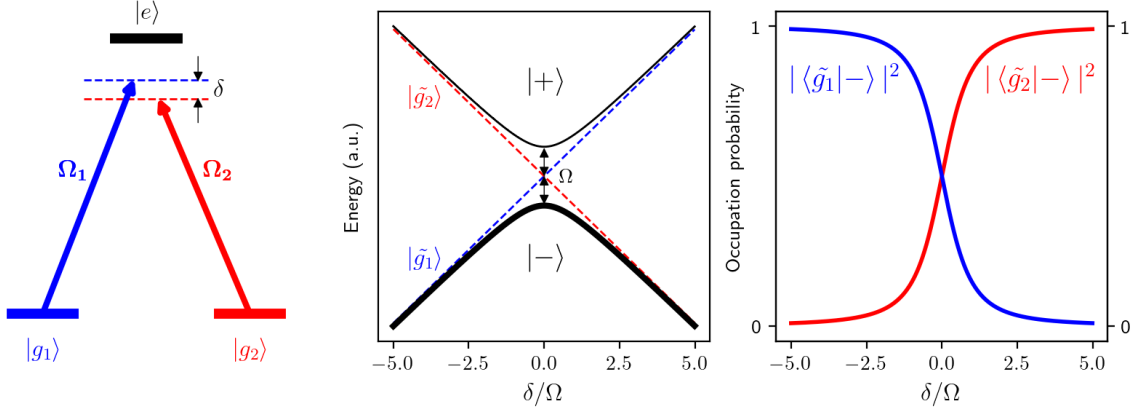


Figure C.1: Two photons coupling with respect to Raman detuning  $\delta$ . Left: atomic states  $|g_1\rangle$  and  $|g_2\rangle$  coupled to excited state  $|e\rangle$  with off resonant electric dipole interactions with respective Rabi frequencies  $\Omega_1$  and  $\Omega_2$ . The detuning between the frequencies of the two electric fields is noted  $\delta$ . Middle: energy spectrum of the dressed states and eigenstates with respect to  $\delta$ , where the excited state has been rule out. At Raman resonance  $\delta = 0$ , the degeneracy is lifted by exactly twice the effective Rabi coupling  $2\Omega$ . Right: projection of the eigenstate  $|-\rangle$  along dressed states  $|\tilde{g}_1\rangle$  and  $|\tilde{g}_2\rangle$  with respect to  $\delta$ .

Adiabatic passage can be seen in the frame of nuclear magnetic resonance. A spin in precession will stay colinear to a rotating magnetic field if the rotation speed is slow with respect to the Larmor frequency, such that the axis of precession stays in phase with the magnetic field. This condition is analog to  $\dot{\delta} \ll \Omega^2$  regarding Raman adiabatic passage. In this discussion, the two ground states are considered degenerate. If they are not, it is all the same but that the Raman resonance happens at  $\delta = \varepsilon_2 - \varepsilon_1$  where  $\varepsilon_1, \varepsilon_2$  are the eigenenergies of the bare atomic states  $|g_1\rangle, |g_2\rangle$ .

In order to maximize the probability of success of the adiabatic passage, three conditions must be respected. First, the initial conditions of the passage must be so that the initial atomic state is colinear to the followed eigenstate, *i.e.*  $\delta \ll \Omega \Rightarrow |g_1\rangle \simeq |-\rangle$ . Second, the final conditions of the passage must be so that the final atomic state is colinear to the same followed eigenstate, *i.e.*  $\delta \gg \Omega \Rightarrow |g_2\rangle \simeq |-\rangle$ . These two first similar conditions ensure that the connexion between the atomic states and eigenstates

is smooth, preventing Rabi oscillations. The third condition is that the rate of the adiabatic transfer must be slow with respect to the effective coupling between the atomic states, *i.e.*  $\dot{\delta} \ll \Omega^2$ . This last condition is embeded in the Landau Zener condition for adiabatic passage, which is that the probability of success of the adiabatic passage is given by:

$$P_{L.Z.}(\Omega, \dot{\delta}) = 1 - \exp\left(-2\pi \frac{\Omega^2}{4\dot{\delta}}\right) \quad (\text{C.4})$$

and this equation highlights the high sensitivity in  $\Omega^2/\dot{\delta}$  as it is exponential.

## C.2 Three states manifold

Let's now consider a more complicated case: three degenerate  $|m_F\rangle$  spin states  $|-1\rangle$ ,  $|0\rangle$ ,  $|1\rangle$ , two photon fields  $\mathbf{E}_\pi$ ,  $\mathbf{E}_{\sigma_+}$  with respective angular frequencies  $\omega_\pi$ ,  $\omega_{\sigma_+}$  and polarizations  $\pi, \sigma_+$ , and an excited states manifold. Obviously,  $|m_F\rangle \leftrightarrow |m_F \pm 1\rangle$  are coupled by absorption of a  $\pi$  ( $\sigma_+$ ) photon and spontaneous emission of a  $\sigma_+$  ( $\pi$ ) photon. In the dressed state basis, the energy difference between two consecutive dressed spin states, *i.e.*  $|\tilde{-1}\rangle$ ,  $|\tilde{0}\rangle$ , and  $|\tilde{0}\rangle$ ,  $|\tilde{1}\rangle$  is the energy difference between the absorbed and emitted photons  $\hbar\delta = \hbar(\omega_\pi - \omega_{\sigma_+})$ . Hence, dressed states  $|\tilde{-1}\rangle$  and  $|\tilde{1}\rangle$  have energy difference  $2\hbar\delta$ , which corresponds to a four photons transition. This is consistent with conservation of energy which imposes that the energy difference between any two dressed states is equal to the remaining energy of the corresponding photon exchanges. This principle can be extended to more than three states and is discussed in chapter [4](#). To fully determine the effective hamiltonian in the dressed state basis, we need the effective couplings between the spin states. Similarly to the previous case in [C.1](#), the excited state manifold can be ruled out using second order perturbation if the photon fields are sufficiently detuned from resonance with the excited states. In this case, the effective couplings  $|m_F\rangle \leftrightarrow |m_F + 1\rangle$  couplings read:

$$\begin{aligned} \Omega_{-1,0} &= \langle -1 | \hat{\mathbf{D}} \cdot \mathbf{E}_{\sigma_+}^* | e \rangle \langle e | \hat{\mathbf{D}} \cdot \mathbf{E}_\pi | 0 \rangle / \Delta_e \\ \Omega_{0,1} &= \langle 0 | \hat{\mathbf{D}} \cdot \mathbf{E}_{\sigma_+}^* | e \rangle \langle e | \hat{\mathbf{D}} \cdot \mathbf{E}_\pi | 1 \rangle / \Delta_e \end{aligned} \quad (\text{C.5})$$

where  $\Delta_e$  is the detuning with the transition  $\omega_0 - \omega_\pi \simeq \omega_0 - \omega_{\sigma_+}$ . Now, all the matrix elements of the effective hamiltonian in the dressed state basis are known, and it reads:

$$\hat{H}_{eff}(\delta) = \hbar \begin{pmatrix} \delta & \Omega_{-1,0}/2 & 0 \\ \Omega_{-1,0}^*/2 & 0 & \Omega_{0,1}/2 \\ 0 & \Omega_{0,1}^*/2 & -\delta \end{pmatrix} \quad (\text{C.6})$$

where  $\delta = \omega_\pi - \omega_{\sigma_+}$  is the Raman detuning. In this derivation, the three states are degenerate. Actually, even if they are not degenerate, the physical arguments hold if the energy difference between the ground states is much lower than  $\Delta_e = \omega_0 - \omega$ , where  $\omega \simeq \omega_\pi \simeq \omega_{\sigma_+}$ . In this case, the effective hamiltonian obviously reads:

$$\hat{H}_{eff}(\delta) = \hbar \begin{pmatrix} \delta & \Omega_{-1,0}/2 & 0 \\ \Omega_{-1,0}^*/2 & 0 & \Omega_{0,1}/2 \\ 0 & \Omega_{0,1}^*/2 & -\delta \end{pmatrix} + \hbar \begin{pmatrix} \varepsilon_{-1} & 0 & 0 \\ 0 & \varepsilon_0 & 0 \\ 0 & 0 & \varepsilon_1 \end{pmatrix} \quad (\text{C.7})$$

where  $\varepsilon_{-1}$ ,  $\varepsilon_0$ ,  $\varepsilon_1$  are the eigenenergies of respective bare atomic states  $|{-1}\rangle$ ,  $|0\rangle$ ,  $|1\rangle$ . Hence, the degeneracy lift is simply propagated into the energies of the associated respective dressed states. In this case, the 2 photon Raman resonances happen at  $\delta = \varepsilon_{-1} - \varepsilon_0$  and  $\delta = \varepsilon_0 - \varepsilon_1$ , which can be non-zero.

The spectrum of this hamiltonian, obtained after diagonalization, is presented on figure [C.2](#), (a). The crossing between dressed states  $|{-1}\rangle$ ,  $|\tilde{0}\rangle$  at the Raman resonance  $\delta = -6 \text{ kHz}$  is avoided by the two photon effective coupling  $\Omega = 400 \text{ Hz}$ , as well as the  $|\tilde{0}\rangle$ ,  $|\tilde{1}\rangle$  crossing at  $\delta = +2 \text{ kHz}$ . The four photons coupling between  $|{-1}\rangle$  and  $|\tilde{1}\rangle$  at  $\delta = -2 \text{ kHz}$  is zoomed in the bottom right inset, highlighting that the four photons coupling, scaling as  $\Omega^2$ , is much lower than the two photons coupling, and hence is the degeneracy lift.

*Adiabatic state following* is simulated in this manifold and the result for different simulations is presented on figure [C.2](#), (b). The atomic state  $|\psi\rangle$  is initially along  $|\tilde{0}\rangle$  at  $\delta = -14 \text{ kHz}$ , and the detuning is ramped up to  $\delta = 11 \text{ kHz}$  for a total chirp of  $23 \text{ kHz}$ . In this simulation, we follow the projection of  $|\psi\rangle$  onto each of the three dressed states all along to the detuning ramp, for different rates of the ramp. Figure (b.1) shows a

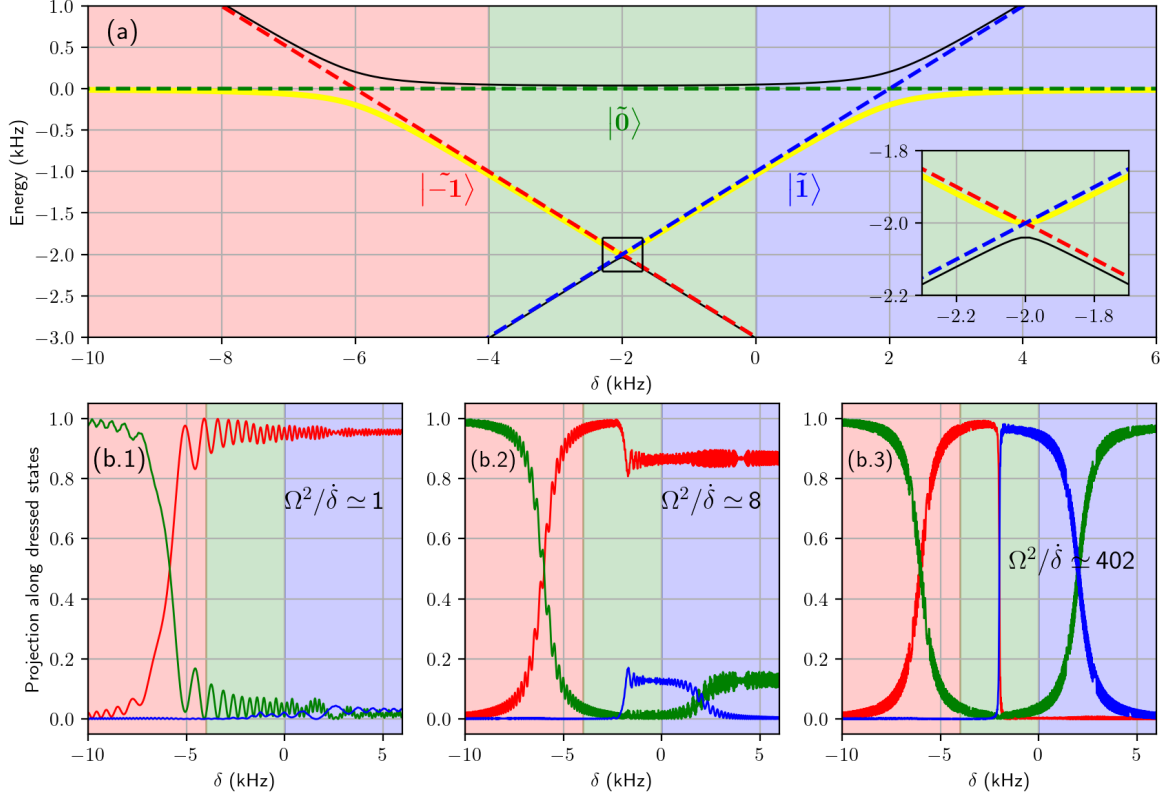


Figure C.2: Adiabatic state following in a three level manifold. For this computation, the energies of the bare atomic states are  $\varepsilon_{-1} = -6 \text{ kHz}$ ,  $\varepsilon_0 = 0 \text{ kHz}$ , and  $\varepsilon_1 = -2 \text{ kHz}$ , and  $\Omega = 400 \text{ Hz}$ . The Clebsch-Gordan coefficients are neglected. (a) Colored dashed lines: energies of the dressed states, and solid black lines: eigenenergies of hamiltonian defined in equation C.7, both with respect to the Raman detuning  $\delta$ . Bottom right inset shows the avoided crossing between  $|\tilde{-1}\rangle$  and  $|\tilde{1}\rangle$  by four photons coupling at  $\delta = -2 \text{ kHz}$ . (b) Simulations for adiabatic following of the yellow eigenstate in (a), from initial state  $|\psi\rangle$  along  $|\tilde{0}\rangle$  at  $\delta = -14 \text{ kHz}$ , up to  $\delta = 11 \text{ kHz}$ . Solid lines represent the projection of the atomic state along the dressed states  $|\langle \tilde{d} | \psi \rangle|^2$ ,  $d = -1, 0, 1$ , with respect to the detuning  $\delta$ , with colors respective to (a). The detuning is ramped up to  $\delta = 11 \text{ kHz}$ , and each simulation corresponds to a different chirp rate. (b.1) Frequency ramp in  $30 \text{ ms}$ . (b.2) Frequency ramp in  $200 \text{ ms}$ . (b.3) Frequency ramp in  $10000 \text{ ms}$ .

fast ramp during  $30 \text{ ms}$  which corresponds to  $\Omega^2/\dot{\delta} \simeq 1$ . Even though the atomic state seems to flip from  $|\tilde{0}\rangle$  to  $|\tilde{-1}\rangle$  at the avoided crossing at  $\delta = -6 \text{ kHz}$ , there remains

strong rabi oscillations and the final projection onto  $|\tilde{-1}\rangle$  doesn't converge to 1, which illustrates that the rate of the ramp is too high. The four photon transition is crossed without following, and hence the final population in  $|\tilde{1}\rangle$  is negligible, even though a slight increase of the population in  $|\tilde{1}\rangle$  is visible. With such a fast ramp, it is then possible to cross the whole spectrum with the frequency ramp and target the  $|\tilde{0}\rangle \Rightarrow |\tilde{-1}\rangle$  transition with 95 % efficiency. Figure (b.2) shows a slower ramp of duration 200 *ms*, which corresponds to  $\Omega^2/\dot{\delta} \simeq 8$ . Obviously, the two photons transition at  $\delta = 6 \text{ kHz}$  is now properly followed, and the four photons transition at  $\delta = -2 \text{ kHz}$  is also initiated, such that the population in  $|\tilde{1}\rangle$  initially at zero grows to nearly 15 %. The last two photon transition at  $\delta = 2 \text{ kHz}$  is also properly followed with same conditions than the first one, and populations in  $|\tilde{0}\rangle$  and  $|\tilde{1}\rangle$  are properly exchanged. This simulation illustrates that with  $\Omega^2/\dot{\delta} \simeq 8$ , it is enough to maximize the efficiency of the two photon adiabatic following, while the efficiency of the four photon transition is as low as 15 %. Figure (b.3) shows a simulation with frequency ramp duration of ten seconds. This corresponds to a much slower rate such that  $\Omega^2/\dot{\delta} \simeq 400$ . This is the maximum ramp rate such that the probability of success of the four photons transition reaches almost 100 %, and the eigenstate is properly followed all along the ramp.

This eigenstate following, although useless since the initial and final states are the same, illustrates the different situations that can be encountered in a three levels manifold. The efficiency of a targeted two photon transition for a  $|\tilde{0}\rangle \Rightarrow |\tilde{-1}\rangle$  transition can be easily reduced by the near four photons transition as shown by the simulation (b.2), while maximizing the efficiency of the four photon transition requires very low chirp rates compared to the two photons transitions, as shown by simulation (b.3). Actually, even with multiple crossing of the dressed states energies along the frequency ramp, it is possible to achieve maximal efficiency for targeted transitions while avoiding non-wanted transitions.

### C.3 Experimental optimization of adiabatic passage

On experiments, multiple crossing of the dressed states energies are often met. In this case, it might be possible to tune the rate of the frequency ramp to minimize

the probability of the success of the non-wanted transitions, such as four photons, while keeping the targeted transition at maximal efficiency. In section [C.2](#), such a situation is presented, as well as its limits: with a chirp rate fast enough to suppress the four photons transition, the following of the targeted two photons transition is not perfect, and a slight decrease of the rate is enough to start the four photons transition. Actually, the four photons transition can be easily avoided by choosing initial and final frequencies of the ramp such that it is not crossed. Such a case is presented in figure [C.3](#), left, where the spectrum is computed from hamiltonian defined in equation [C.7](#). The black arrow shows the narrow frequency ramp centered around the  $|\tilde{-1}\rangle \Rightarrow |\tilde{0}\rangle$  two photons transitions at  $\delta = -6 kHz$ , for an adiabatic state following to flip atomic state from initial  $|0\rangle$  to final  $|-1\rangle$ . On figure [C.3](#), center, the result of the simulation for adiabatic following with a ramp duration of  $20 ms$  shows that by narrowing the frequency ramp, the smooth connexions between dressed states and eigenstates is not ensured. Indeed, at  $\delta_i$ , dressed state and eigenstate are not colinear, and hence quickly turning on the coupling light results in Rabi oscillations. Hence, even at the end of the ramp, oscillations remain and the final state is a superposition of  $|\tilde{0}\rangle$  and  $|\tilde{-1}\rangle$ , the adiabatic following has failed. To circumvent this issue, it is possible to smoothly turn on and off the intensity of the coupling light simultaneously to the frequency ramp. This way, atoms smoothly connect to the eigenstate at the beginning of the ramp, and then smoothly reconnect to the atomic state at the end of the ramp. Figure [C.3](#), right, shows such a simulation, where the intensity ramp is plotted in the inset. The Rabi oscillations are completely suppressed and atoms end in  $|-1\rangle$  with probability 1, the adiabatic following is successfully achieved.

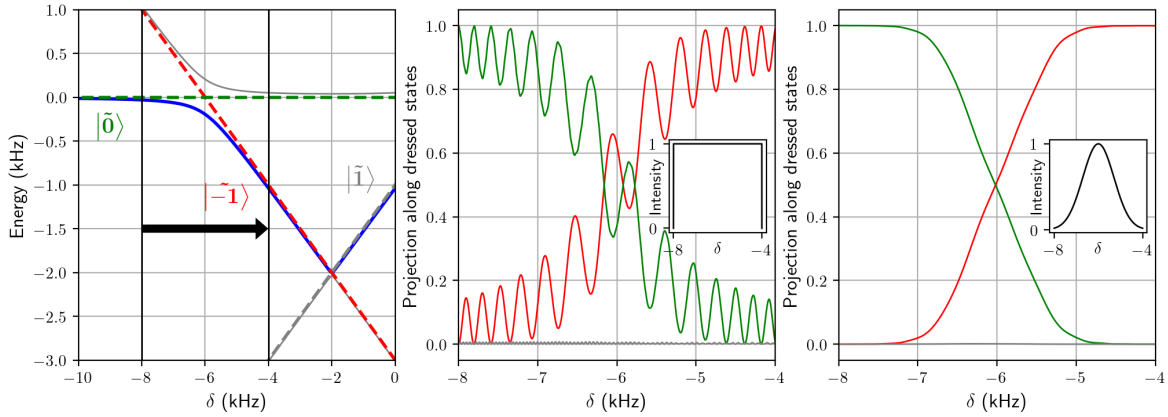


Figure C.3: Left: diagonalization of hamiltonian defined in equation [C.7](#), with respect to Raman detuning  $\delta$ . Green(red) dashed line: dressed state  $|\tilde{0}\rangle(|\tilde{-1}\rangle)$ . Dressed state  $|\tilde{1}\rangle$  is not involved in this scheme and greyd. Black vertical lines: initial and final frequencies of the ramp, indicated by the large black arrow. Blue solid line: followed eigenstate. Center and right : simulation of adiabatic state following with  $\delta_i = -8 \text{ kHz}$  and  $\delta_f = -4 \text{ kHz}$ , with ramp duration  $20 \text{ ms}$ . Center: square intensity window. Right: gaussian intensity window with standard deviation  $\sigma = 5 \text{ ms}$ . The intensity windows are shown in respective insets.



# Appendix D

## Guided expansion - parallax - anticonfinement

This appendix is dedicated to the following problem: we let a thermal Boltzmann gas expand while channeled in a far red detuned laser beam. The gas is tightly confined in two directions, and is allowed to expand in the axial direction of the laser beam. The motion of each individual atom is determined by gravity and the atom-light dipole force. Along the longitudinal extension of the channeling atomic gas, the dipole force can be locally approximated as a mean force acting on the center of mass of the atoms, and a local curvature acting on the spread of the atomic gas. The red-detuned trapping beam at  $\lambda = 1070 \text{ nm}$  is focused at 4 Rayleigh lengths above the initial position of the gas, with a  $25 \mu\text{m}$  waist. Therefore, the atoms lay after the inflexion point of the dipole potential, such that the atoms feel an anharmonic trapping. The position dependant local curvature can then be associated with an imaginary frequency  $\omega$ . Furthermore, the laser beam has angle  $\theta$  with respect to the vertical direction. Gravity is then affected by parallax  $\theta$ , and the sizes and center of mass positions of the atomic gas during its channeled expansion are imaged with the same parallax,  $\theta$ . The goal is to measure the frequency associated with the anharmonic trapping, and the parallax.

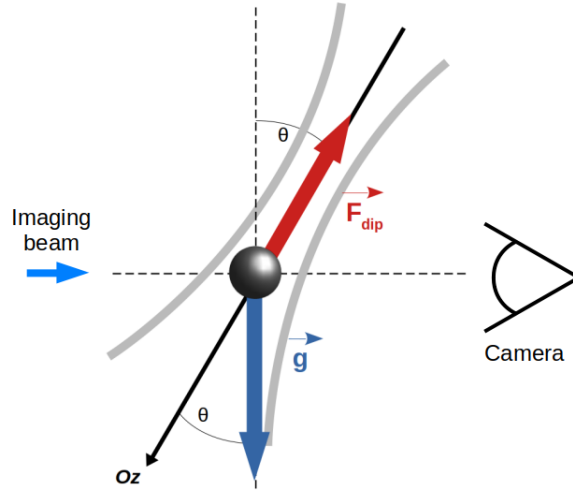


Figure D.1: Geometry of the problem. Atoms (black ball) expand while falling along the far red detuning laser beam whose direction, here noted  $Oz$  makes angle  $\theta$  with the gravity axis. The waist of the beam is located above the atoms, resulting in a axial attractive force  $F_{dip}$ . Absorption images are realized with parallaxe  $\theta$ .

## D.1 Derivation

### D.1.1 Effective gravity

Let's consider a single atom trapped by an **isotropic and non-astigmatic** laser beam, and falling along the axis of the laser beam. The dipole force associated with the atom-light interaction along the axis of the beam can be written as

$$U_{dip}(z) = \frac{U_0}{w(z)^2} \quad (D.1)$$

$$w(z) = w_0 \sqrt{1 + \left(\frac{z - z_0}{z_R}\right)^2}$$

where  $U_0$  is depth of the dipole potential,  $z_R$  the Rayleigh length, and  $w(z)$  the width of the laser beam at  $I_0 e^{-2}$ . The mean force  $F_{dip} = -\partial_z U_{dip}$  can be derived from the potential.

$$F_{dip}(z) = -2 \frac{U_0}{w_0^2} \frac{(z - z_0)/z_R^2}{(1 + (z - z_0)^2/z_R^2)^2} \quad (D.2)$$

Since the atoms start at  $4z_R$  from the focus of the beam, we can approximate  $z - z_0 \gg z_R$  such that

$$F_{dip}(z) \simeq -2 \frac{U_0}{\omega_0^2} \frac{1}{\bar{z}^3}. \quad (\text{D.3})$$

We write  $z - z_0 = \bar{z}$  for simplicity. For a short time of channeling into the laser beam with low initial velocity, the dipole force can be approximated as a uniform force field along the trajectory of the atoms, and then associated with an effective gravity  $g_{eff}$

$$F_{dip}(z) \simeq -mg_{eff} \quad (\text{D.4})$$

The local curvature can then be associated with a frequency  $\omega$  such that

$$\partial_z F_{dip} = -m\omega^2 \quad (\text{D.5})$$

Using eq. [D.3](#), [D.4](#) and [D.5](#), we can link the effective gravity  $g_{eff}$  with the frequency  $\omega$  such that  $-m\omega^2 = \frac{-3}{\bar{z}}(-mg_{eff})$  and

$$g_{eff} = -\frac{1}{3}\omega^2\bar{z}. \quad (\text{D.6})$$

The atoms lay after the inflexion point of the dipole potential, such that the atoms feel an anharmonic trapping. The position dependant local curvature can then be associated with an imaginary frequency  $\omega$ . Thus we define  $\omega = i\sqrt{\alpha} \Leftrightarrow \alpha = -\omega^2 > 0$ . Finally

$$g_{eff} = \frac{1}{3}\alpha\bar{z}. \quad (\text{D.7})$$

### D.1.2 Center of mass

The atoms fall along the axis of the beam with a slope  $\theta$ , see fig.[D.1](#). Furthermore, the channelled fall of the atoms is slowed down by an effective anti-gravity coming from the dipole attraction of the focus of the beam. The motion of the atoms is then given by

$$\ddot{z} = g \cos\theta - g_{eff} \quad (\text{D.8})$$

The positions of the atoms are imaged by absorption imaging at different times of channelled fall. The camera chip, supposed to be orthogonal to the imaging beam and parallel to gravity, the atoms are imaged with parallax  $\theta$ . Thus in the camera frame, the motion  $z_M$  is imaged with parallax  $\theta$  such that

$$z_M(t) = \cos(\theta) \left( \frac{1}{2} g \cos(\theta) t^2 - \frac{1}{2} g_{eff} t^2 \right) \quad (\text{D.9})$$

The integration constants  $v_0$  and  $z_0$  can be neglected since the measurement is made on the center of mass of the thermal gas. A direct measurement of fall acceleration  $g_M$  without taking into account the effective gravity and parallax would be  $z_M(t) = \frac{1}{2} g_M t^2$ , such that the measurement can be linked to the parallax  $\theta$  and effective gravity  $g_{eff}$ . Using eq. [D.7](#)

$$g_M = g \cos(\theta)^2 - \frac{1}{3} \alpha \bar{z} \cos(\theta) \quad (\text{D.10})$$

We now need a second measurement to solve the system.

### D.1.3 Cloud width

The gas is initially trapped at thermal equilibrium with distribution

$$f(z, v) \propto \exp\left(-\frac{1}{2} \frac{m \omega_0^2 z^2}{k_B T}\right) \exp\left(-\frac{1}{2} \frac{m v^2}{k_B T}\right) \quad (\text{D.11})$$

with  $\omega_0$  the frequency of the harmonic trapping potential, and  $T$  the temperature of the gas. Assuming that an atom is isolated into the laser beam, its motion along the axis of the beam depends only on the dipole force. Using the anharmonic trap local approximation and  $\omega = i\sqrt{\alpha}$ , the equation of motion can be written as  $\ddot{z} = \alpha(t)z$ , and then integrated to

$$z(t) = z_0 \cosh(\sqrt{\alpha}t) + \frac{v_0}{\sqrt{\alpha}} \sinh(\sqrt{\alpha}t) \quad (\text{D.12})$$

The position probability distribution  $P(x_0, t) = \int dx dv f(x, v) \delta(x(t) - x_0)$  can then be computed from eq. [D.11](#) and eq. [D.12](#). The width of the probability distribution  $\sigma_z$  is

$$\sigma_z^2(t) = \frac{k_B T}{m} \left( \frac{\sinh^2(\sqrt{\alpha}t)}{\alpha} + \frac{\cosh^2(\sqrt{\alpha}t)}{\omega_0^2} \right) \quad (\text{D.13})$$

The measurement of the size  $\sigma_z$  with parallax  $\theta$  gives  $\sigma_M = \cos(\theta)\sigma_z$ . Furthermore, the temperature is inferred from the measurement of the size  $\sigma_{3D}^2 = k_B T/m$  after a time of flight of a gas totally released from the trap. For a long enough time of flight,  $\sigma_{3D}^2(t) \simeq \frac{k_B T}{m} t^2$ , such that

$$\frac{\sigma_M^2}{\sigma_{3D}^2}(t) \simeq \frac{\cos^2(\theta)}{t^2} \left( \frac{\sinh^2(\sqrt{\alpha}t)}{\alpha} + \frac{\cosh^2(\sqrt{\alpha}t)}{\omega_0^2} \right) \quad (\text{D.14})$$

With the two equations [D.10](#) and [D.14](#), we define a set of two equations with two unknowns  $\alpha$  and  $\theta$ , and dependent on two experimentally measurable quantities, the fall of the center of mass and the expansion of the channelled thermal gas. Hence, it is now possible to infer the anticonfinement parametrized by  $\alpha$  and the parallax  $\theta$ .

## D.2 Measurements

The measurements of the centers of mass and sizes, shown on figure [D.2](#), are made on hot thermal gas  $T > 2 T_F$ , and for time of flights  $t_{tof} \geq 14 \text{ ms}$  long enough such that the approximation  $\sigma_{3D}^2(t) \simeq \frac{k_B T}{m} t^2$  holds. The channelling gas is imaged with absorption imaging, while inside the beam, and this *in-situ* absorption imaging requires to correct the imaged densities such that the size  $\sigma_z$  is correctly measured, see chapter [2](#).

On figure [D.2](#), (a), the effective gravity  $g_{eff} \simeq 7.2 \text{ m/s}^2$  is inferred from the measurement of the channelled fall, and the gravity is calibrated from time of flight measurement. The agreement between the measured effective gravity, and its expected value from equation [D.10](#), for all values of  $(\alpha, \theta)$ , is shown on figure [D.2](#), (b). All sets of  $(\alpha, \theta)$  values which verify equation [D.10](#), so that the expected value match the measured value, are obtained and plotted on the white dotted line. The sizes of the channelled gas and the freely expanding gas are measured and plotted on figure [D.2](#), (c), with respect to time. The agreement between the measured effective gravity, and its expected value from equation [D.10](#), for all values of  $(\alpha, \theta)$ , is shown on figure [D.2](#), (d). All sets of  $(\alpha, \theta)$  values which verify equation [D.14](#) and so that the expected value is in agreement with the size measurement (c), are obtained and plotted on the white dotted line.

The two sets of  $(\alpha, \theta)$  values obtained from the center of fall measurements and size

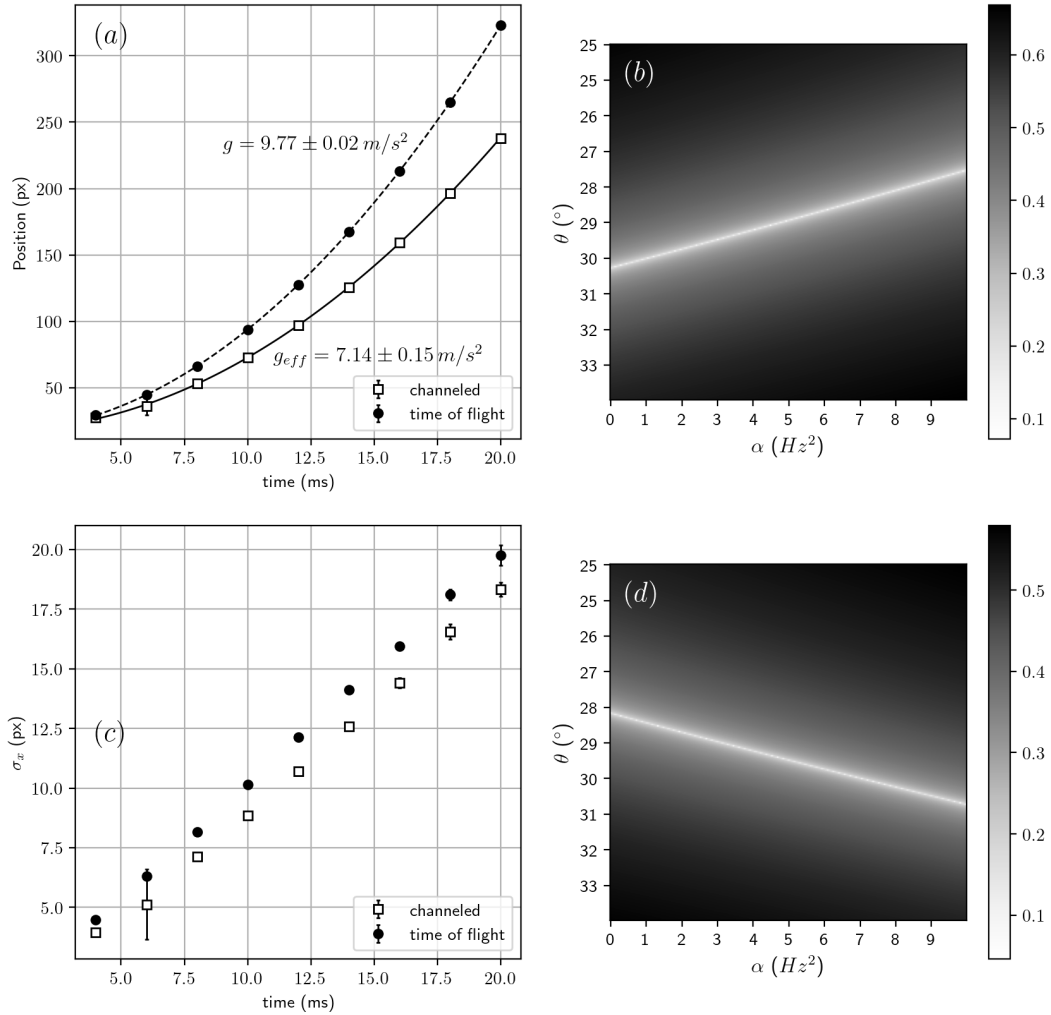


Figure D.2: (a) Measurement of the position of the center of mass, for the channeled expansion (squares) and time of flight experiment (dots), with respect to the time. (b) 2D resolution of equation [D.10](#) with respect to  $\alpha$  and  $\theta$ . The white line (closest to zero) indicates the values with best agreement with the data shown on (a). (c) Measurement of the size of the gas, for the channeled expansion (squares) and time of flight experiment (dots), with respect to the time. (d) 2D resolution of equation [D.14](#) with respect to  $\alpha$  and  $\theta$ . The white line (closest to zero) indicates the values with best agreement with the data shown on (c). For (a) and (c), the size of a pixel is  $6.45 \mu\text{m}$ .

expansion measurements are put together, see figure [D.3](#). The 2D system is then solved as only one tuple  $(\alpha, \theta)$  is solution, here  $(2^2 \text{ Hz}^2, 30.21^\circ)$ . On figure [D.4](#), we compare

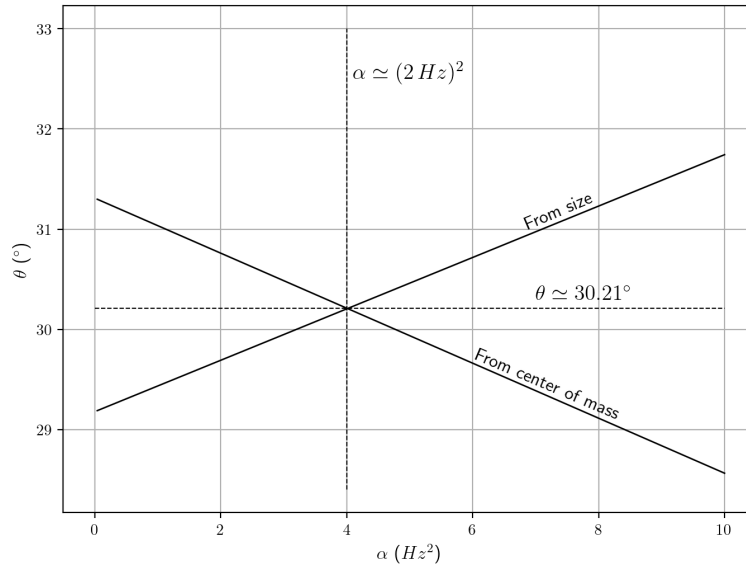


Figure D.3: Combination of the resolutions of equations [D.14](#) and [D.10](#) shown on figures [D.2](#) (b) and (d). The crossing reveals the unique solution  $(\alpha, \theta) = (2^2, 30.21^\circ)$ .

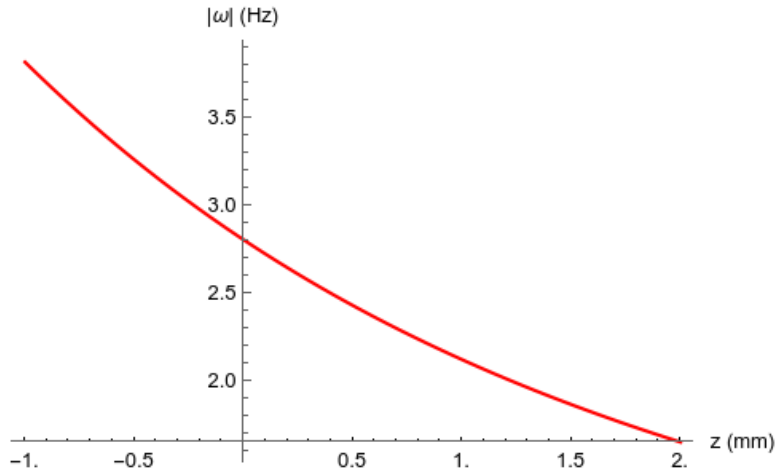


Figure D.4: Curvature of the axial dipole potential in (Hz). The atoms start the channeled fall at position 0 and are imaged at 15 mm away from initial position after 20 ms of channeled fall. This expectation is obtained from the known focus, size and depth of our optical dipole trap, which were calibrated from center of mass oscillations and beating of the cloud size.

the obtained anti-confinement with expected value (geometry optimization of the trap with oscillation frequencies). After 20 ms of channeled fall, the atoms are 1.5 mm away from the initial position. At this position, the anti-confinement is expected to be a little below 2  $Hz$ , which is in good agreement with the measurement measurement. Furthermore, the parallax has been measured directly on the experiment with a ruler,  $\theta_{ruler} = 29.5 \pm 1.5^\circ$ , also in good agreement with this method.

# Bibliography

- [AB59] Y. Aharonov and D. Bohm. “Significance of electromagnetic potentials in the quantum theory”. In: *Physical Review* (1959).
- [Aid+11] M. Aidelsburger et al. “Experimental realization of strong effective magnetic fields in an optical lattice”. In: *Physical Review Letters* (2011).
- [Aka+21] T. Akatsuka et al. “Three-stage laser cooling of Sr atoms using the  $5s5p\ ^3P_2$  metastable state below Doppler temperatures”. In: *Physical Review A* (2021).
- [Ala22] Y. A. Alaoui. “Studies of correlations in an ensemble of latticetrapped dipolar atoms”. PhD thesis. Laboratoire de physique des Lasers, U.S.P.N., 2022.
- [AM38] J. F. Allen and A. D. Misener. “Flow phenomena in liquid helium II”. In: *Nature* (1938).
- [And+95] M. H. Anderson et al. “Observation of Bose-Einstein condensation in a dilute atomic vapor”. In: *Science* (1995).
- [And87] P. W. Anderson. “The resonating valence bond state in  $\text{La}_2\text{CuO}_4$  and superconductivity”. In: *Science* (1987).
- [Arm+10] J. Armijo et al. “Probing three-body correlations in a quantum gas using the measurement of the third moment of density fluctuations”. In: *Phys. Rev. Lett.* (2010).
- [Arn+19] M. Arnal et al. “Evidence for cooling in an optical lattice by amplitude modulation”. In: *Physical Review A* (2019).
- [Ast+21] L. Asteria et al. “Quantum gas magnifier for sub-lattice-resolved imaging of 3D quantum systems”. In: *Nature* (2021).
- [Bak+09] W. S. Bakr et al. “A quantum gas microscope for detecting single atoms in a Hubbard-regime optical lattice”. In: *Nature* (2009).

- [Bar+16] D. Barredo et al. “An atom-by-atom assembler of defect-free arbitrary two-dimensional atomic arrays”. In: *Science* (2016).
- [Bat+20] P. Bataille et al. “Adiabatic spin-dependent momentum transfer in an  $SU(N)$  degenerate Fermi gas”. In: *Physical Review A* (2020).
- [Bat22] P. Bataille. PhD thesis. Laboratoire de physique des Lasers, U.S.P.N., 2022.
- [BDZ08] I. Bloch, J. Dalibard, and W. Zwerger. “Many-body physics with ultracold gases”. In: *Reviews of Modern Physics* (2008).
- [Ben+17] S. Bennetts et al. “Steady-state magneto-optical trap with 100-fold improved phase-space density”. In: *Physical Review Letters* (2017).
- [Blo+14] B. J. Bloom et al. “An optical lattice clock with accuracy and stability at the  $10^{-18}$  level”. In: *Nature* (2014).
- [Bol+16] M. Boll et al. “Spin- and density-resolved microscopy of antiferromagnetic correlations in Fermi-Hubbard chains”. In: *Science* (2016).
- [Bou04] T. Bourdel. “Gaz de Fermi en interaction forte: du condensat de molécules aux paires de Cooper”. In: *Université Pierre et Marie Curie - Paris VI* (2004).
- [Boy07] M. Boyd. “High precision spectroscopy of strontium in an optical lattice: towards a new standard for frequency and time, PhD Thesis”. In: *B.S., University of Washington* (2007).
- [BR97] D. A. Butts and D. S. Rokhsar. “Trapped Fermi gases”. In: *Physical Review A* (1997).
- [BVS15] K. Bergmann, N. V. Vitanov, and B. W. Shore. “Perspective: Stimulated Raman Adiabatic Passage: The status after 25 years”. In: *The Journal of Chemical Physics* (2015).
- [CCL98] Y. Castin, J. I. Cirac, and M. Lewenstein. “Reabsorption of light by trapped atoms”. In: *Physical Review Letters* (1998).
- [CD96] Y. Castin and R. Dum. “Bose-Einstein condensates in time dependent traps”. In: *Physical Review Letters* (1996).
- [CDG98] C. Cohen-Tannoudji, J. Dupont-Roc, and G. Grynberg. *Atom—Photon Interactions*. Wiley, 1998.
- [CH86] C. E. Carroll and F. T. Hioe. “Transition probabilities for the three-level Landau-Zener model”. In: *Journal of Physics A: Mathematical and General* (1986).

- [Che+15] L. W. Cheuk et al. “Quantum-gas microscope for fermionic atoms”. In: *Physical Review Letters* (2015).
- [Chi+10] C. Chin et al. “Feshbach resonances in ultracold gases”. In: *Reviews of Modern Physics* (2010).
- [CHU09] M. A. Cazalilla, A. F. Ho, and M. Ueda. “Ultracold gases of ytterbium: ferromagnetism and Mott states in an SU(6) Fermi system”. In: *New Journal of Physics* (2009).
- [Com+22] T. Comparin et al. “Scalable spin squeezing from spontaneous breaking of a continuous symmetry”. In: *Physical Review Letters* (2022).
- [CR14] M. A. Cazalilla and A. M. Rey. “Ultracold Fermi gases with emergent SU( $N$ ) symmetry”. In: *Reports on Progress in Physics* (2014).
- [DC85] J. Dalibard and C. Cohen-Tannoudji. “Dressed-atom approach to atomic motion in laser light: the dipole force revisited”. In: *Journal of the Optical Society of America B* (1985).
- [DCM92] J. Dalibard, Y. Castin, and K. Mølmer. “Wave-function approach to dissipative processes in quantum optics”. In: *Physical Review Letters* (1992).
- [DeM01] B. DeMarco. “Quantum behavior of an atomic Fermi gas”. PhD thesis. B.A. Physics, SUNY Geneseo, 2001.
- [Den+02] J. H. Denschlag et al. “A Bose-Einstein condensate in an optical lattice”. In: *Journal of Physics B: Atomic, Molecular and Optical Physics* (2002).
- [DeS+10] B. J. DeSalvo et al. “Degenerate Fermi gas of  $^{87}\text{Sr}$ ”. In: *Phys. Rev. Lett.* (3 2010).
- [DJ99] B. DeMarco and D. S. Jin. “Onset of Fermi degeneracy in a trapped atomic gas”. In: *Science* (1999).
- [DK10] D. van Delft and P. Kes. “The discovery of superconductivity”. In: *Physics Today* (2010).
- [Dre+17] J. Drewes et al. “Antiferromagnetic correlations in two-dimensional fermionic Mott-insulating and metallic phases”. In: *Physical Review Letters* (2017).
- [Dre+83] R. W. P. Drever et al. “Laser phase and frequency stabilization using an optical resonator”. In: *Applied Physics B Photophysics and Laser Chemistry* (1983).
- [Ess10] T. Esslinger. “Fermi-Hubbard physics with atoms in an optical lattice”. In: *Annual Review of Condensed Matter Physics* (2010).

- [Est+06] J. Esteve et al. “Observations of density fluctuations in an elongated Bose gas: ideal gas and quasicondensate regimes”. In: *Phys. Rev. Lett.* (2006). Publisher: American Physical Society.
- [Fel+11] M. Feld et al. “Observation of a pairing pseudogap in a two-dimensional Fermi gas”. In: *Nature* (2011).
- [Fey82] R. P. Feynman. “Simulating physics with computers”. In: *International Journal of Theoretical Physics* (1982).
- [FIM05] M. Fleischhauer, A. Imamoglu, and J. P. Marangos. “Electromagnetically induced transparency: Optics in coherent media”. In: *Reviews of Modern Physics* (2005).
- [FJL00] F. K. Fatemi, K. M. Jones, and P. D. Lett. “Observation of optically induced Feshbach resonances in collisions of cold atoms”. In: *Physical Review Letters* (2000).
- [Fri+12] A. Frisch et al. “Narrow-line magneto-optical trap for erbium”. In: *Physical Review A* (2012).
- [Fuk+09] T. Fukuhara et al. “Mott insulator of ultracold alkaline-earth-metal-like atoms”. In: *Physical Review A* (2009).
- [GB17] C. Gross and I. Bloch. “Quantum simulations with ultracold atoms in optical lattices”. In: *Science* (2017).
- [GD10] F. Gerbier and J. Dalibard. “Gauge fields for ultracold atoms in optical superlattices”. In: *New Journal of Physics* (2010).
- [Geh+03] M. E. Gehm et al. “Unitarity-limited elastic collision rate in a harmonically trapped Fermi gas”. In: *Phys. Rev. A* (2003). Publisher: American Physical Society.
- [Gor+10] A. V. Gorshkov et al. “Two-orbital SU(N) magnetism with ultracold alkaline-earth atoms”. In: *Nature Physics* (2010).
- [GPS08] S. Giorgini, L. P. Pitaevskii, and S. Stringari. “Theory of ultracold atomic Fermi gases”. In: *Reviews of Modern Physics* (2008).
- [Gre+01] M. Greiner et al. “Exploring phase coherence in a 2D lattice of Bose-Einstein condensates”. In: *Physical Review Letters* (2001).
- [Gre+16] D. Greif et al. “Site-resolved imaging of a fermionic Mott insulator”. In: *Science* (2016).
- [Gri+06] P. F. Griffin et al. “Spatially selective loading of an optical lattice by light-shift engineering using an auxiliary laser field”. In: *New Journal of Physics* (2006).

- [GWO00] R. Grimm, M. Weidemüller, and Y. B. Ovchinnikov. “Optical dipole traps for neutral atoms”. In: *Advances In Atomic, Molecular, and Optical Physics*. Edited by B. Bederson and H. Walther. Academic Press, 2000.
- [Ham+98] S. E. Hamann et al. “Resolved-sideband raman cooling to the ground state of an optical lattice”. In: *Physical Review Letters* (1998).
- [He+20] C. He et al. “Collective excitations in two-dimensional SU(N) Fermi gases with tunable spin”. In: *Physical Review Research* (2020).
- [Hei+20] A. Heinz et al. “State-dependent optical lattices for the strontium optical qubit”. In: *Physical Review Letters* (2020).
- [HGR09] M. Hermele, V. Gurarie, and A. M. Rey. “Mott insulators of ultracold fermionic alkaline earth atoms: underconstrained magnetism and chiral spin liquid”. In: *Physical Review Letters* (2009).
- [Hof+02] W. Hofstetter et al. “High-temperature superfluidity of fermionic atoms in optical lattices”. In: *Physical Review Letters* (2002).
- [HS22] O. Hassouneh and W. Salah. “Novel accurate atomic data of strontium-87 isotope”. In: *The European Physical Journal Plus* (2022).
- [Hua87] K. Huang. *Statistical Mechanics*. Wiley, 1987.
- [Hub63] J. Hubbard. “Electron correlations in narrow energy bands”. In: *Proceedings of the Royal Society of London. Series A. Mathematical and Physical Sciences* (1963).
- [Hub64] J. Hubbard. “Electron correlations in narrow energy bands. II. The degenerate band case”. In: *Proceedings of the Royal Society of London. Series A. Mathematical and Physical Sciences* (1964).
- [Huc+09] J. H. Huckans et al. “Quantum and classical dynamics of a Bose-Einstein condensate in a large-period optical lattice”. In: *Physical Review A* (2009).
- [IIK00] T. Ido, Y. Isoya, and H. Katori. “Optical-dipole trapping of Sr atoms at a high phase-space density”. In: *Physical Review A* (2000).
- [Jör+08] R. Jördens et al. “A Mott insulator of fermionic atoms in an optical lattice”. In: *Nature* (2008).
- [JPS04] B. Jackson, P. Pedri, and S. Stringari. “Collisions and expansion of an ultracold dilute Fermi gas”. In: *Europhysics Letters (EPL)* (2004).
- [Kap38] P. Kapitza. “Viscosity of liquid helium below the  $\lambda$ -point”. In: *Nature* (1938).

- [Kat+99] H. Katori et al. “Magneto-optical trapping and cooling of strontium atoms down to the photon recoil temperature”. In: *Physical Review Letters* (1999).
- [Ker+00] A. J. Kerman et al. “Beyond optical molasses: 3D Raman sideband cooling of atomic cesium to high phase-space density”. In: *Physical Review Letters* (2000).
- [Köh+05] M. Köhl et al. “Fermionic atoms in a three dimensional optical lattice: observing Fermi surfaces, dynamics, and interactions”. In: *Physical Review Letters* (2005).
- [KSS96] Y. Kagan, E. L. Surkov, and G. V. Shlyapnikov. “Evolution of a Bose-condensed gas under variations of the confining potential”. In: *Physical Review A* (1996).
- [Kum+18] A. Kumar et al. “Sorting ultracold atoms in a three-dimensional optical lattice in a realization of Maxwell’s demon”. In: *Nature* (2018).
- [Kuw+99] T. Kuwamoto et al. “Magneto-optical trapping of Yb atoms using an intercombination transition”. In: *Physical Review A* (1999).
- [KZ08] W. Ketterle and M. W. Zwierlein. “Making, probing and understanding ultracold Fermi gases”. In: *Riv. Nuovo Cim.* (2008).
- [Leb+18] M. Lebrat et al. “Band and correlated insulators of cold fermions in a mesoscopic lattice”. In: *Physical Review X* (2018).
- [Lee+21] S. Lee et al. “Compact modulation transfer spectroscopy module for highly stable laser frequency”. In: *Optics and Lasers in Engineering* (2021).
- [Lew75] G. H. Lewes. *Problems of life and mind*. Edited by I. J.R. Osgood. Michigan University, 1875.
- [Li+16] J. Li et al. “Spin-orbit coupling and spin textures in optical superlattices”. In: *Physical Review Letters* (2016).
- [Lit+21] A. Litvinov et al. “Measuring densities of cold atomic clouds smaller than the resolution limit”. In: *Phys. Rev. A* (2021). Publisher: American Physical Society.
- [LJS11] Y.-J. Lin, K. Jiménez-García, and I. B. Spielman. “Spin orbit-coupled Bose-Einstein condensates”. In: *Nature* (2011).
- [LRW96] O. J. Luiten, M. W. Reynolds, and J. T. M. Walraven. “Kinetic theory of the evaporative cooling of a trapped gas”. In: *Phys. Rev. A* (1996). Publisher: American Physical Society.

- [Lud08] A. D. Ludlow. “The strontium optical lattice clock: optical spectroscopy with sub-Hertz accuracy, PhD Thesis”. In: *B.S. Physics, Brigham Young University* (2008).
- [LZB19] M. Lacki, P. Zoller, and M. A. Baranov. “Stroboscopic painting of optical potentials for atoms with subwavelength resolution”. In: *Phys. Rev. A* (2019). Publisher: American Physical Society.
- [Man+03] O. Mandel et al. “Coherent transport of neutral atoms in spin-dependent optical lattice potentials”. In: *Physical Review Letters* (2003).
- [Man20] D. Manzano. “A short introduction to the Lindblad master equation”. In: *AIP Advances* (2020).
- [MD11] D. C. McKay and B. DeMarco. “Cooling in strongly correlated optical lattices: prospects and challenges”. In: *Reports on Progress in Physics* (2011).
- [Mic+09] P. G. Mickelson et al. “Repumping and spectroscopy of laser-cooled Sr atoms using the  $(5s5p)^3P_2-(5s4d)^3D_2$  transition”. In: *Journal of Physics B: Atomic, Molecular and Optical Physics* (2009).
- [Mic10] P. G. Mickelson. “Trapping and evaporation of  $^{87}\text{Sr}$  and  $^{88}\text{Sr}$  mixtures, PhD Thesis”. In: *Rice University, Houston, Texas* (2010).
- [MKC08] D. J. McCarron, S. A. King, and S. L. Cornish. “Modulation transfer spectroscopy in atomic rubidium”. In: *Measurement Science and Technology* (2008).
- [MOR86] N. Manakov, V. Ovsiannikov, and L. Rapoport. “Atoms in a laser field”. In: *Physics Reports* (1986).
- [MPS02] C. Menotti, P. Pedri, and S. Stringari. “Expansion of an interacting Fermi gas”. In: *Physical Review Letters* (2002).
- [MS99] H. J. Metcalf and P. van der Straten. *Laser cooling and trapping*. Springer New York, 1999.
- [MSB96] J. Martin, B. W. Shore, and K. Bergmann. “Coherent population transfer in multilevel systems with magnetic sublevels. III. Experimental results”. In: *Physical Review A* (1996).
- [Muk+03] T. Mukaiyama et al. “Recoil-limited laser cooling of  $^{87}\text{Sr}$  atoms near the Fermi temperature”. In: *Physical Review Letters* (2003).
- [Née48] M. L. Néel. “Propriétés magnétiques des ferrites ; ferrimagnétisme et antiferromagnétisme”. In: *Annales de Physique* (1948).

- [Nor+21] M. A. Norcia et al. “Two-dimensional supersolidity in a dipolar quantum gas”. In: *Nature* (2021).
- [OHa+02] K. M. O’Hara et al. “Observation of a strongly interacting degenerate fermi gas of atoms”. In: *Science* (2002).
- [Ovs+06] V. D. Ovsyannikov et al. “Polarisation and dispersion properties of light shifts in ultrastable optical frequency standards”. In: *Quantum Electronics* (2006).
- [Oza+18] H. Ozawa et al. “Antiferromagnetic spin correlation of SU(N) Fermi gas in an optical superlattice”. In: *Physical Review Letters* (2018).
- [Pag+14] G. Pagano et al. “A one-dimensional liquid of fermions with tunable spin”. In: *Nature Physics* (2014).
- [Par+04] B. Paredes et al. “Tonks-Girardeau gas of ultracold atoms in an optical lattice”. In: *Nature* (2004).
- [Par+16] M. F. Parsons et al. “Site-resolved measurement of the spin-correlation function in the Fermi-Hubbard model”. In: *Science* (2016).
- [Pei+03] S. Peil et al. “Patterned loading of a Bose-Einstein condensate into an optical lattice”. In: *Physical Review A* (2003).
- [PGS03] P. Pedri, D. Guéry-Odelin, and S. Stringari. “Dynamics of a classical gas including dissipative and mean field effects”. In: (2003).
- [PM82] W. D. Phillips and H. Metcalf. “Laser deceleration of an atomic beam”. In: *Physical Review Letters* (1982).
- [Pol+05] N. Poli et al. “Cooling and trapping of ultracold strontium isotopic mixtures”. In: *Physical Review A* (2005).
- [Rei+07] G. Reinaudi et al. “Strong saturation absorption imaging of dense clouds of ultracold atoms”. In: *Optics Letters* (2007).
- [Rey+07] A. Rey et al. “Preparation and detection of magnetic quantum phases in optical superlattices”. In: *Physical Review Letters* (2007).
- [RF99] M. V. Romalis and E. N. Fortson. “Zeeman frequency shifts in an optical dipole trap used to search for an electric-dipole moment”. In: *Physical Review A* (1999).
- [Sch+08] U. Schneider et al. “Metallic and insulating phases of repulsively interacting fermions in a 3D optical lattice”. In: *Science* (2008).
- [Sch+20] F. Schäfer et al. “Tools for quantum simulation with ultracold atoms in optical lattices”. In: *Nature Reviews Physics* (2020).

- [SGS11] S. Stellmer, R. Grimm, and F. Schreck. “Detection and manipulation of nuclear spin states in fermionic strontium”. In: *Physical Review A* (2011).
- [SGS13] S. Stellmer, R. Grimm, and F. Schreck. “Production of quantum-degenerate strontium gases”. In: *Physical Review A* (2013).
- [Shi+15] C. Shi et al. “Polarizabilities of the  $^{87}\text{Sr}$  clock transition”. In: *Physical Review A* (2015).
- [Sle+92] T. Sleator et al. “Experimental demonstration of the optical Stern-Gerlach effect”. In: *Physical Review Letters* (1992).
- [SN10] J. E. Sansonetti and G. Nave. “Wavelengths, transition probabilities, and energy levels for the spectrum of neutral strontium (SrI)”. In: *Journal of Physical and Chemical Reference Data* (2010).
- [Son+20] L. Sonderhouse et al. “Thermodynamics of a deeply degenerate  $\text{SU}(N)$ -symmetric Fermi gas”. In: *Nature Physics* (2020).
- [SS14] S. Stellmer and F. Schreck. “Reservoir spectroscopy of  $5s5^3P_2-5snd^3D_{1,2,3}$  transitions in strontium”. In: *Physical Review A* (2014).
- [SSK14] S. Stellmer, F. Schreck, and T. C. Killian. “Degenerate quantum gases of strontium”. In: *Annual Review of Cold Atoms and Molecules*. WORLD SCIENTIFIC, 2014.
- [Sta+98] D. M. Stamper-Kurn et al. “Collisionless and hydrodynamic excitations of a Bose-Einstein condensate”. In: *Physical Review Letters* (1998).
- [Ste13] S. Stellmer. “Degenerate quantum gases of strontium, PhD Thesis”. PhD thesis. Faculty of Mathematics, ComputerScience and Physics of the University of Innsbruck, 2013.
- [Sun+18] W. Sun et al. “Highly controllable and robust 2D spin-orbit coupling for quantum gases”. In: *Physical Review Letters* (2018).
- [Sun+21] H. Sun et al. “Realization of a bosonic antiferromagnet”. In: *Nature Physics* (2021).
- [SVH05] C. Slowe, L. Vernac, and L. V. Hau. “High flux source of cold rubidium atoms”. In: *Review of Scientific Instruments* (2005).
- [SWW91] D. W. Sesko, T. G. Walker, and C. E. Wieman. “Behavior of neutral atoms in a spontaneous force trap”. In: *Journal of the Optical Society of America B* (1991).
- [Tai+10] S. Taie et al. “Realization of a  $\text{SU}(2)\times\text{SU}(6)$  System of Fermions in a Cold Atomic Gas”. In: *Physical Review Letters* (2010).

- [Tai+12] S. Taie et al. “An SU(6) Mott insulator of an atomic Fermi gas realized by large-spin Pomeranchuk cooling”. In: *Nature Physics* (2012).
- [Tai+20] S. Taie et al. “Observation of antiferromagnetic correlations in an ultracold SU(N) Hubbard model”. In: *Arxiv* (2020).
- [Tey+10] M. K. Tey et al. “Double degenerate Bose-Fermi mixture of strontium”. In: *Physical Review A* (2010).
- [Tho+13] J. D. Thompson et al. “Coherence and Raman sideband cooling of a single atom in an optical tweezer”. In: *Physical Review Letters* (2013).
- [Vit+01] N. Vitanov et al. “Coherent manipulation of atoms molecules by sequential laser pulses”. In: *Advances In Atomic, Molecular, and Optical Physics*. Elsevier, 2001.
- [VS99] L. Vichi and S. Stringari. “Collective oscillations of an interacting trapped Fermi gas”. In: *Phys. Rev. A* (1999). Publisher: American Physical Society.
- [Wal21] J. Walraven. “Atomic Physics, lecture notes”. In: *University of amsterdam* (2021).
- [WE89] H. Wallis and W. Ertmer. “Broadband laser cooling on narrow transitions”. In: *Journal of the Optical Society of America B* (1989).
- [Wer+92] H. G. C. Werij et al. “Oscillator strengths and radiative branching ratios in atomic Sr”. In: *Physical Review A* (1992).
- [WSW90] T. Walker, D. Sesko, and C. Wieman. “Collective behavior of optically trapped neutral atoms”. In: *Physical Review Letters* (1990).
- [Yas+06] M. Yasuda et al. “Photoassociation spectroscopy of  $^{88}\text{Sr}$ : Reconstruction of the wave function near the last node”. In: *Physical Review A* (2006).
- [YK04] M. Yasuda and H. Katori. “Lifetime measurement of the  $^3\text{P}_2$  metastable state of strontium atoms”. In: *Physical Review Letters* (2004).

# Manipulation of the nuclear spin states of $^{87}\text{Sr}$ in degenerate SU(N)-symmetric Fermi gases

## Abstract

This thesis reviews our implementation of a quantum simulator for the Fermi-Hubbard model with strontium 87. Closed-shell  $^{87}\text{Sr}$  with large nuclear spin  $I=9/2$  benefits from a 7.4 kHz narrow intercombination line that played a central role in this thesis. It offers ideal conditions for the realization of spin orbit coupling schemes to coherently manipulate the 10 nuclear spin states with minimal spontaneous emission. First, we demonstrated a method to measure local densities smaller than the resolution limit of our imaging system. We overcome the limits due to aberrations and fast variations of the density profiles. Derived from the Beer-Lambert law, the non-linear correction lets us infer sizes as small as 1/4 pixel. Then, we prepare polarized Fermi seas of  $^{87}\text{Sr}$  at  $T/T_F \simeq 0.25$ , with a spin purification by optical pumping. The spin populations are measured with a spin orbit coupling scheme associated with the narrow line, realizing a spin dependent momentum transfer. We then demonstrate a method to coherently and selectively flip the spin states. The degeneracy of the ground state is lifted with a quadratic light shift. With a Raman adiabatic passage, the spins are flipped with 80 % efficiency that will be improved up to 95 %. Designed as an optical super lattice, this scheme will permit to write deterministic spin textures that will be the initial state for the quantum simulator. Finally, we study the loading of Fermi gases into the ground band of a 1D lattice with large sites spacing  $2\ \mu\text{m}$ . Our experiment highlights the critical importance of maintaining a sufficient collision rate to adiabatically follow the 3D to 2D dimensionality cross-over, and we simultaneously produce four 2D Fermi seas.

**Keywords:** nuclear spins, strontium 87, spin orbit coupling, Raman adiabatic passage, degenerate Fermi gas, SU(N) symmetry, optical lattices.

---

## Manipulation des états de spin nucléaire du $^{87}\text{Sr}$ dans des gaz de Fermi dégénérés en symétrie SU(N)

### Résumé

Cette thèse présente notre implémentation d'un simulateur quantique pour le modèle de Fermi-Hubbard avec des atomes de strontium 87. Le  $^{87}\text{Sr}$  de grand spin nucléaire  $I=9/2$  bénéficie d'une raie d'intercombinaison étroite de 7.4 kHz jouant un rôle central dans cette thèse. Elle offre un cadre idéal pour manipuler les 10 états de spin nucléaires par couplage spin-orbite avec une émission spontanée minimale. D'abord, nous démontrons une méthode pour mesurer des densités locales non résolues par notre système d'imagerie. Nous surpassons les limites dues aux aberrations et variations rapides du profil de densité, par une correction non-linéaire établie à partir de la loi de Beer-Lambert. Nous déduisons des tailles jusqu'à 0.25 pixel. Ensuite, nous préparons des mers de Fermi de  $^{87}\text{Sr}$  polarisées à  $T/T_F \simeq 0.25$  en utilisant une purification de spin par pompage optique. Les populations de spin sont mesurées par des transferts d'impulsion sélectifs en spin grâce au couplage spin orbit. Nous démontrons de plus une méthode pour retourner les spins de manière cohérente et sélective. La dégénérescence de l'état fondamental est levée par un déplacement lumineux quadratique. Par passage Raman adiabatique, les spins sont retournés avec une efficacité de 80 % qui sera améliorée à 95 %. Conçu comme un réseau optique, cette méthode permettra l'écriture déterministe d'une texture de spin qui sera l'état initial du simulateur quantique. Enfin, nous étudions le chargement d'un gaz de Fermi dans la bande fondamentale d'un réseau 1D de grande période  $2\ \mu\text{m}$ . Nous montrons l'importance de maintenir un taux de collision suffisant pour suivre le cross-over de géométrie de 3D à 2D, et nous produisons simultanément 4 mers de Fermi 2D.

**Mots clefs:** spins nucléaires, strontium 87, couplage spin-orbit, passage adiabatique Raman, gas de Fermi dégénérés, symétrie SU(N), réseaux optiques.